



HAL
open science

Fast transient dynamic multi-model coupling with fluid-structure interaction for complex flows in a finite volume framework

Alexis Picard

► **To cite this version:**

Alexis Picard. Fast transient dynamic multi-model coupling with fluid-structure interaction for complex flows in a finite volume framework. Fluid mechanics [physics.class-ph]. Université Paris-Saclay, 2022. English. NNT: 2022UPAST068 . tel-03865334

HAL Id: tel-03865334

<https://theses.hal.science/tel-03865334v1>

Submitted on 22 Nov 2022

HAL is a multi-disciplinary open access archive for the deposit and dissemination of scientific research documents, whether they are published or not. The documents may come from teaching and research institutions in France or abroad, or from public or private research centers.

L'archive ouverte pluridisciplinaire **HAL**, est destinée au dépôt et à la diffusion de documents scientifiques de niveau recherche, publiés ou non, émanant des établissements d'enseignement et de recherche français ou étrangers, des laboratoires publics ou privés.

Fast transient dynamic multi-model coupling with fluid-structure interaction for complex flows in a finite volume framework

*Couplage multi-modèle en dynamique rapide avec
interaction fluide-structure pour des fluides complexes
calculés par une approche volumes finis*

Thèse de doctorat de l'université Paris-Saclay

École doctorale n°579 : Sciences mécaniques et énergétiques,
matériaux et géosciences (SMEMaG)

Spécialité de doctorat : Mécanique des fluides

Graduate School : Sciences de l'ingénierie et des systèmes

Référent : Faculté des sciences d'Orsay

Thèse préparée dans le **Service d'Études Mécaniques et Thermiques (Université Paris-Saclay, CEA)**, sous la direction de **Christian TENAUD**, directeur de recherche, la co-direction de **Vincent FAUCHER**, directeur de recherche, le co-encadrement de **Nicolas LELONG**, ingénieur-chercheur et **Olivier JAMOND**, ingénieur-chercheur.

Thèse soutenue à Paris-Saclay, le 17 juin 2022, par

Alexis PICARD

Composition du jury

Elisabeth LONGATTE LACAZEDIEU Professeure, Université Paris-Saclay, ENS Paris-Saclay	Présidente
Christophe CORRE Professeur, École Centrale de Lyon	Rapporteur & Examineur
Thierry COUPEZ Professeur, Mines ParisTech	Rapporteur & Examineur
Virginie DARU Maîtresse de conférences, Arts et Métiers ParisTech	Examinatrice
Florian DE VUYST Professeur, Université de Technologie de Compiègne	Examineur
Pascal OMNES Directeur de recherche, Université Paris-Saclay, CEA	Examineur
Christian TENAUD Directeur de recherche, Université Paris-Saclay, CNRS	Directeur de thèse

Titre: Couplage multi-modèle en dynamique rapide avec interaction fluide-structure pour des écoulements complexes calculés par une approche volumes finis

Mots clés: Dynamique rapide, grilles superposées, Chimère, interaction fluide-structure, écoulements compressibles, multi-composants.

Résumé: Le sujet de cette thèse consiste à développer une méthode de calcul numérique permettant de superposer dans un modèle global, un modèle numérique local afin d'introduire des détails géométriques n'existant pas dans le modèle global. Cette méthode s'applique à des écoulements de natures variées (monophasique, multi-composants, réactifs) dans un contexte d'interaction fluide-structure en grands déplacements.

Dans un premier temps, une méthode de grilles superposées appelée méthode Chimère a été implémentée dans un cadre volumes finis avec des milieux fluides. Cette implémentation s'appuie sur des cellules de maillage du fluide pour échanger de l'information entre plusieurs grilles. Une reconstruction de la solution est effectuée en utilisant des cellules dites envoyeuses. La solution fluide transférée est évaluée avec une reconstruction au premier ordre utilisant une moyenne de la solution sur les volumes des cellules envoyeuses intersectées par chaque cellule receveuse. Cette approche a été améliorée avec un passage au deuxième ordre utilisant une reconstruction linéaire de la solution au sein des cellules envoyeuses. Les deux approches ont été testées sur des cas test analytiques dont l'advection d'une perturbation sinusoïdale, le tube à choc de Sod, une onde de choc stationnaire et enfin l'advection d'un vortex isentropique. Ces différents cas ont démontré la capacité de la méthode Chimère à transférer des structures fluides compressibles simples telles que des ondes de choc ou des ondes de détente sans introduire de perturbations à l'échelle globale. La méthode Chimère de second ordre s'est montrée plus proche d'une solution monogridde et moins dépendante de la configuration géométrique des grilles que la méthode de premier ordre en présence de maillages présentant des résolutions très différentes.

La méthode de Chimère de second ordre a été évaluée sur des cas tests de la littérature en 2D dont l'écoulement supersonique autour d'un cylindre circulaire, un cas d'interaction choc-bulle (Hélium et R22) et enfin le cas de la double réflexion de Mach (DMR). Dans chacun de ces cas, la méthode Chimère de second ordre fournit des résultats comparables à une solution monogridde avec une erreur liée à l'utilisation de la méthode Chimère négligeable pour des ratios de taille de cellule entre grilles inférieurs à 8. La méthode Chimère de second ordre permet d'augmenter localement la précision de la solution, autour d'un détail géométrique d'intérêt, sans impacter lourdement le temps de calcul comparé à une approche monogridde raffinée.

Enfin, la méthode Chimère de second ordre a été couplée à une méthode d'interaction fluide-structure, appelée *Mediating Body Method* (MBM). Afin de rendre la méthode Chimère compatible avec la MBM, le couplage Chimère-MBM, s'appuie sur une extrapolation de la solution de part et d'autre de la structure lorsque cette dernière traverse une zone d'échange Chimère. La méthode Chimère-MBM est évaluée sur un cas test analytique de piston libre séparant deux cavités fluides au repos avec des pressions différentes. L'impact de la méthode Chimère-MBM sur la solution fluide est négligeable pour des ratios de taille de cellule entre grilles inférieurs à 8. Un exemple en 3D, s'appuyant sur une cavité haute pression séparée d'une cavité basse pression par une plaque perforée, est présenté. Ce cas test utilise trois grilles fluides indépendantes et sollicite les méthodes Chimère et Chimère-MBM dans le même calcul, démontrant la flexibilité d'usage des méthodes développées. L'utilisation conjointe de ces méthodes permet d'obtenir des niveaux de précision des solutions numériques équivalents à une approche monogridde fine avec des temps de calculs et des contraintes de maillage réduits.

Ce couplage apporte une plus-value notable dans le contexte de l'énergie nucléaire, pour des simulations de situations accidentelles à l'échelle du circuit primaire d'un réacteur nucléaire à eau pressurisée.

Title: Fast transient dynamic multi-model coupling with fluid-structure interaction for complex flows in a finite volume framework

Keywords: Fast dynamics, overlapping grids, Chimera, fluid-structure interaction, compressible flows, multicomponent flows

Abstract: This thesis topic aims to develop a numerical strategy that allows refined local models (mesh size, geometry details, physical models) to be patched on a global model to account for modelling details that are not captured by the larger scale model. This approach is developed in the context of the fluid-structure interaction.

To do so, a method of overlapping grids, referred as the Chimera method, was implemented in a finite volume framework with fluid media only. This implementation relies on grid cells to exchange information between several grids. A reconstruction of the solution is carried out using grid cells marked as sending cells. In this work, the transmitted fluid solution is interpolated with a first order reconstruction by averaging the solution on the volumes of the sending cells intersected by each receiving cell. This approach has been improved using a linear reconstruction of the solution within the sending cells. This improved version is referred to as the second order Chimera method. Both approaches were tested on analytical test cases, including the advection of a sinusoidal perturbation, the Sod shock tube, a stationary shock wave and finally the advection of an isentropic vortex. These different cases have demonstrated the ability of the Chimera method to transfer simple compressible flow structures such as shock waves or rarefaction waves without introducing perturbations on the global scale solution. Overall, the second order Chimera method solution is equivalent to a single grid solution in terms of accuracy. It is also less dependent on the geometric configuration of the grids, compared to the first order Chimera method, in the presence of grid size discrepancies.

The second order Chimera method has been evaluated on two-dimensional test cases from the literature, including the supersonic flow around a circular cylinder, a shock-bubble interaction (Helium and R22) and the Double Mach Reflection (DMR) test case. In each of these cases, the second-order Chimera method provides results comparable to a single grid solution with a Chimera error negligible for cell size ratios between grids lower than 8. The second order Chimera method allows to locally increase the accuracy of the solution, around a geometric detail of interest, without heavily impacting CPU time compared to a refined single grid approach. Finally, the second-order Chimera method was coupled with a fluid-structure interaction method, called Mediating Body Method (MBM). To make the Chimera method compatible with the MBM method, the Chimera-MBM coupling is based on an extrapolation of the solution on both sides of the structure when it crosses a Chimera exchange zone.

The Chimera-MBM is assessed on an analytical test case based on a free piston separating two fluid cavities at rest at different pressures. The impact of the Chimera-MBM on the fluid solution is negligible for cell size ratios between grids lower than 8. A 3D example based on a high-pressure chamber separated from a low-pressure chamber by a perforated plate is presented. This test involves three independent fluid grids and uses both the Chimera method and Chimera-MBM in the same calculation demonstrating the flexibility of the developed methods. Indeed, the combination of these methods makes it possible to obtain levels of accuracy of numerical solutions equivalent to a fine single grid approach with much lower CPU times and less grid constraints.

This multi-model approach provides a significant added value in the context of nuclear energy for brutal accidental situations modelling at the scale of the primary fluid circuit of a pressurized water reactor.

Un problème à la fois,
Une personne sage.

Remerciements

Je tiens à profiter de ces quelques mots pour remercier les personnes qui ont contribué de près comme de loin à la réalisation de ce travail de thèse.

Tout d'abord, je tiens à remercier mes directeurs de thèse à commencer par Christian qui a su m'accompagner pendant ces trois années. Je le remercie pour m'avoir poussé à faire preuve de plus de rigueur dans mes réflexions scientifiques et pour m'avoir incité à parfois revenir à des choses simples comme une feuille de papier et un crayon. Je souhaite ensuite remercier Vincent qui m'a grandement aidé à prendre du recul sur mes travaux et à consolider le fil conducteur de mon travail.

Je tiens évidemment à remercier mes deux encadrants: Olivier et Nicolas. Avec moi au quotidien avant la crise du COVID-19, ils ont su m'écouter dans mes questionnements existentiels et ce n'est pas rien. Je souhaite remercier Olivier pour m'avoir permis de développer sur Mefisto et d'approfondir mes connaissances en C++. Un bagage qui m'accompagne aujourd'hui dans ma vie quotidienne et pour lequel je lui suis très reconnaissant. Je souhaite remercier Nicolas qui a su être à l'écoute de mes questions et de mes doutes au cours de ces trois années. Je tiens aussi à le remercier pour les moments passés à discuter de sujets diverses et variés sortants du cadre de la thèse comme les jeux vidéos pour n'en citer qu'un.

Je souhaite témoigner ma profonde gratitude aux membres du jury pour l'intérêt qu'ils ont porté à mon travail et leurs questions pertinentes et constructives. Je tiens à remercier en particulier Christophe Corre et Thierry Coupez pour leur examen détaillé de mon manuscrit de thèse et la qualité de leur rapport. Enfin, je tiens à remercier Elisabeth Longatte Lacazedieu pour avoir accepté de présider ma soutenance de thèse.

Ensuite, je souhaiterais remercier les membres du laboratoire DYN et le SEMT pour m'avoir accueilli pendant ces trois années dans une ambiance conviviale et chaleureuse. Une pensée particulière pour mes collègues doctorants: Stan, Huan et Roberto qui ont partagé mon quotidien pendant toute cette période et qui ont contribué à leur manière à mes travaux de thèse.

On dit que derrière chaque grand homme se cache une femme. Si je n'ai pas la prétention de me qualifier de grand homme, je peux affirmer avoir trouvé une grande femme. Même si les mots me manquent pour décrire l'impact positif qu'elle a eu dans mon travail, je tiens à remercier ma fiancée, Isadora, pour avoir été présente à mes côtés dans un voyage qu'elle n'a pas choisie et qui pourtant a orienté notre chemin de vie. Tu as su m'épauler comme personne dans ce projet et me supporter dans les moments difficiles. Je ne saurais te remercier suffisamment pour la motivation et la rigueur que tu m'as apportées, tes conseils lors des étapes de rédaction ainsi que ton aide et ton soutien indéfectible lors des sessions de préparation de l'oral.

Pour terminer, je tiens à remercier ma famille qui m'a toujours poussé à aller au bout des choses et à ne rien lâcher.

À vous tous, merci.

Contents

Introduction	1
1 Finite volume framework for fast dynamic problems	13
1.1 Governing equations for fast transient inviscid flow problems	13
1.1.1 Inviscid compressible flow model: the Euler equations	14
1.1.2 Perfect gas equation of state	15
1.2 Discretization of the inviscid equation model	16
1.2.1 The Godunov method	16
1.2.2 Riemann problem for the one-dimensional Euler equations	17
1.2.3 An approximate Riemann solver: the HLLC solver	19
1.2.4 The second order MUSCL reconstruction	22
1.2.5 Time discretization: the second order MUSCL-Hancock method (MHM)	24
1.2.6 Discretization of the non-conservative term for multicomponent flows	25
1.3 Chapter conclusion	26
2 Development of a finite volume multi-grid Chimera method in a fast dynamic framework	27
2.1 The Chimera method principle	28
2.2 Development of a finite volume Chimera method	30
2.2.1 Chimera framework and notations	30
2.2.2 Identification and marking of the ghost cells allowing two grid communication	32
2.2.3 Derivation of a first and second order Chimera interpolation	36
2.2.4 Study of the number of ghost cell layers dependency on the discretization scheme	41
2.2.5 Impact of the Chimera method on the time step	42
2.3 Implementation of the Chimera method in MANTA software	43
2.3.1 Presentation of MANTA software	43
2.3.2 Implementation of the Chimera procedure within the solver	43
2.4 Validation of the Chimera method on 1D test cases	48
2.4.1 Solution reconstruction over overlapping grid domains	48
2.4.2 Sinus advection	49
2.4.3 Split Sod shocktube	61
2.4.4 Conservation properties of the present Chimera method	71
2.5 Advection of an isentropic vortex	76
2.5.1 Impact of the Chimera sending on the order of convergence	78
2.5.2 Impact of the cell ratio (χ) on the solution	81
2.6 Chapter conclusion	83
3 Numerical study of the finite volume Chimera method ability to transfer compressible flow structures based on reference test cases	85
3.1 Flow around a circular cylinder at Mach = 3	86
3.1.1 Presentation of the case	86
3.1.2 Steady state horizontal pressure force analysis	87
3.1.3 Shock standoff measurements	92
3.2 Interaction of a shock wave moving in air with a bubble	93

3.2.1	Presentation of the case	93
3.2.2	Helium bubble-shock wave interaction	94
3.2.3	R22 bubble-shock wave interaction	97
3.2.4	Summary of the findings on the behavior of the Chimera method with multi- component flows	100
3.3	Double Mach Reflection problem	101
3.3.1	Presentation of the case	101
3.3.2	Comparison of the Chimera case with the single grid case ($\chi = 1$)	103
3.3.3	Comparison of the Chimera case with the equivalent fine single mesh (EFSM) for various values of χ	103
3.4	Chapter conclusion	108
4	An overlapping grid embedded boundary method for compressible flows coupled to deformable thin structures: the Chimera Mediating Body Method	109
4.1	Governing equations and discretization of the problem	110
4.1.1	Structural system of equations	110
4.1.2	Coupling conditions	110
4.1.3	Structure discretization : the finite element method	111
4.1.4	Explicit time integration of the structure	111
4.2	Discretization of the coupling conditions: the Chimera-MBM	112
4.2.1	Presentation of the Mediating Body Method	112
4.2.2	Coupling of the Mediating Body Method with the Chimera method: the Chimera-MBM	121
4.3	Numerical validation of the method and applications	134
4.3.1	One-dimensional free piston	134
4.3.2	Three-dimensional separated chambers with a perforated plate	154
4.4	Chapter conclusion	166
5	Conclusion and open prospects	167
	Appendices	169
A	Ghost cell layer dependency for an advection equation using a second order MUSCL- Hancock scheme	171
B	Von Neumann stability analysis of the Chimera method	173
C	Problematic configurations using the Chimera-MBM	177
C.1	Ghost cells belonging to a $+/-$ neighboring active cell set and receiving from an active cell	177
C.2	Ghost cells belonging to a $+/-$ neighboring active cell set and receiving from an indefinite sending cell	178
C.3	Indefinite active cells using ghost cells (MBM extrapolation)	179
D	Analytical solution for the free piston test case	181
D.1	Presentation of the problem	181
D.2	Study of the piston dynamics	182
D.2.1	Fundamental principle of dynamics applied to the piston	182
D.2.2	Computation of the left fluid pressure $p(x_s^L, t)$ exerted on the piston	184
D.2.3	Computation of the right fluid pressure $p(x_s^R, t)$ exerted on the piston	184

D.2.4	Time integration of the piston dynamics	185
D.3	Computation of the fluid solution	187
D.3.1	L^* region	187
D.3.2	R^* region	188
	Synthèse du manuscrit en français	191

List of Figures

1	Reactor vessel internals (left) and lower core support structure (right). Examples of complex multi scale geometries. (source: [175]).	2
2	The retaining plate perforations (circled in black) and the core vessel are independently meshed. The proposed strategy is to superimpose local alterations (mesh on the right) of the plates in the domain representing the reactor (mesh on the left) in order to improve the accuracy of the global calculation without altering the grids of the global parts.	3
3	Separated chambers example: The global fluid mesh (\mathcal{W}) is represented in black, the separating wall (\mathcal{S}) in green, the first patch (\mathcal{V}_1) that contains the structure is in blue while the finer second patch (\mathcal{V}_2) that captures the perforation is represented in red.	8
1.1	Structure of the solution of the Riemann problem for the one-dimensional Euler equations on the $\eta-t$ plane. Unknown waves (shock waves or rarefaction fans) are depicted by a pair of rays emanating from the origin.	18
1.2	Possible wave patterns in the solution of the Riemann problem: (a) left rarefaction, contact, right shock, (b) left shock, contact, right rarefaction, (c) left rarefaction, contact, right rarefaction, (d) left shock, contact, right shock.	19
1.3	Control volume $[\eta_L, \eta_R] \times [0, T]$ on the $\eta-t$ plane. S_L and S_R are respectively the extreme characteristic velocity for the left-hand side wave and the right-hand side wave from the solution of the Riemann problem. Unknown waves (shock waves or rarefaction fans) are depicted by a pair of rays emanating from the origin.	20
1.4	Area where the solution is limited with the K-Dubois limiter in a single model approach. The area is identical for the Barth and Jespersen limiter [97].	24
2.1	Three main implementations of the Chimera method found in the literature.	29
2.2	Explicit and Implicit Chimera coupling.	30
2.3	Sketch of the transfer procedure in the developed Chimera method.	31
2.4	Definition of the resolved cells set for an immersed patch (\mathcal{V}).	31
2.5	Standard detection procedure of the developed Chimera method.	33
2.6	Schema of an overlapping grid configuration with a recirculation zone (\mathcal{V}^{rc}).	34
2.7	Ghost cell detection procedures for $k_{GC} = 2$ with $\chi = 4$	35
2.8	Identification of the recirculation zones for high cell ratios (χ).	35
2.9	Example of a ghost cell intersection \tilde{K}_i' with \mathcal{W} for a first order interpolation.	36
2.10	Example of a ghost cell intersection \tilde{K}_i' with \mathcal{W} for a second order interpolation.	37
2.11	Definition of the reconstruction sets \mathcal{W}^r and \mathcal{V}^r given the ghost cell sets $\tilde{\mathcal{W}}$ and $\tilde{\mathcal{V}}$	38
2.12	Hypothetical extension of the exchange zone to ensure empty intersections between the ghost cell sets and the reconstruction sets (with the same grid configuration as in Fig. 2.11).	39
2.13	Search areas for the K-Dubois limiter in a single model approach and the modified K-Dubois limiter used in the Chimera method. The searchable area in the single model approach is identical to the Barth and Jespersen limiter searchable area [97].	40
2.14	Evolution of the positions between the center of the intersection with the sending cell and the center of the sending cell.	40
2.15	Chimera boundary condition.	41
2.16	Neighbor dependency near the cleaned patch boundary ($\Gamma_{\tilde{\mathcal{V}}}$).	42

2.17	Chimera configuration with the exchange zone gap (δ_{GC}) and the exchange zone shift (δ_S).	42
2.18	Structure of the code MANTA.	43
2.19	Implementation of the Chimera procedures within the fluid solver for a first order sending.	45
2.20	Implementation of the Chimera procedures within the fluid solver for a second order sending.	47
2.21	Field merging of overlapping grid configurations for comparisons with single grid cases.	48
2.22	Scalar advection test case: initial solution of a square sinus distribution (see equation 2.22).	50
2.23	Sinus advection test case: grid arrangements for the split Chimera configuration.	50
2.24	Grid convergence analysis of the sinus advection case for the split domain with equivalent cell sizes between the patch and the substrate ($\chi = 1$) and non-coincident grids ($\delta_S = 0.3 h_W$). $h = h_W = h_V$ and h_0 corresponds to $N_{cells} = 3200$	52
2.25	Exchange zone shift analysis: results on density (ρ) errors obtained with with the present Chimera approach using a patch with same grid spacing as the substrate ($N_{cells} = 200$, $\chi = 1.0$) with variable exchange zone shift (δ_S) and the standard detection procedure.	53
2.26	Density profile at $t = t_f$ for the single grid case and the first order Chimera sending with matching grids ($\delta_S = 0$) and non-matching grids ($\delta_S = 0.9 h_W$) with $N_{cells} = 200$ and $\chi = 1$, compared to the analytical solution. The markers on the plots are not representative of the number of points of the numerical solution.	54
2.27	Sinus advection test case: grid arrangements for the patched Chimera configuration.	57
2.28	Grid convergence analysis of the sinus advection case for the patched configuration with equivalent cell sizes between the patch and the substrate ($\chi = 1$). $h = h_W = h_V$ and h_0 corresponds to $N_{cells} = 3200$	58
2.29	Shocktube test case: grid arrangements for the single grid and Chimera configurations.	61
2.30	Shocktube test case - focus on the expansion wave: density profile at $t = t_f$ for both the Chimera methods and the single grid configurations with $N_{cells} = 200$, $\chi = 1$ and $\delta_S = 0.6 h_W$. The markers on the plots are not representative of the number of points of the numerical solution.	62
2.31	Shocktube test case - focus on the expansion wave: density profile at $t = t_f$ for single grid configurations with $N_{cells} = 200$ and different values of χ . The markers on the plots are not representative of the number of points of the numerical solution.	64
2.32	Shocktube test case - focus on the expansion wave: density profile at $t = t_f$ for single grid and Chimera configurations with $N_{cells} = 200$, $\chi = 16$ and $\delta_S = 0.6 h_W$. The markers on the plots are not representative of the number of points of the numerical solution.	65
2.33	Shocktube test case - focus on the shock wave: density profile at $t = t_f$ for both the Chimera methods and the single grid configurations with $N_{cells} = 200$, $\chi = 1$ and $\delta_S = 0.6 h_W$. The markers on the plots are not representative of the number of points of the numerical solution.	66
2.34	Shocktube test case - focus on the shock wave: density profile at $t = t_f$ for single grid configurations with $N_{cells} = 200$ and different values of χ . The markers on the plots are not representative of the number of points of the numerical solution.	68

2.35 Shocktube test case - focus on the shock wave: density profile at $t = t_f$ for single grid and Chimera configurations with $N_{cells} = 200$, $\chi = 16$ and $\delta_S = 0.6 h_{\mathcal{W}}$. The markers on the plots are not representative of the number of points of the numerical solution.	69
2.36 Stationary shock wave grid configuration for coincident grids and non-coincident grids with the shock wave located at $x = 0$	72
2.37 Density profile of the stationary shock wave converged solution in a single grid configuration with $N_{cells} = 25$ and Chimera configurations (first and second order exchanges) with coincident and non-coincident grids for $N_{cells} = 25$ and $\chi = 1$ compared to the reference solution. The markers on the plots are not representative of the number of points of the numerical solution.	72
2.38 Density profile of the stationary shock wave converged solution of Chimera configurations with coincident ($\delta_S = 0$) and non-coincident ($\delta_S = 0.3 h_{\mathcal{W}}$) grids for $N_{cells} = 25$ and χ varying from 2 to 16 compared to the reference solution. The markers on the plots are not representative of the number of points of the numerical solution.	75
2.39 Resulting pressure field of the isentropic vortex case at $t^* = t_f^*$ for the single grid configuration with $N_{cells} = 640$	77
2.40 Isentropic vortex grid configuration for the Chimera case with $\chi = 2$	78
2.41 Grid convergence analysis of the isentropic vortex case with equivalent cell sizes between the patch and the substrate ($\chi = 1$). $h = h_{\mathcal{W}} = h_{\mathcal{V}}$ and h_0 corresponds to $N_{cells} = 640$	79
2.42 Pressure profile at $t^* = t_f^*$ along $y = 0$ for the single grid configuration as well as the Chimera cases with $N_{cells} = 80$ and $\chi = 1$. The markers on the plots are not representative of the number of points of the numerical solution.	79
2.43 Resulting pressure field of the isentropic vortex case at $t^* = t_f^*$ for the Chimera case using the first order sending (a) and the second order sending (b) with $N_{cells} = 40$ and $\chi = 16$ both using the standard detection procedure.	81
2.44 Pressure profile at $t^* = t_f^*$ along $y = 0$ for the single grid configuration as well as the Chimera cases with $N_{cells} = 40$ and $\chi = 16$. The markers on the plots are not representative of the number of points of the numerical solution.	82
3.1 Circular cylinder test case: computational domain and initial solution.	86
3.2 Grid configuration for the single mesh case and the Chimera case.	87
3.3 Steady state density field for both Chimera case (on the left), and the single grid case (on the right) with a cell ratio of unity ($\chi = 1$), obtained at a dimensionless time $t^* = 52$ and for $N_{cells} = 200$ grid cells along the cylinder perimeter.	88
3.4 Time history of the pressure drag force for several number of grid cells (N_{cells}) obtained on both the single grid configuration, and the overlapping grids with however similar grid spacings ($\chi = 1$). The markers on the plots are not representative of the number of points of the numerical solution.	89
3.5 Zoom in the interval dimensionless times $t^* \in [45, 52.5]$ of the pressure drag force history for several number of grid cells (N_{cells}), obtained on both the single grid configuration and the overlapping grids with however similar grid spacings ($\chi = 1$). The markers on the plots are not representative of the number of points of the solution.	90
3.6 Resulting pressure force over time for the second study cases ($N_{cells} = 100$, $\chi = 1$), ($N_{cells} = 200$, $\chi = 2$) and ($N_{cells} = 400$, $\chi = 4$). The markers on the plots are not representative of the number of points of the numerical solution.	91

3.7	Resulting pressure force over time for the second study cases ($N_{cells} = 100, \chi = 1$), ($N_{cells} = 200, \chi = 2$) and ($N_{cells} = 400, \chi = 4$) zoomed in the time interval [45, 52.5]. The markers on the plots are not representative of the number of points of the numerical solution.	91
3.8	Geometric illustration of the flow structure in front of the cylinder.	92
3.9	Shock wave / Bubble interaction: initial conditions taken from Layes <i>et al.</i> experiments [106] and computational domain.	93
3.10	Bubble shock test case numerical configuration.	94
3.11	Helium volume fraction field obtained with a single grid configuration with $N_{cells} = 200$ at two different dimensionless times $t^* = 0.24$ and $t^* = 1.6$	94
3.12	Helium volume fraction field obtained in the single mesh case at $t^* = 1.6$, for a number of cells along the bubble diameter of $N_{cells} = 50$ (on the left), 100 (in the middle), and 200 (on the right).	95
3.13	Helium volume fraction field obtained with the present Chimera method with overlapping grids with the same cell ratio ($\chi = 1$) at $t^* = 1.6$, for a number of cells along the bubble diameter of $N_{cells} = 50$ (on the left), 100 (in the middle), and 200 (on the right).	96
3.14	Helium volume fraction field obtained with the present Chimera approach, at a dimensionless time $t^* = 1.6$, by using several cell ratios ($\chi = 1, 2, 4, 8$).	97
3.15	R22 volume fraction field obtained with a single grid configuration with $N_{cells} = 200$ at two different dimensionless times $t^* = 0.23$ and $t^* = 2.28$	98
3.16	R22 volume fraction field obtained in the single mesh case at $t^* = 2.28$, for a number of cells along the bubble diameter of $N_{cells} = 50$ (on the left), 100 (in the middle), and 200 (on the right).	98
3.17	R22 volume fraction field obtained with the present Chimera method with overlapping grids with the same cell ratio ($\chi = 1$) at $t^* = 2.28$, for a number of cells along the bubble diameter of $N_{cells} = 50$ (on the left), 100 (in the middle), and 200 (on the right).	99
3.18	R22 volume fraction field obtained with the present Chimera approach, at a dimensionless time $t^* = 2.28$, by using several cell ratios ($\chi = 1, 2, 4, 8$).	100
3.19	Sketch of the self-similar structure of the Double Mach Reflexion (DMR) problem	101
3.20	Computational domains and initial conditions: configurations of the single mesh case (a), and the Chimera case (b) displayed with a cell ratio $\chi = 4$	102
3.21	Density contours obtained with the present Chimera approach (black iso-contour lines) with the standard detection compared to the single mesh case (red iso-contour lines) at an equivalent dimensionless time $t^* - t_0^* = 0.2$ for $N_{cells} = 160$ and $\chi = 1$. 30 density contours from $\rho = 1.4$ to 21.4. Dashed white line materializes the patch boundary.	103
3.22	Density contours obtained with the present Chimera approach (black iso-contour lines) by using $N_{cells} = 80$ cells on the substrate and a cell ratio $\chi = 2$ on the patch, compared to the single mesh case (red iso-contour lines) with $N_{cells} = 160$, at an equivalent dimensionless time $t^* - t_0^* = 0.2$. 30 density contours from $\rho = 1.4$ to 21.4. Standard detection procedure (a) compared to the extended detection procedure (b).	104
3.23	Density contours obtained with the present Chimera approach (black iso-contour lines) by using $N_{cells} = 80$ cells on the substrate and a cell ratio $\chi = 4$ on the patch, compared to the single mesh case (red iso-contour lines) with $N_{cells} = 320$, at an equivalent dimensionless time $t^* - t_0^* = 0.2$. 30 density contours from $\rho = 1.4$ to 21.4. Standard detection procedure (a) compared to the extended detection procedure (b).	105

3.24	Density contours obtained with the present Chimera approach (black iso-contour lines) by using $N_{cells} = 80$ cells on the substrate and a cell ratio $\chi = 8$ on the patch, compared to the single mesh case (red iso-contour lines) with $N_{cells} = 640$, at an equivalent dimensionless time $t^* - t_0^* = 0.2$. 30 density contours from $\rho = 1.4$ to 21.4. Standard detection procedure (a) compared to the extended detection procedure (b).	106
3.25	Density contours obtained with the present Chimera approach (black iso-contour lines) by using $N_{cells} = 80$ cells on the substrate and a cell ratio $\chi = 16$ on the patch, compared to the single mesh case (red iso-contour lines) with $N_{cells} = 640$, at an equivalent dimensionless time $t^* - t_0^* = 0.2$. 30 density contours from $\rho = 1.4$ to 21.4. Standard detection procedure (a) compared to the extended detection procedure (b).	107
4.1	Simplified flow chart of the coupling algorithm.	112
4.2	mediating body construction for a single grid.	113
4.3	Fluid cell intersection with the structure.	114
4.4	Example of virtual remeshing of a two-dimensional face.	116
4.5	Examples of virtual remeshing of the faces at the interface between the active fluid (\mathcal{U}_*) and the mediating body (\mathcal{U}_{Γ_s}), whose cells are represented in yellow shade, for two-dimensional simple meshes. The permeable interfaces are represented by thin green lines while the moving walls are represented by thin red lines.	117
4.6	Indefinite active cells in grey shade	119
4.7	Time integration scheme for the Mediating Body Method with a MUSCL-Hancock integration for the fluid and a central difference scheme for the structure.	119
4.8	Mediating body construction with an overlapping grid configuration.	121
4.9	Cleaned patch (\mathcal{V}_c) and cleaned substrate (\mathcal{W}_c) sets of cells.	122
4.10	Underestimation of the fluid forces computed using the mediating bodies \mathcal{W}_{Γ_s} and \mathcal{V}_{Γ_s} .	124
4.11	Indefinite sending cells and indefinite ghost cells when using the Mediating Body Method combined with the Chimera method with a number of ghost cell layers $k_{GC} = 1$ and a Chimera cell ratio $\chi = 2$.	126
4.12	Indefinite sending cells subcell decomposition and extrapolation	127
4.13	Indefinite sending cells complete treatment.	129
4.14	Indefinite ghost cell impact on the fluid domain.	130
4.15	Indefinite ghost cell treatment possibilities.	131
4.16	Time integration scheme for the Chimera-Mediating Body Method with a MUSCL-Hancock integration for the fluid and a central difference scheme for the structure.	132
4.17	Free piston case presentation.	135
4.18	Free piston split configuration.	135
4.19	Free piston density (ρ), velocity (u) and pressure (p) profiles of the split configuration for the Chimera-MBM case as well as the single grid MBM case when $\chi = 1$ and $N_{cells} = 300$ at $t = t_f^*$. The markers on the plots are not representative of the number of points of the numerical solution.	136
4.20	Free piston density (ρ), velocity (u) and pressure (p) profiles of the split configuration for the Chimera-MBM case as well as the single grid MBM case when $\chi = 1$ and $N_{cells} = 1200$ at $t = t_f^*$. The markers on the plots are not representative of the number of points of the numerical solution.	137
4.21	Grid convergence analysis of the free piston test case with the split configuration and equivalent cell sizes between the patch and the substrate ($\chi = 1$).	137

4.22	Free piston density (ρ) profile of the split configuration for the Chimera-MBM as well as the single grid MBM when $N_{cells} = 300$ and $\chi = 1, 2, 4$ at $t = t_f^*$. The markers on the plots are not representative of the number of points of the numerical solution.	139
4.23	Free piston density (ρ) profile of the split configuration for the Chimera-MBM as well as the single grid MBM when $N_{cells} = 300$ and $\chi = 4, 8, 16$ at $t^* = t_f^*$. The markers on the plots are not representative of the number of points of the numerical solution.	139
4.24	Free piston density (ρ) profile of the split configuration for the Chimera-MBM as well as the single grid MBM when $N_{cells} = 4800$ and $\chi = 0.25, 0.125, 0.0625$ at $t^* = t_f^*$. The markers on the plots are not representative of the number of points of the numerical solution.	140
4.25	Free piston system mass relative error of the split configuration for the Chimera-MBM as well as the single grid MBM when N_{cells} varies and $\chi = 1$ over time. The markers on the plots are not representative of the number of points of the numerical solution.	142
4.26	Explanation of the variations in system total mass at the patch boundaries when the structure enters the patch.	142
4.27	Free piston system mass relative error of the split configuration for the Chimera-MBM as well as the single grid MBM when $N_{cells} = 300$ and $\chi = 1, 2$ and 4 (finer patch) over time. The markers on the plots are not representative of the number of points of the numerical solution.	143
4.28	Free piston system mass relative error of the split configuration for the Chimera-MBM as well as the single grid MBM when $N_{cells} = 300$ and $\chi = 4, 8$ and 16 (finer patch) over time. The markers on the plots are not representative of the number of points of the numerical solution.	143
4.29	Free piston system mass relative error of the split configuration for the Chimera-MBM as well as the single grid MBM when $N_{cells} = 300$ and $\chi = 1, 0.5$ and 0.25 (coarser patch) over time. The markers on the plots are not representative of the number of points of the numerical solution.	144
4.30	Free piston system mass relative error of the split configuration for the Chimera-MBM as well as the single grid MBM when $N_{cells} = 300$ and $\chi = 0.25, 0.125$ and 0.0625 (coarser patch) over time. The markers on the plots are not representative of the number of points of the numerical solution.	145
4.31	Free piston patched configuration.	146
4.32	Free piston density (ρ), velocity (u) and pressure (p) profiles of the patched configuration for the Chimera-MBM as well as the single grid MBM when $\chi = 1$ and $N_{cells} = 300$ at $t = t_f^*$. The markers on the plots are not representative of the number of points of the numerical solution.	147
4.33	Grid convergence analysis of the free piston case with the patched configuration and equivalent cell sizes between the patch and the substrate ($\chi = 1$).	148
4.34	Free piston density (ρ) profile of the patched configuration for the Chimera-MBM as well as the single grid MBM when $N_{cells} = 300$ and $\chi = 1, 2, 4$ at $t = t_f^*$. The markers on the plots are not representative of the number of points of the numerical solution.	149
4.35	Free piston density (ρ) profile of the patched configuration for the Chimera-MBM as well as the single grid MBM when $N_{cells} = 1200$ and $\chi = 4, 8, 16$ at $t^* = t_f^*$. The markers on the plots are not representative of the number of points of the numerical solution. The markers on the plots are not representative of the number of points of the numerical solution.	150

4.36	Free piston system mass relative error of the patched configuration for the Chimera-MBM case as well as the single grid MBM case when N_{cells} varies and $\chi = 1$ over time. The markers on the plots are not representative of the number of points of the numerical solution.	151
4.37	Free piston system mass relative error of the patched configuration for the Chimera-MBM case as well as the single grid MBM case when $N_{cells} = 300$ and $\chi = 1, 2$ and 4 (finer patch) over time. The markers on the plots are not representative of the number of points of the numerical solution.	151
4.38	Free piston system mass relative error of the patched configuration for the Chimera-MBM case as well as the single grid MBM case when $N_{cells} = 300$ and $\chi = 4, 8$ and 16 (finer patch) over time. The markers on the plots are not representative of the number of points of the numerical solution.	152
4.39	3D chambers case presentation	154
4.40	3D chambers grid configuration for the plate. The first row of cells around the perimeter of the hole contains square cells of a side $h_U = 0.04$ m.	155
4.41	Three-dimensional chambers grid configuration for the Chimera-MBM case. The computational domain contains a coarse substrate (in black), a finer first patch (in blue) that contains the perforated membrane (in green) and an even finer second patch (in red) that helps improving the accuracy around the perforation	156
4.42	x -displacement of the plate extremity around the perforation perimeter at $z = 0$. The monitored node is initially located at $(x, y, z) = (0., r_c, 0.)$	157
4.43	y -displacement of the plate extremity around the perforation perimeter at $z = 0$. The monitored node is initially located at $(x, y, z) = (0., r_c, 0.)$	157
4.44	Velocity magnitude field ($\ \underline{u}\ $) obtained with the coarse single grid MBM case (a), the Chimera-MBM case (b) and the fine single grid MBM case (c) at the dimensionless time $t^* = 0.1$	158
4.45	Velocity magnitude field ($\ \underline{u}\ $) obtained with the coarse single grid MBM case (a), the Chimera-MBM case (b) and the fine single grid MBM case (c) at the dimensionless time $t^* = 0.5$	159
4.46	Velocity magnitude field ($\ \underline{u}\ $) obtained with the coarse single grid MBM case (a), the Chimera-MBM case (b) and the fine single grid MBM case (c) at the dimensionless time $t^* = 1$	161
4.47	Velocity magnitude field ($\ \underline{u}\ $) obtained with the coarse single grid MBM case (a), the Chimera-MBM case (b) and the fine single grid MBM case (c) at the dimensionless time $t^* = 2$	162
4.48	Velocity magnitude field ($\ \underline{u}\ $) obtained with the coarse single grid MBM case (a), the Chimera-MBM case (b) and the fine single grid MBM case (c) at the dimensionless time $t^* = 3$	163
4.49	Velocity magnitude field ($\ \underline{u}\ $) obtained with the coarse single grid MBM case (a), the Chimera-MBM case (b) and the fine single grid MBM case (c) at the dimensionless time $t^* = t_j^* = 3.75$	164
A.1	Chimera boundary condition.	171
B.1	Chimera configuration with exchange zone gap (δ_{GC}) and exchange zone shift (δ_S).	173
C.1	Problematic configuration where the indefinite sending cell K_j extrapolates from a ghost cell K_l	177

C.2	Problematic configuration where the ghost cell \tilde{K}_m belongs to the $+/-$ neighboring of K_j but receives from indefinite sending cells K'_p and K'_m	179
C.3	Problematic configuration where the indefinite active cell K'_k uses the ghost cell \tilde{K}'_i to extrapolate its value.	180
D.1	Free piston case presentation with an infinite domain.	181
D.2	Wave pattern of the free piston case.	183
D.3	Characteristics of the left hand side domain of the free piston solution.	184
D.4	Characteristics of the right hand side domain of the free piston solution.	185
D.5	Piston position x_s and velocity \dot{u} over time.	186
D.6	Description of the characteristics in the expansion fan region.	187
D.7	Description of the characteristics in the compression wave region.	189
D.8	Free piston density ρ , velocity u and pressure p profiles at $t^* = t_f^*$ of the analytical solution.	190
5.9	Les perforations des plaques de cloisonnement (entourées en noir) et la cuve du réacteur sont maillés indépendamment. La stratégie proposée consiste à superposer des altérations locales (maillage de droite) sur plaques de cloisonnement au sein d'un modèle global à grande échelle représentant la cuve du réacteur (maillage de gauche) dans le but d'améliorer la qualité des résultats numériques sans altérer les grilles du modèle global.	192
5.10	Exemple simplifié représentatif des applications visées. Chambres séparées par une paroi hermétique à l'échelle globale. Une chambre contenant de l'eau liquide sous haute pression en bleu foncé et une chambre contenant de la vapeur d'eau sous basse pression en bleu clair. Perforation locale de la paroi ajoutée à l'aide d'un patch induisant une fuite entre les deux chambres à l'échelle locale.	192
5.11	Exemple de méthode <i>Adaptive Mesh Refinement</i> appliquée à une grille typiquement utilisée pour modéliser un écoulement fluide autour d'un cylindre ou bien une perforation de plaque.	193
5.12	Exemple d'utilisation de la Méthode Arlequin avec une grille de fond appelée substrat (en noir) et une grille locale appelée patch (en rouge). La zone de couplage est ici représentée en vert.	193
5.13	Exemple d'utilisation de la Méthode Chimère avec une grille de fond appelée substrat (en noir) et une grille locale appelée patch (en rouge). La zone d'échange est matérialisée par les deux contours fermés définis par les points d'interpolations.	194
5.14	Interpolation Chimère de premier ordre basée sur les volumes d'intersection entre chaque cellule fantôme et ses cellules envoyeuses.	196
5.15	Interpolation Chimère de second ordre basée sur une reconstruction linéaire de la solution au sein de chaque cellule envoyeuse. Chaque solution est ensuite évaluée au centre de l'intersection entre la cellule fantôme et la cellule envoyeuse correspondante.	197
5.16	Présentation schématique de la <i>Mediating Body Method</i> . Le <i>mediating body</i> est représenté en jaune. Lorsque la structure subit de grands déplacements, les anciennes cellules du <i>mediating body</i> désormais cellules de fluide sont appelées cellules de fluide indéfinies et sont représentées en gris.	199
5.17	Exemple de configuration de grille dans le cadre de la méthode Chimère-MBM. Le <i>mediating body</i> du patch est représenté en bleu tandis que le <i>mediating body</i> du substrat est représenté en jaune.	200

5.18 Schéma de l'extrapolation +/- exécutée pour une cellule envoyeuse intersectée par la structure. Deux états sont reconstruits pour cette cellule de part et d'autre de la structure. 200

List of Tables

2.1	Grid convergence analysis of the split configuration: results on density (ρ) errors obtained with a single grid configuration as well as with the present Chimera approach using a patch with same grid spacing as the substrate ($\chi = 1$) and coincident grids ($\delta_S = 0$).	51
2.2	Grid convergence analysis of the split configuration: results on density (ρ) errors obtained with a single grid configuration as well as with the present Chimera approach using a patch with same grid spacing as the substrate ($\chi = 1$) and non-coincident grids ($\delta_S = 0.3 h_W$).	52
2.3	Cell ratio analysis of the split configuration: results on density (ρ) errors obtained with with the present Chimera approach using a patch with a coincident Chimera interface ($\delta_S = 0$) and variable cell ratios (χ) with the standard detection procedure. The transfer occurs from a coarse substrate ($N_{cells} = 200$) to a finer patch. We have also reported the errors of the equivalent coarse single mesh (ECSM) and the equivalent N_{cells} on the patch for equivalent fine single mesh (EFSM) comparisons.	55
2.4	Cell ratio analysis of the split configuration: results on density (ρ) errors obtained with with the present Chimera approach using a patch with a coincident Chimera interface ($\delta_S = 0$) and variable cell ratios (χ) with the standard detection procedure. The transfer occurs from a fine substrate ($N_{cells} = 3200$) to a coarser patch. We have also reported the errors of the equivalent coarse single mesh (ECSM) and the equivalent N_{cells} on the patch for equivalent coarse single mesh (ECSM) comparison.	55
2.5	Cell ratio analysis of the split configuration: results on density (ρ) errors obtained with with the present Chimera approach using a patch with non-coincident Chimera interface ($\delta_S = 0.6 h_W$) and variable cell ratios (χ) for both the standard and extended detection procedures. The transfer occurs from a coarse substrate ($N_{cells} = 200$) to a finer patch. Equivalent N_{cells} on the patch are reported for equivalent fine single mesh (EFSM) comparison.	56
2.6	Cell ratio analysis of the split configuration: results on density (ρ) errors obtained with with the present Chimera approach using a patch with non-coincident Chimera interface ($\delta_S = 0.6 h_W$) and variable cell ratios (χ) for both the standard and extended detection procedures. The transfer occurs from a fine substrate ($N_{cells} = 3200$) to a coarser patch. Equivalent N_{cells} on the patch are reported for equivalent coarse single mesh (ECSM) comparison.	56
2.7	Grid convergence analysis of the patched configuration: results on density (ρ) errors obtained with a single grid configuration as well as with the present Chimera approach using a patch with same grid spacing as the substrate ($\chi = 1$).	58
2.8	Cell ratio analysis of the patched configuration: results on density (ρ) errors obtained with the present Chimera approach using a patch and variable cell ratios (χ) for both the standard and extended detection procedures. The substrate comprises $N_{cells} = 200$ grid cells. Equivalent N_{cells} on the patch are reported for equivalent fine single mesh (EFSM) comparison.	59

2.9	Grid convergence analysis of the Sod shocktube - focus on the expansion wave: results on density (ρ) errors obtained with a single grid configuration as well as with the present Chimera approach using a patch with same grid spacing as the substrate ($\chi = 1$) and non-coincident grids ($\delta_S = 0.6 h_W$).	63
2.10	Cell ratio analysis of the Sod shocktube - focus on the expansion wave: results on density (ρ) errors obtained with the single grid configuration as well as with the present Chimera approach using a patch with non-coincident Chimera interface ($\delta_S = 0.6 h_W$) and variable cell ratios (χ) for both the standard and extended detection procedures. The transfer occurs from a coarse substrate ($N_{cells} = 200$) to a finer patch. Equivalent N_{cells} on the patch are reported for equivalent fine single mesh (EFSM) comparison.	64
2.11	Grid convergence analysis of the Sod shocktube - focus on the shock wave: results on density (ρ) errors obtained with a single grid configuration as well as with the present Chimera approach using a patch with same grid spacing as the substrate ($\chi = 1$) with non-coincident grids ($\delta_S = 0.6 h_W$).	67
2.12	Cell ratio analysis of the Sod shocktube - focus on the shock wave: results on density (ρ) errors obtained with the single grid configuration as well as with the present Chimera approach using a patch with non-coincident Chimera interface ($\delta_S = 0.6 h_W$) and variable cell ratios (χ) for both the standard and extended detection procedures. The transfer occurs from a coarse substrate ($N_{cells} = 200$) to a finer patch. Equivalent N_{cells} on the patch are reported for equivalent fine single mesh (EFSM) comparison.	68
2.13	System mass, momentum and energy relative error computed on the converged solution with a single grid configuration as well as with the present Chimera approach using a patch with the same grid spacing as the substrate ($N_{cells} = 25$, $\chi = 1$) with a stationary shock wave matching the patch boundary.	72
2.14	System mass, momentum and energy relative error computed on the converged solution with a single grid configuration as well as with the present Chimera approach using a patch with different grid spacings and a stationary shock wave matching the patch boundary and coincident interfaces ($\delta_S = 0$).	76
2.15	System mass, momentum and energy relative error computed on the converged solution with a single grid configuration as well as with the present Chimera approach using a patch with different grid spacings and a stationary shock wave matching the patch boundary and non-coincident interfaces ($\delta_S = 0.3 h_W$).	76
2.16	Grid convergence analysis of the vortex case: results on pressure (p) errors obtained with a single grid configuration as well as with the present Chimera approach using a patch with same grid spacing as the substrate ($\chi = 1$).	80
2.17	Cell ratio analysis of the vortex case: results on pressure (p) errors obtained with the present Chimera approach using a variable cell ratios (χ) and $N_{cells} = 80$. Equivalent N_{cells} on the patch are reported for equivalent fine single mesh (EFSM) comparison.	81
2.18	Time and memory cost of the Chimera method: time and memory ratio of the present Chimera approach using a variable cell ratios (χ) compared to the equivalent fine single mesh (EFSM). The higher the better. Equivalent N_{cells} on the patch are reported for equivalent fine single mesh (EFSM) comparison.	82
3.1	Average resulting pressure force over $t^* \in [40, 52.5]$ for the first study cases ($\chi = 1$).	88

3.2	Results obtained with the Chimera cases when the patch is refined and the substrate resolution is fixed (equivalent to $N_{cells} = 100$), compared with their equivalent fine single mesh computations (EFSM).	90
3.3	Detachment distance of the bow shock wave in front of the cylinder: overlapping grids with the proposed Chimera cases. On the left side, number of cells are increased keeping the cell ratio ($\chi = 1$) constant. On the right side, cell ratio (χ) is varied with a prescribed number of cells in the substrate model (equivalent to $N_{cells} = 100$). . .	92
3.4	Results obtained with the Chimera cases ($N_{cells} = 80$) for different values of χ , compared with their equivalent fine single mesh (EFSM) computations.	108
4.1	Cell type combinations for the coupling of the Chimera method with the MBM. . . .	125
4.2	Grid convergence analysis of the free piston with the split configuration: results on density (ρ) errors obtained with a single grid MBM as well as with the present Chimera-MBM using a patch with same grid spacing as the substrate ($\chi = 1.0$) but with non-coincident grids ($\delta_S = 0.6 h_W$).	138
4.3	Cell ratio analysis of the free piston with the split configuration: results on density (ρ) errors obtained with a single grid MBM as well as with the present Chimera-MBM using a finer grid in the patch region ($N_{cells} = 300, \chi \geq 1$).	140
4.4	Cell ratio analysis of the free piston case with the split configuration: results on density (ρ) errors obtained with a single grid MBM as well as with the present Chimera-MBM using a coarser grid in the patch region ($N_{cells} = 4800, \chi \leq 1$).	141
4.5	Grid convergence analysis of the free piston with the patched configuration: results on density (ρ) errors obtained with a single grid MBM as well as with the present Chimera-MBM using a patch with same grid spacing as the substrate ($\chi = 1.0$) but with non-coincident grids ($\delta_S = 0.3 h_W$).	148
4.6	Cell ratio analysis of the free piston with the patched configuration: results on density (ρ) errors obtained with the present Chimera-mediated body approach using a finer grid in the patch ($N_{cells} = 300, \chi \geq 1$).	150
4.7	Fluid mass variation of the low pressure chamber between $t^* = 0$ and $t^* = t_f^* = 3.75$	165
4.8	CPU time ratio and memory usage ratio of the fine single grid MBM configuration to the coarse single grid MBM configuration and the Chimera-MBM configuration.	166

Nomenclature

Finite volume and Chimera important notations

- \mathcal{U} Discretized domain or grid represented as a set of cells.
- $\Omega_{\mathcal{U}}$ Set of indices of the cells belonging to \mathcal{U} .
- K_i Fluid cell with $i \in \Omega_{\mathcal{U}}$.
- $\gamma(i)$ Index set of the cells adjacent to K_i , $i \in \Omega_{\mathcal{U}}$.
- $|K_i|$ Volume of the fluid cell K_i .
- $\mathcal{F}_{ij}^{\mathcal{U}}$ Interface separating the cell K_i to the cell K_j , $(i, j) \in \Omega_{\mathcal{U}} \times \gamma(i)$.
- (x, y, z) Global cartesian coordinate system.
- (η, ξ, ζ) Local coordinate system in the frame of a face $\mathcal{F}_{ij}^{\mathcal{U}}$.
- $\underline{U}_i^{\mathcal{U}^n} / \underline{W}_i^{\mathcal{U}^n}$ Vector of conservative/ primitive variables of the cell $K_i \in \mathcal{U}$ at the discrete time t^n .
- $\underline{U}_{ij}^{\mathcal{U}^n} / \underline{W}_{ij}^{\mathcal{U}^n}$ Interface state based on conservative/ primitive variables at $\mathcal{F}_{ij}^{\mathcal{U}}$ at the discrete time t^n .
- $\overline{U}_{ij}^{\mathcal{U}^n} / \overline{W}_{ij}^{\mathcal{U}^n}$ Reconstructed interface state based on conservative/ primitive variables at $\mathcal{F}_{ij}^{\mathcal{U}}$ at the discrete time t^n .
- \underline{u} Fluid velocity vector.
- \mathcal{W}/\mathcal{V} Global/Local grid referred as Substrate/Patch.
- $\Gamma_{\mathcal{V}}$ Patch boundary.
- $\widetilde{\mathcal{W}}/\widetilde{\mathcal{V}}$ Substrate/Patch cells that receive information from the other grid. They are referred as ghost cells.
- $\mathcal{W}^s/\mathcal{V}^s$ Substrate/Patch cells that send information to the other grid. They are referred as sending cells.
- N_{cells} Number of grid points over a specified length that determine the grid resolution on the substrate.
- χ Ratio of the minimum cell size of the substrate to the minimum cell size of the patch in the exchange zone.
- $\mathcal{W}_c/\mathcal{V}_c$ Substrate/Patch cells that do not belong to the ghost cell sets. They are referred as resolved cells and the resulting set is called cleaned substrate/patch. In the case of the cleaned substrate, it also includes the cells that are fully overlapped by the cleaned patch.
- \mathcal{W}_p Substrate cells belonging to $\mathcal{W} \setminus \widetilde{\mathcal{W}}$ fully overlapped by the cleaned patch \mathcal{V}^c .
- $\Gamma_{\widetilde{\mathcal{V}}}$ Interface between the ghost cell set $\widetilde{\mathcal{V}}$ and the cleaned patch \mathcal{V}^c .

ECSM Equivalent coarse single mesh of a Chimera configuration involving grids with different resolutions. The ECSM corresponds to a single grid configuration with a uniform grid resolution equivalent to the coarsest grid in the Chimera configuration.

EFSM Equivalent fine single mesh of a Chimera configuration involving grids with different resolutions. The EFSM corresponds to a single grid configuration with a uniform grid resolution equivalent to the finest grid in the Chimera configuration.

Fluid-structure interaction important notations

\mathcal{S} Discretized structural domain represented as a set of elements.

$\Gamma_{\mathcal{S}}$ Structure midsurface defined as the mediane plane to the structure meshed using \mathcal{S} .

C_i Structure element with $i \in \Omega_{\mathcal{S}}$.

$\underline{u}, \underline{\dot{u}}, \underline{\ddot{u}}$ Structure displacement, velocity and acceleration vectors.

$\mathcal{S}_{\mathcal{V}}$ Structure element set containing elements fully immersed inside \mathcal{V}^c .

$\mathcal{N}_{\mathcal{S}}$ Structure node set.

$\mathcal{N}_{\mathcal{S}}^{\mathcal{V}}$ Structure nodes located inside \mathcal{V}^c .

$\mathcal{U}_{\Gamma_{\mathcal{S}}}$ Mediating Body defined using fluid cells from the grid \mathcal{U} .

\mathcal{U}_{*} Active fluid cells of the grid \mathcal{U} defined as $\mathcal{U} \setminus \mathcal{U}_{\Gamma_{\mathcal{S}}}$.

$\mathcal{U}_{*\text{indef}}$ Indefinite active fluid cells of the grid \mathcal{U} .

Introduction

Studying accidental situations involving highly pressurized systems or explosive transients in large and complex geometries is of importance for dimensioning facilities and for safety issues in industrial environments. Such accidental situations can be found in the nuclear framework of Pressurized Water Reactor (PWR) when Loss of Primary Coolant Accidents (LOCAs) [132] or H₂ explosions [99] occur. PWRs involve high temperature and pressure conditions (≈ 153 atm and $275 - 315^\circ\text{C}$ [153]) that make accidental situations of such systems abrupt with severe possible consequences.

The brutal accidental context implies compressible flow features such as discontinuities (shock waves or contact discontinuities), rarefaction fans or acoustic waves travelling at high speeds. These flow features interact with each other resulting in complex flows with vortical structures from baroclinic effect when multi-phasic or multicomponent mixtures are at play. Fast transient energetic flows may also finally interfere with deformable structures inducing coupled phenomena at very small time scales ($10^{-6} - 10^{-3}$ s [56]). Considering the scale discrepancies and the high pressures involved, deformable structural elements can also undergo displacements of finite amplitude.

Due to the risks and the general difficulty to perform tests with fully representative geometry and initial conditions in the range described above, numerical simulation appears to be a powerful way to characterize the response of the systems during such transients. Producing accurate and reliable results in these configurations represents a challenging task since the computational domain must account simultaneously for the largest scale of the geometry and for small geometrical details inducing local flow patterns with significant influence on the global solution. Dealing with all the scales within one mesh classically yields huge numbers of grid points and complex meshing procedures that can end up with poor quality grids. The geometrical complexity and the scale discrepancies of such systems is illustrated in Figure 1 representing the internals (a) and the support structure (b) of a PWR core. In addition to the geometrical complexity constraint, the single mesh approach is also restrictive when fluid and structural domains are modelled with conformant meshes for immersed structures. The meshing procedure difficulty increases and the displacement of structural components is restricted to preserve the shape of the cells in the connected fluid mesh.

One elegant solution to address those two folds is then to associate, within one composite simulation, independent numerical models, in terms of both geometry and mesh, each adapted to the physical phenomena of interest at different time and space scales. This helps decomposing the complex geometry into simpler parts and allows for modular meshing that helps reducing the overall computational cost of the simulation while being more fitted to the problem geometry. With a composite grid approach, structural components can undergo large displacements without altering the grid of the fluid domains. In the mean time, local fluid grids can be added to take into account the local flow features generated by the moving structures.

Despite the many benefits that characterize the composite approach, it rises several concerns that do not exist with a single grid approach and that need to be addressed. One of them is the impact of a coupling between different fluid grids or between different structural grids on the global solution. Another one is the compatibility of the coupling process for fluid-structure interactions (FSI) with the fluid grid coupling mentioned above. In most cases, the use of composite grids in a large scale simulation also involves non-matching grids with different cell sizes and different critical time steps. If a unique time step is chosen, it is based on the smallest cell size and its impact on the stability of global domain remains to be assessed.

In this thesis, we address the need for a numerical tool able to improve global complex simulations of fast transient dynamics by adding local geometrical details that can be deformable. This numerical

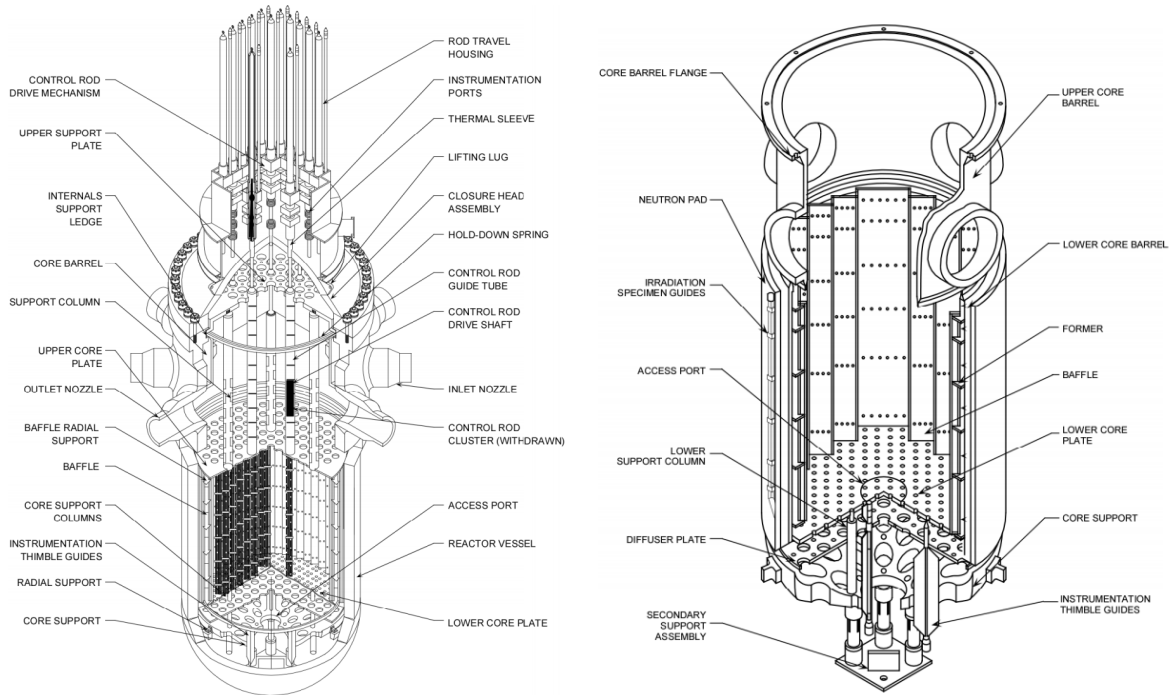


Figure 1: Reactor vessel internals (left) and lower core support structure (right). Examples of complex multi scale geometries. (source: [175]).

strategy is based on a composite grid approach and proposes a solution to the concerns mentioned above. As a result, the proposed numerical strategy must fulfil the following requirements:

1. It must allow the introduction of localized geometrical alterations or details in a large scale global numerical model.
2. As compressible flow features such as shock waves, contact discontinuities and rarefaction fans are at play and can interact with each others, a particular attention is paid to system mass, momentum and total energy conservation of the numerical scheme for the fluid domains. Therefore, the proposed approach is chosen to be developed in the framework of the finite volume method.
3. In readiness for an industrial usage, this strategy should offer a high flexibility and user-friendliness. In particular, the proposed method must be as unconstrained from the grid used as possible and the local grid must not require any modification of the large scale one. This is why, the proposed approach relies on the introduction of the considered alteration in a local grid which is overlaid over the global one.
4. The local model can be meshed finer than the global grid to increase the accuracy of the solution near the introduced alteration. Therefore, the proposed approach must be able to deal with multiple grids, each one having its own refinement.
5. It must be fully compatible with fluid-structure interactions (FSI) and more specifically with deformable structural components that undergo large displacements.

An example of the targeted approach is illustrated in Figure 2 with a global scale grid representing the core vessel and a patched overlaid grid that can contain a geometrical detail like the perforation of a retaining plate with an adapted local grid. In this configuration, the core vessel can be modelled

with a coarse grid containing the retaining plates without any perforation that is referred as global model. A local fluid patch containing a local perforation of the retaining plate can be patched onto this global model. It is referred as local model. The local fluid grid aims to capture local fluid phenomena generated by the local perforation.

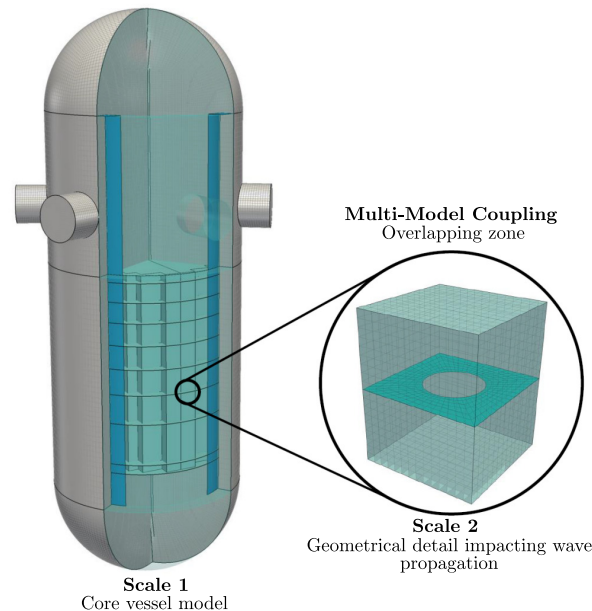


Figure 2: The retaining plate perforations (circled in black) and the core vessel are independently meshed. The proposed strategy is to superimpose local alterations (mesh on the right) of the plates in the domain representing the reactor (mesh on the left) in order to improve the accuracy of the global calculation without altering the grids of the global parts.

Now that the characteristics of the numerical strategy are specified, we review existing methods that aim to tackle similar issues. In order to give a comprehensive review, we chose to go through known composite grid methods and underline if and how they are compatible with the requirements that we outlined.

Bibliography

Composite grid methods have been a topic of interest since 1960s with initial work from *Volkov* [180, 181] on the use of additional grids to smooth the high order finite difference solution of the Laplace equation and the Poisson equation at the boundaries of the domain. Composite grid methods have been mainly developed from a finite difference framework for both elliptic and hyperbolic problems [163, 164, 117] with an important interest for aircraft applications [9, 10]. Since then, the composite grid field has been closely related to multi-model methods and multi-scale methods as it allows the use of different models on different grids with possibly large spatial scale discrepancies [105]. In the following, we consider two families of composite grid methods : the hierarchical grid techniques and the overlapping grid techniques. Both categories use multiple grids and allow local numerical zooms.

Hierarchical grid techniques

The first category of composite grid techniques that we review gathers various methods under the name of hierarchical grid techniques. Each of these methods use multiple grid hierarchically organized

to model different scales of the same physical problem. These methods are usually designed to model a two-scale physical phenomenon with a macroscopic grid and a microscopic one. Other methods use several scale levels to provide a smooth and modular grid refinement. The different grid levels are coupled through operators able to transfer information between grids of different levels. This type of methods has often been used for heterogeneous media modelling [186] and often rely on homogenisation techniques to ensure compatibility between the large and small scale domains as used in [152].

The first hierarchical grid methods considered are the multi-grid methods. Multi-grid methods have initially been used for elliptic problems [76] using an implicit finite difference method and rely on high wave number filtering of elliptical operators. The use of coarse and fine grids allows a better capture of the frequency components of the discrete solutions in a reduced number of iterations compared to a single grid approach. The transfer of the solution happens through restriction operators or prolongation operators [26]. As demonstrated by *Fish* and *Belsky*, multi-grid methods are adapted to study the behavior of periodical composite structures [65, 66]. The multi-grid methods have been extended to hyperbolic systems [102, 5] and specifically to the Euler equations with implicit [128] and explicit [90] schemes. The main idea is to increase the order of the numerical scheme using a refined version of a base coarse grid for steady state applications [91]. However, multi-grid methods have been mainly used to model steady state problems [124, 125] and they have not been designed to introduce local geometrical alterations.

Following this idea of a localized increased accuracy, Adaptive Mesh Refinement (AMR) has been developed jointly by *Berger*, *Oliger* and *Colela* [22, 20]. The method consists in adapting the accuracy of a solution within certain sensitive or turbulent regions of a simulation, dynamically and during the time the solution is being calculated. The global mesh ends up as a composite grid with different levels of grids adjusting dynamically to the flow. However, with the AMR approach, the introduction of a localized alteration of the geometry in the large scale numerical model is not straightforward. Also it does not provide the flexibility of using non-matching grids. Then the proposed approach does not involve AMR, even though it could certainly be used in a complementary way.

The same conclusion can be drawn for the Multi-Scale Finite Volume Method (MSFV) [95]. Initially developed for incompressible flows and transport in porous media, the MSFV method consists in using a coarse Cartesian grid with a finite volume conservative scheme and to reconstruct from the coarse pressure field, a local fine velocity field using two sets of basis functions and transmission operators. This method has been extended to multiphase porous media [96] and compressible flows [116] but also poroelasticity [161]. Regarding composite grid methods, the MSFV method has been adapted to a multi-levels of grids [103] instead of two and has been used similarly to AMR as an adaptive refinement tool in [127]. As mentioned earlier, even though this type of methods allows for local adaptive refinement, it does not allow the use of independently meshed grids.

Some multi-grid methods using independent grids have been experimented. The Hierarchical Dirichlet Projection Method (HDPM) [129] is one of them and uses a hierarchical set of grids corresponding to the level of physical description of the problem. Sorted from the coarsest to the finest level, a first coarse solution is computed. A user-based error criteria is used to estimate the quality of the solution. Areas where the error criteria is not matched are refined with the coarse solution as a boundary value. Once, the error criteria is met on the entirety of the domain, the fine solutions are projected back onto the coarse grid. This method has mainly been used to model the behavior of composite structures [131, 130]. Like the HDPM, various techniques have been developed using independent grids to model multi-scale phenomena like the Two-scale Finite Element (FE²) method [63] that uses microscopic grids at key integration points of a coarse grid in order to get a more accurate physical description of the problem. This method allowed *Feyel et al.* to model elastoviscoplastic behavior of composite materials [62] and *Ramière et al.* to approximate the

behavior of heterogeneous nuclear fuel [146]. Similar approaches with independent grids have been developed for incompressible inviscid flow in [3, 4] with the use of a secondary grid, representing a fixed obstacle, patched onto a cartesian global mesh. However, it is more comparable to a restricted fluid-structure interaction (FSI) method with non-deformable solid than a multi-grid fluid method as the secondary grid does not model fluid.

Even though some of these multi-grid methods use independent grids to model different scales or to model local geometrical details, they have mainly been designed and validated for the computations of steady state solutions which is a limiting factor for our brutal accidental context. Also, they mainly focus on the multi-scale aspect which is not the primary objective of our work. The solution that suits our need is a composite grid method with non-matching grids allowing for geometrical details to be added on a global finite volume simulation through a local grid. This is the objective of overlapping grid techniques.

Overlapping grid techniques

The Arlequin Method

The first overlapping grid method that we are interested in is the so-called Arlequin method that has been introduced by H. Ben Dhia [37]. He conceived an approach for the resolution of superimposed models with non conforming meshes and/or different modelling for static and quasi-static cases [38]. The main idea of the Arlequin method is to use a partition of unity to superimpose models with weights parameters to split the total energy between each model and to use a coupling operator defined over a volumic area on the periphery of the local model. It has been applied to a large panel of problems starting from structural problems like beam study [151, 43, 27, 39], crack propagation [41] and contact problems [40]. In [42, 149], the Arlequin method is extended to a 3D framework with plates and hulls. More recently, the Arlequin method has been used with an explicit-implicit time integration allowing the modelling of rotating machinery with multiple time stepping [69, 68]. Even though we are not interested in multi-scale methods, the Arlequin method has been extensively used in multi-scale modelling with a global continuum model and a local atomistic model [142, 143, 13, 30].

Regarding fluid dynamics, the Arlequin method has been applied to fast transient problems [61] as well as some incompressible flow problems [93, 45]. The present work also benefits from the previous work carried out by *Fernier et al.* [60], in which the relevance of the Arlequin method for structural fast transient dynamic simulations with explicit-explicit time integration is demonstrated. However, the Arlequin method shows some limitations with fluid fast transient dynamics in [59] with the appearance of ghost forces and numerical artifacts that require a filtering procedure. Also, it has been designed for a finite-element framework and would require a conversion to our framework as, to the best of our knowledge, the Arlequin method has not been used in a finite volume context.

The Chimera Method

The second method considered is the Chimera method developed by Steger and Benek [166] and further extended in [17] and [165]. The main idea of the Chimera method is to allow independent and non-matching grids to transfer information using existing cells or nodes as a receiving container. Like the Arlequin method, the Chimera method requires an overlapping zone for the information to be transferred. It also presents the same flexibility but has been designed for a finite difference framework and has been translated to a finite volume framework. The Chimera method has been extensively reviewed with a finite difference framework for compressible turbulent flows with the code Overture [82, 83, 84, 32, 157] and NASA [119, 120, 141, 12], mostly for aircraft applications as the Chimera method can be used to simplify mesh generation with independent composite grid assemblies. The

method has also been used for wave propagation [7], incompressible flows [174, 50] and inviscid compressible flows [184, 185]. In each case, the Chimera method provides a good solution for overlapping grids apart from introducing an interpolation error which can be compensated by using a higher order interpolation for the exchange procedure than the order of the numerical scheme. Recently, the Chimera method has been transposed to a finite volume framework and has been tested for various aircraft applications with compressible turbulent flows with the codes elsA [64, 136] and TAU [154, 187] but also in [8].

The Chimera method has also been used with inviscid compressible flows in [19] where the time integration is implicit as they are not dealing with fast transient dynamics. In [86, 87], the Chimera method is combined with AMR for reactive flows. Several references can be found on the use of a Chimera method combined with moving cartesian grids [19], [150] for rotor computations or complex aircraft geometries [104]. In this thesis, the topic of moving grids is not of primary importance and will not be investigated. In other words, we are focusing on applications in which a geometrical detail contained inside a local grid generates compressible flow structures such as shock waves, contact discontinuities or rarefaction fans. These local flow structures propagate from the local grid and cross the overlapping grid interface to spread over the global grid and eventually affect the global grid solution. Without a local grid, these flow structures would not be captured by a coarse global grid and a fine global grid would dramatically increase computational costs. More recently, high order Chimera methods have also been developed like in [107] with global to local frame transformations and in [148, 147] with a Moving Least Squares reconstruction technique.

When dealing with overlapping grids and compressible transient flows, system mass, momentum and total energy conservation must be ensured for capturing discontinuities involved in shock waves and contact discontinuities. *Berger* gave a definition of the concept of global conservation for multi-grid hyperbolic systems [21]. This definition states that an overlapping grid system is globally conservative if, for a steady state flow, on the outside boundary of the global domain, the numerical approximation of $\int_{\Gamma} \underline{u}(\underline{x}, t) dS$, is independent of time, with $\underline{u}(\underline{x}, t)$ the exact solution of the hyperbolic system. In [133] and [18], conservative interpolation schemes are reviewed. It is stated that the only way to achieve a conservative interpolation is to use a flux interpolation scheme. However, it is pointed out that schemes based on flux interpolation are not stable. Therefore, a compromise between stability and conservation has to be made. Also, it is advised to avoid discontinuities crossing the overlapping interface. However, *Pärt* and *Sjögreen* [133], obtained a strongly stable and nearly conservative interface condition which is based on conservative variables. In [188], *Wu* demonstrated using the stability theory of Gustafsson Kreiss Sundström (GKS) [74] that a conservative treatment of overlapping exchange zone leads to weakly stable solutions. In [189, 108], *Lerat* and *Wu* also concluded that stability with non-conservative interpolations should be favored instead of conservative interpolations with unstable solutions.

Other approaches have bypassed the interpolation problem by modifying the discretization in the overlapping region. In [184, 184, 25], the overlapping grid interface is intersected by the global grid and fluxes are splitted accordingly forcing local conservation. In [101, 100, 23], the entire overlapping zone is remeshed with unstructured grids. Remeshing the overlapping zone has been proven to be conservative and stable but computationally expensive [183].

In most of the mentioned applications, if the Chimera method is not used as a flexible mesh generation tool it is often used to improve the accuracy around a patched geometrical detail for a better capture of the boundary layer for instance [150, 87]. In this thesis, the local grid aims to improve the geometrical complexity by introducing geometrical details that will generate flow features like shock waves, contact discontinuities or rarefaction fans. These flow features can remain inside the patch but they can also cross the overlapping grid boundary. Either way, they impact the global solution and could only be captured with a complex and fine grid with a standard single mesh

approach. Even if *Péron* [136] stated that it is more desirable to have similar cell sizes, few works have been found to thoroughly assess the Chimera method with variable cell sizes between the grids. As a result, the Chimera method seems the most promising method for adding local geometrical details in a finite volume framework even though some properties of the method still need to be tested in the context of fast transient dynamics.

The review made on the composite grid techniques only includes fluid-fluid or structure-structure cases. As the Chimera method has been retained as the solution for our finite volume framework, we now focus on the coupling of the Chimera method with fluid-structure interaction (FSI) methods.

Fluid-Structure Interaction methods for large displacements and coupling with Chimera methods

Fast transient phenomena involve compressible flow structures like shock waves, contact discontinuities and rarefaction waves. These flow components interact with structural deformable components. As a result, structures can undergo large displacements and rotations. Non-linear behaviors like plasticity and/or damage can be associated to the various structural components of the system. As a consequence, well-known Arbitrary Lagrangian Eulerian (ALE) approaches [44, 85, 123] reach a limit where it is not possible for the fluid to follow the displacements of the structures without impacting the fluid solution due to extremely low quality cells. It often induces a remeshing of the fluid domain. In the case of fixed complex 3D geometries, the meshing procedures are already extremely difficult for single mesh fluid simulation and become even more complex for ALE simulations due to conformity constraints. These constraints generally increase the number of grid points and can cause low quality elements that will impact the numerical fluid solution. The grid constraint between fluid and structural components can be lifted by using an Immersed Boundary (IB) method [138, 139, 36]. Initially proposed by *Peskin*, the IB method breaks the topological connection between the fluid and structure grids and provides the flexibility and robustness to handle complex structural geometries in motion for industrial applications [55, 94]. Since then, immersed boundary approaches have been extended with immersed interface methods [109, 111, 112], Fictitious Domain approaches [71, 72], Ghost Fluid methods [58, 57, 54, 173], Direct Forcing approaches [122, 191, 51, 137], cut-cell methods [135, 52, 34, 46, 155, 81, 88, 123, 144, 145] or Discrete Interface methods [29, 14, 182, 92]. The immersed boundary type of method is often preferred where ALE methods fails. However, immersed boundary methods can be used with ALE fluid meshes to enforce a Lagrangian behavior of an interface or to track a particular region [53].

Among the immersed boundary methods, cut-cell methods have been specifically developed for hyperbolic problems like compressible flows. They consist in subdividing fluid cells that are intersected by the structural mesh to conform to the fluid-structure interface which naturally cope with the fluid cells passing from one side of an obstacle to the other. With this type of approach, merging techniques for the small cells are required to preserve stability. Even though cut-cell methods can ensure system mass, momentum and total energy conservation, they are not designed to work with thin structures. Also, they are incompatible with non-manifold and non-connex structure parts within a cell. This makes cut-cell methods difficult to use in a context of large scale fluid simulation where structural parts like plates are often modelled using shells.

Discreted Interface methods like the Mediating Body Method (MBM) [14, 92] use fluid cells crossed by the structure interface as a mediating body between the fluid and the structure. In [92], the structure geometry is averaged within each crossed fluid cell through the introduction of an averaged normal pseudo-projection operator. This operator allows a virtual remeshing of the mediating body cell faces to decompose each face into an impermeable wall part acting as a moving wall for the fluid and a permeable wall that will absorb part of the fluxes. This virtual remeshing allows for an accurate estimation of the pressure force exerted by the fluid on the structure. A

particular treatment is applied to fluid cells which cross the embedded structure *i.e.*, which lie at a given time on one side of the structure and lie on the other side at further time. This problem was initially adressed in [115] under the name "extrapolation of the solution" and further extended in [193] as "ghost to real". In [182], an extrapolation based on the work of [54] is done while in [92], the extrapolation is done using neighboring cells that are not crossed by the structure. An ALE emulation technique is detailed in [92] to take into account the fluid volume swept by the structure when it remains contained inside the same fluid cell set between two discrete time steps. The ALE emulation reduces the impact of the method on system mass, momentum and total energy conservation when the structure undergoes small displacements.

The extrapolation problem is still under development with recent work from [156] that uses a hybrid cartesian immersed boundary method [70] with ghost cells for solution reconstruction near immersed boundary interface. As they are dealing with sharp edges, an interface tracking procedure based on ray tracing algorithm and a new three step solution reconstruction has been developed. Such procedures provide accurate results but require heavy reconstruction procedures and geometrical computations.

In a framework of large scale system involving fast transient FSI, the coupling of an immersed boundary (IB) technique like the Mediating Body Method [92] and an overlapping grid technique like the Chimera method for the finite volume fluid simulation is interesting for several reasons which can be illustrated with the example of the separated chambers shown in Figure 3. The global fluid mesh \mathcal{W} contains the outer geometry of the chambers. The global mesh is chosen coarse as it covers a large geometrical domain. A local grid referred as first patch \mathcal{V}_1 brings with it the separating wall \mathcal{S} independently meshed from the fluid. The coupling between the first patch and the structure is made using an IB method such as the MBM [92] while the coupling between the first patch \mathcal{V}_1 and the global grid \mathcal{W} is made using a Chimera method. The separating wall \mathcal{S} contains a perforation that is smaller than the first patch grid cell size. Therefore, the perforation is not captured by the fluid model and the chambers remain sealed. Using a coupling between the IB method and the Chimera method that we call Chimera-IB method, a second patch \mathcal{V}_2 finer than the first one can be added in order to capture the perforation and generate a leak between the two chambers.

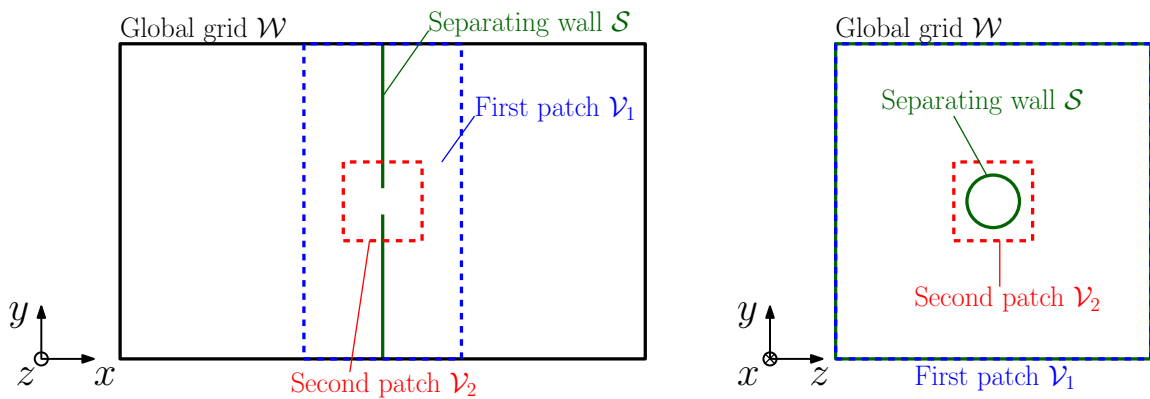


Figure 3: Separated chambers example: The global fluid mesh (\mathcal{W}) is represented in black, the separating wall (\mathcal{S}) in green, the first patch (\mathcal{V}_1) that contains the structure is in blue while the finer second patch (\mathcal{V}_2) that captures the perforation is represented in red.

This example is a direct simplification of the problematics involved in brutal accidents like LOCAs or H_2 explosions with complex geometries like the one presented in Figure 2. Large and geometrically complex systems cannot be modelled with a single grid with a reasonable amount of time. A numerical tool that allows a set of simpler local grids compatible with fluid-structure interactions (FSI) to be patched onto a coarser global grid can drastically improve the workflow of the numerical modelling

of complex systems. First, a Chimera-IB method can improve the global solution with local grids that fit the geometry of the problem or the flow physics but with a reduced impact on computational cost compared to a fine single grid approach as it uses less total grid points. Secondly, as the Chimera method is coupled with an immersed boundary (IB) method, the structure deformations and displacements do not impact the fluid grid which preserves its initial quality unlike a Chimera-ALE approach [67, 121]. Finally, a Chimera-IB method could offer the flexibility to easily change the interior layout of the large model reducing the time currently required for grid generation process. Even though it is not the primary objective of this thesis, a possible feature of a Chimera-IB method could be to follow the motion of each structure component with a local moving fluid grid attached to it. This would be particularly useful if small structural components undergo large displacements like in debris modelling.

The topic of Chimera-IB coupling techniques is relatively new with initial work on incompressible flow from [126] and more recent works like [140, 168, 137] on compressible turbulent flows for aircraft applications. All of those works use a direct forcing IB method. To the best of our knowledge, very few references are available on the Chimera-IB coupling for inviscid compressible flows in transient regimes and we have not been able to find any work on a Chimera-IB coupling using a discrete interface immersed boundary method like the MBM [92].

Partial conclusion

A wide variety of methods have been used to superimpose local geometrical alterations onto a global domain. As we are mainly interested in the flexibility of the method and the independence between the grids employed, the composite grid techniques like the Arlequin method and the Chimera method appear as a promising solution. They allow local grids to be patched onto global models without modifying the large scale grids. The Arlequin method has already been experimented with an equivalent context but in a finite element framework in [59]. It has shown limitations regarding fast transient fluid dynamics and the translation to a finite volume framework is not straightforward. On the contrary, the Chimera method has been widely investigated and is used as an industrial meshing tool for aircraft applications. Therefore, the Chimera method has been retained in our work and needs to be implemented and assessed for different fast transient dynamic applications with industrial accuracy requirements, user-friendliness and robustness constraints. Various aspects of the Chimera method still need to be examined from a finite volume perspective like the compatibility with high cell ratios between the grids or the impact of the interpolation used in a context of fast transient dynamics involving shock waves, contact discontinuities and rarefaction waves but also interfaces between different fluid components.

In a framework of brutal accidental situations with fast transient dynamics involving large structural displacements, immersed boundary methods are widely used for complex geometries involved in industrial applications. As conservation is key when dealing with compressible flow structures like shock waves and contact discontinuities, cut-cell methods [123, 144, 145] are promising regarding total system mass, momentum and total energy conservation but they involve computationally heavy geometrical procedures at each iterations. On the other hand, discrete interface methods like the Mediating Body Method [92], require less geometrical intersections and benefits from an ALE emulation that improves conservation properties of the method. As a result, it is an interesting compromise between conservation and computational cost that suits industrial specifications. To the best of our knowledge, the coupling of an IB method like the MBM with an overlapping grid technique like the Chimera method has not been done yet.

These shortcomings justify the work presented in this thesis. It consists in developing a numerical tool able to superimpose different grids when simulating fast transient phenomena in a finite volume framework with an explicit time integration. This tool aims to improve the workflows of large and

complex fast transient systems modelling such as LOCAs or H_2 explosions. Therefore, it must be compatible with fluid-structure interaction (FSI) through the use of an immersed boundary method such as the MBM [92]. This numerical strategy must be user-friendly and flexible as it must use independent grids and must be robust enough to handle large cell ratios between the grids. The proposed strategy is automated and implemented inside the MANTA software designed for explicit dynamics and currently in development at the DYN laboratory in the *Service d'étude mécaniques et thermiques* (SEMT) at the Commissariat à l'Énergie Atomique et aux Énergies Alternatives.

Presentation of the scientific approach of this work

The present manuscript is organised as follows:

In chapter 1, we introduce the fluid models and the finite volume framework that we will be using including the spatial and time integration schemes and the type of limiters for high order finite volume schemes considered in this work.

In chapter 2, we detail the development of a finite volume Chimera method for fast transient dynamics. We start by introducing the concepts involved in the framework of Chimera methods such as cell detection, marking and interpolation. As our version of the Chimera method relies on the injection of information from one grid to the other using existing fluid cells as receiving containers, we detail the detection and marking procedure that we have chosen. The impact of boundary conditions is examined in order to ensure that the border of the patched grid does not interfere with the interior of the domain. Then, a first order interpolation method in space is initially proposed and has been improved to a second order interpolation method. The second order interpolation is limited using a modified version of a well-known finite volume limiter. This modification allows the second order reconstruction to be used with high cell ratios between the grids. The implementation in the MANTA software is detailed with the inclusion of the Chimera procedure within the integration scheme. The differences between the first and second order Chimera methods are reviewed using analytical test cases like a sinus advection, a stationary shock wave, a Sod shock tube and finally an isentropic vortex advection. These test cases have been chosen as they highlight the differences between the two methods including the improvements that the second order reconstruction brings. Finally, a reference configuration is provided for using our finite volume Chimera method.

In chapter 3, the impact of the reference configuration of the developed Chimera method on the physics of fast transient dynamics is assessed using three well known test cases from the literature. A patched cylinder is used to exhibit the ability of the Chimera method to transfer discontinuities like shock waves from one grid to another. Then, a patched Helium bubble hit by a shock wave allows us to evaluate the ability of the method to transfer two-component interfaces from one domain to another. This case is then tested in a different version with an R22 bubble hit by a shock wave. Finally, a Double Mach reflection is used to assess the impact of the Chimera transfer on transient fast dynamics when shock waves, triple points, Mach stems and slip lines cross the overlapping grid interface. The Chimera versions of those test cases are compared to standard single grid versions.

In chapter 4, the developed Chimera method is extended to FSI applications using a coupling with the Mediating Body Method (MBM) [92] introduced above in this section. The base MBM is presented and extended to work with the Chimera method. The idea is to ensure valid coupling conditions in the presence of multiple fluid grids. The MBM affects the Chimera method as cells that are used to send information between grids become unusable because of the MBM. An extrapolation technique based on a two-side reconstruction is proposed to ensure the compatibility of the Chimera method when the immersed structure crosses multiple fluid grids. The method is then assessed on two test cases. The first test case is a free moving piston that separates two chambers with a pressure

jump. This test case allows us to assess the impact of a structure crossing multiple grid on the flow field. An analytical solution can be derived for this case enabling a comprehensive analysis of the method. Finally, a 3D case is proposed as a combination of the developed features and gives an idea of the industrial applications of the method.

The developements achieved during this thesis can be found inside the MANTA software. It is an object oriented C++ code for explicit and implicit fast transient dynamics.

In this work, we adopt the following writting convention: every vector is expressed through the column matrix of its components in a fixed orthonormal basis of the 3D Euclidian space $\{\vec{e}_i\}_{i \in \{1,2,3\}}$. Such a column matrix is denoted with a single underline. The second order tensors are expressed through the matrix of their components in the basis $\{\vec{e}_i \otimes \vec{e}_j\}_{(i,j) \in \{1,2,3\}^2}$. Such a matrix is denoted with a double underline. For the sake of clarity, we adopt the following notations : $\underline{a} \cdot \underline{b} = \underline{a}^t \underline{b}$ and $\underline{a} \otimes \underline{b} = \underline{\underline{ab}}^t$, where the right superscript "t" corresponds to the matrix transposition.

1 - Finite volume framework for fast dynamic problems

Contents

1.1	Governing equations for fast transient inviscid flow problems	13
1.1.1	Inviscid compressible flow model: the Euler equations	14
1.1.2	Perfect gas equation of state	15
1.2	Discretization of the inviscid equation model	16
1.2.1	The Godunov method	16
1.2.2	Riemann problem for the one-dimensional Euler equations . . .	17
1.2.3	An approximate Riemann solver: the HLLC solver	19
1.2.4	The second order MUSCL reconstruction	22
1.2.5	Time discretization: the second order MUSCL-Hancock method (MHM)	24
1.2.6	Discretization of the non-conservative term for multicomponent flows	25
1.3	Chapter conclusion	26

In this chapter, we present the equation models that are used in this work. The equations are discretized using a second order Godunov-type finite volume method with explicit time integration. The time integration is explicit as it is more adapted to simulate fast transient phenomena with small time scales. As we are focusing on the addition of geometrical details instead of multi-modelling, the equation sets and discretization methods are identical across a set of overlapping grids even though each grid is meshed independently. This framework is used in chapters 2 and 3. It is then combined with an immersed boundary (IB) method for FSI problems in the last chapter.

1.1 - Governing equations for fast transient inviscid flow problems

In fast transient dynamics, the flows are characterized by the predominance of inertial phenomena and acoustic waves induced by the compressibility of the fluids. The physics of such systems is governed by wave propagations generated by high pressure gradients as well as high velocity gradients. As viscosity time scale is higher than the fast transient dynamics problem time scale, focusing on fast transient flows allows us to neglect viscous effects in favor of convective transport and more specifically wave propagation. Therefore, the flows considered in this work are inviscid.

1.1.1 - Inviscid compressible flow model: the Euler equations

A . Presentation of the Euler equations for single phase flows

The problem is governed by the Euler system of equations for compressible flows. The fluid occupies a fixed open set \mathcal{T} . The governing equations written in a local conservative vectorial form, express the conservation of mass, momentum and total energy for a single fluid medium as follows:

$$\frac{\partial}{\partial t}(\underline{U}) + \nabla \cdot \underline{\underline{F}}(\underline{U}) = 0 \quad (1.1)$$

with the vector of conservative variables (\underline{U}) and the Euler fluxes ($\underline{\underline{F}}(\underline{U})$):

$$\underline{U} = \begin{pmatrix} \rho \\ \rho \underline{u} \\ \rho E \end{pmatrix}, \quad \underline{\underline{F}}(\underline{U}) = \begin{pmatrix} \rho \underline{u} \\ \rho \underline{u} \otimes \underline{u} + p \underline{\underline{I}}_d \\ (\rho E + p) \underline{u} \end{pmatrix} \quad (1.2)$$

where $\underline{\underline{I}}_d$ stand for $d \times d$ identity matrix with d the space dimension. Here we consider $d = 3$. We also note $\underline{W} = (\rho, u, v, w, p)^t$ the vector of primitive variables. In these equations, ρ is the density, p the pressure, $\underline{u} = (u, v, w)^t$ the velocity vector, and E the total energy per unit of mass.

B . Five equation model for inviscid interface problems

In the context of brutal accidents, fast transient dynamics involve multiphase flows with liquid-gas phase changes and multicomponent reactive flows with gas-gas mixing interfaces like in H_2 explosions for example. Multiphase flows are often considered when one phase only occupies a fraction of the total volume [47] whereas multicomponent flows are considered for fluid components with comparable densities. In multicomponent flows, different chemical species are mixed and generally share the same velocity and temperature. The chemical species may also interact through chemical reactions making the resulting multicomponent flow reactive.

In this work, we do not take into account thermodynamics of phase changes nor chemical reactions between species as they are not the main governing physical phenomena involved in the considered problems. Also the purpose of this work is not to investigate multiphase or multicomponent reactive flows but to provide a numerical strategy compatible with multicomponent flows. As a result, multicomponent flows are modelled based on species interface tracking. To do so, we use the compressible version of the reduced five-equation two-component flow model proposed by Allaire *et al.* [2], specially designed for interface problems. This model preserves system mass and total energy while ensuring the absence of oscillations near the interface. It has been primarily designed for compressible flow problems involving two-components and it applies to the Euler equations. The governing equations in a vectorial form are written as follows:

$$\frac{\partial}{\partial t}(\underline{U}) + \nabla \cdot \underline{\underline{F}}(\underline{U}) = \underline{B}(\underline{U}) \nabla \cdot \underline{u}, \quad (1.3)$$

where the modified vector of independent variables (\underline{U}), the modified Euler fluxes ($\underline{\underline{F}}(\underline{U})$), and the source terms ($\underline{B}(\underline{U})$) write:

$$\underline{U} = \begin{pmatrix} \rho_1 \alpha_1 \\ \rho_2 \alpha_2 \\ \rho \underline{u} \\ \rho E \\ \alpha_1 \end{pmatrix}, \quad \underline{\underline{F}}(\underline{U}) = \begin{pmatrix} \rho_1 \alpha_1 \underline{u} \\ \rho_2 \alpha_2 \underline{u} \\ \rho \underline{u} \otimes \underline{u} + p \underline{\underline{I}}_d \\ (\rho E + p) \underline{u} \\ \alpha_1 \underline{u} \end{pmatrix} \quad \text{and} \quad \underline{B}(\underline{U}) = \begin{pmatrix} 0 \\ 0 \\ 0 \\ 0 \\ \alpha_1 \end{pmatrix}, \quad (1.4)$$

In these equations, ρ , p , $\underline{u} = (u, v, w)^t$ and E are respectively the density, the pressure, the velocity vector and the total energy per unit of mass of the two-fluid mixture. α_k is the volume fraction of the component k . Thus for a two-component fluid, the following constraint has to be considered $\alpha_1 = 1 - \alpha_2$. ρ_k is the density of the component k ($k = 1, 2$), and the density of the mixture (ρ) is defined as: $\rho = \rho_1\alpha_1 + \rho_2\alpha_2$ to recover mass conservation. The two components of the fluid are supposed to have the same velocity \underline{u} . In addition to an equation of state (EOS) an additional closure law is required with this model. In this work, an isobaric closure is chosen so that:

$$p = p_1 = p_2 \quad (1.5)$$

The isobaric closure is preferable to the isothermal closure as it does not introduce spurious pressure oscillations at the interface as shown in [2].

1.1.2 - Perfect gas equation of state

The model presented for both single phase and multicomponent flows requires a thermodynamic closure ensured by an equation of state of the form:

$$p = p(\rho, T), \text{ and } e = e(\rho, T), \quad (1.6)$$

where T is the fluid temperature and e its specific internal energy. For the development of our numerical strategy, we focus on simple thermodynamic situations with calorically perfect gas knowing that such assumption is only valid up to certain temperature levels [6].¹ A calorically perfect gas is characterized by the fact that the specific internal energy (e) and the specific enthalpy (h) are linear functions with respect to temperature (T). The specific internal energy and the specific enthalpy are defined as follows :

$$e = E - \|\underline{u}\|^2/2, \quad h = e + \frac{p}{\rho}. \quad (1.7)$$

For a calorically perfect gas, e and h write:

$$e = c_v T, \quad h = c_p T, \quad (1.8)$$

where c_v and c_p are the specific heats respectively at constant volume and constant pressure. Also, the specific heats are assumed constant and as a consequence, the specific heat ratio $\gamma = \frac{c_p}{c_v}$ is constant. The specific heats $c_v = \left(\frac{\partial e}{\partial T}\right)_v$ and $c_p = \left(\frac{\partial h}{\partial T}\right)_p$ can be expressed using the Mayer relationship:

$$c_p - c_v = \frac{R}{\mathcal{M}}, \quad (1.9)$$

where, $R = 8.314 \text{ K} \cdot \text{K}^{-1} \cdot \text{mol}^{-1}$ is the ideal gas constant and \mathcal{M} is the molar mass of the gas. For Air in normal temperature and pressure (NTP) conditions, the molar mass is approximately $\mathcal{M} \approx 29 \cdot 10^{-3} \text{ kg} \cdot \text{mol}^{-1}$. It can be approximated as a diatomic gas (N_2 and O_2) with a specific heat ratio (γ) equal to $\frac{7}{5}$. Using the specific heat ratio (γ) and the Mayer relation 1.9 leads to :

$$c_p = \frac{\gamma R}{(\gamma - 1)\mathcal{M}}, \quad c_v = \frac{R}{(\gamma - 1)\mathcal{M}}. \quad (1.10)$$

Using the definition of the specific enthalpy and equation 1.8, the equation of state for a calorically perfect gas writes:

$$p = (\gamma - 1)\rho e. \quad (1.11)$$

¹More complex EOS could be tested with the proposed method.

This equation also known as the ideal gas equation of state is the only equation of state considered in this work. The isentropic sound speed for an ideal gas writes :

$$c = \sqrt{\frac{\gamma p}{\rho}}. \quad (1.12)$$

In the case of a multicomponent flow with two species, the pressure ($p = p_1 = p_2$) is related to the conservative quantities through the previously introduced ideal gas equation of state. In this context, each fluid k is characterized by its equation of state:

$$p = (\gamma_k - 1)\rho_k e_k, \quad (1.13)$$

where γ_k is the heat capacity ratio, and e_k is the internal energy relative to phase k . The speed of sound in the phase k is $c_k = \sqrt{\frac{\gamma_k p}{\rho_k}}$.

Regarding the mixture, the specific internal energy e is defined as $\rho e = \rho_1 \alpha_1 e_1 + \rho_2 \alpha_2 e_2$. The speed of sound (c) associated to the mixture is defined in [2] by:

$$\rho \xi c^2 = \rho_1 \alpha_1 \xi_1 c_1^2 + \rho_2 \alpha_2 \xi_2 c_2^2, \quad (1.14)$$

with $\xi_k = \rho_k (\partial e_k / \partial p_k)$ and $\xi = \xi_1 \alpha_1 + \xi_2 \alpha_2$. In the following, this model is referred as to two-component model.

1.2 - Explicit Total Variation Diminishing discretization of the inviscid equation model

In this section, we present the finite volume discretization that we have used in our work. The discretization is illustrated on the Euler system of conservative equations. The non-conservative term introduced by the two-component model is detailed separately. The finite volume method is a natural choice when dealing with conservative equations as it has been designed to ensure conservation.

1.2.1 - The Godunov method

The integration of the system of equations 1.1 is based on an explicit finite volume method. The computational domain of interest is divided in 3D-polygonal control volumes (K_i) $\in \mathcal{U}$, where \mathcal{U} , is the ensemble of control volumes. We denote by $\Omega_{\mathcal{U}}$ the number of cells within the domain \mathcal{U} . We write $|K_i|$ the volume of K_i . We note $\gamma(i)$ the set of adjacent cells² to K_i . We introduce the discrete times: $\forall n \geq 0$, $t^{n+1} = t^n + \Delta t_n$ where Δt_n is the variable time step at the n -th time iteration. By integrating equation 1.1 over the cell $|K_i|$ between the times t^n and t^{n+1} , we get the integral form of the Euler equation:

$$\int_{t^n}^{t^{n+1}} \int_{K_i} \frac{\partial \underline{U}(\underline{x}, t)}{\partial t} dV dt + \int_{t^n}^{t^{n+1}} \int_{K_i} \nabla \cdot \underline{F}(\underline{U}(\underline{x}, t)) dV dt = \underline{0}, \quad (1.15)$$

to which we can apply the Green-Ostrogradski theorem:

$$\int_{K_i} \underline{U}(\underline{x}, t^{n+1}) - \underline{U}(\underline{x}, t^n) dV + \int_{t^n}^{t^{n+1}} \int_{\partial K_i} \underline{F}(\underline{U}(\underline{x}, t)) \cdot \underline{n} dS dt = \underline{0}, \quad (1.16)$$

²a cell K_j is adjacent to the cell K_i , $i \neq j$, if they share a common face in 3D, edge in 2D and node in 1D.

with ∂K_i the boundary of the cell K_i . We introduce \underline{U}_i^n the mean cell conservative variables at the cell K_i and at the time t^n defined as:

$$\underline{U}_i^n = \frac{1}{|K_i|} \int_{K_i} \underline{U}(\underline{x}, t^n) dV. \quad (1.17)$$

\underline{U}_i^n is a numerical approximation of the conservative variables, solution of equation 1.1. For all cells K_j , $j \in \gamma(i)$, the interface that separates K_i from K_j is denoted indifferently \mathcal{F}_{ij} or \mathcal{F}_{ji} . \underline{n}_{ij} is the normal of \mathcal{F}_{ij} directed from K_i to K_j and $|\mathcal{F}_{ij}|$ is the surface of the face \mathcal{F}_{ij} . Using 1.17 in 1.16, we have:

$$\underline{U}_i^{n+1} = \underline{U}_i^n - \frac{1}{|K_i|} \int_{t^n}^{t^{n+1}} \sum_{j \in \gamma(i)} \int_{\mathcal{F}_{ij}} \underline{F}(\underline{U}(\underline{x}, t)) \cdot \underline{n}_{ij} dS dt. \quad (1.18)$$

Using the Godunov method, we introduce the numerical flux function:

$$\Delta t_n \hat{F}(\underline{U}_{ij}^{*n}, \underline{n}_{ij}) \approx \frac{1}{|\mathcal{F}_{ij}|} \int_{t^n}^{t^{n+1}} \int_{\mathcal{F}_{ij}} \underline{F}(\underline{U}(\underline{x}, t)) \cdot \underline{n}_{ij} dS dt, \quad (1.19)$$

where \underline{U}_{ij}^{*n} is the approximate solution at the interface \mathcal{F}_{ij} at the time t^n . It is the solution of the Riemann problem RP $(\underline{U}_{ij}^n, \underline{U}_{ji}^n)$ along the ray $x/t = 0$ in the local frame of the interface \mathcal{F}_{ij} , with \underline{U}_{ij}^n and \underline{U}_{ji}^n the interface states at the face \mathcal{F}_{ij} . As demonstrated in [170], if the time step Δt_n satisfies the CFL condition:

$$\Delta t_n \leq \min_{i \in \Omega_u} \frac{h_i}{S_{\max}^n}, \quad (1.20)$$

with h_i the characteristic length of the cell K_i and S_{\max}^n the maximum wave velocity present through the domain at time t^n , the Riemann problem solution \underline{U}_{ij}^{*n} is constant in the local frame of the interface \mathcal{F}_{ij} , between t^n and t^{n+1} . Equation 1.18 can be written using the numerical flux function 1.19 as:

$$\underline{U}_i^{n+1} = \underline{U}_i^n - \frac{\Delta t_n}{|K_i|} \sum_{j \in \gamma(i)} |\mathcal{F}_{ij}| \hat{F}(\underline{U}_{ij}^{*n}, \underline{n}_{ij}). \quad (1.21)$$

This equation results from the well-known Godunov scheme presented in [73] with an explicit time integration. In the following, we detail the Riemann problem with the approximate Riemann solver that we use for providing an expression to the numerical flux function 1.19. The numerical flux function can also be written with the interface states \underline{U}_{ij}^n and \underline{U}_{ji}^n used in the computation of the approximate solution $(\underline{U}_{ij}^{*n})$ as $\hat{F}(\underline{U}_{ij}^n, \underline{U}_{ji}^n, \underline{n}_{ij})$.

1.2.2 - Riemann problem for the one-dimensional Euler equations

As presented in equation 1.21, a flux function $\hat{F}(\underline{U}_{ij}^{*n}, \underline{n}_{ij})$ needs to be computed at every face \mathcal{F}_{ij} of the cell K_i . This flux requires the solution \underline{U}_{ij}^{*n} that results from the resolution of a Riemann problem (RP) at the face \mathcal{F}_{ij} , in the normal direction \underline{n}_{ij} that is referred as *local frame*. The local frame of the interface \mathcal{F}_{ij} is defined by the normal vector \underline{n}_{ij} and two vectors tangent to the interface \mathcal{F}_{ij} , denoted \underline{t}_{ij}^1 and \underline{t}_{ij}^2 , such that $\underline{n}_{ij} \cdot \underline{t}_{ij}^1 = 0$ and $\underline{t}_{ij}^2 = \underline{n}_{ij} \times \underline{t}_{ij}^1$. As a result, multiple one-dimensional Riemann problems need to be solved - one for each face of the cell K_i - in the direction normal to the interface of interest. This problem is referred as *x-split three-dimensional Riemann problem*. In this section, the normal direction \underline{n}_{ij} is assimilated to the η -axis and the time indices are ignored as all the numerical variables considered here are expressed at the time t^n .

A Riemann problem is defined by a system of hyperbolic conservation laws with simple but non-trivial initial conditions. The Riemann problem for the one-dimensional time-dependant Euler equations is the initial value problem (IVP) for the conservation laws

$$\frac{\partial \underline{U}}{\partial t} + \frac{\partial \underline{F}(\underline{U})}{\partial \eta} = 0, \quad (1.22)$$

where $\underline{U} = (\rho, \rho u_n, \rho u_{t_1}, \rho u_{t_2}, \rho E)^t$ and $\underline{F}(\underline{U}) = (\rho u_n, \rho u_n^2 + p, \rho u_n u_{t_1}, \rho u_n u_{t_2}, u_n(\rho E + p))^t$, with u_n the velocity component normal to the face \mathcal{F}_{ij} of the cell K_i and (u_{t_1}, u_{t_2}) the tangential velocity components. The initial conditions (IC) of this problem are defined by:

$$\underline{U}(\eta, 0) = \begin{cases} \underline{U}_L & \text{if } \eta < 0, \\ \underline{U}_R & \text{if } \eta > 0. \end{cases} \quad (1.23)$$

The domain of interest in the $\eta - t$ plane are points (η, t) with $-\infty < \eta < \infty$ and $t > 0$. In practice, η varies in a finite interval $[-h_i/2, h_i/2]$, with h_i the characteristic length of the cell K_i . Initial conditions consist of two constant states \underline{U}_L for $\eta < 0$ and \underline{U}_R for $\eta > 0$ in the local frame of the face \mathcal{F}_{ij} . These states correspond to the interface states $\bar{\underline{U}}_{ij}$ and $\bar{\underline{U}}_{ji}$. Instead of solving $\underline{U}^*_{ij}(\eta, 0) = \text{RP}(\bar{\underline{U}}_{ij}, \bar{\underline{U}}_{ji})$, we solve $\underline{U}^*_{ij}(\eta/t) = \text{RP}(\underline{U}_L, \underline{U}_R)$ and we evaluate the similarity solution of the Riemann problem defined by equation 1.22 and 1.23 at $\eta/t = 0$.

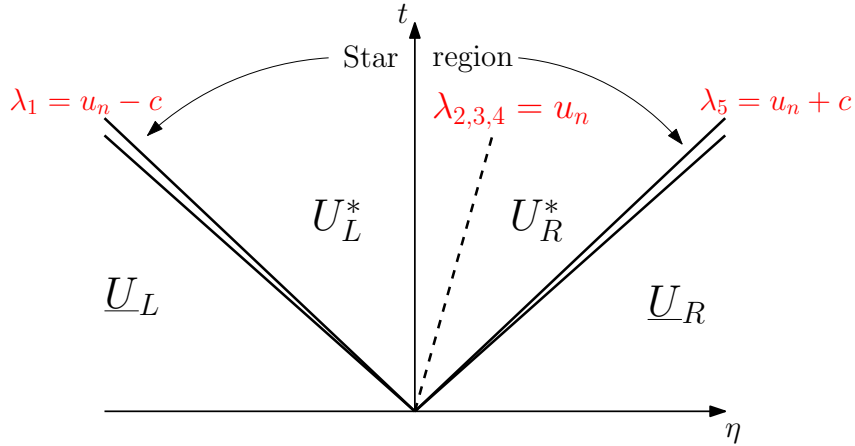


Figure 1.1: Structure of the solution of the Riemann problem for the one-dimensional Euler equations on the $\eta - t$ plane. Unknown waves (shock waves or rarefaction fans) are depicted by a pair of rays emanating from the origin.

Figure 1.1 illustrates the structure of the similarity solution $\underline{U}^*_{ij}(\eta/t)$ of the Riemann problem for the x -split three-dimensional Euler equations. It corresponds to a Riemann problem in the local frame and takes into account the tangential velocity components u_{t_1} and u_{t_2} .

This three dimensional Riemann problem has five waves associated to the eigen values $\lambda_1 = u_n - c$, $\lambda_{2,3,4} = u_n$ and $\lambda_5 = u_n + c$ and the characteristic fields corresponding to the right eigenvectors $\underline{R}^{(i)}$, $i = 1, 2, 3, 4, 5$. We choose the convention of representing unknown waves by a pair of rays emanating from the origin and the middle wave by a dashed line. Each wave is depicted along with the corresponding eigen value. It can be proven that the λ_2 , λ_3 and λ_4 fields are linearly degenerate, *i.e.* $\nabla \lambda_i(\underline{U}) \cdot \underline{R}^{(i)}(\underline{U}) = 0$, $i = 2, 3, 4$ (see [78]). As a result, the middle wave associated with the $\underline{R}^{(2)}$ characteristic field is always a contact discontinuity. The characteristic fields associated to $\lambda_3 = u_n$ and $\lambda_4 = u_n$ ($\underline{R}^{(3)}$ and $\underline{R}^{(4)}$ characteristic fields) correspond to two shear waves across which the tangential velocities u_{t_1} and u_{t_2} are discontinuous. The $\underline{R}^{(1)}$ and $\underline{R}^{(5)}$ characteristic fields are genuinely nonlinear, *i.e.* $\nabla \lambda_i(\underline{U}) \cdot \underline{R}^{(i)}(\underline{U}) \neq 0$, $i = 1, 5$. As a result, they are associated with rarefactions or shock waves.

The three waves associated to the eigen values λ_1 , λ_2 and λ_5 separate four constant states. From left to right, we find the left constant state \underline{U}_L , the star region between the λ_1 -wave and λ_5 -wave and the right constant state \underline{U}_R on the right-hand side of the λ_5 -wave. The star region is composed of two subregions \underline{U}_L^* and \underline{U}_R^* separated by the contact discontinuity associated to λ_2 . Both pressure (p) and normal velocity (u_n) are constant in the star region.

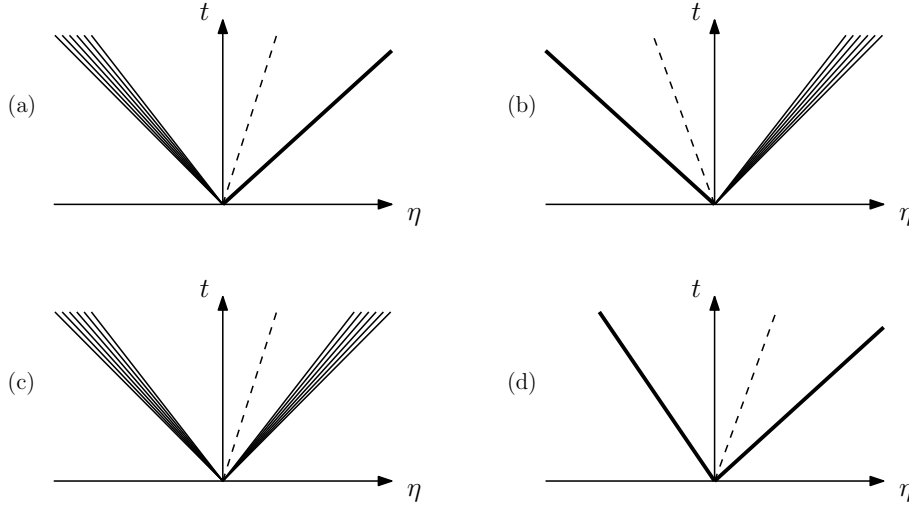


Figure 1.2: Possible wave patterns in the solution of the Riemann problem: (a) left rarefaction, contact, right shock, (b) left shock, contact, right rarefaction, (c) left rarefaction, contact, right rarefaction, (d) left shock, contact, right shock.

While the Riemann problem definition is relatively simple, it contains fundamental wave propagation physics and it ensures conservation in the context the Godunov scheme. In [73], a numerical iterative solver called exact Riemann solver is presented. This solver identifies the wave among the four possibilities shown in Figure 1.2 and computes the entirety of the states over the star region. Even though the exact Riemann solver has been extensively reviewed [170], it is not advised for practical applications as only a small portion of the solution is required in the Godunov method. In practice, less computationally expensive approximate Riemann solvers are preferred instead of the exact solver. In this work, we use the HLLC solver as it is able to capture contact discontinuities and shear waves unlike the HLL solver and does not require as much computational time as the exact Riemann solver. In return, the HLLC is somewhat more dissipative while being robust³.

1.2.3 - An approximate Riemann solver: the HLLC solver

The HLLC solver is an improved version of the HLL scheme introduced by Harten, Lax and van Leer in [79] in which the contact and shear waves are missing. Introduced in [172], the HLLC solver is built considering a control volume $[\eta_L, \eta_R] \times [0, T]$ as illustrated in Figure 1.3 with the signal speeds S_L , S^* and S_R corresponding to the eigen values $\lambda_1 = u_n - c$, $\lambda_{2,3,4} = u_n$ and $\lambda_5 = u_n + c$.

The approximate Riemann solution $\underline{U}^*(\eta, t)$ in the local frame $(\underline{n}_{ij}, t_{ij}^1, t_{ij}^2)$ of the face \mathcal{F}_{ij} is given as follows:

$$\underline{U}^*(\eta, t) = \begin{cases} \underline{U}_L, & \text{if } \frac{\eta}{t} \leq S_L \\ \underline{U}_L^*, & \text{if } S_L \leq \frac{\eta}{t} \leq S^* \\ \underline{U}_R^*, & \text{if } S^* \leq \frac{\eta}{t} \leq S_R \\ \underline{U}_R, & \text{if } \frac{\eta}{t} \geq S_R, \end{cases} \quad (1.24)$$

³By robust, we mean that the solver does not generate non-physical waves nor negative pressures even with complex wave interactions.

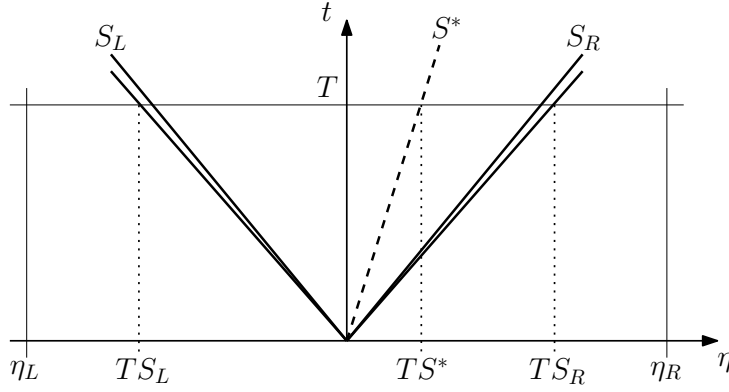


Figure 1.3: Control volume $[\eta_L, \eta_R] \times [0, T]$ on the $\eta - t$ plane. S_L and S_R are respectively the extreme characteristic velocity for the left-hand side wave and the right-hand side wave from the solution of the Riemann problem. Unknown waves (shock waves or rarefaction fans) are depicted by a pair of rays emanating from the origin.

and the corresponding HLLC numerical flux is defined by:

$$\underline{F}^{\text{HLLC}}(\underline{U}^*(\eta, t)) = \begin{cases} \underline{F}_L, & \text{if } 0 \leq S_L \\ \underline{F}_L^*, & \text{if } S_L \leq 0 \leq S^* \\ \underline{F}_R^*, & \text{if } S^* \leq 0 \leq S_R \\ \underline{F}_R, & \text{if } 0 \geq S_R. \end{cases} \quad (1.25)$$

We see that \underline{U}_L^* , \underline{U}_R^* , \underline{F}_L^* and \underline{F}_R^* are the unknown of this problem. Integrating equation 1.22 over the control volume $[\eta_L, \eta_R] \times [0, T]$ gives:

$$\frac{1}{T(S_R - S_L)} \int_{TS_L}^{TS_R} \underline{U}(\eta, T) dx = \frac{S_R \underline{U}_R - S_L \underline{U}_L + \underline{F}_L - \underline{F}_R}{S_R - S_L}, \quad (1.26)$$

which is known as the consistency condition. The consistency condition ensures that the approximate Riemann solver preserves the integral form of the conservation laws. An approximate solution $\hat{\underline{U}}(\eta, t)$ is consistent with the integral form of the conservation laws if, when substituted to the exact solution $\underline{U}(\eta, t)$ in the left-hand side of the consistency condition 1.26, the right-hand side remains unaltered.

By decomposing the left-hand side integral, according to the two star regions:

$$\begin{aligned} \frac{1}{T(S_R - S_L)} \int_{TS_L}^{TS_R} \underline{U}(\eta, T) dx &= \frac{1}{T(S_R - S_L)} \int_{TS_L}^{TS^*} \underline{U}(\eta, T) dx \\ &+ \frac{1}{T(S_R - S_L)} \int_{TS^*}^{TS_R} \underline{U}(\eta, T) dx, \end{aligned} \quad (1.27)$$

and using the integral averages:

$$\begin{cases} \underline{U}_L^* = \frac{1}{T(S^* - S_L)} \int_{TS_L}^{TS^*} \underline{U}(\eta, T) dx, \\ \underline{U}_R^* = \frac{1}{T(S_R - S^*)} \int_{TS^*}^{TS_R} \underline{U}(\eta, T) dx, \end{cases} \quad (1.28)$$

the consistency condition 1.26, can be written:

$$\left(\frac{S^* - S_L}{S_R - S_L}\right) \underline{U}_L^* + \left(\frac{S_R - S^*}{S_R - S_L}\right) \underline{U}_R^* = \frac{S_R \underline{U}_R - S_L \underline{U}_L + \underline{F}_L - \underline{F}_R}{S_R - S_L}. \quad (1.29)$$

Applying the Rankine-Hugoniot conditions across each of the waves λ_1 , λ_2 and λ_5 of speeds S_L , S^* and S_R , gives:

$$\underline{F}_L^* = \underline{F}_L + S_L(\underline{U}_L^* - \underline{U}_L) \quad (1.30)$$

$$\underline{F}_R^* = \underline{F}_L^* + S^*(\underline{U}_R^* - \underline{U}_L^*) \quad (1.31)$$

$$\underline{F}_R^* = \underline{F}_R + S_R(\underline{U}_R^* - \underline{U}_R). \quad (1.32)$$

These relations can also be used to recover the consistency condition 1.26. As a result, we have four unknowns and three equations. Combination of equations 1.30-1.32 can be done to find $\underline{U}_K^*(\underline{U}_K, S^*)$, ($K = R, L$). However, some additional conditions need to be imposed in order to close this system and find S^* and then \underline{F}_K^* , ($K = R, L$). As we have seen before, the exact solution imposes constant pressure and constant normal velocity in the star region *i.e.*

$$\begin{cases} p_L^* = p_R^* = p^*, \\ u_{nL}^* = u_{nR}^* = u_n^*. \end{cases} \quad (1.33)$$

The tangential velocity components are continuous across the genuinely nonlinear characteristic fields $\underline{R}^{(1)}$ and $\underline{R}^{(5)}$, associated to the left-hand side and right-hand side waves, imposing:

$$\begin{cases} u_{t1L}^* = u_{t1L}, & u_{t1R}^* = u_{t1R}, \\ u_{t2L}^* = u_{t2L}, & u_{t2R}^* = u_{t2R}, \end{cases} \quad (1.34)$$

We also have $S^* = u_n^*$. Using equation 1.30 and 1.32, we can extract the following solutions for pressure in the star regions:

$$\begin{cases} p_L^* = p_L + \rho_L(S_L - u_{nL})(S^* - u_{nL}), \\ p_R^* = p_R + \rho_R(S_R - u_{nR})(S^* - u_{nR}). \end{cases} \quad (1.35)$$

The use of the condition 1.33 into equation 1.35, gives an expression for the speed S^* in terms of known speeds S_L and S_R :

$$S^* = \frac{p_R - p_L + \rho_L u_{nL}(S_L - u_{nL}) - \rho_R u_{nR}(S_R - u_{nR})}{\rho_L(S_L - u_{nL}) - \rho_R(S_R - u_{nR})}. \quad (1.36)$$

Finally, using equation 1.25 and manipulations of 1.30 and 1.32 allows us to compute the intermediate fluxes \underline{F}_L^* and \underline{F}_R^* when needed:

$$\underline{F}_K^* = \underline{F}_K + S_K(\underline{U}_K^* - \underline{U}_K), \quad (1.37)$$

with $K = R, L$, with the intermediate states given as:

$$\underline{U}_K^* = \rho_K \left(\frac{S_K - u_{nK}}{S_K - S^*} \right) \begin{bmatrix} 1 \\ S^* \\ u_{t1K} \\ u_{t2K} \\ E_K + (S^* - u_{nK}) \left[S^* + \frac{p_K}{\rho_K(S_K - u_{nK})} \right] \end{bmatrix}. \quad (1.38)$$

For completeness, some variants of the HLLC approximate solver have been developed but are not considered in this work (see [170]).

Remark. With the HLLC approximate Riemann solver, the flux $\underline{F}^{\text{HLLC}}(\underline{U}_{ij}^{*n}, \underline{n}_{ij})$ is provided in the local reference frame of the face \mathcal{F}_{ij} . In equation 1.21, the fluxes are expressed in a global frame defined by the orthonormal basis of the three-dimensional Euclidian space $\{\vec{e}_i\}_{i \in \{1,2,3\}}$. As a result, the flux $\underline{F}^{\text{HLLC}}(\underline{U}_{ij}^{*n}, \underline{n}_{ij})$ is transformed from the local reference frame of the face \mathcal{F}_{ij} to the global reference frame and the global frame flux is referred as $\hat{\underline{F}}^{\text{HLLC}}(\underline{U}_{ij}^{*n}, \underline{n}_{ij})$ or $\hat{\underline{F}}^{\text{HLLC}}(\underline{\bar{U}}_{ij}^n, \underline{\bar{U}}_{ji}^n, \underline{n}_{ij})$, using the interface states.

1.2.4 - The second order MUSCL reconstruction

The spatial and time order of the finite volume framework based on the Godunov method presented in equation 1.21 depends on the expression of the fluxes. For industrial applications, high order methods are preferable. Various high order methods have been developed like the Essentially Non-Oscillatory method (ENO) [80] or the improved Weighted ENO method (WENO) [114] which are based on a polynomial reconstruction of the derivatives in addition to a smoothing criteria to avoid spurious oscillations. We can also cite the Weighted Average Flux (WAF) method [171] where the intercell flux results from an integral average of the flux across the entire local Riemann problem solution. In this work, we focus on the second order MUSCL method [171] as it provides a robust second order approximation in space for developing our overlapping grid method while maintaining a reasonable computational cost.

A . The MUSCL reconstruction

The Monotone Upwind Scheme for Conservation Laws or MUSCL method [176, 11, 110] is based on equation 1.21 which can be written:

$$\underline{U}_i^{n+1} = \underline{U}_i^n - \frac{\Delta t_n}{|K_i|} \sum_{j \in \gamma(i)} |\mathcal{F}_{ij}| \hat{F}^{\text{HLLC}}(\underline{U}_{ij}^n, \underline{U}_{ji}^n, \underline{n}_{ij}), \quad (1.39)$$

where the numerical HLLC flux $\hat{F}^{\text{HLLC}}(\underline{U}_{ij}^n, \underline{U}_{ji}^n, \underline{n}_{ij})$ at the face \mathcal{F}_{ij} is computed using the interface states \underline{U}_{ij}^n and \underline{U}_{ji}^n . We recall that the Godunov method is based on a constant approximation of the solution \underline{U} over each cell $\{K_i\}_{i \in \Omega_{\mathcal{U}}}$ at the discrete time t^n :

$$\underline{U}_i^n = \frac{1}{|K_i|} \int_{K_i} \underline{U}(\underline{x}, t^n) dV. \quad (1.40)$$

The MUSCL method consists in reconstructing a linear approximation of the solution \underline{U} over each cell $\{K_i\}_{i \in \Omega_{\mathcal{U}}}$ in order to interpolate the interface states \underline{U}_{ij}^n and \underline{U}_{ji}^n at each face \mathcal{F}_{ij} . The reconstruction is used to improve the flux computation. The reconstruction can be done on the numerical solution expressed in terms of primitive variables \underline{W} or conservative variables \underline{U} . In our case, the reconstruction is carried out on the primitive variables \underline{W}_i^n . We define $\underline{\nabla}(\underline{W}_i^n)$ the constant approximation of the gradient in the cell K_i at the time t^n . Using the discrete gradient approximation, the linear reconstruction of the solution \underline{W}_i^n inside the cell K_i writes:

$$\overline{\underline{W}}_i^n(\underline{x}) = \underline{W}_i^n + \underline{\nabla}(\underline{W}_i^n) \cdot (\underline{x} - \underline{x}_i), \quad (1.41)$$

where \underline{x}_i is the position of the barycenter of the cell K_i and $\underline{x} \in K_i$. The linear reconstruction preserves the mean value of the reconstructed field as:

$$\frac{1}{|K_i|} \int_{K_i} \overline{\underline{W}}_i^n(\underline{x}) dV = \underline{W}_i^n. \quad (1.42)$$

The interface states are reconstructed based on the primitive variables \underline{W} while the Riemann problems are solved using the conservative variables \underline{U} . In any case, we note the interface states resulting from the reconstruction at the face \mathcal{F}_{ij} , $\overline{\underline{W}}_{ij}^n / \overline{\underline{W}}_{ji}^n$ defined as:

$$\overline{\underline{W}}_{ij}^n(\underline{x}) = \underline{W}_i^n + \underline{\nabla}(\underline{W}_i^n) \cdot (\underline{x}_{(\text{face})_{ij}} - \underline{x}_i), \quad (1.43)$$

with $\underline{x}_{(\text{face})_{ij}}$ the barycenter of the face \mathcal{F}_{ij} . The corresponding conservative states are written $\overline{\underline{U}}_{ij}^n / \overline{\underline{U}}_{ji}^n$.

B . The gradient reconstruction: least squares method

In equation 1.43, the gradient needs to be approximated. To do so, we use a least squares method [118] which approximates the gradient $\nabla(W_i^n)$ of the cell K_i using the solution \underline{W}_i^n defined inside the cell K_i and solutions $\{\underline{W}_j^n\}_{j \in \gamma(i)}$ inside the neighbors of K_i , with $\gamma(i)$ the index set of cells adjacent to K_i . The least squares method has the benefit of being compatible with any cell type. The gradient tensor is defined by ensuring the condition:

$$\forall j \in \gamma(i), \overline{W}_i^n(\underline{x}_j) = \underline{W}_j^n. \quad (1.44)$$

This system of equations is overloaded and needs to be solved componentwise. We introduce $[\underline{W}_i^n]_k$ and $[\underline{W}_j^n]_k$ respectively the k -th component of \underline{W}_i^n and \underline{W}_j^n . $[\nabla(W_i^n)]_k$ is the gradient of $[\underline{W}_i^n]_k$. That is to be the k -th line of the gradient matrix $\nabla(W_i^n)$. Finding the solution to the problem 1.44, is equivalent to minimizing for each component k the function:

$$I_k = \sum_{j \in \gamma(i)} \frac{1}{2} \left([\overline{W}_i^n(\underline{x}_j)]_k - [\underline{W}_j^n]_k \right)^2 = \sum_{j \in \gamma(i)} \frac{1}{2} \left(([\underline{W}_i^n]_k - [\underline{W}_j^n]_k + [\nabla(W_i^n)]_k(\underline{x}_j - \underline{x}_i)) \right)^2. \quad (1.45)$$

The solution to this problem writes:

$$[\nabla(W_i^n)]_k = \underline{M}_i^{-1} \sum_{j \in \gamma(i)} (\underline{x}_j - \underline{x}_i) ([\underline{W}_i^n]_k - [\underline{W}_j^n]_k), \quad (1.46)$$

where \underline{M}_i is the matrix defined by :

$$\underline{M}_i = \sum_{j \in \gamma(i)} (\underline{x}_j - \underline{x}_i) \otimes (\underline{x}_j - \underline{x}_i). \quad (1.47)$$

\underline{M}_i is a 3×3 matrix in 3D and a 2×2 matrix in 2D. \underline{M}_i is a positive definite matrix and is therefore invertible. As a result, the tensor $\nabla(W_i^n)$ is well defined.

C . The K-Dubois slope limiter

One way to ensure that the second order MUSCL scheme on the Euler equation (see equation 1.41) does not introduce spurious oscillations is to use flux limiters [169] or slope limiters to build non-linear solutions respecting TVD constraints [170]. In this work we focus on limited slopes using the K-Dubois limiter [162] which is based on the Barth and Jespersen limiter [97] and is therefore compatible with unstructured grids. In each cell K_i , $i \in \Omega_{\mathcal{U}}$, the slope limiter Ψ_i needs to be computed at every time step. The reconstructed solution from equation 1.41 becomes:

$$\overline{W}_i^n = \underline{W}_i^n + \Psi_i \nabla(W_i^n) \cdot (\underline{x} - \underline{x}_i). \quad (1.48)$$

The limiters are built per component in order to properly limit the slope $\nabla(W_i^n)$. For the sake of clarity, the time step reference is willingly omitted in this section as every quantity involved in the slope limiter computation corresponds to the n -th time step. As the purpose of the limiter is to avoid the appearance of local extrema, for all $j \in \gamma(i)$, we have for each component k :

$$[\underline{W}_i^{\min}]_k < [\overline{W}_i(\underline{x}_{(\text{face})_{ij}})]_k < [\underline{W}_i^{\max}]_k, \quad (1.49)$$

with,

$$\begin{cases} [\underline{W}_i^{\max}]_k &= \max_{j \in \gamma(i)} \left([\underline{W}_i]_k, [\underline{W}_j]_k \right) \\ [\underline{W}_i^{\min}]_k &= \min_{j \in \gamma(i)} \left([\underline{W}_i]_k, [\underline{W}_j]_k \right). \end{cases} \quad (1.50)$$

The K-Dubois limiter [162] formulation is relatively close to that of the Barth and Jespersen limiter [97]. However, it introduces a parameter K that allows the user to modify the behavior of the limiter (that can be more or less compressive⁴). The k -th component of the K-Dubois limiter is expressed as:

$$[\Psi_i]_k = \min \left(1, K \cdot \frac{\min \left([W_i^{\max} - W_i]_k, [W_i - W_i^{\min}]_k \right)}{\max_{j \in \gamma(i)} \left([\nabla(W_i) \cdot (\underline{x}_{(\text{face})_{ij}} - \underline{x}_i)]_k \right)} \right), \quad (1.51)$$

where the quantity $(\underline{x}_{(\text{face})_{ij}} - \underline{x}_i)$ represents the distance between the center of the cell face \mathcal{F}_{ij} and the cell center \underline{x}_i . Taking the maximum value of $(\underline{x}_{(\text{face})_{ij}} - \underline{x}_i)$ among all faces of the considered cell ensures that the solution is limited in the sense of equation 1.49. This implies that the limited reconstructed solution can be searched inside a neighborhood (*i.e.* a circle in 2D, and a sphere in 3D) with a typical radius of $R = \max_{j \in \gamma(i)} (\underline{x}_{(\text{face})_{ij}} - \underline{x}_i)$ as shown in Figure 1.4. In [162], the parameter K is recommended to be set to 0.75 which is the value used in this work.

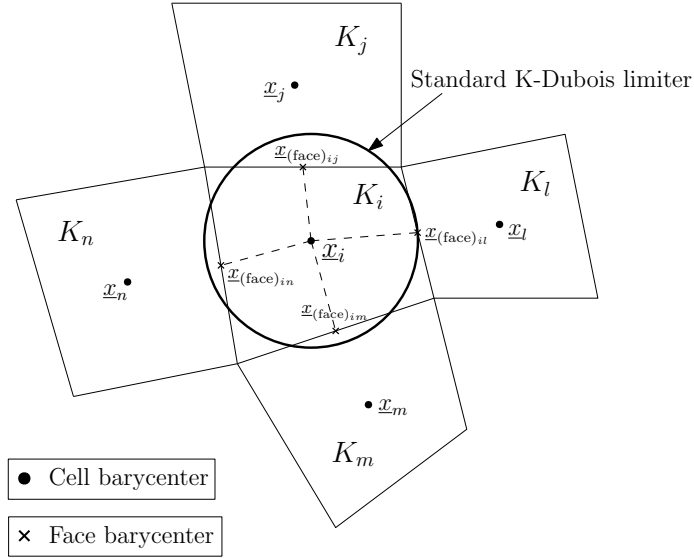


Figure 1.4: Area where the solution is limited with the K-Dubois limiter in a single model approach. The area is identical for the Barth and Jespersen limiter [97].

1.2.5 - Time discretization: the second order MUSCL-Hancock method (MHM)

From equation 1.39, the limited MUSCL reconstruction provides a second order accurate scheme in space. However, the explicit time integration inherited from the Godunov method is first order accurate in time. Several methods like the Piecewise Linear Method (PLM) [33] or the Generalized Riemann Problem (GRP) [16, 15] propose a second order generalization of the Godunov method. In this work, we focus on the MUSCL-Hancock Method (MHM) [177]. The MHM provides a second order accurate scheme in time advancing fluxes at half time step. It is based on the MUSCL reconstruction which ensures second order accuracy in space. For the cell K_i at the discrete time t^n , the method can be decomposed into four steps:

⁴By more compressive, we mean that the limiter is capable of better capturing a contact discontinuity or a shock wave with less numerical scheme diffusivity

1. Linear data reconstruction of the primitive variables at the interfaces \mathcal{F}_{ij} with boundary extrapolated values, namely:

$$\overline{W}_{ij}^n = \underline{W}_i^n + \Psi_i \nabla(\underline{W}_i^n) \cdot (\underline{x}_{(\text{face})_{ij}} - \underline{x}_i). \quad (1.52)$$

2. Evolution of the conservative variables \overline{U}_{ij}^n , at a half time step $\left(\frac{1}{2}\Delta t_n\right)$ according to:

$$\overline{U}_{ij}^{n+\frac{1}{2}} = \overline{U}_{ij}^n + \frac{\Delta t_n}{2|K_i|} \sum_{j \in \gamma(i)} |\mathcal{F}_{ij}| \underline{F}(\overline{U}_{ij}^n) \cdot \underline{n}_{ij}. \quad (1.53)$$

3. Solution of the piecewise constant data Riemann problems in the normal frames of the interfaces \mathcal{F}_{ij} :

$$\begin{aligned} \frac{\partial \underline{U}}{\partial t} + \frac{\partial \underline{F}(\underline{U})}{\partial \eta} &= \underline{0}, \\ \underline{U}(\eta, 0) &= \begin{cases} \overline{U}_{ij}^{n+\frac{1}{2}}, & \eta < 0 \\ \overline{U}_{ji}^{n+\frac{1}{2}}, & \eta > 0 \end{cases} \end{aligned} \quad (1.54)$$

4. Evolution of \underline{U}_i^n , at a time $t + \Delta t_n$ according to:

$$\underline{U}_i^{n+1} = \underline{U}_i^n + \frac{\Delta t}{|K_i|} \sum_{j \in \gamma(i)} |\mathcal{F}_{ij}| \hat{\underline{F}}^{\text{HLLC}}(\overline{U}_{ij}^{n+\frac{1}{2}}, \overline{U}_{ji}^{n+\frac{1}{2}}, \underline{n}_{ij}). \quad (1.55)$$

The time step Δt_n is set using the already introduced Courant-Friedrichs-Lewy (CFL) condition (see equation 1.20). The numerical flux function $\hat{\underline{F}}^{\text{HLLC}}(\overline{U}_{ij}^{n+\frac{1}{2}}, \overline{U}_{ji}^{n+\frac{1}{2}}, \underline{n}_{ij})$ is evaluated using the HLLC approximate Riemann solver detailed in section 1.2.3 while the flux $\underline{F}(\overline{U}_{ij}^n)$ can be directly evaluated from \overline{U}_{ij}^n .

1.2.6 - Discretization of the non-conservative term for multicomponent flows

So far, the numerical methods presented are valid for conservative equations like the Euler equations (see equation 1.1). When the right-hand side of the equation is not equal to the null vector ($\underline{0}$) like the five-equation model presented in equation 1.3, the non-conservative term needs a specific discretization. In our case, the term $\underline{B}(\underline{U})$ is approximated at the first order in time and space which, using the Green-Ostrogradski theorem leads to:

$$\int_{t^n}^{t^{n+1}} \int_{K_i} \nabla \cdot \underline{u} \, dV \, dt = \int_{t^n}^{t^{n+1}} \sum_{j \in \gamma(i)} \int_{\mathcal{F}_{ij}} \underline{B}(\underline{U}) \underline{u} \cdot \underline{n}_{ij} \, dS \, dt. \quad (1.56)$$

We introduce the numerical function,

$$\Delta t_n \hat{u}_{ij}(\underline{U}_{ij}^{*n}, \underline{n}_{ij}) \approx \frac{1}{|\mathcal{F}_{ij}|} \int_{t^n}^{t^{n+1}} \int_{\mathcal{F}_{ij}} \underline{u} \cdot \underline{n}_{ij} \, dS \, dt, \quad (1.57)$$

whose purpose is to approximate the normal velocity over the interface \mathcal{F}_{ij} . The interface velocity $u_{ij}^* = \hat{u}_{ij}(\underline{U}_{ij}^{*n}, \underline{n}_{ij})$ is given by the modified HLLC Riemann solver for the advection equation presented in [98]. As a result, the non-conservative term 1.56 can then be added to the fourth step of the MHM given by equation 1.55 which then writes:

$$\underline{U}_i^{n+1} = \underline{U}_i^n - \frac{\Delta t_n}{|K_i|} \sum_{j \in \gamma(i)} |\mathcal{F}_{ij}| \hat{\underline{F}}^{\text{HLLC}}(\overline{U}_{ij}^{n+\frac{1}{2}}, \overline{U}_{ji}^{n+\frac{1}{2}}, \underline{n}_{ij}) - \frac{\Delta t_n}{|K_i|} \underline{B}(\underline{U}_i^n) \sum_{j \in \gamma(i)} |\mathcal{F}_{ij}| u_{ij}^*. \quad (1.58)$$

1.3 - Chapter conclusion

The finite volume framework has been chosen as it ensures conservation of the Euler system of equation. We have detailed the different models that will be used in this work to assess the developed overlapping grid method. The numerical scheme is based on a Godunov type method with a limited MUSCL-Hancock scheme which is second order accurate in time and space. This method has been chosen as it corresponds to industrial standard of accuracy and robustness. The time integration is explicit as it is more adapted to simulate fast transient phenomena with small time scales. The particular treatment for the non-conservative term in the case of multicomponent flows has also been reviewed. In the next chapter, we detail the development of an overlapping grid method within the finite volume framework presented.

2 - Development of a finite volume multi-grid Chimera method in a fast dynamic framework

Contents

2.1	The Chimera method principle	28
2.2	Development of a finite volume Chimera method	30
2.2.1	Chimera framework and notations	30
2.2.2	Identification and marking of the ghost cells allowing two grid communication	32
2.2.3	Derivation of a first and second order Chimera interpolation	36
2.2.4	Study of the number of ghost cell layers dependency on the discretization scheme	41
2.2.5	Impact of the Chimera method on the time step	42
2.3	Implementation of the Chimera method in MANTA software	43
2.3.1	Presentation of MANTA software	43
2.3.2	Implementation of the Chimera procedure within the solver	43
2.4	Validation of the Chimera method on 1D test cases	48
2.4.1	Solution reconstruction over overlapping grid domains	48
2.4.2	Sinus advection	49
2.4.3	Split Sod shocktube	61
2.4.4	Conservation properties of the present Chimera method	71
2.5	Advection of an isentropic vortex	76
2.5.1	Impact of the Chimera sending on the order of convergence	78
2.5.2	Impact of the cell ratio (χ) on the solution	81
2.6	Chapter conclusion	83

In this chapter, we present the different implementations of the Chimera method that we can find in the literature and we explain the main differences with the Chimera method that we developed. Then, we detail the development of a Chimera method for fast transient dynamics in a finite volume framework. The method relies on a local conservation hypothesis using actual cells called ghost cells acting as receiving containers. We provide a detection and marking procedure to identify potential ghost cells given a set of two overlapping grids. An extended version of the marking procedure is provided. Then, a first and second order interpolation formulas are proposed to reconstruct a solution that will be sent from one grid to the other and vice versa. The second order interpolation uses a modified slope limiter that prevents the appearance of spurious oscillations especially when using high cell size discrepancies between the sending grid and the receiving grid. The different versions of the developed Chimera method are assessed using one-dimensional test cases like the advection of a sinusoidal density perturbation, the Sod shocktube and a stationary shock wave as well as a two-dimensional isentropic vortex advection. An optimal configuration for the developed Chimera method is provided as a reference.

2.1 - The Chimera method principle

In this work, we are interested in superimposing local geometrical alterations onto a large global fluid domain. The local geometrical alterations can generate local flow perturbations that will impact the fluid solution at the global domain scale. As the numerical approach that we want to develop must rely on independent grids with different refinements on each grid, we have chosen to focus on composite grid techniques that allow information transfer in both directions¹. The multi-model method that we have developed falls within the framework of the Chimera method [166, 17, 165]. It is a multi-model approach that allows overlapping grids to exchange information. In this chapter, we consider two grids: a baseline grid $\mathcal{W} = \{K_i\}_{i \in \Omega_{\mathcal{W}}}$ that is referred as substrate and a secondary grid $\mathcal{V} = \{K'_i\}_{i \in \Omega_{\mathcal{V}}}$ that is referred as patch (see Fig. 2.1). The substrate refers to the global grid while the patch is a local grid, partially or completely, superimposed onto the substrate.

The various implementations of the Chimera method found in the literature require a pre-processing grid treatment called *hole cutting* on the substrate. This step prepares the substrate by disabling the redundant cells located under the patch. As shown in Figure 2.1, the hole cutting step can be done in order to define a transition zone [101, 100, 23], which corresponds to the first category of Chimera methods, or to reduce the amount of overlapped cells between the grids to the bare minimum [82, 83, 84, 32, 157, 136] which corresponds to the second category of Chimera methods. The first category requires a remeshing of the transition zone and solves the system of equation on a single grid. It is referred as method 1 in Figure 2.1 and it is not considered here as an overlapping grid technique.

The second category of Chimera methods deactivates substrate cells that are completely located under the patch and are not necessary to transfer information between the grids. The substrate with its overlapped cells disabled is referred as *cut substrate*. In many applications, the second category of Chimera methods is preferred to the first category, as it has shown to be less computationally expensive and more flexible regarding high cell size discrepancies between the patch and the substrate. Indeed, with the first hole cutting approach, the transition zone uses cells conforming to both the patch and the substrate. Using high cell size discrepancies between the grids would require a larger transition zone to ensure high quality cells in this region. Two versions of the Chimera method derive from the second category and are shown in Figure 2.1:

- The first version is referred as method 2 and imposes transmission conditions at the outer boundary of the patch and at the inner boundary of the cut substrate. Using a finite volume scheme, the transmission conditions often relate to the fluxes imposed at the boundaries of the domains.
- The second method is referred as method 3 and uses extension cells called ghost cells. The ghost cells are usually virtual cell extensions that can receive information interpolated from the sending grid exclusively [86, 19] or from both grids using a combination of the numerical solutions [48]. Here we focus on information coming exclusively from the other grid. As we are focusing on independent grids that are non-coincident and may have different grid resolutions, the information received by the ghost cells needs to be interpolated using an appropriate set of sending cells located on the sending grid but in the same area as the ghost cell. This step is referred as interpolation in the following. The interpolation of the information can be based on conservative variables or primitive variables and can be achieved using various techniques like multi-linear interpolations [82, 83, 84, 32, 157], multi-linear interpolations with global to local frame transformations [107] or least square based methods [147].

¹From the local grid to the global grid and from the global grid to the local grid

Even though imposing an interpolated flux at the borders of the domains through method 2 is the most physically accurate approach due to ensured conservation, it is not recommended for industrial applications as it involves stability issues [133]. As a consequence, we focus on method 3 as it offers minimal intrusiveness and stability.

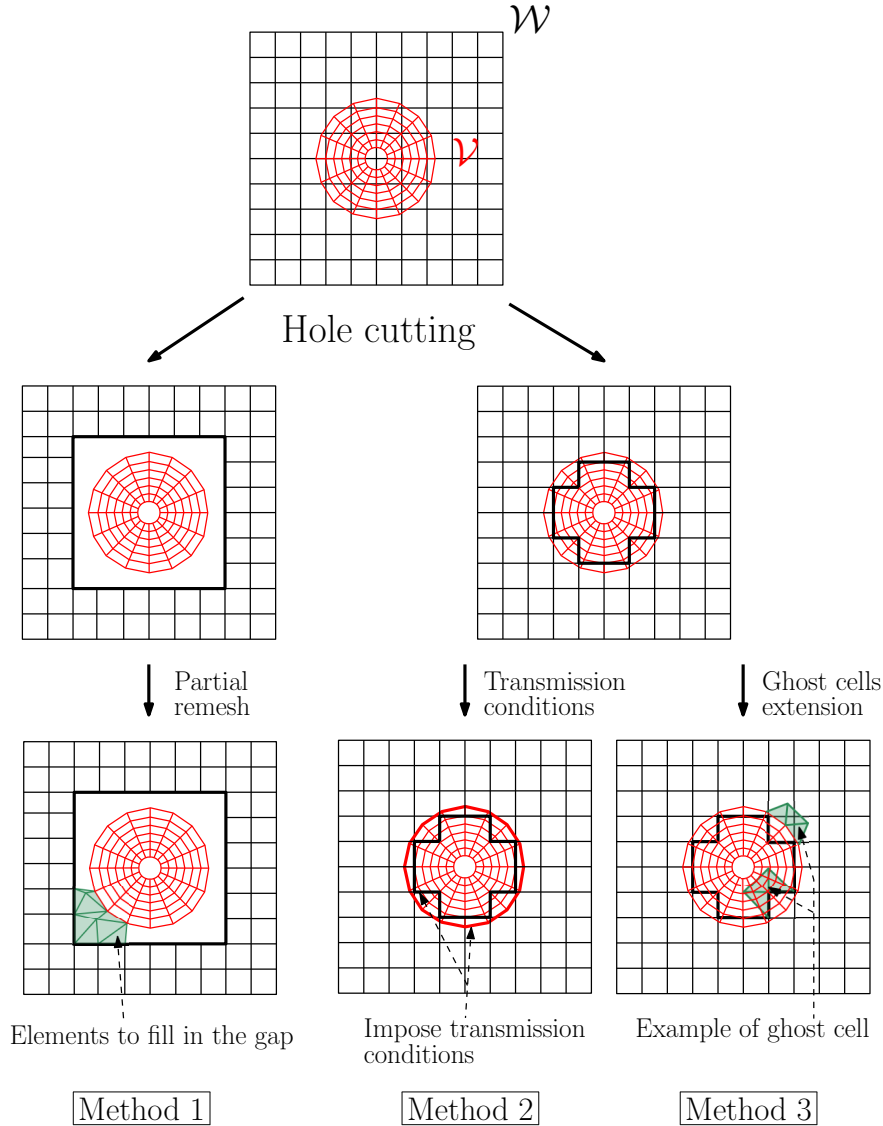


Figure 2.1: Three main implementations of the Chimera method found in the literature.

Method 3 presents two variants regarding the interpolation of the solution across the domains referred as explicit and implicit interpolations in the literature. For the sake of clarity, we denote, $\tilde{\mathcal{V}}$ the set of patch ghost cells and $\tilde{\mathcal{W}}$ the set of substrate ghost cells. Figure 2.2 illustrates the differences between an explicit interpolation and an implicit interpolation: the explicit interpolation is defined by an empty intersection between the two sets of ghost cells. Therefore, the exchange of information is independent between the grids as the ghost cells are only receiving information from cells that are not ghost cells. With an implicit coupling, the intersection of the sets of ghost cells $\tilde{\mathcal{V}}$ and $\tilde{\mathcal{W}}$ is no longer empty resulting in a dependence of the ghost cell solutions across the two grids. Considering that the time integration of the numerical scheme is explicit, we have chosen an explicit coupling between grids for the Chimera procedure [82, 86] as its implementation in an explicit time-integration context is straightforward.

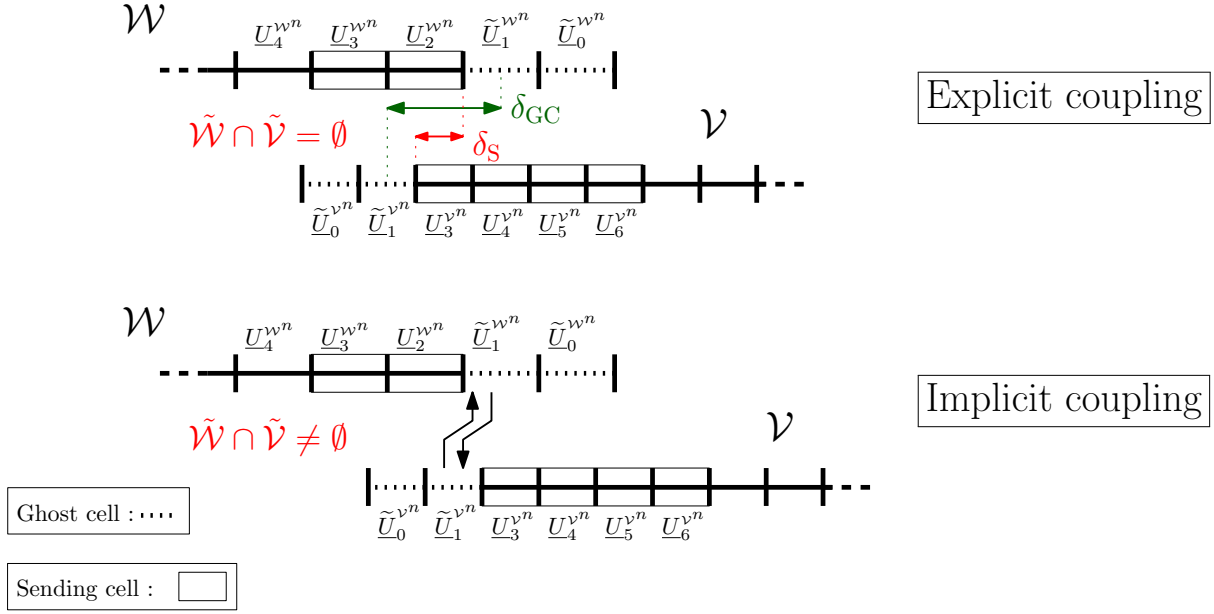


Figure 2.2: Explicit and Implicit Chimera coupling.

2.2 - Development of a finite volume Chimera method

In this work, we present a version of the Chimera method that slightly differs from the method 3 as it uses actual cells from the grid as ghost cells instead of virtual cell extensions and does not use a hole cutting grid pre-processing which means that we do not deactivate any cells from the substrate. These choices have been made in order to design the method as less intrusive as possible regarding the substrate as we do not want to modify the grids when introducing the patch. Actual cells are identified and marked as ghost cells using geometrical criteria to ensure that the ghost cell support is compatible with the explicit Chimera interpolation. Also, the number of ghost cell layers needs to be sufficiently large to ensure hermeticity between the outer region of the substrate and the inner region of the substrate located under the patch. By hermetic, we mean that the numerical solution of the substrate cells located under the patch must not impact the numerical solution of the non-overlapped substrate cells.

2.2.1 - Chimera framework and notations

Our finite volume Chimera method relies on the injection inside ghost cells of conservative variables interpolated using the corresponding neighbor cells on the other mesh, at every time step. We note $\{\underline{U}_i^{\mathcal{W}}\}_{i \in \Omega_{\mathcal{W}}}$, the conservative variables resolved on the substrate and $\{\underline{U}_i^{\mathcal{V}}\}_{i \in \Omega_{\mathcal{V}}}$ the conservative variables resolved on the patch. The set of ghost cells are denoted $\tilde{\mathcal{V}} \subset \mathcal{V}$ and $\tilde{\mathcal{W}} \subset \mathcal{W}$. The interpolated solutions are written $\{\tilde{U}_i^{\mathcal{W}}\}_{i \in \Omega_{\tilde{\mathcal{W}}}}$ for the substrate and $\{\tilde{U}_i^{\mathcal{V}}\}_{i \in \Omega_{\tilde{\mathcal{V}}}}$ for the patch as represented in Figure 2.3. The sending cells are denoted $\mathcal{W}^s \subset \mathcal{W}$ and $\mathcal{V}^s \subset \mathcal{V}$ and are intersected by the ghost cell sets $\tilde{\mathcal{V}}$ and $\tilde{\mathcal{W}}$ respectively. The interface between two adjacent cells $(K_i, K_j)_{(i,j) \in \Omega_{\mathcal{U}} \times \gamma(i)}$, is denoted $\mathcal{F}_{ij}^{\mathcal{U}}$, $\mathcal{U} = \{\mathcal{W}, \mathcal{V}\}$.

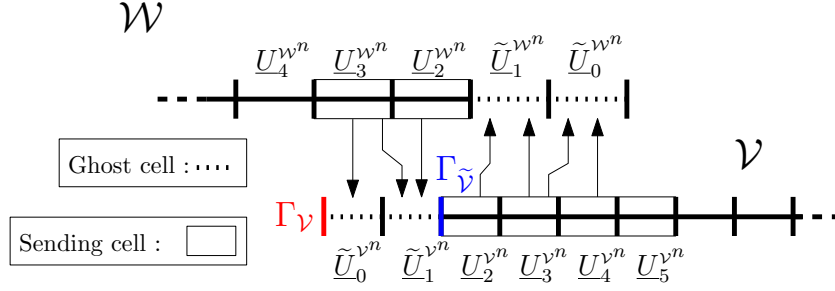


Figure 2.3: Sketch of the transfer procedure in the developed Chimera method.

Given a substrate \mathcal{W} , an immersed patch \mathcal{V} and their respective sets of ghost cells $\tilde{\mathcal{W}}$ and $\tilde{\mathcal{V}}$ as shown in Figure 2.4, we define the cleaned patch and cleaned substrate cell sets respectively \mathcal{W}_c and \mathcal{V}_c as:

$$\mathcal{V}_c = \mathcal{V} \setminus \tilde{\mathcal{V}}, \text{ and } \mathcal{W}_c = \mathcal{W} \setminus \mathcal{W}_p, \quad (2.1)$$

where,

$$\mathcal{W}_p = \{K_i \in \mathcal{W} \setminus \tilde{\mathcal{W}}, |K_i \cap \mathcal{V}_c| = |K_i|\}, \quad (2.2)$$

is the set containing substrate cells that are not ghost cells and that are fully overlapped by the cleaned patch. The cell sets \mathcal{W}_c and \mathcal{V}_c contain cells with a valid solution after each iteration of the MUSCL-Hancock scheme applied to the fluid domains \mathcal{W} and \mathcal{V} . These cells are referred as *resolved cells* as their values result from the resolution of the MUSCL-Hancock scheme detailed in section 1.2.5. We define the cleaned patch Chimera boundary denoted $\Gamma_{\tilde{\mathcal{V}}}$, the interface between the ghost cell set $\tilde{\mathcal{V}}$ and the resolved cells set \mathcal{V}_c . Similarly, we define the substrate Chimera boundary denoted $\Gamma_{\tilde{\mathcal{W}}}$.

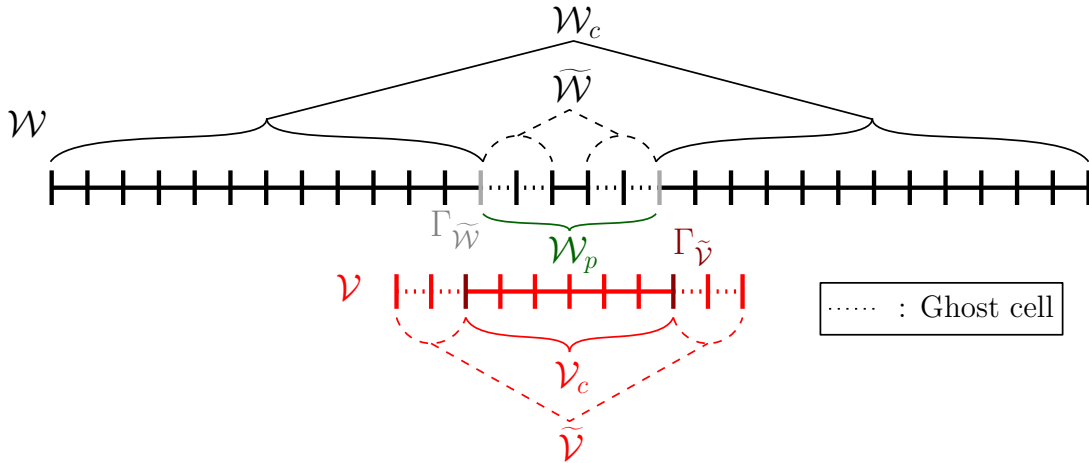


Figure 2.4: Definition of the resolved cells set for an immersed patch (\mathcal{V}).

Using the notations introduced in Figure 2.3 and Figure 2.4, we note $h_i^{\mathcal{V}}$ and $h_j^{\mathcal{W}}$, respectively, characteristic lengths of the cells $\tilde{K}_i \in \tilde{\mathcal{V}}$ and $\tilde{K}_j \in \tilde{\mathcal{W}}$. For each ghost cell from the patch \tilde{K}_i , $i \in \Omega_{\tilde{\mathcal{V}}}$, we define the local cell ratio between the patch and the substrate as :

$$\chi_i^{\mathcal{V}} = \max_{j \in \Omega_{\tilde{K}_i' \cap \mathcal{W}_c}} \left(\frac{h_j^{\mathcal{W}}}{h_i^{\mathcal{V}}} \right). \quad (2.3)$$

The equivalent definition can be made for a local cell ratio between the substrate and the patch and is the inverse of the previous definition:

$$\chi_i^{\mathcal{W}} = \max_{j \in \Omega_{\tilde{K}_i \cap \mathcal{V}_c}} \left(\frac{h_j^{\mathcal{V}}}{h_i^{\mathcal{W}}} \right). \quad (2.4)$$

In our multi-model approach, we are interested in adding local models to the baseline model, thus the local cell ratio between the patch and the substrate is more adapted to our approach. We define the cell ratio (χ) as a global grid parameter for both models using the definition:

$$\chi = \max_{i \in \Omega_{\tilde{\mathcal{V}}}} (\chi_i^{\mathcal{V}}). \quad (2.5)$$

The global definition makes sense in the case of regular grid spacing inside each model.

2.2.2 - Identification and marking of the ghost cells allowing two grid communication

Compared to the original and previous Chimera methods described in [82, 83, 48, 86, 87], we modified the ghost cell detection since we do not want to deactivate any cell nor modify grids. The proposed Chimera procedure is designed to be as flexible and independent as possible from the baseline simulation. The detection of ghost cells happens only once because the patch is considered fixed during calculation. The steps of the detection procedure that is referred as *standard detection* in the following are illustrated in Figure 2.5.

1. Given a set of two overlapping grids \mathcal{W} (substrate) and \mathcal{V} (patch) (see Fig. 2.5-1), we prescribe a number of ghost cell layers (denoted k_{GC}) required to calculate the numerical fluxes at the cleaned patch boundary $\Gamma_{\tilde{\mathcal{V}}}$ without any influence of the boundary condition at the boundary $\Gamma_{\mathcal{V}}$. We will see hereafter how to choose k_{GC} .
2. Then, given the boundary $\Gamma_{\mathcal{V}}$ of the patch domain (see Fig. 2.5-2), the procedure identifies cells from the patch that will be marked as ghost cells $\tilde{\mathcal{V}}$ (see Fig. 2.5-3).
3. Once ghost cells $\tilde{\mathcal{V}}$ are identified, the geometrical intersection $\tilde{\mathcal{V}} \cap \mathcal{W}$ is calculated to mark the corresponding sending cells \mathcal{W}^s (see Fig. 2.5-4).
4. Symetrically, $\tilde{\mathcal{W}}$ is defined by searching the closest k_{GC} ghost cell layers to $\tilde{\mathcal{V}}$ (see Fig. 2.5-5) that respects the following condition for an explicit Chimera interpolation [82]:

$$\tilde{\mathcal{W}} \cap \tilde{\mathcal{V}} = \emptyset \quad \text{and} \quad \tilde{\mathcal{W}} \cap \mathcal{V} \neq \emptyset. \quad (2.6)$$

5. Similarly to the patch, once substrate ghost cells ($\tilde{\mathcal{W}}$) are identified, the intersection $\tilde{\mathcal{W}} \cap \mathcal{V}$, is computed to mark the corresponding sending cells \mathcal{V}^s (see Fig. 2.5-5).

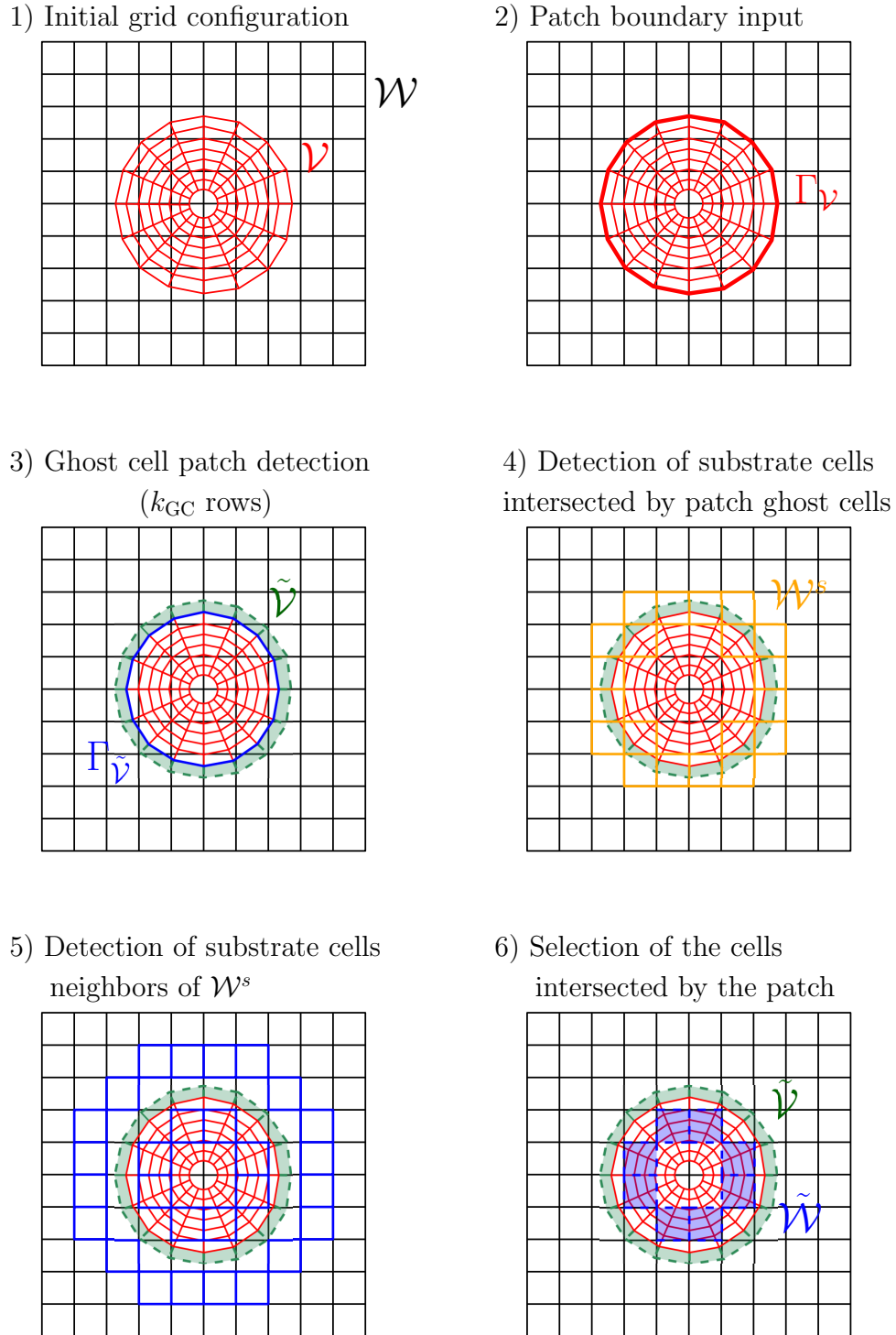


Figure 2.5: Standard detection procedure of the developed Chimera method.

As we are interested in the effect of the cell ratio (χ) within the framework of the Chimera exchange, we need to define the exchange zone gap as:

$$\delta_{GC} = \min_{i \in \Omega_{\tilde{W}}} \left(\min_{j \in \Omega_{\tilde{V}}} (|\underline{x}_j - \underline{x}_i|) \right). \quad (2.7)$$

The exchange zone gap (δ_{GC}) corresponds to the minimal distance separating the substrate ghost

cell set ($\tilde{\mathcal{W}}$) to the patch ghost cell set ($\tilde{\mathcal{V}}$). We also define the exchange zone shift as:

$$\delta_S = \delta_{GC} - \frac{\tilde{h}_{\max}^{\mathcal{W}} + \tilde{h}_{\max}^{\mathcal{V}}}{2}, \quad (2.8)$$

which corresponds to the minimum gap between the the patch Chimera boundary ($\Gamma_{\tilde{\mathcal{V}}}$) (illustrated as a thick red line in Fig. 2.7) and the substrate Chimera boundary ($\Gamma_{\tilde{\mathcal{W}}}$) (illustrated as a thick black line in Fig. 2.7). In a one-dimensional case with uniform grid spacing on each independent grid, $\delta_S = 0$ implies that the patch and the substrate have coincident Chimera interfaces.

Using Figure 2.6, we can see that with high enough cell ratios like $\chi = 10$, we can have $\delta_{GC} \geq h_{\max}$, where $h_{\max} = \max(\tilde{h}_{\max}^{\mathcal{V}}, \tilde{h}_{\max}^{\mathcal{W}})$ is the maximum characteristic cell measure between the patch and the substrate within the exchange zone and

$$\tilde{h}_{\max}^{\mathcal{U}} = \max_{i \in \Omega_{\tilde{\mathcal{U}} \cup \mathcal{U}^s}}(h_i^{\mathcal{U}}), \quad \mathcal{U} = \{\mathcal{V}, \mathcal{W}\}. \quad (2.9)$$

As shown in Figure 2.6, high cell ratios involve the appearance of group of cells located inside the exchange zone while neither being sending cells nor a ghost cells. We call these groups, recirculation zones. Using the configuration in Figure 2.6, in the case of a very high cell ratio ($\chi > 4$), if a flow perturbation, like a shock wave, initially located outside the patch travels from the substrate to the patch (left to right in Fig. 2.6), it is transferred to the substrate using the ghost cells $\tilde{\mathcal{V}}$. Using a unique time step for both grids respecting the CFL condition on the finest one (the patch), the shock wave propagates simultaneously in the patch and in the substrate which have different resolutions. Therefore, the solution on the patch diverges from the original solution in the substrate as it propagates in the recirculation zone. Once the perturbation reaches the sending cells \mathcal{V}^s , the perturbation is transferred back to the substrate which could potentially create numerical instabilities at the substrate Chimera interface ($\Gamma_{\tilde{\mathcal{W}}}$). As the Chimera exchange is performed in both directions, the presence of a recirculation zone could introduce numerical artifacts generated in the exchange zone. The impact of the recirculation zones on the global solution will be assessed in the next sections.

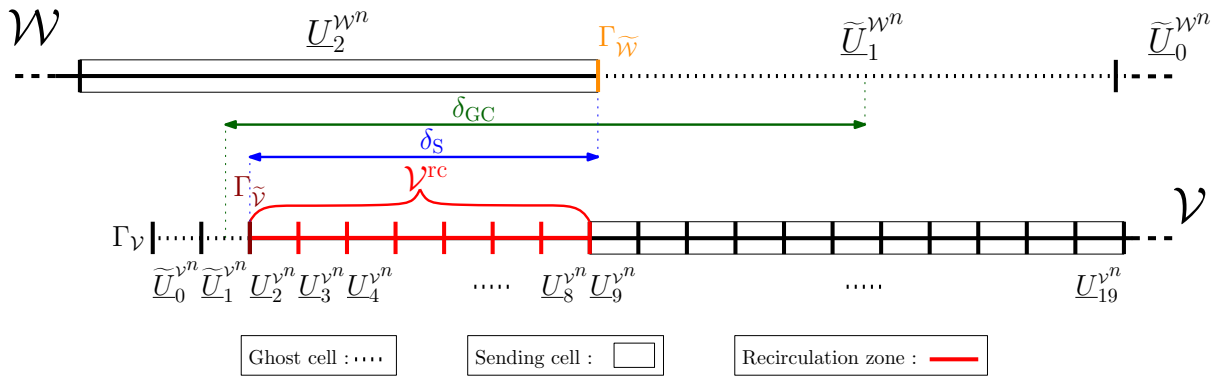


Figure 2.6: Schema of an overlapping grid configuration with a recirculation zone (\mathcal{V}^{rc}).

One way to avoid the presence of recirculation zones is to ensure that $\delta_{GC} \leq h_{\max}$. It can be achieved from the standard detection by marking additional cells as ghost cells if they geometrically lie in between the ghost cell layers of the patch and the ghost cell layers of the substrate, without breaking the condition 2.6. As a result, the ghost cell layers of the patch are extended to fit the ghost cell layers of the substrate as shown in Figure 2.7 and the recirculation zones are minimized as seen in Figure 2.8. This ghost cell extension step combined with the standard detection procedure is referred as *extended detection* in the following.

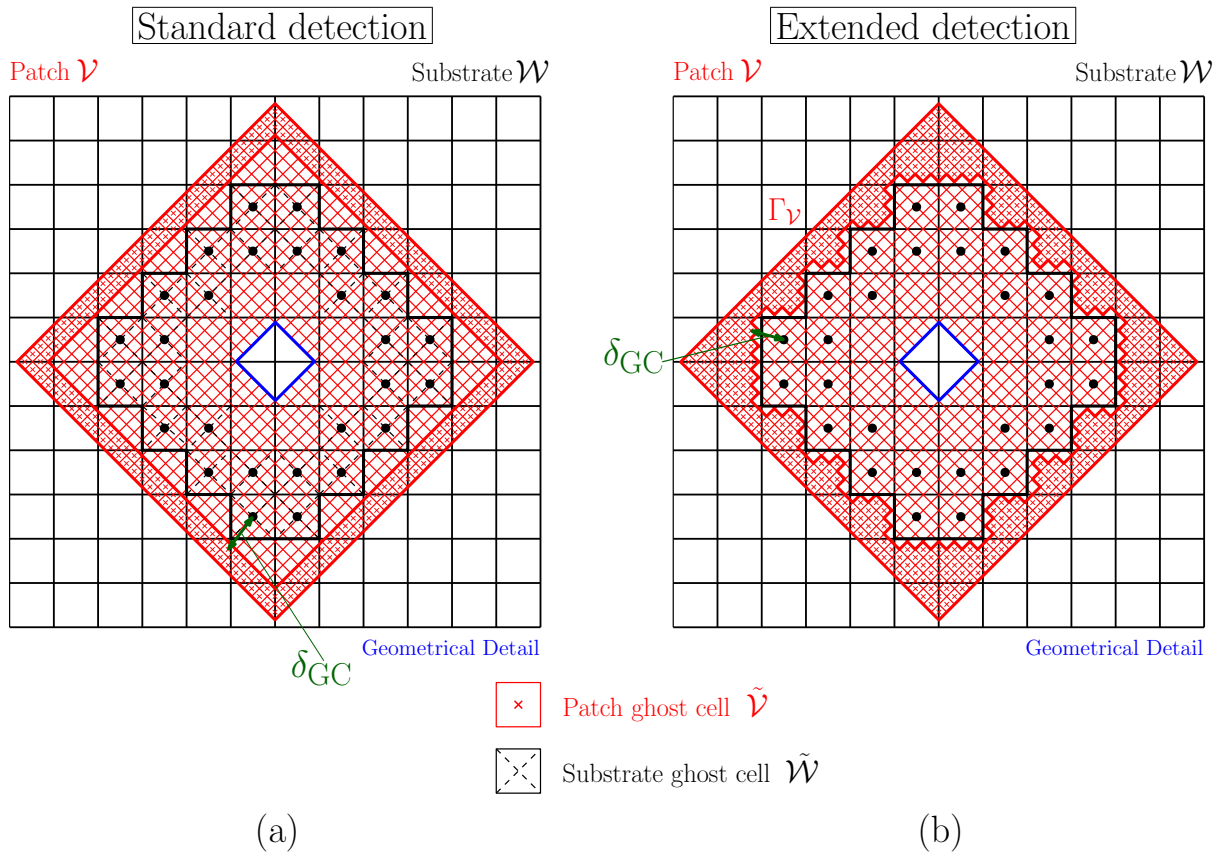


Figure 2.7: Ghost cell detection procedures for $k_{GC} = 2$ with $\chi = 4$

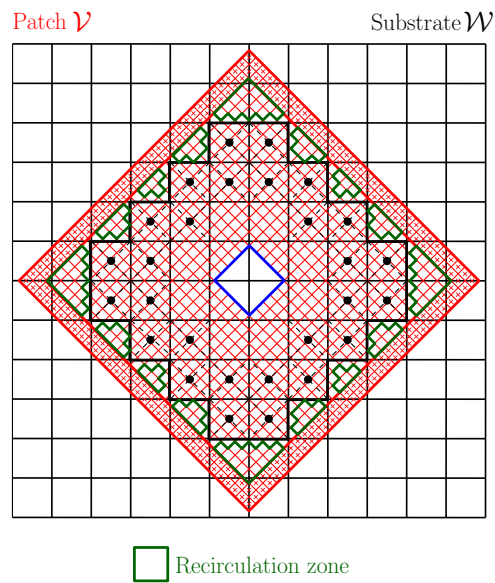


Figure 2.8: Identification of the recirculation zones for high cell ratios (χ).

2.2.3 - Derivation of a first and second order Chimera interpolation

A . First order interpolation

As we are using a conservative finite volume approach, the present Chimera method is based on local conservation hypothesis when the transfer occurs between opposite grids. Indeed as it is shown in Figure 2.9, the method relies on the intersection of ghost cells with the opposite grid.

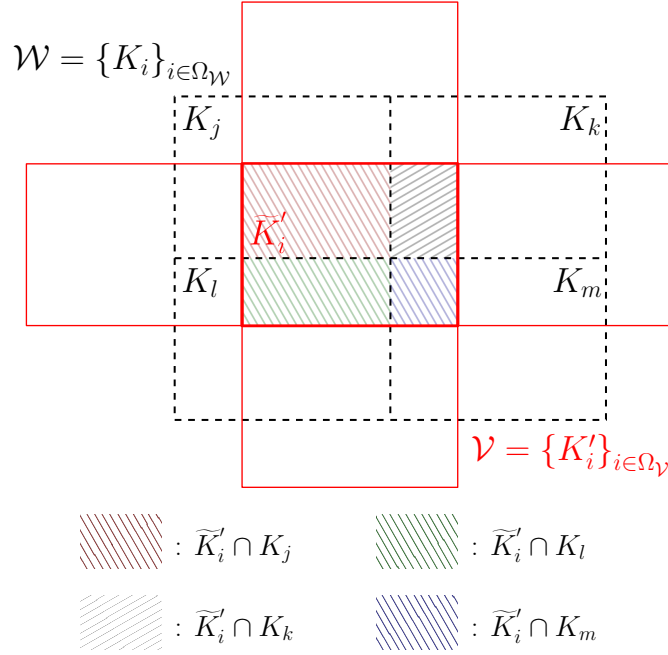


Figure 2.9: Example of a ghost cell intersection \tilde{K}'_i with \mathcal{W} for a first order interpolation.

From a finite volume framework, considering the substrate ghost cell \tilde{K}_i , $i \in \Omega_{\mathcal{W}}$ we suppose that:

$$\int_{\tilde{K}_i} \tilde{U}^{\mathcal{W}} dV = \int_{\tilde{K}_i \cap \mathcal{V}} U^{\mathcal{V}} dV. \quad (2.10)$$

The local conservation hypothesis can be recast in a piecewise constant approximation which gives:

$$\tilde{U}_i^{\mathcal{W}^n} = \sum_{j \in \Omega_{\mathcal{V}}} \frac{|\tilde{K}_i \cap K'_j|}{|\tilde{K}_i|} U_j^{\mathcal{V}^n}, \quad (2.11)$$

In the case of equivalent cell size between the grids ($\chi \approx 1$) and non-coincident grids, this interpolation formula is comparable to the linear interpolations done in [133, 32, 82, 83] with finite difference schemes. In the literature it is considered as a polynomial interpolation, and the order of the approximation depends on the number of patch cells intersected by \tilde{K}_i , $i \in \Omega_{\mathcal{W}}$. However, with $\chi \gg 1$, different ghost cells can end up receiving the same constant state from the same sending cell. As a consequence, this method is referred as first order Chimera method in the followings.

B . Second order interpolation

We propose to improve the first order interpolation for configurations where $\chi \neq 1$. Similarly to what is done in the MUSCL reconstruction, a piecewise linear reconstruction of the transferred solution is adequate to achieve the suitable order of accuracy independently from the grid configuration

compared to a constant piecewise approximation of the solution. We define the barycenter position of the intersection $\tilde{K}_i \cap K'_j$ inside the ghost cell \tilde{K}_i , denoted \tilde{x}_{ij} as shown in Figure 2.10.

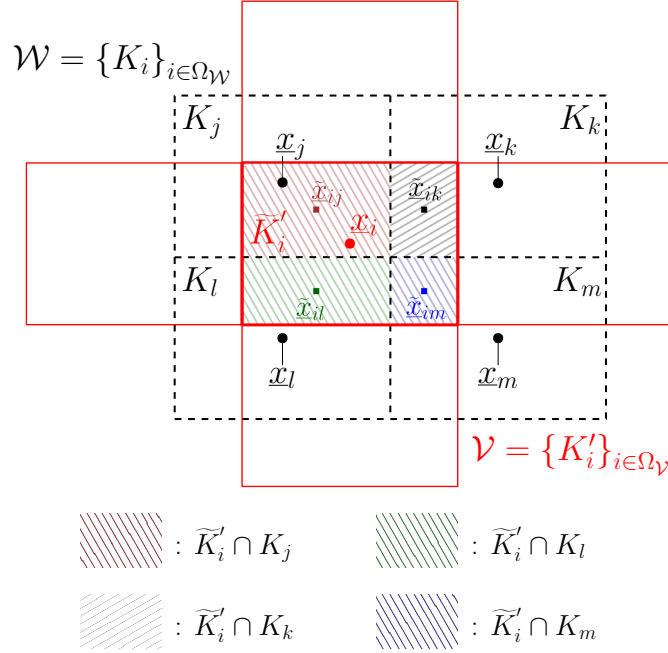


Figure 2.10: Example of a ghost cell intersection \tilde{K}_i with \mathcal{W} for a second order interpolation.

Then, we discretize equation 2.10 with a piecewise linear reconstruction: $\forall i \in \Omega_{\tilde{\mathcal{W}}}$,

$$\tilde{U}_i^{\mathcal{W}^n} = \sum_{j \in \Omega_{\mathcal{V}}} \frac{|\tilde{K}_i \cap K'_j|}{|\tilde{K}_i|} \bar{U}_j^{\mathcal{V}^n}(\tilde{x}_{ij}) = \sum_{j \in \Omega_{\mathcal{V}}} \frac{|\tilde{K}_i \cap K'_j|}{|\tilde{K}_i|} \left(U_j^{\mathcal{V}^n} + \Psi_j^{\mathcal{V}} \nabla(U_j^{\mathcal{V}^n}) \cdot (\tilde{x}_{ij} - \underline{x}_j) \right), \quad (2.12)$$

where $\nabla(U_j^{\mathcal{V}^n})$ is the gradient of the solution $U_j^{\mathcal{V}^n}$ based on conservative variables. The gradient is calculated for each sending cell set (\mathcal{W}^s and \mathcal{V}^s) using the presented centered *least squares method* [118]. $\Psi_j^{\mathcal{V}}$ is a slope limiter employed to avoid spurious oscillations and to keep the TVD property of the solution when transfer on the grid model is performed like for the MUSCL reconstruction 1.48. The present formulation ensures a spatial second order accurate interpolation in ghost cells without any constraint on the grids, *i.e.* meshes can either be structured or unstructured. Equations 2.11 and 2.12, can reciprocally be written for $i \in \Omega_{\tilde{\mathcal{V}}}$.

Even though these interpolations result from a conservative assumption, the resulting procedure is not fully conservative as it has been demonstrated that the only conservative approach is based on flux interpolation [184, 185, 133]. Nonetheless, using an integral formulation on conservative variables for transferring solutions remains consistent with the finite volume approach.

Remark. *The proposed reconstructions are based on volume intersections between the ghost cells and the sending cells. As a result, intersection volumes are used to reconstruct the solution inside each ghost cell with both the first order and the second order interpolations. Additionally, the center of the intersection volumes is used to evaluate the linearly reconstructed state inside the sending cells for the second order interpolation. In the literature, the finite volume implementations of the Chimera method do not use grid intersections volumes. Instead, each ghost cell state is linearly interpolated using the positions of the centers of the sending cells acting like an interpolation molecule. These implementations can be found inside the codes like elsA [64, 136] or TAU [154, 187] and derive from the finite difference version of the Chimera method. Found inside codes like Overture [82, 83, 84, 32,*

157] or NASA [119, 120, 141, 12], these finite difference implementations of the Chimera method use grid points acting as sending nodes to build an interpolation molecule that surrounding a receiving node. Therefore, our implementation is more inline with a finite volume approach as it is built around local conservation of conservative quantities instead of distances.

C . Impact of the second order interpolation on the detection procedure

When using a second order interpolation (see equation 2.12), for any sending cell $K_j \in \mathcal{W}^s$, a gradient $\nabla(U_j^{w^n})$ needs to be reconstructed at every time step. As we want the Chimera gradient reconstruction to be independent from the numerical scheme reconstruction, we define a reconstruction cell set \mathcal{W}^r as a subset of the domain cell set \mathcal{W} . The gradient being interpolated inside each sending cell of \mathcal{W}^s using a centered least squares method (see section 1.2.4 B), we define \mathcal{W}^r as:

$$\mathcal{W}^r = \mathcal{W}^s \cup \gamma(\mathcal{W}^s), \quad (2.13)$$

where

$$\gamma(\mathcal{W}^s) = \{K_i, i \in \Omega_{\mathcal{W}} \setminus K_i \notin \mathcal{W}^s\} \cap \{K_j, j \in \gamma(i), i \in \Omega_{\mathcal{W}^s}\}, \quad (2.14)$$

is the set of cells adjacent to the sending cell set \mathcal{W}^s . As illustrated in Figure 2.11, each sending cell set \mathcal{W}^s and \mathcal{V}^s has an associated reconstruction set \mathcal{W}^r and \mathcal{V}^r . The reconstruction sets allow the use of a different gradient interpolation or a different limiter compared to the one used within the numerical scheme. It makes the Chimera method less intrusive but requires additional computations. This additional cost will be measured later on.

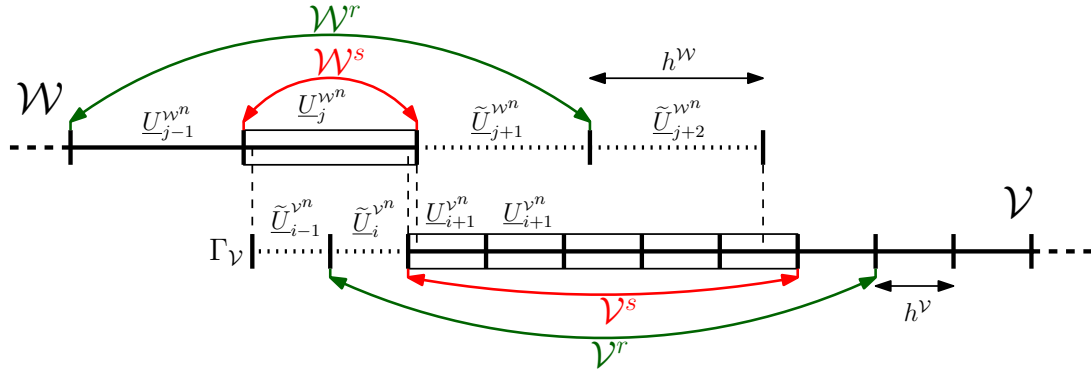


Figure 2.11: Definition of the reconstruction sets \mathcal{W}^r and \mathcal{V}^r given the ghost cell sets $\tilde{\mathcal{W}}$ and $\tilde{\mathcal{V}}$.

Using Figure 2.11, we can see that even though $\tilde{\mathcal{W}} \cap \tilde{\mathcal{V}} = \emptyset$, we have $\tilde{\mathcal{W}} \cap \mathcal{W}^r \neq \emptyset$ and $\tilde{\mathcal{V}} \cap \mathcal{V}^r \neq \emptyset$. As a result, the ghost cells are involved in the gradient reconstruction of the sending cells. The values of the ghost cells between the grids \mathcal{W} and \mathcal{V} become coupled which involves solving a system. One way to adress this issue would be to add the following geometrical criteria on top of the criterion 2.6 during the ghost cell detection and marking steps:

$$\tilde{\mathcal{W}} \cap \mathcal{W}^r = \emptyset, \text{ and } \tilde{\mathcal{V}} \cap \mathcal{V}^r = \emptyset. \quad (2.15)$$

This additional criteria effects on the exchange zone are illustrated in Figure 2.12 using the same grid configuration as in Figure 2.11. The exchange zone is enlarged and the Chimera method becomes more restrictive on the grid configuration which is not what we are looking for.

In order to keep the exchange zone contained as in Figure 2.11 while maintaining a second order explicit interpolation, we propose a solution that uses information already available:

- First, a first order Chimera exchange is used to interpolate the value of the ghost cell sets $\tilde{\mathcal{V}}$ and $\tilde{\mathcal{W}}$.

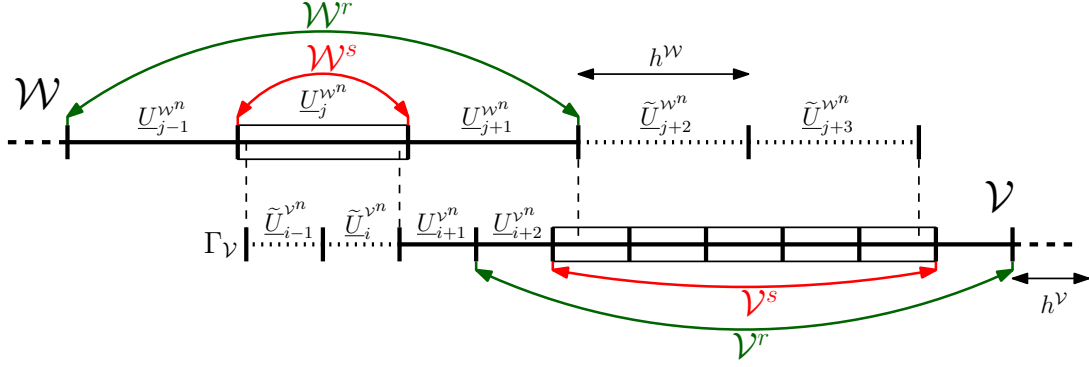


Figure 2.12: Hypothetical extension of the exchange zone to ensure empty intersections between the ghost cell sets and the reconstruction sets (with the same grid configuration as in Fig. 2.11).

- Second, the gradient is interpolated inside the reconstruction sets \mathcal{W}^r and \mathcal{V}^r .
- Third, the solution is reconstructed inside the sending cell sets \mathcal{W}^s and \mathcal{V}^s .
- Finally, the values of the ghost cell sets $\tilde{\mathcal{V}}$ and $\tilde{\mathcal{W}}$ are updated using the second order interpolation.

This solution ensures an appropriate gradient interpolation inside the sending cell sets \mathcal{W}^s and \mathcal{V}^s with a contained exchange zone, even with a second order exchange.

D . Modified K-Dubois limiter for Chimera interpolation

The second order Chimera method (see equation 2.12) requires a limiting procedure to satisfy total variation diminishing (TVD) constraints and avoid the occurrence of local extrema when reconstructing the solution inside the sending cells. To avoid a possible limitation on mesh constructions and to make the method suitable for both structured and unstructured meshes, we have privileged the *K-Dubois* limiter [162] applied to the primitive variables as detailed in section 1.2.4.C. Let us underline that the well-known Barth and Jespersen limiter [97] could also be used with the present method.

The standard utilization of the K-Dubois limiter uses coordinates of the barycenter of the cells $K_i, i \in \Omega_{\mathcal{U}}$ and the center of the faces \mathcal{F}_{ij} respectively denoted \underline{x}_i and $\underline{x}_{(\text{face})_{ij}}$, with $i \in \Omega_{\mathcal{U}}$, $\mathcal{U} = \{\mathcal{W}, \mathcal{V}\}$ and $j \in \gamma(i)$. Taking the maximum value of $|\underline{x}_{(\text{face})_{ij}} - \underline{x}_i|$ ensures that the limited reconstructed solution can be searched inside a neighborhood (*i.e.* a circle in 2D, and a sphere in 3D) with a typical radius of $R = \max_{j \in \gamma(i)} |\underline{x}_{(\text{face})_{ij}} - \underline{x}_i|$ (see Fig. 2.13).

When several overlapping grids are at play, the previous constraint apply to the solution is not restrictive enough to enforce non-oscillatory property, and the search zone must be enlarged to recover TVD properties as it is shown in Figure 2.14. In fact, when refining the patch $\mathcal{V} = \{K'_k\}_{k \in \Omega_{\mathcal{V}}}$, ghost cells can be intersected by a cell portion that is outside of the search region, K_i in this example. The reconstruction then gives:

$$\begin{aligned} \tilde{U}_k^{vn} &= \frac{|\tilde{K}_k \cap K'_i|}{|\tilde{K}_k|} \left(U_i^{wn} + \Psi_i^w \nabla(U_i^{wn}) \cdot (\tilde{x}_{ki} - \underline{x}_i) \right) \\ &+ \sum_{p \in \Omega_{\mathcal{W}} \setminus \{i\}} \frac{|\tilde{K}_k \cap K'_p|}{|\tilde{K}_k|} \left(U_p^{wn} + \Psi_p^w \nabla(U_p^{wn}) \cdot (\tilde{x}_{kp} - \underline{x}_p) \right). \end{aligned} \quad (2.16)$$

Here, we can see that $|\tilde{x}_{ki} - \underline{x}_i|$ can be greater than $|\underline{x}_{(\text{face})_{ij}} - \underline{x}_i|$ depending on the location of the cells. It is even more emphasized when χ increases. In those particular cases, the limiter is not

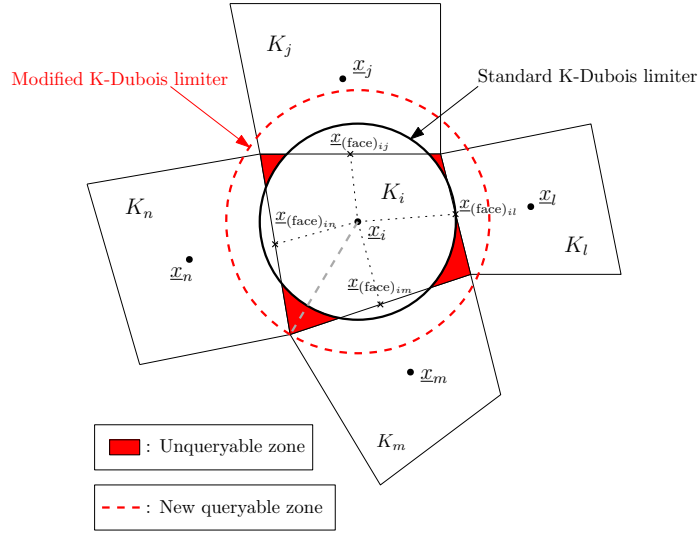


Figure 2.13: Search areas for the K-Dubois limiter in a single model approach and the modified K-Dubois limiter used in the Chimera method. The searchable area in the single model approach is identical to the Barth and Jespersen limiter searchable area [97].

adapted as the solution will be searched outside the search zone described in Figure 2.13. Thus, the transfer can generate local extrema. We propose to recast the previous limiter to make it work with

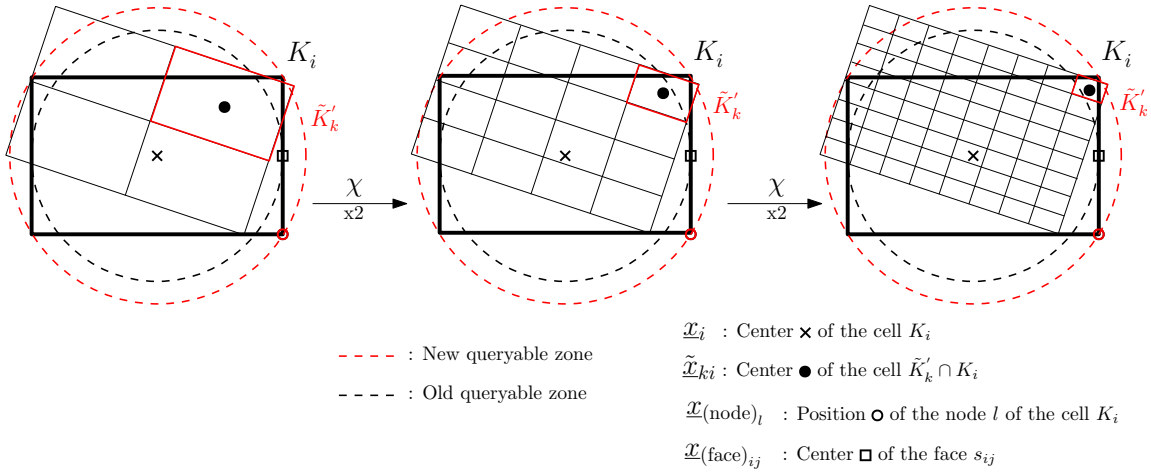


Figure 2.14: Evolution of the positions between the center of the intersection with the sending cell and the center of the sending cell.

the present Chimera method. The k -th component of the modified K-Dubois limiter writes:

$$[\Psi_i^{wv}]_k = \min \left(1, K \cdot \frac{\min \left([U_i^{wv \max} - U_i^w]_k, [U_i^w - U_i^{wv \min}]_k \right)}{\max_{l \in \zeta(i)} \left([\nabla(U_i^{wv}) \cdot (\mathbf{x}_{(\text{node})_l} - \mathbf{x}_i)]_k \right)} \right), \quad (2.17)$$

where $\mathbf{x}_{(\text{node})_l}$ is the cell corner position, and $\zeta(i)$ is the corner set of the cell K_i (see Fig. 2.13). The modified version of the K-Dubois limiter adapted to the present Chimera method is based on the radius calculated from the cell corners instead of centers of cell faces. The radius of the search region is now enlarged with an extended radius $R = \max_{l \in \zeta(i)} (\mathbf{x}_{(\text{node})_l} - \mathbf{x}_i)$. This extends the research zone of the limited solution so as to be valid whatever the geometric configuration of the ghost cells as well as the cell ratio are.

2.2.4 - Study of the number of ghost cell layers dependency on the discretization scheme

As we indicated above, we need to prescribe a number of ghost layers (k_{GC}) before labeling the ghost cells. As mentioned in [178], a second order accurate evaluation of the numerical flux at the interface between two consecutive cells needs a stencil over a neighborhood of at least two consecutive cells from each side of the interface.

When a resolved cell $K'_i, i \in \Omega_{\mathcal{V}_c}$, belonging to \mathcal{V}_c , is close to the boundary of the resolved domain $\Gamma_{\tilde{\mathcal{V}}}$, the number of ghost cell layers (k_{GC}) must be large enough to ensure that the numerical flux evaluation at the interface $\Gamma_{\tilde{\mathcal{V}}}$ does not intercept the patch boundary ($\Gamma_{\mathcal{V}}$) (see K'_2 and a flux evaluation at the interface $\mathcal{F}_{12}^{\mathcal{V}}$ in Fig. 2.15 for reference). If k_{GC} is large enough, the Chimera exchange zone is considered *hermetic* as the patch boundary condition on $\Gamma_{\mathcal{V}}$ has no impact on the solution of the patch resolved cell set (\mathcal{V}_c). The reasoning is equivalent for substrate fluid cells located under the patch ($\mathcal{W}_p \setminus \tilde{\mathcal{W}}$) that must not impact the solution of the substrate resolved cell set (\mathcal{W}_c).

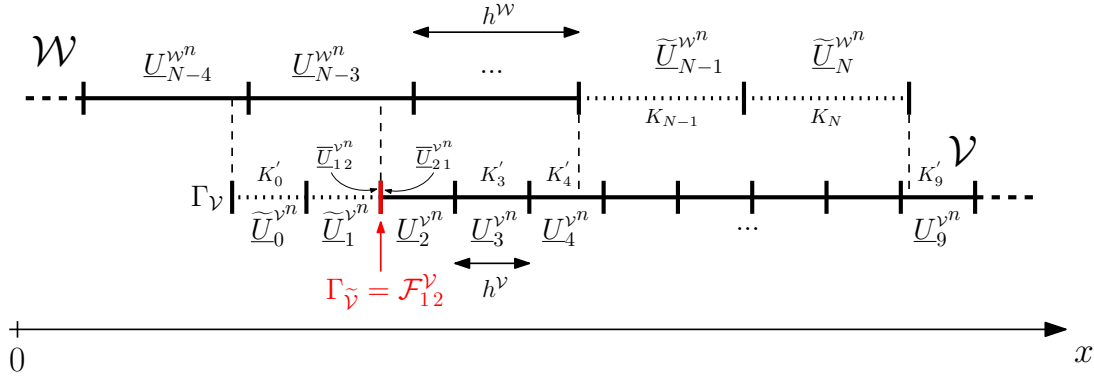


Figure 2.15: Chimera boundary condition.

In this section, we provide a minimum value for k_{GC} depending on the order of the Chimera method that is used. Using the configuration illustrated in Figure 2.15, a second order MUSCL-Hancock scheme is applied to an advection equation in Appendix A. A constant advection velocity a is considered such that $a > 0$. As a result, we assume that the information travels from the substrate to the patch, this analysis exhibits that the solution in the resolved cell $K'_2 \in \mathcal{V}_c$ depends on the solutions of the cells $\tilde{K}'_1 \in \tilde{\mathcal{V}}$ and $\tilde{K}'_0 \in \tilde{\mathcal{V}}$ due to gradient reconstruction. The situation is illustrated in Figure 2.16. This study shows that with a second order MUSCL-Hancock scheme, $k_{GC} \geq 2$ is required to ensure the hermeticity of the domains. For a first order scheme, the same analysis gives $k_{GC} \geq 1$.

If this condition is respected, as values inside ghost cells are updated at each time step from the opposite model, the boundary condition at $\Gamma_{\mathcal{V}}$ has no impact on the solution in the resolved patch cells (\mathcal{V}_c). In a similar way, cells that belong to the substrate portion covered by the patch ($\mathcal{W}_p \setminus \tilde{\mathcal{W}}$) but are not ghost cells have no impact on the solution inside the cleaned substrate (\mathcal{W}_c). As a conclusion, when a first order interpolation is used, $k_{GC} \geq 1$ is required while $k_{GC} \geq 2$ is necessary for a second order interpolation.

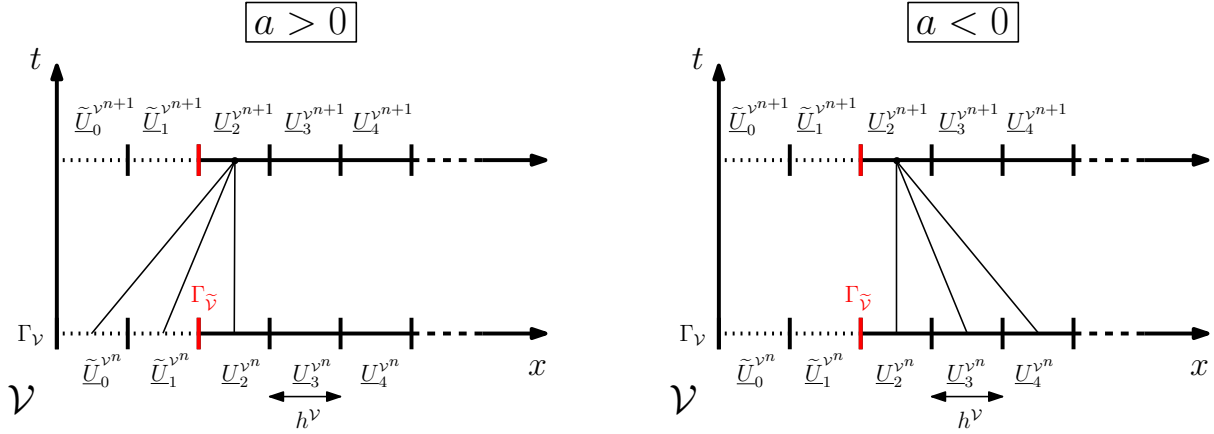


Figure 2.16: Neighbor dependency near the cleaned patch boundary ($\Gamma_{\bar{\mathcal{V}}}$).

2.2.5 - Impact of the Chimera method on the time step

The Chimera method involves a communication process between different grids with a cell ratio (χ) that can be different to 1. In this case, the critical time step Δt_{crit} defined by the CFL condition (see equation 1.20) will be different between the grids, with a smaller one for the finest grid. Using the same notation previously introduced in section 2.2.4, a Von Neumann stability analysis [31] is carried out in Appendix B for a scalar hyperbolic equation with overlapping grids (see Fig. 2.17).

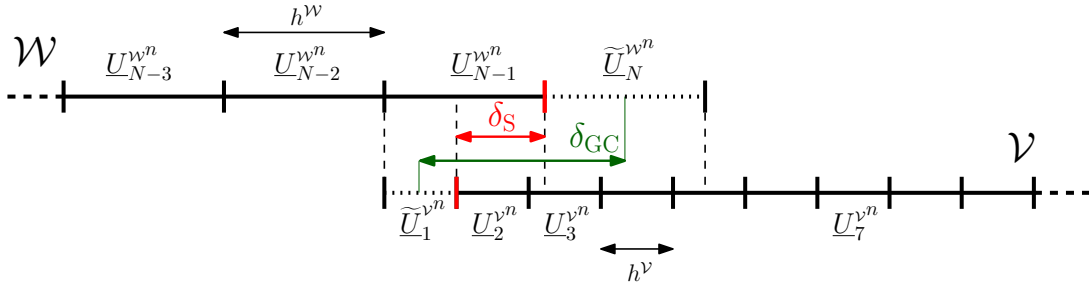


Figure 2.17: Chimera configuration with the exchange zone gap (δ_{GC}) and the exchange zone shift (δ_S).

The Von Neumann stability analysis highlights that very high cell ratios (χ) between grids and obviously time step discrepancies between domains can lead to unstable behavior as advised in [136]. The influence of the grid size on the stability of the Chimera exchange is investigated experimentally later on. As a conclusion, we have chosen to carry out our investigations with a unique time step chosen in order to respect the CFL condition on both domains which translates into:

$$\Delta t_n = \min(\Delta t_n^{\mathcal{W}}, \Delta t_n^{\mathcal{V}}), \quad (2.18)$$

where $\Delta t_n^{\mathcal{W}}$ and $\Delta t_n^{\mathcal{V}}$ are respectively the time steps computed at the time t^n for the substrate and for the patch. This restrictive condition on the time step allows us to experiment various grid configurations with different cell ratios and different test cases without worrying about time stability. For industrial applications, a decoupled time step would need to be implemented in order to optimize the computational time with a smaller time step on the finest domain only.

2.3 - Implementation of the Chimera method in MANTA software

2.3.1 - Presentation of MANTA software

The presented Chimera method is implemented inside a C++ in-house code currently in development at the Service d'Études Mécaniques et Techniques at the CEA called MANTA (Mechanical Analysis Numerical Toolbox and Applications). This code aims to tackle several issues raised by legacy codes written with older languages like factorization, memory management and performance requirements. The code structure is illustrated in Figure 2.18 with a layer based organization. The code is organized around a generic core that handles the I/O (Input/Output) procedures, mesh handling, data format and the linear system assembly and resolution. Some of these elements have been developed internally while others use external libraries with dedicated interfaces. This ensures a high modularity of the code thanks to encapsulation. The numerical methods like finite elements or finite volumes are developed above the core layer and interact with it through formulations.

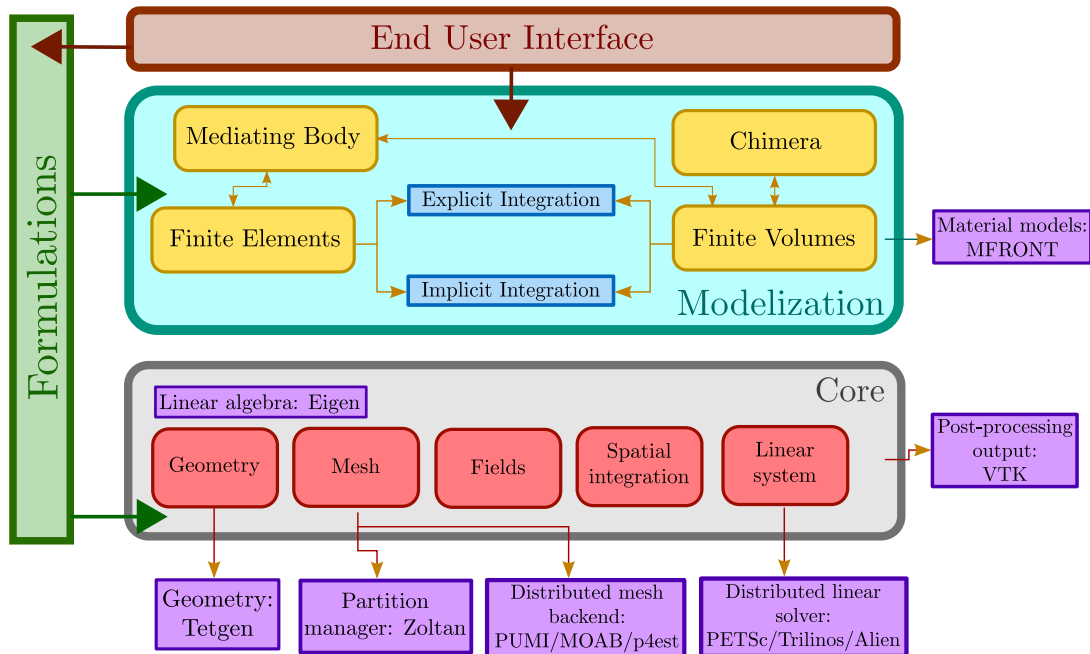


Figure 2.18: Structure of the code MANTA.

Finally, the end user interface is currently a main C++ file to compile containing the initialization, the time loop and the output of the computation. It is worth mentioning that MANTA is still in early development with important features in development at the time of writing. In this work, we focus on the modelization layer containing the numerical methods.

2.3.2 - Implementation of the Chimera procedure within the solver

The main programming contribution to MANTA from this work are two folds: the first one is the implementation of the Chimera framework (see Fig. 2.18) that allows any cell based field to transfert information using identified ghost cells. This framework includes the ghost cell detection and marking, the sending procedure with the presented interpolation methods, the modified limiter and tools to compute any fields or quantities like the system mass, momentum or total energy over an overlapped domain. The second fold is the coupling of the Chimera method with an immersed boundary method called the Mediating Body Method [92] that will be detailed later on.

In this section we present the computational steps added to a standard calculation using the Chimera method. Starting with the first order interpolation, Figure 2.19 shows that only two steps (coloured in red) are added compared to single grid computation. The first step is the geometrical detection and marking procedures of the ghost cell sets $\widetilde{\mathcal{W}}, \widetilde{\mathcal{V}}$ and their respective sending cell sets $\mathcal{V}^s, \mathcal{W}^s$ detailed in section 2.2.2. This step is performed before the initialization of the domains and does not need to be executed again if the grids are fixed which is the case in our work. It mainly consists in computing the grid intersections $\mathcal{W}^s = \widetilde{\mathcal{V}} \cap \mathcal{W}$ given $\Gamma_{\mathcal{V}}$ and k_{GC} using tetrahedral decomposition of polyhedron volumes. The resulting barycenters and volumes of the intersections are stored along with the cell indexes of the intersected sending cells inside a container called *exchangeData*. The storage of these data allows us to build our first order interpolation without computing the intersections at each sending.

The second step is the Chimera sending. For a first order sending, this step only consists in building the interpolated values using *exchangeData* and setting the corresponding ghost cells values. The order of the sendings does not matter and this step is repeated at every time iteration.

Let us emphasize that the integration of the solution is performed everywhere except on the ghost cells that are only used for computing the numerical fluxes at sending cell interfaces. The solution on ghost cells is only updated through the Chimera procedure at every time step. Let us also underline that the procedure is built as symmetrical, meaning that the way to transfer information from the patch to the substrate is identical as to transfer information from substrate to the patch.

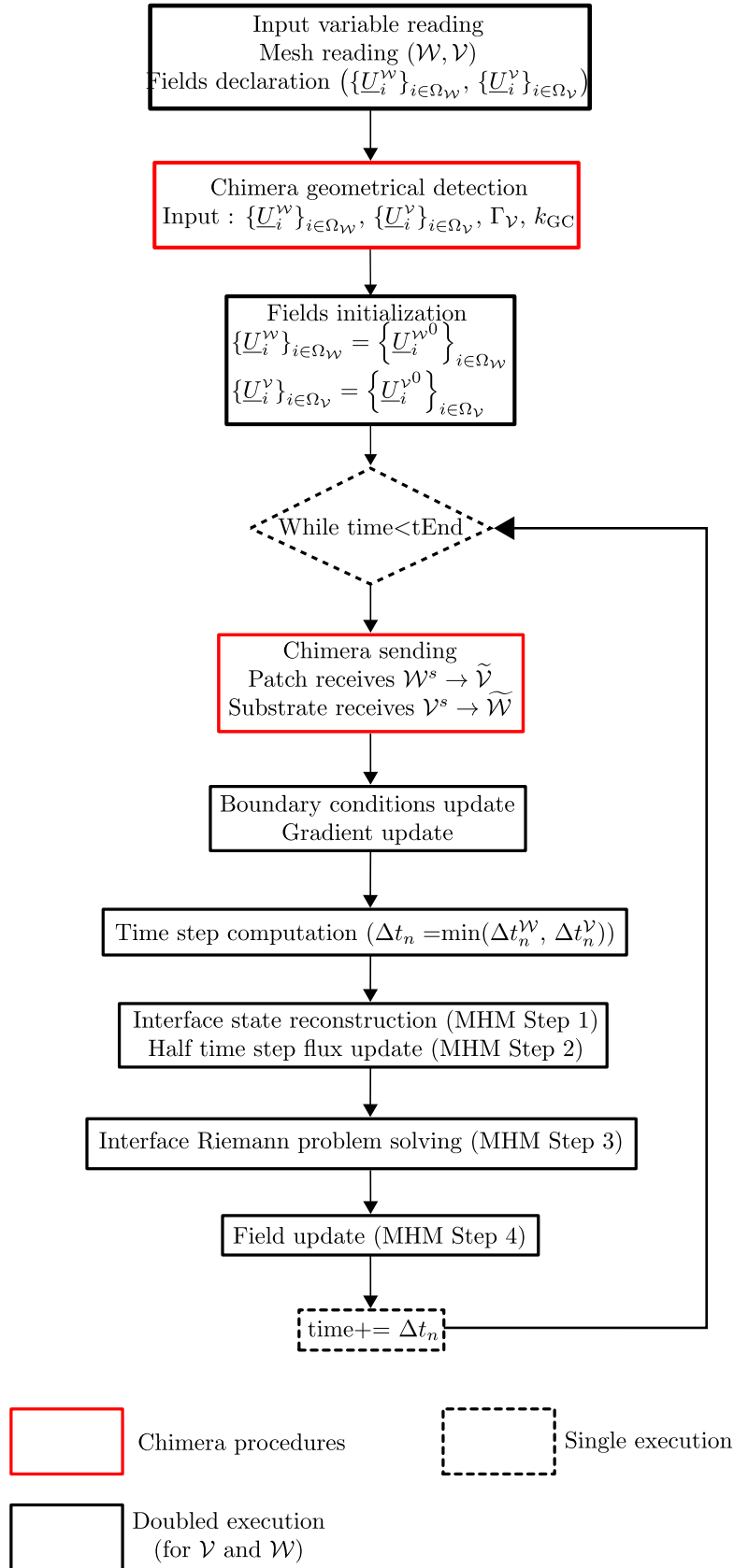


Figure 2.19: Implementation of the Chimera procedures within the fluid solver for a first order sending.

Figure 2.20 illustrates the computational steps of the second order Chimera exchange. For a second order interpolation, the first step is very similar to the first order interpolation. The ghost

cell sets $\widetilde{\mathcal{W}}, \widetilde{\mathcal{V}}$ and their respective sending cell sets $\mathcal{V}^s, \mathcal{W}^s$ detection procedure is identical given $\Gamma_{\mathcal{V}}$ and k_{GC} . The main difference is the addition of the reconstruction supports $\mathcal{W}^r = \widetilde{\mathcal{W}} \cup \gamma(\widetilde{\mathcal{W}})$ and $\mathcal{V}^r = \widetilde{\mathcal{V}} \cup \gamma(\widetilde{\mathcal{V}})$ detailed in section 2.2.3.C. As for the first order Chimera exchange, if the grids are fixed, these steps need to be executed only once.

Within the time loop, the single Chimera step for the first order exchange is kept as explained in section 2.2.3.C. Two additional steps are added with the gradient interpolation step in each cell belonging to the reconstruction sets and finally, the reconstruction and sending of the values inside the ghost cells.

Regarding the Chimera framework implementation, it consists in a Chimera class with two different constructors (one for the patched grid and the other for the overlapped grid). For every instance of the Chimera class, the corresponding ghost cell set, the reconstruction set, sending cell set and the *exchangeData* container are computed. The first constructor requires a patch (\mathcal{V}), a substrate (\mathcal{W}), a patch boundary ($\Gamma_{\mathcal{V}}$) and a number of ghost cell layers (k_{GC}) as inputs. The second constructor only requires a patch Chimera instance as an input as it corresponds to a substrate Chimera instance.

As a result, the implemented Chimera method is symmetrical and modular as it can send information only one-way or both-ways and requires very few constraints on the input meshes apart from overlapping each other. For each sending direction, one Chimera instance needs to be declared and therefore, the implementation is fully compatible with configuration involving several grids. Also implementation keeps a certain level of independence between the grids as the methods for the numerical scheme remain the same as for a single grid configuration. Therefore, the standard numerical scheme steps shown in Figure 2.19 and Figure 2.20 like the boundary conditions update or the time step computations need to be executed for each grid. This is possible thanks to the update of the values inside the ghost cells at the beginning of every iteration.

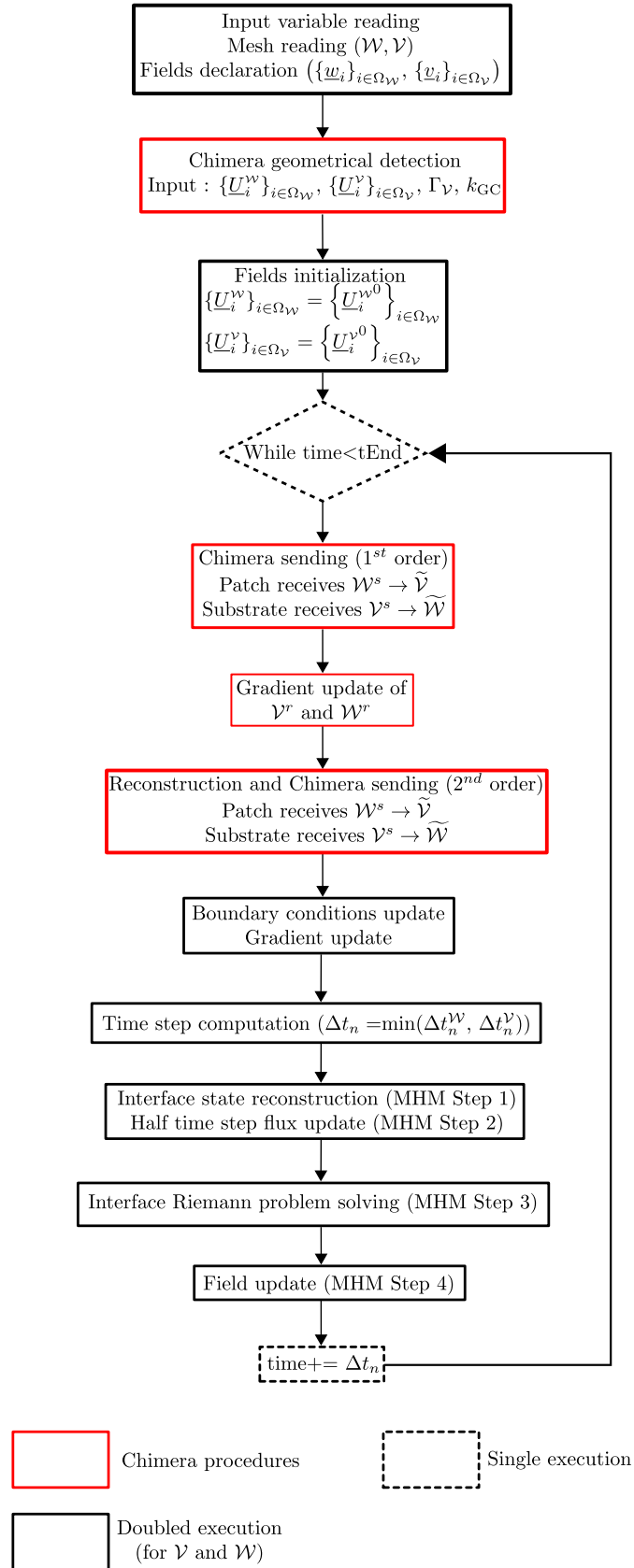


Figure 2.20: Implementation of the Chimera procedures within the fluid solver for a second order sending.

2.4 - Validation of the finite volume Chimera method on one-dimensional test cases

In the previous sections, we have presented our implementation of the finite volume Chimera method. In the following, we check the impact of the Chimera sending on one-dimensional analytical test cases. The first and second order Chimera sendings are reviewed for both the standard detection procedure and the extended detection procedure presented in section 2.2.2. For each case, the assessed Chimera configurations will be specified. However, the finite volume method set-up is kept constant across all the cases tested which corresponds to a MUSCL-Hancock scheme with an HLLC Riemann solver and the K-Dubois limiter with $k = 0.75$ (see section 1.2 for details on the numerical scheme configuration). The scheme is second order accurate in both time and space. The CFL number is set to 0.9 for the one-dimensional test cases.

2.4.1 - Solution reconstruction over overlapping grid domains

When using overlapping grid methods, it is difficult to compare the overlapped fields to a single grid solution as the solution is duplicated on the overlapped regions. In this section, we propose a grid merging approach to post-process the solution obtained using an overlapping grid method. Given a substrate (\mathcal{W}), an immersed patch (\mathcal{V}) and their respective sets of ghost cells ($\widetilde{\mathcal{W}}$ and $\widetilde{\mathcal{V}}$) as shown in Figure 2.21, we use the resolved cell sets (\mathcal{W}_c and \mathcal{V}_c) defined in equation 2.1 to reconstruct a unique solution over the computational domain.

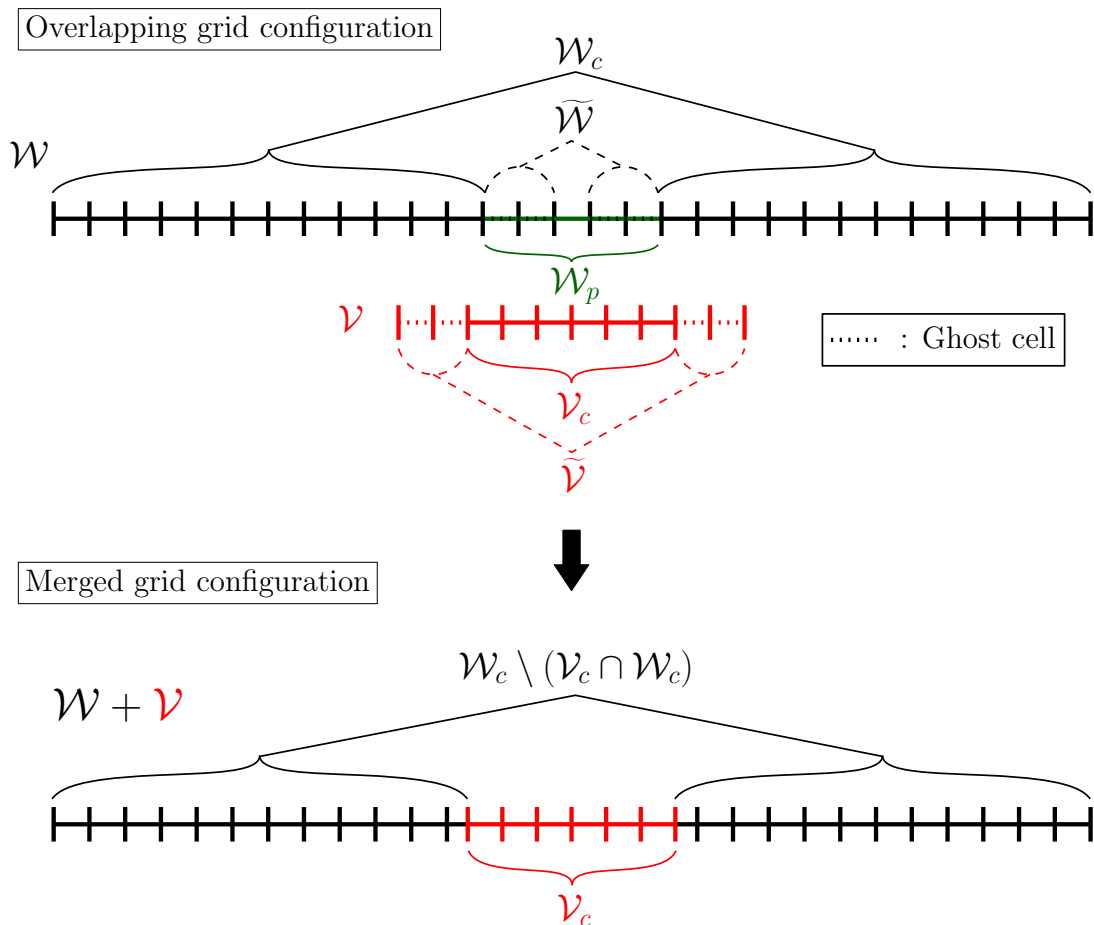


Figure 2.21: Field merging of overlapping grid configurations for comparisons with single grid cases.

We consider the conservative variable field \underline{U} over the physical domain \mathcal{U} . This field is discretized as $\{\underline{U}_i^{\mathcal{W}}\}_{i \in \Omega_{\mathcal{W}}}$ and $\{\underline{U}_i^{\mathcal{V}}\}_{i \in \Omega_{\mathcal{V}}}$ respectively on the substrate (\mathcal{W}) and the patch (\mathcal{V}). As a result the field \underline{U} is duplicated in the overlapped regions. In order to post process overlapping grid configurations, we define the composite conservative variable field:

$$\underline{U} = \left[1 - \alpha(\underline{x}) \right] \underline{U}^{\mathcal{W}} + \alpha(\underline{x}) \underline{U}^{\mathcal{V}}, \quad (2.19)$$

where α is a weighting function of space. As the patch is used to improve the accuracy of a global computation, we choose the following formulation for α :

$$\alpha(\underline{x}) = \begin{cases} 1 & \text{if } \underline{x} \in \mathcal{V}_c, \\ 0 & \text{otherwise.} \end{cases} \quad (2.20)$$

This formulation favors the patch solution and is equivalent to merging grids by cutting the overlapped cells of the substrate as shown in Figure 2.21. The resulting merged grid is used for error computations only and is referred as $\mathcal{W} + \mathcal{V}$ in the following. In equation 2.19, the composite field is based on conservative variables \underline{U} . This definition can also be derived for error fields computed with analytical solutions as done in equation 2.23 in the followings.

2.4.2 - Sinus advection

In order to assess the order of accuracy of the numerical scheme, and the impact of the interpolation used in the Chimera exchange on the global order of convergence, the linear advection of a smooth analytical solution is considered similarly as in [113, 35, 89]. This test case is also useful to assess the impact of the exchange zone shift (δ_S) combined with the different ghost cell detection procedures. We superimpose a regular fluctuation on a one-dimensional density field that is convected with a constant velocity:

$$\begin{aligned} \rho &= \rho_0(1 + \delta_\rho) \\ u &= u_0 = 100 \text{ m.s}^{-1} \\ p &= p_0 = 10^5 \text{ Pa} \end{aligned} \quad (2.21)$$

with the normalized density fluctuation given by,

$$\delta_\rho = \begin{cases} A \sin^2\left(\frac{\pi(x-x_s)}{l}\right) & \text{if } 0 \leq x - x_s \leq l \\ 0 & \text{elsewhere,} \end{cases} \quad (2.22)$$

where $A = 0.1$ is the amplitude of the perturbation, $\rho_0 = 1 \text{ kg.m}^{-3}$ is the initial constant density field, $l = L/5$ is the length on which the density is perturbed, T is the period of the perturbation and $L = u_0 T = 10 \text{ m}$ is the length of the computational domain $[0, L]$. $x_s = 0.5 \text{ m}$ is the perturbation shift set to ensure that the initial center of the perturbed density region is located at $x_c(0) = 0.15 L$, as seen in Figure 2.22. The simulation stops at $t_f = 0.6 T$ which is the time for which the center of the density fluctuation is located at $x_c(t_f) = 0.75 L$.

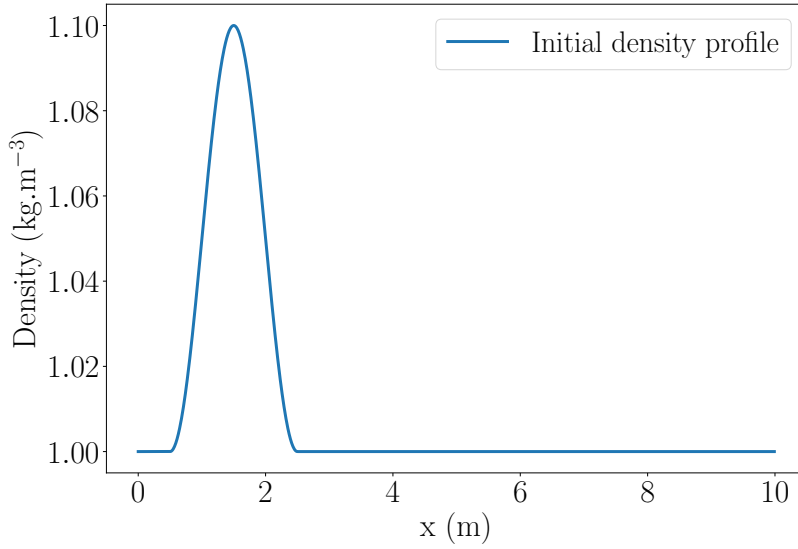


Figure 2.22: Scalar advection test case: initial solution of a square sinus distribution (see equation 2.22).

A . Split domain

The first configuration tested is called split domain and consists in a single grid split into a substrate and a patch whose left interface is located at $x_i = 1/2 L$ as shown in Figure 2.23. The cleaned patch domain boundary ($\Gamma_{\mathcal{V}}$) is kept fixed across the various Chimera configurations and one or two ghost cells are added on top of the boundary $\Gamma_{\mathcal{V}}$ depending on the order of the Chimera sending. Given δ_S , the substrate is positioned in accordance with the geometrical criteria given in equation 2.6.

The sinus advection test case with the split domain configuration allows us to accurately review the impact of the Chimera exchange as the patch (\mathcal{V}) receives information coming from the substrate at only one region of the patch grid. This is compared to a fully immersed patch which receives information from both regions corresponding to the extremities of the patch (\mathcal{V}). As the information is only going in one direction, we can quantify the impact of the exchange zone shift (δ_S), measure the impact of a coarse-to-fine grid transfer and vice versa, but first, we focus on the impact of the Chimera sending on the global order of convergence.

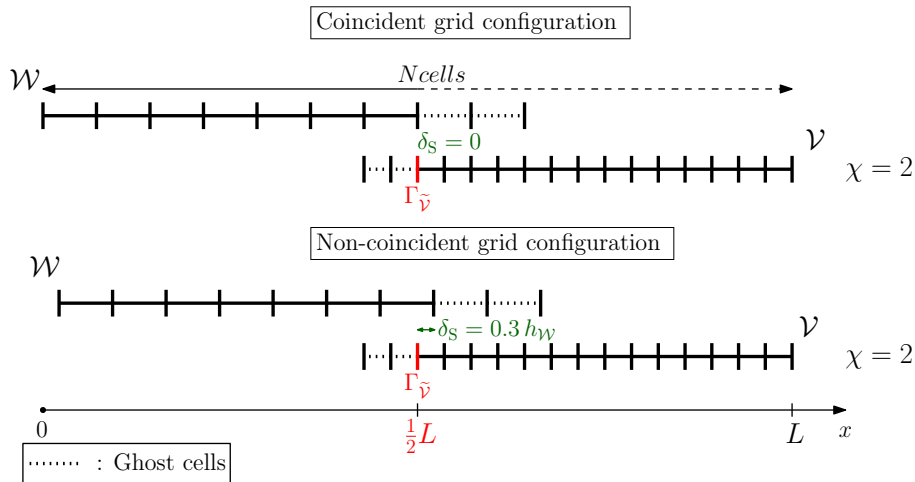


Figure 2.23: Sinus advection test case: grid arrangements for the split Chimera configuration.

A.1 - Impact of the Chimera sending on the order of convergence

For the grid convergence study with the split domain case, we have tested two different configurations: one with coincident grids ($\delta_S = 0$) and the other one with non-coincident grids ($\delta_S = 0.3 h_{\mathcal{W}}$). We review the first and the second order Chimera sending with the standard detection procedure. Computations have been performed on both a single grid domain (without any patch) and on the split domain with a patch. For both cases, we used 6 different grids from the coarsest $N_{cells} = 100$ cells regularly distributed over L to the finest using $N_{cells} = 3200$ cells, *i.e.* the grid spacing evolves with power of 2 between two meshes. We note N_{cells} the number of grid cells over L . As we would like to highlight the spatial accuracy, whatever the grid is, a constant time step $\Delta t = 10^{-5}$ s giving a very low CFL number (0.03 – 0.3) has been used for lowering the time integration error.

We set the cell ratio between the patch and the substrate to $\chi = 1$. This allows us to study the grid convergence as well as the impact of the Chimera interpolation on the global accuracy. At the final time t_f , we compare numerical solutions obtained on both the single grid configuration and the Chimera configuration, to the analytical solution which is the simple convection of the initial density profile without any diffusion. To measure numerical errors, we calculate the L_1 norm of the density error, computed as follows:

$$\begin{aligned} L_1(\varepsilon_\rho) &= \frac{1}{L} \int_0^L |\varepsilon_\rho| dx = \frac{1}{L} \left[\int_0^L |\alpha(x)\varepsilon_\rho^{\mathcal{V}} + [1 - \alpha(x)]\varepsilon_\rho^{\mathcal{W}}| dx \right] \\ &\approx \frac{1}{|\mathcal{W} + \mathcal{V}|} \sum_{i=0}^{\Omega_{\mathcal{W}+\mathcal{V}}} |\rho_i - \rho_{th}(x_i)| \Delta x_i, \end{aligned} \quad (2.23)$$

with ρ_{th} the analytical density profile, α the weighting function introduced in equation 2.20 and $\varepsilon_\rho^{\mathcal{V}} = \rho_{num}^{\mathcal{V}} - \rho_{th}$ with $\rho_{num}^{\mathcal{V}}$ the numerical density solution on \mathcal{V} . The equivalent definition applies to $\varepsilon_\rho^{\mathcal{W}}$. The total volume of the domain is written: $|\mathcal{U}|$ for the single grid cases and $|\mathcal{W} + \mathcal{V}|$ for the Chimera configurations.

The coincident grid results ($\delta_S = 0$) reported on Table 2.1 are identical between the single mesh configuration and both Chimera methods. This is expected by design of the developed method as coincident grid cases combined with our version of the Chimera method are equivalent to a single grid configuration. For the coincident grid configurations (single grid and Chimera), the second order of accuracy is clearly recovered for finest grids (at least from 400 grid points over L) by using the MUSCL-Hancock scheme.

Therefore, even though the first order Chimera method is a lower order method than the numerical scheme, it does not alter the overall order of convergence.

Table 2.1: Grid convergence analysis of the split configuration: results on density (ρ) errors obtained with a single grid configuration as well as with the present Chimera approach using a patch with same grid spacing as the substrate ($\chi = 1$) and coincident grids ($\delta_S = 0$).

Ncells	$L_1(\varepsilon_\rho) (\times 10^4)$			Order of convergence p		
	Single	Chimera		Single	Chimera	
		First order	Second order		First order	Second order
100	9.093	9.093	9.093	1.34	1.34	1.34
200	3.584	3.584	3.584	1.72	1.72	1.72
400	1.091	1.091	1.091	1.95	1.95	1.95
800	2.825e-1	2.825e-1	2.825e-1	2.12	2.12	2.12
1600	6.462e-2	6.462e-2	6.462e-2	2.37	2.37	2.37
3200	1.242e-2	1.242e-2	1.242e-2	-	-	-

The evolution of the L_1 norm of density errors versus the grid spacing is plotted in Figure 2.24 for the non-coincident grid configuration ($\delta_S = 0.3 h_{\mathcal{W}}$). Using the present Chimera method on a split

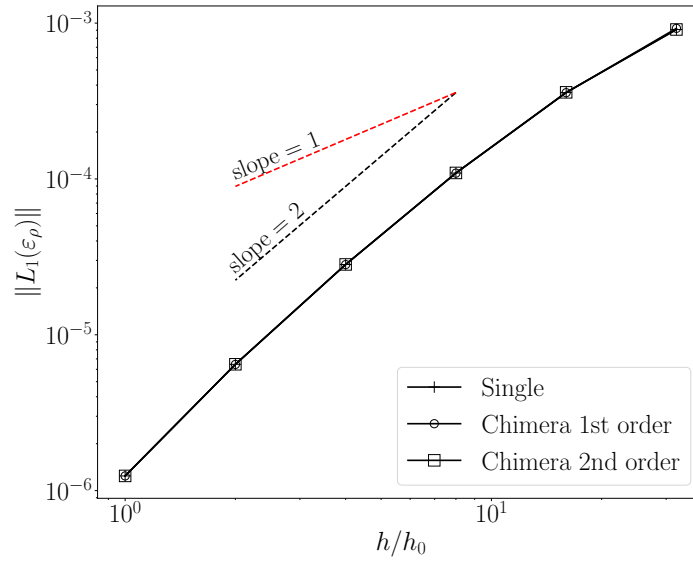


Figure 2.24: Grid convergence analysis of the sinus advection case for the split domain with equivalent cell sizes between the patch and the substrate ($\chi = 1$) and non-coincident grids ($\delta_S = 0.3 h_W$). $h = h_W = h_V$ and h_0 corresponds to $N_{cells} = 3200$.

domain configuration with equivalent cell sizes ($\chi = 1$) does not seem to notably deteriorate the order of accuracy of the original method. The global order of accuracy is almost recovered although small discrepancies compared to single grid results can hardly be noticed in the coarsest grid configurations (see Fig. 2.24). To judge the very low intensity of these differences, we report in Table 2.2 the L_1 density errors as well as the measured order of accuracy. Even when using the first order Chimera method, the order of convergence is not notably altered.

Table 2.2: Grid convergence analysis of the split configuration: results on density (ρ) errors obtained with a single grid configuration as well as with the present Chimera approach using a patch with same grid spacing as the substrate ($\chi = 1$) and non-coincident grids ($\delta_S = 0.3 h_W$).

Ncells	$L_1(\varepsilon_\rho) (\times 10^4)$			Order of convergence p		
	Single	Chimera		Single	Chimera	
		First order	Second order		First order	Second order
100	9.093	9.257	9.100	1.34	1.37	1.34
200	3.584	3.577	3.595	1.72	1.71	1.72
400	1.091	1.090	1.093	1.95	1.95	1.95
800	2.825e-1	2.820e-1	2.827e-1	2.12	2.12	2.13
1600	6.462e-2	6.452e-2	6.466e-2	2.37	2.37	2.38
3200	1.242e-2	1.242e-2	1.242e-2	-	-	-

A.2 - Impact of the exchange zone shift (δ_S) on the solution

Keeping the same split configuration, notations and time step parameter as above, we assess the impact of the geometrical configuration and more specifically the exchange zone shift (δ_S) by setting $N_{cells} = 200$ and $\chi = 1$. As the patch domain boundary remains fixed at $1/2 L$, increasing the value of δ_S from 0 (coincident grid configuration) to $0.9 h_W$ (non-coincident grid configuration) is equivalent to shifting the substrate in the positive direction of the x -axis by a value δ_S (see Fig. 2.23).

The L_1 density errors are plotted in Figure 2.25. When $\delta_S = 0$, the ghost cells have only one sending cell. When $0 < \delta_S \neq h_W$, each ghost cell receives information from two sending cells as

shown in Figure 2.23. The first order Chimera exchange and the second order Chimera exchange exhibit different behaviors. The first order sending cell is a convex function of the exchange zone shift with a minimum reached for $\delta_S = 0.4$. From this point, the error increases as one moves further away. As seen in Table 2.2, the peculiar behavior of the first order Chimera is confirmed in Figure 2.25 with lower errors compared to both the second order sending and the equivalent single grid configuration with $N_{cells} = 200$ and $\chi = 1$.

In Figure 2.26, we can see that both Chimera and single grid cases present a symmetry breaking of the density profile compared to the analytical solution. Therefore, the first order Chimera exchange compensates the symmetry breaking which slightly improves the overall accuracy of the solution. For the second order Chimera method, the maximum error is obtained with the largest exchange zone shift and the smallest error is obtained with matching grids. It is worth noting that the second order exchange error amplitude is lower compared to the first order Chimera method making it less dependent on the grid configuration. As a result, the second order Chimera method seems preferable as it is more predicable regarding the grid configurations when $\chi = 1$.

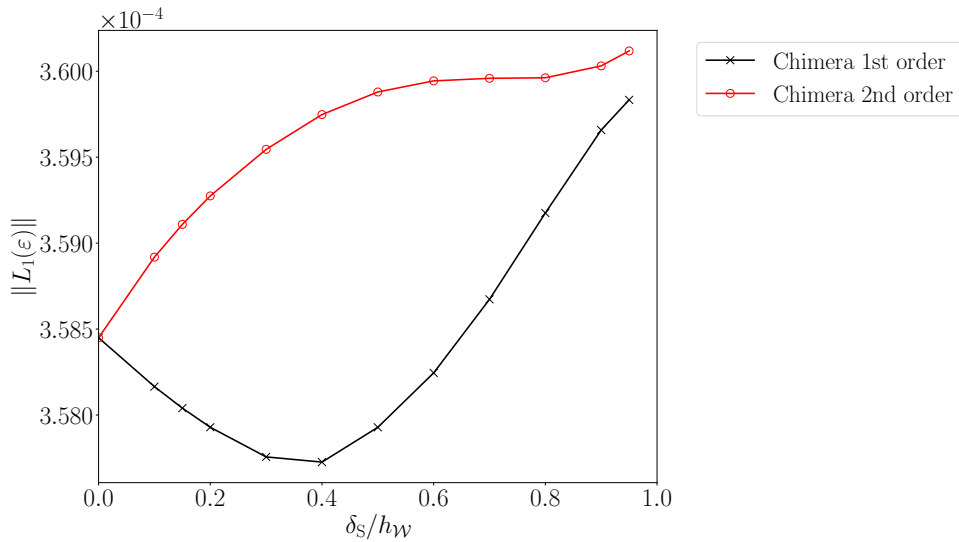


Figure 2.25: Exchange zone shift analysis: results on density (ρ) errors obtained with with the present Chimera approach using a patch with same grid spacing as the substrate ($N_{cells} = 200$, $\chi = 1.0$) with variable exchange zone shift (δ_S) and the standard detection procedure.

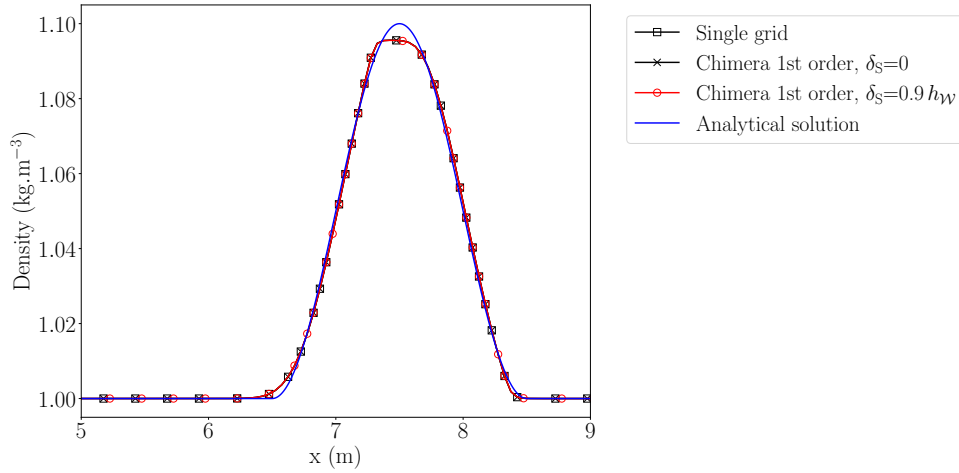


Figure 2.26: Density profile at $t = t_f$ for the single grid case and the first order Chimera sending with matching grids ($\delta_S = 0$) and non-matching grids ($\delta_S = 0.9 h_{WW}$) with $N_{cells} = 200$ and $\chi = 1$, compared to the analytical solution. The markers on the plots are not representative of the number of points of the numerical solution.

A.3 - Impact of the cell ratio (χ) on the solution

In more geometrically complex cases, the condition $\chi = 1$ is restrictive for composite large scale domains and may become a constraint for our approach. Therefore, this part focuses on the impact of the cell ratio (χ) between the patch and the substrate for both coincident ($\delta_S = 0$) and non-coincident ($\delta_S \neq 0$) grid interfaces. We keep the same parameters and notations previously introduced. For each configuration (coincident and non-coincident), the study is based on two folds: the first one assesses the transfer from a base grid with $N_{cells} = 200$ (substrate) to a finer one (patch) as $\chi \geq 1$. The second one reviews the transfer from a base grid with $N_{cells} = 3200$ (substrate) to a coarser one (patch) as $\chi \leq 1$.

Let us recall that solution errors are calculated at $t_f = 0.6T$ once the density profile passed through the exchange zone region and is completely arrived inside the patch. That way, errors obtained must mainly be compared to the ones of single grid configurations corresponding to the coarsest equivalent N_{cells} between the patch and the substrate, *i.e.*, for the coarse-to-fine transfers, errors must be compared to the single grid case with $N_{cells} = 200$ whereas for the fine-to-coarse transfers, errors must be compared to the single grid cases where N_{cells} is equal to equivalent N_{cells} on the patch. We call these single grid configurations equivalent coarse single mesh (ECSM).

Similarly, we define the equivalent fine single mesh (EFSM) of a Chimera configuration, the single grid configuration with the same grid resolution as the finest mesh of the Chimera grid configuration.

A.3.1 - Coincident grid interfaces ($\delta_S = 0$)

Starting with the coincident interface case and $\chi > 1$ (coarse-to-fine transfer), the L_1 norm of the density errors are reported in Table 2.3. We can see that the first order Chimera sending is not relevant as it generates a higher error than the single grid configuration while using a finer patch for every cell ratio tested. The second order Chimera sending on the other hand is promising as it allows an increase in the overall accuracy while it is obvious that the solution errors are mostly dominated by the ones generated on the coarser substrate as the Chimera error is closer to ECSM error than the EFSM error. As an example, while being lower, the Chimera errors with $N_{cells} = 200$ and $\chi = 4$ have the same order of magnitude as the single grid with $N_{cells} = 200$ but cannot be compared to the error of the single with $N_{cells} = 800$. As a conclusion, unlike the first order Chimera exchange, the second order Chimera exchange between two facing grids does not deteriorate the global solution

error when the patch is finer than the substrate.

When $\chi < 1$ (fine-to-coarse transfer), the fine substrate compensates the induced error of the first order Chimera method as the errors of the first order Chimera case are lower than the coarse equivalent single grid cases (see Table 2.4). However, the first order errors are higher than the second order Chimera method which remains preferable when χ varies. The difference between the two Chimera methods drops when χ decreases. This is caused by the increasing spatial errors involved by the coarser patches. As a conclusion, the fine-to-coarse transfer is not heavily impacted by the Chimera methods as the Chimera errors are blended with the spatial error of the coarsest grids.

Table 2.3: Cell ratio analysis of the split configuration: results on density (ρ) errors obtained with with the present Chimera approach using a patch with a coincident Chimera interface ($\delta_S = 0$) and variable cell ratios (χ) with the standard detection procedure. The transfer occurs from a coarse substrate ($N_{cells} = 200$) to a finer patch. We have also reported the errors of the equivalent coarse single mesh (ECSM) and the equivalent N_{cells} on the patch for equivalent fine single mesh (EFSM) comparisons.

χ	$L_1(\varepsilon_\rho) (\times 10^4)$			Equivalent N_{cells} on the patch (for EFSM comparison)
	First order	Second order	Equivalent coarse single mesh (ECSM)	
1	3.584	3.584	3.584	200
2	5.371	2.741	//	400
4	5.066	2.526	//	800
8	4.959	2.481	//	1600
16	4.948	2.477	//	3200

Table 2.4: Cell ratio analysis of the split configuration: results on density (ρ) errors obtained with with the present Chimera approach using a patch with a coincident Chimera interface ($\delta_S = 0$) and variable cell ratios (χ) with the standard detection procedure. The transfer occurs from a fine substrate ($N_{cells} = 3200$) to a coarser patch. We have also reported the errors of the equivalent coarse single mesh (ECSM) and the equivalent N_{cells} on the patch for equivalent coarse single mesh (ECSM) comparison.

χ	$L_1(\varepsilon_\rho) (\times 10^4)$			Equivalent N_{cells} on the patch (for ECSM comparisons)
	First order	Second order	Equivalent coarse single mesh (ECSM)	
1	1.242e-2	1.242e-2	1.242e-2	3200
0.5	6.216e-2	3.431e-2	6.462e-2	1600
0.25	1.487e-1	1.306e-1	2.825e-1	800
0.125	5.159e-1	5.080e-1	1.091	400
0.0625	1.824	1.821	3.584	200

A.3.2 - Non-coincident grid interfaces ($\delta_S = 0.6 h_{\mathcal{W}}$)

We now focus on the impact of χ on the overall solution but with non-coincident grid interfaces ($\delta_S = 0.6 h_{\mathcal{W}}$). Apart from the exchange zone shift, the grid configuration remains the same as before with $N_{cells} = 200$ for coarse-to-fine transfers and $N_{cells} = 3200$ for fine-to-coarse transfers. We review the impact of the ghost cell detection procedure (standard and extended) in addition to the order of the Chimera method, for various cell ratios (χ).

Table 2.5, contains the L_1 norm of the density error for $\chi > 1$ (coarse-to-fine transfer). Using the extended detection procedure reduces δ_S when possible and ensures $\delta_S \leq 0.6 h_{\mathcal{W}}$. Therefore, for the first order Chimera method, the standard detection provides lower errors compared to the extended detection procedure as we have seen with Figure 2.25, especially when increasing χ as it makes δ_S tend to 0. For the second order Chimera method, the extended detection procedure improves slightly the accuracy of the method compared to the standard detection but deteriorates it a little when using high cell ratios $\chi > 10$.

When $\chi < 1$ (fine-to-coarse transfer), the Chimera methods behave similarly to the coincident grid case with an increasing error due to the coarsening of the patch. The extended detection has

no effect on the solution as the ghost cell configurations are identical to the standard detection. Also, the Chimera errors are blent in with the spatial error induced by the coarse patch reducing significantly the gap between the first and the second order Chimera sendings. Therefore, we can conclude that the order of the Chimera method and the detection procedure do not matter when transferring information from a baseline grid to a coarser one.

Table 2.5: Cell ratio analysis of the split configuration: results on density (ρ) errors obtained with with the present Chimera approach using a patch with non-coincident Chimera interface ($\delta_S = 0.6 h_{\mathcal{W}}$) and variable cell ratios (χ) for both the standard and extended detection procedures. The transfer occurs from a coarse substrate ($N_{cells} = 200$) to a finer patch. Equivalent N_{cells} on the patch are reported for equivalent fine single mesh (EFSM) comparison.

χ	$L_1(\varepsilon_\rho)(\times 10^4)$				Equivalent N_{cells} on the patch (for EFSM comparison)
	First order		Second order		
	Standard detection	Extended detection	Standard detection	Extended detection	
1	3.582	3.582	3.599	3.599	200
2	2.438	3.944	2.785	2.756	400
4	2.519	4.614	2.537	2.531	800
8	2.115	4.538	2.475	2.481	1600
16	2.107	4.855	2.466	2.489	3200

Table 2.6: Cell ratio analysis of the split configuration: results on density (ρ) errors obtained with with the present Chimera approach using a patch with non-coincident Chimera interface ($\delta_S = 0.6 h_{\mathcal{W}}$) and variable cell ratios (χ) for both the standard and extended detection procedures. The transfer occurs from a fine substrate ($N_{cells} = 3200$) to a coarser patch. Equivalent N_{cells} on the patch are reported for equivalent coarse single mesh (ECSM) comparison.

χ	$L_1(\varepsilon_\rho)(\times 10^4)$				Equivalent N_{cells} on the patch (for ECSM comparison)
	First order		Second order		
	Standard detection	Extended detection	Standard detection	Extended detection	
1	1.243e-2	1.243e-2	1.243e-2	1.243e-2	3200
0.5	3.266e-2	3.266e-2	3.219e-2	3.219e-2	1600
0.25	1.356e-1	1.356e-1	1.402e-1	1.402e-1	800
0.125	5.103e-1	5.103e-1	5.129-1	5.129-1	400
0.0625	1.822	1.822	1.823	1.823	200

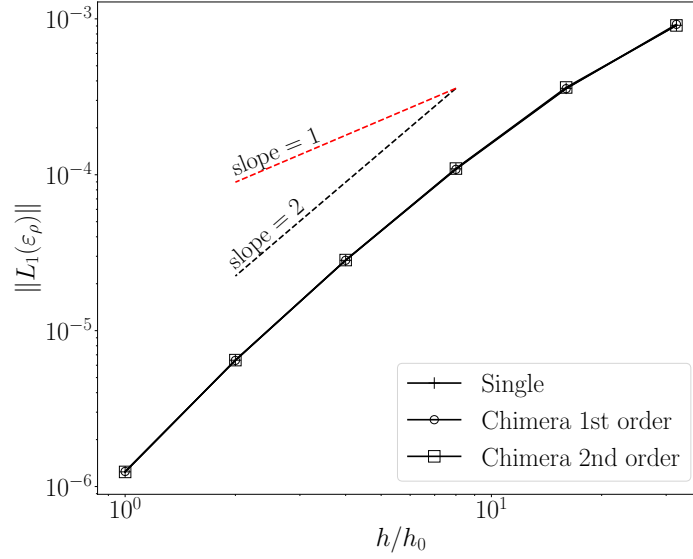


Figure 2.28: Grid convergence analysis of the sinus advection case for the patched configuration with equivalent cell sizes between the patch and the substrate ($\chi = 1$). $h = h_{\mathcal{V}} = h_{\mathcal{Y}}$ and h_0 corresponds to $N_{cells} = 3200$.

Table 2.7: Grid convergence analysis of the patched configuration: results on density (ρ) errors obtained with a single grid configuration as well as with the present Chimera approach using a patch with same grid spacing as the substrate ($\chi = 1$).

Ncells	$L_1(\varepsilon_\rho) (\times 10^4)$			Order of convergence p		
	Single	Chimera		Single	Chimera	
		First order	Second order		First order	Second order
100	9.093	9.223	9.074	1.34	1.37	1.32
200	3.584	3.567	3.630	1.72	1.72	1.73
400	1.091	1.083	1.096	1.95	1.94	1.95
800	2.825e-1	2.828e-1	2.837e-1	2.12	2.13	2.13
1600	6.462e-2	6.445e-2	6.472e-2	2.37	2.37	2.38
3200	1.242e-2	1.250e-2	1.241e-2	-	-	-

B.2 - Impact of the cell ratio (χ) on the solution

Secondly, we prescribe the cell number on the substrate to $N_{cells} = 200$ and we refine the grid on the patch in order to assess the impact of the transfer between a coarse substrate and a finer patch which seems to be the most sought-after configuration. Cell ratios between the patch and the substrate spread from $\chi = 1$ to $\chi = 16$ where the grid spacing on the patch is 16 times smaller than on the substrate. Results on the normalized L_1 norm of density errors are reported in Table 2.8.

The last column reports the equivalent number of cells (N_{cells}) that would be needed on the substrate to recover the same grid refinement as used in the patched region. Let us recall that solution errors are calculated at $t_f = 0.6T$ once the density profile passed through the patch and completely left the patch. That way, errors obtained must mainly be compared to the ones of single grid configuration with $N_{cells} = 200$ cells.

For the first order sending, refining the patch slightly improves the accuracy of the overall solution up to $\chi = 4$ using the standard detection procedure and $\chi = 2$ for the extended detection procedure. This is coherent with the results obtained with the split configuration and comes from the coarse-to-fine sending. We can see here that this effect persists with a patched configuration.

Table 2.8: Cell ratio analysis of the patched configuration: results on density (ρ) errors obtained with the present Chimera approach using a patch and variable cell ratios (χ) for both the standard and extended detection procedures. The substrate comprises $N_{cells} = 200$ grid cells. Equivalent N_{cells} on the patch are reported for equivalent fine single mesh (EFSM) comparison.

χ	$L_1(\varepsilon_\rho) (\times 10^4)$				Equivalent N_{cells} on the patch (for EFSM comparison)
	First order		Second order		
	Standard detection	Extended detection	Standard detection	Extended detection	
1	3.567	3.567	3.630	3.630	200
2	2.905	2.905	2.370	2.370	400
4	2.714	5.155	2.112	2.142	800
8	5.094	5.095	2.023	2.023	1600
16	4.405	5.358	1.994	2.023	3200

As a result, the first order sending is not recommended for cell ratios higher than 2. On the contrary, the second order sending always improves the accuracy of the solution compared to the single grid with $N_{cells} = 200$. The standard detection is preferable in this one-dimensional case as it allows slightly lower errors compared to the extended detection. Using the second order exchange, this emphasizes that errors due to Chimera exchange between the two facing grids do not impact the global solution error when the patch is finer than the substrate.

C . Summary of the findings on the advection case

With the sinus advection test case, various configurations have been tested in order to assess key aspects of the different versions of the developed Chimera method:

- A split domain configuration has been tested as it represents the simplest configuration to assess the Chimera method with one localized exchange zone at the end of the substrate which corresponds to the beginning of the patch. Each configuration depends on the number of cells (N_{cells}), the exchange zone shift (δ_S) and the cell ratio (χ).
 1. First, with coincident grids and equivalent cell size between the patch and the substrate ($\chi = 1$ and $\delta_S = 0$) we have verified that both the first order and the second order Chimera methods give identical results to the single grid configuration.
 2. With non-coincident grids and equivalent cell size between the patch and the substrate ($\chi = 1$ and $\delta_S = 0.3 h_W$), we showed that the impact of both the first and second order Chimera methods on the global order of convergence is negligible.
 3. Then, we assessed the impact of the exchange zone shift (δ_S) with equivalent cell size between the patch and the substrate ($\chi = 1$) and $N_{cells} = 200$. The analysis showed that the second order Chimera method is preferable as it is less dependent on the grid configuration and has a more predictable behavior regarding the Chimera error generated.
 4. The impact of the cell ratio (χ) has been assessed using $N_{cells} = 200$ with coincident grids ($\delta_S = 0$). In a coarse-to-fine transfer ($\chi > 1$), the second order Chimera method systematically improves the overall solution which is not the case for the first order Chimera method. In a fine-to-coarse transfer ($\chi < 1$), the Chimera method errors are blended with the spatial error generated by the coarse grids.
 5. Finally, the impact of the cell ratio (χ) has been assessed using $N_{cells} = 200$ with non-coincident grids ($\delta_S = 0.6 h_W$). In a coarse-to-fine transfer ($\chi > 1$), the second order Chimera method with the extended detection does not systematically lower the

error when χ increases unlike the first order Chimera method. On the other hand, the second order Chimera method with the standard detection procedure is the most accurate configuration when χ increases. In a fine-to-coarse transfer ($\chi < 1$), the Chimera method errors are blended with the spatial error generated by the coarse grids and the extended detection does not improve the global solution.

- A patched domain configuration has been tested as it represents a simplified configuration of the targeted applications with immersed patched grids. The grids are non-coincident and each configuration depends on the number of cells (N_{cells}) and the cell ratio (χ). When $\chi = 1$, the impact of both Chimera methods on the order of convergence is negligible. With $N_{cells} = 200$, the second order method with the standard detection procedure systematically improves the overall solution when χ increases and provides the most accurate results among all the tested configurations of the Chimera method.

2.4.3 - Split Sod shocktube

We now consider a non-linear test case which is the well known Sod shocktube [160, 170]. This test is relevant in the assesement of the developped Chimera method as its solution consists of a left expansion wave, a contact discontinuity and a right shock wave separated by constant states. This test allows us to examine the impact of the Chimera method when an expansion wave or a shock wave crosses the Chimera exchange zone which will be reviewed in two distinct sections. This test is relevant for the assement of the developped Chimera method as it consists in solving the Euler equations and allows us to review the ability of the Chimera method to transfer non-linearities from one grid to the other. A tube of length $L = 1$ m contains a left state and a right state separated by an interface located at $x_0 = 0.5$ m. The states are respectively given by:

$$\begin{pmatrix} \rho_L \\ u_L \\ p_L \end{pmatrix} = \begin{pmatrix} 1 \text{ kg}\cdot\text{m}^{-3} \\ 0 \\ 10^4 \text{ Pa} \end{pmatrix}, \quad \begin{pmatrix} \rho_R \\ u_R \\ p_R \end{pmatrix} = \begin{pmatrix} 0.125 \text{ kg}\cdot\text{m}^{-3} \\ 0 \\ 10^3 \text{ Pa} \end{pmatrix}, \quad (2.24)$$

with (ρ_L, u_L, p_L) the left state and (ρ_R, u_R, p_R) the right state. The simulation stops at the time $t_f = 2.3 \times 10^{-3}$ s. The computational domains are similar to the ones in section 2.4.2.A and are illustrated in Figure 2.29.

For the Chimera configuration, the domain is composed of a substrate of length $L = x_i + k_{GC}h_{\mathcal{W}}$ with x_i the position of the substrate Chimera interface, k_{GC} the number of ghost cell layers and $h_{\mathcal{W}}$ the substrate cell size. The patch is positioned from x_i according to δ_S as shown in Figure 2.29. We note N_{cells} the number of grid cells over L which gives the substrate grid resolution ($h_{\mathcal{W}}$). The patch cell size ($h_{\mathcal{V}}$) is set given χ . The Chimera interface position (x_i) will vary depending on the solution component (expansion wave, shock wave) we are focusing on. The single grid configuration is identical to the Chimera configuration with $\delta_S = 0$. This will allow us to test the impact of the Chimera procedure on an expansion wave or a shock wave and to compare the results to an equivalent single grid configuration, especially when χ increases given N_{cells} . As a result, the single grid configuration also depends on N_{cells} , x_i and χ . The CFL number is set to 0.9

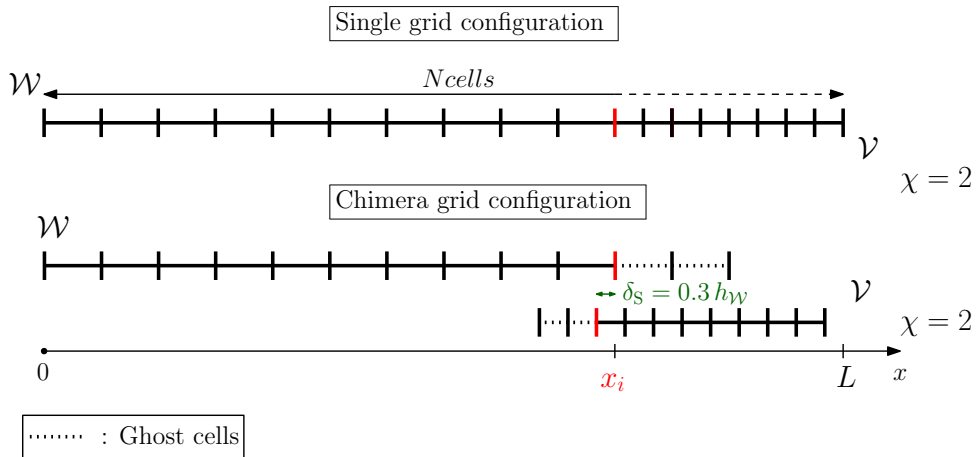


Figure 2.29: Shocktube test case: grid arrangements for the single grid and Chimera configurations.

The results are compared to the analytical solution of the Sod shocktube. The L_1 norm of the density error is computed as in equation 2.23.

A . Focus on the expansion wave

In this first section, we focus on the expansion wave crossing the Chimera interface. As we want to keep the grid configurations and notations as simple as possible across the various cases, the left and right states of the Sod shocktube are inverted in order to make the expansion wave travel from left to right. The Chimera interface (x_i) is set to 0.6 m. As a result, the expansion wave starts from the substrate and at $t = t_f$, the head of the expansion wave is located inside the patch. The objective is to assess the behavior of the Chimera method compared to the single grid configuration when an expansion wave crosses the Chimera interface and to monitor the appearance of oscillations or perturbations induced by the Chimera method.

A.1 - Impact of the Chimera sending on the order of convergence

In this first study, χ is set to 1 and $\delta_S = 0.6 h_W$. The Chimera results have been obtained with the standard detection procedure. We use 6 different grids from the coarsest $N_{cells} = 100$ to the finest $N_{cells} = 3200$.

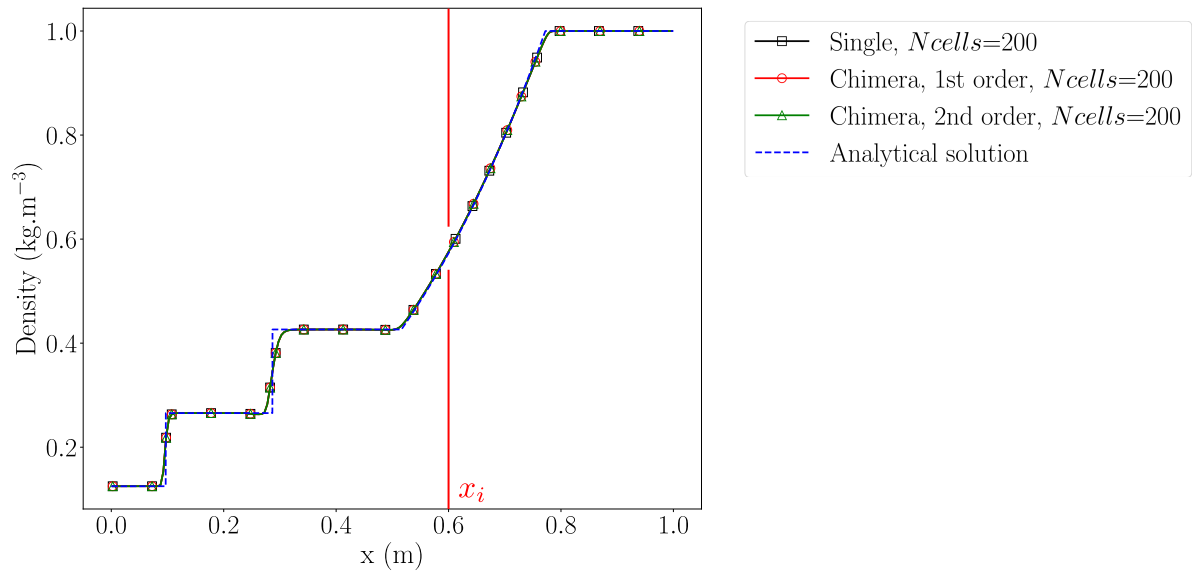


Figure 2.30: Shocktube test case - focus on the expansion wave: density profile at $t = t_f$ for both the Chimera methods and the single grid configurations with $N_{cells} = 200$, $\chi = 1$ and $\delta_S = 0.6 h_W$. The markers on the plots are not representative of the number of points of the numerical solution.

Figure 2.30 shows the density profile obtained with $N_{cells} = 200$ and $\chi = 1$. We can see that the crossing of the Chimera exchange zone by the expansion wave does not generate visible perturbations. The results of the L_1 norm of the density error are reported on Table 2.9. Starting with the orders of convergence, we can clearly see that the non-smoothness of the solution prevents the single grid configurations to reach an order of convergence of 2. Unlike the previous sinus advection case, the Chimera methods contribute to the error and slightly degrade the overall solution. The Chimera method impacts the global solution by 1.9% for the coarsest grid with the first order Chimera exchange and by 0.28% for the coarsest grid with the second order Chimera exchange, compared to the equivalent single grid configuration. When refining the grids, the Chimera error decreases and becomes lower than 0.1% for the finest grids. The difference between the first and the second order Chimera methods also decreases.

Table 2.9: Grid convergence analysis of the Sod shocktube - focus on the expansion wave: results on density (ρ) errors obtained with a single grid configuration as well as with the present Chimera approach using a patch with same grid spacing as the substrate ($\chi = 1$) and non-coincident grids ($\delta_S = 0.6 h_{\mathcal{V}}$).

Ncells	$L_1(\varepsilon_\rho)(\times 10^4)$			Order of convergence p		
	Single	Chimera		Single	Chimera	
		First order	Second order		First order	Second order
100	3.604	3.674	3.614	0.78	0.80	0.78
200	2.095	2.115	2.099	0.72	0.73	0.72
400	1.271	1.276	1.272	0.98	0.98	0.98
800	6.433e-1	6.446e-1	6.435e-1	0.71	0.71	0.71
1600	3.925e-1	3.929e-1	3.926e-1	0.83	0.83	0.83
3200	2.209e-1	2.210e-1	2.209e-1	-	-	-

A.2 - Impact of the cell ratio (χ) on the solution

Now we set $N_{cells} = 200$ on the substrate and χ varies. For the Chimera cases, $\delta_S = 0.6 h_{\mathcal{V}}$. The single grid configuration is also refined from the patch Chimera interface location (x_i) to the end of the domain as shown in Figure 2.29. The results of the L_1 norm of the density error are reported on Table 2.10. The single grid case with a local refinement deteriorates the quality of the overall solution as the patch region gets refined. It is illustrated in Figure 2.31 with the appearance of a small oscillation near the location of the brutal refinement (x_i).

The same trend is observed with the Chimera cases as seen in Figure 2.32, nonetheless, the second order Chimera method limits the error growth unlike the first order Chimera method and the single grid configuration. This is visible as the second order Chimera exchange does not have an oscillation in its solution. With the rarefaction wave crossing the Chimera exchange zone, the extended detection procedure does not improve the quality of the solution and even deteriorates the solution with the first order Chimera method when $\chi > 2$. This highlights the difficulties of the first order method when dealing with high cell ratios and also exhibits some difficulties of standard single grid methods to deal with brutal spatial refinements.

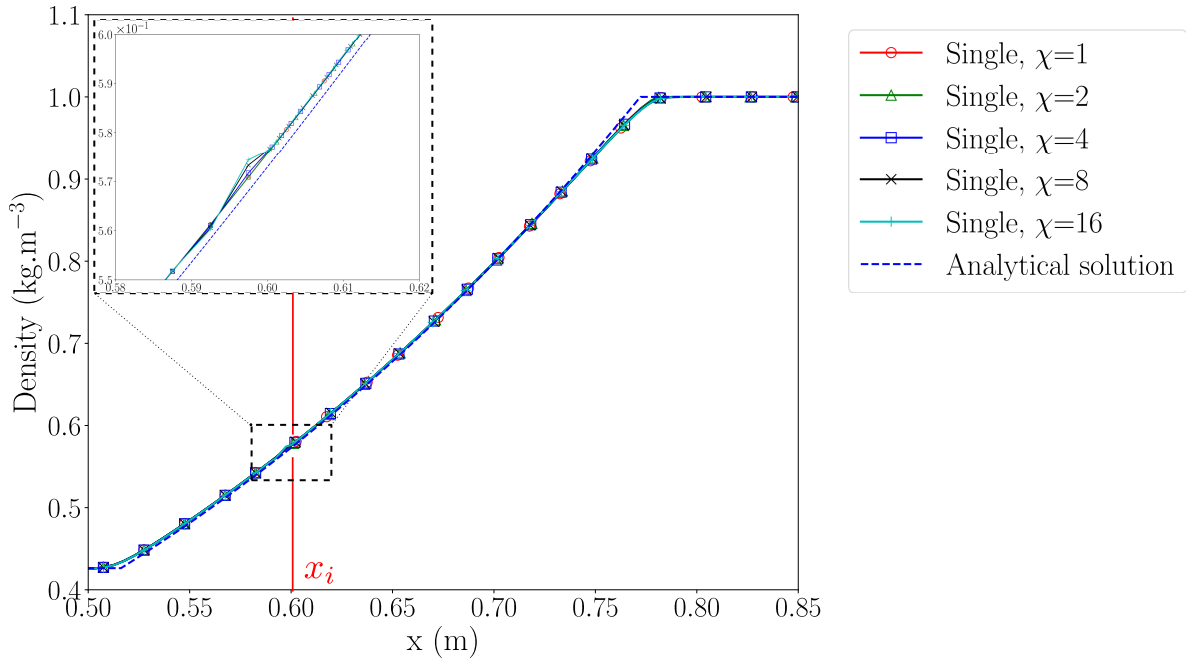


Figure 2.31: Shocktube test case - focus on the expansion wave: density profile at $t = t_f$ for single grid configurations with $N_{cells} = 200$ and different values of χ . The markers on the plots are not representative of the number of points of the numerical solution.

Table 2.10: Cell ratio analysis of the Sod shocktube - focus on the expansion wave: results on density (ρ) errors obtained with the single grid configuration as well as with the present Chimera approach using a patch with non-coincident Chimera interface ($\delta_S = 0.6 h_{\mathcal{V}}$) and variable cell ratios (χ) for both the standard and extended detection procedures. The transfer occurs from a coarse substrate ($N_{cells} = 200$) to a finer patch. Equivalent N_{cells} on the patch are reported for equivalent fine single mesh (EFSM) comparison.

χ	$L_1(\varepsilon_\rho) (\times 10^3)$				Equivalent N_{cells} on the patch (for EFSM comparison)	
	Chimera					
	First order		Second order			
Single	Standard detection	Extended detection	Standard detection	Extended detection		
1	2.095	2.115	2.115	2.099	2.099	200
2	2.096	2.240	2.118	2.094	2.112	400
4	2.109	2.250	2.403	2.102	2.111	800
8	2.138	2.147	2.403	2.106	2.110	1600
16	2.158	2.147	2.489	2.106	2.107	3200

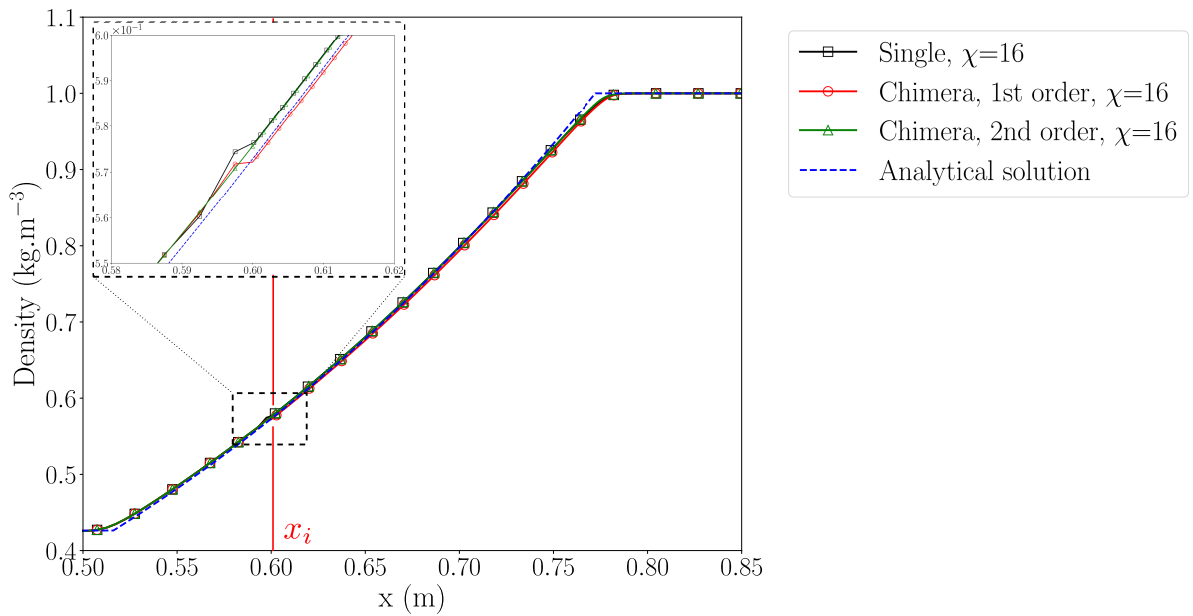


Figure 2.32: Shocktube test case - focus on the expansion wave: density profile at $t = t_f$ for single grid and Chimera configurations with $N_{cells} = 200$, $\chi = 16$ and $\delta_S = 0.6 h_W$. The markers on the plots are not representative of the number of points of the numerical solution.

B . Focus on the shock wave

In this second section, we focus on the shock wave crossing the Chimera interface. The Chimera interface position (x_i) is set to 0.8 m. Using the initial conditions described in equation 2.24, the shock wave naturally crosses the Chimera interface and is located inside the patch at $t = t_f$. The objective is to assess the behavior of the Chimera method compared to the single grid configuration and monitor the appearance of oscillations or perturbations induced by the Chimera method when discontinuities are at play.

B.1 - Impact of the Chimera sending on the order of convergence

We start by reviewing the impact of refinement with equivalent cell size between the patch and the substrate ($\chi = 1$). In this configuration the cells of the single grid cases are uniformly distributed along the domain of length L . The results of the L_1 norm of the density error are reported on Table 2.11. We can see for that for discontinuities, the Chimera method is more impactful on the overall solution with relative Chimera errors of 14% on the coarsest grids compared to the coarsest single grid. The Chimera error decreases when refining the grids and reaches 5% of relative error compared to the equivalent single grid configuration with $N_{cells} = 3200$. Figure 2.33 shows the absence of local oscillations induced by the Chimera method on the density profile at $t = t_f$.

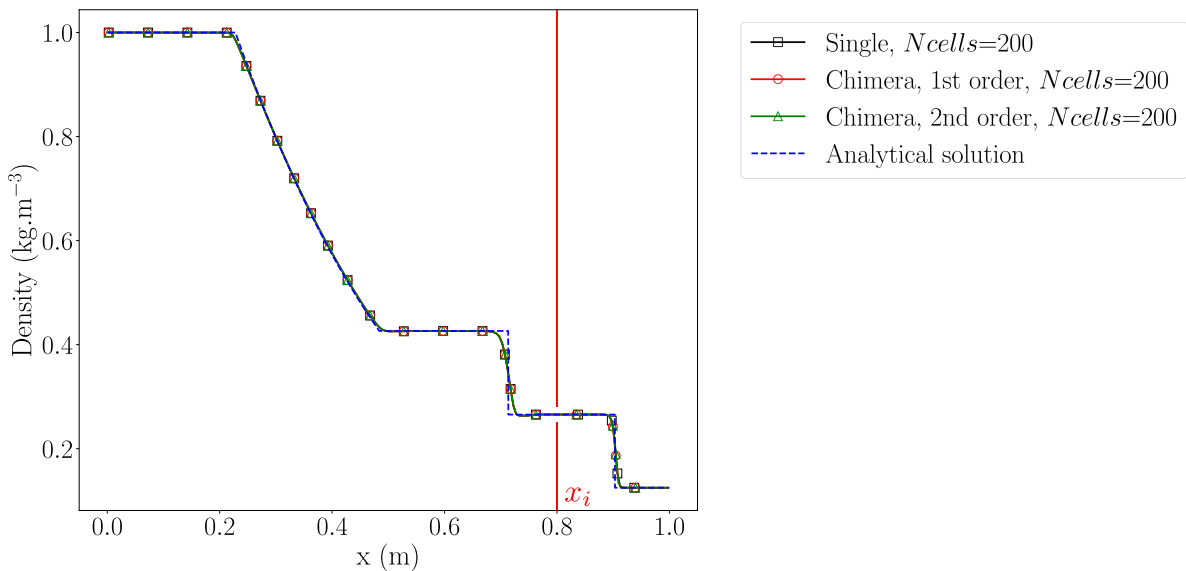


Figure 2.33: Shocktube test case - focus on the shock wave: density profile at $t = t_f$ for both the Chimera methods and the single grid configurations with $N_{cells} = 200$, $\chi = 1$ and $\delta_S = 0.6 h_W$. The markers on the plots are not representative of the number of points of the numerical solution.

Table 2.11: Grid convergence analysis of the Sod shocktube - focus on the shock wave: results on density (ρ) errors obtained with a single grid configuration as well as with the present Chimera approach using a patch with same grid spacing as the substrate ($\chi = 1$) with non-coincident grids ($\delta_S = 0.6 h_{\mathcal{V}}$).

Ncells	$L_1(\varepsilon_\rho)(\times 10^4)$			Order of convergence p		
	Single	Chimera		Single	Chimera	
		First order	Second order		First order	Second order
100	3.604	4.138	4.132	0.78	0.86	0.86
200	2.095	2.281	2.283	0.72	0.88	0.88
400	1.271	1.243	1.237	0.98	0.82	0.82
800	6.433e-1	7.022e-1	7.007e-1	0.71	0.94	0.94
1600	3.925e-1	3.647e-1	3.655e-1	0.83	0.65	0.65
3200	2.209e-1	2.329e-1	2.330e-1	-	-	-

B.2 - Impact of the cell ratio (χ) on the solution

Focusing on the impact of the cell ratio (χ), we set $N_{cells} = 200$ on the substrate portion. For the Chimera cases, $\delta_S = 0.6 h_{\mathcal{V}}$ which means that the grids are non-coincident. The single grid configuration is also refined from the patch Chimera interface location $x = x_i$ to the end of the domain as shown in Figure 2.29. The two Chimera detection procedures (standard and extended) have been tested and the results of the L_1 norm of the density error are reported on Table 2.12. When using different cell ratios between the grids, the local refinement improves the overall error compared to the cases where $\chi = 1$. However, for both the single grid and the Chimera cases, the error is not a linear function of χ as the minimum of the error is not reached for the highest value of χ . We can also see that the extended detection procedure slightly helps decreasing the error compared to the standard detection procedure for both Chimera methods when dealing with discontinuities but not in a significant way.

Figure 2.34 shows the density profile of single grid cases when χ varies. We can see that a brutal refinement generates oscillations that propagate in the flow direction. These oscillations are also present in the Chimera configurations with a very similar behavior of the perturbation between the first order Chimera method and the single grid configuration. When dealing with discontinuities, the second order Chimera method does not mitigate the perturbation but slows it down. Also, the second order Chimera method provides a good estimate of the shock wave velocity whereas the first order method overshoots the shock wave position.

As a result, the second order Chimera method with the standard detection procedure is the most suitable configuration for dealing with shocks and high cell ratios as the extended method does not bring significant improvements to the solution while increasing the number of ghost cells.

Table 2.12: Cell ratio analysis of the Sod shocktube - focus on the shock wave: results on density (ρ) errors obtained with the single grid configuration as well as with the present Chimera approach using a patch with non-coincident Chimera interface ($\delta_S = 0.6 h_{\mathcal{W}}$) and variable cell ratios (χ) for both the standard and extended detection procedures. The transfer occurs from a coarse substrate ($N_{cells} = 200$) to a finer patch. Equivalent N_{cells} on the patch are reported for equivalent fine single mesh (EFSM) comparison.

χ	$L_1(\varepsilon_\rho) (\times 10^3)$					Equivalent N_{cells} on the patch (for EFSM comparison)
	Single	Chimera				
		First order		Second order		
	Standard detection	Extended detection	Standard detection	Extended detection		
1	2.095	2.281	2.281	2.283	2.283	200
2	2.090	2.099	2.008	1.966	1.946	400
4	1.922	2.155	2.040	2.032	1.991	800
8	1.960	2.054	2.050	1.997	1.927	1600
16	1.939	2.072	2.085	2.013	1.928	3200

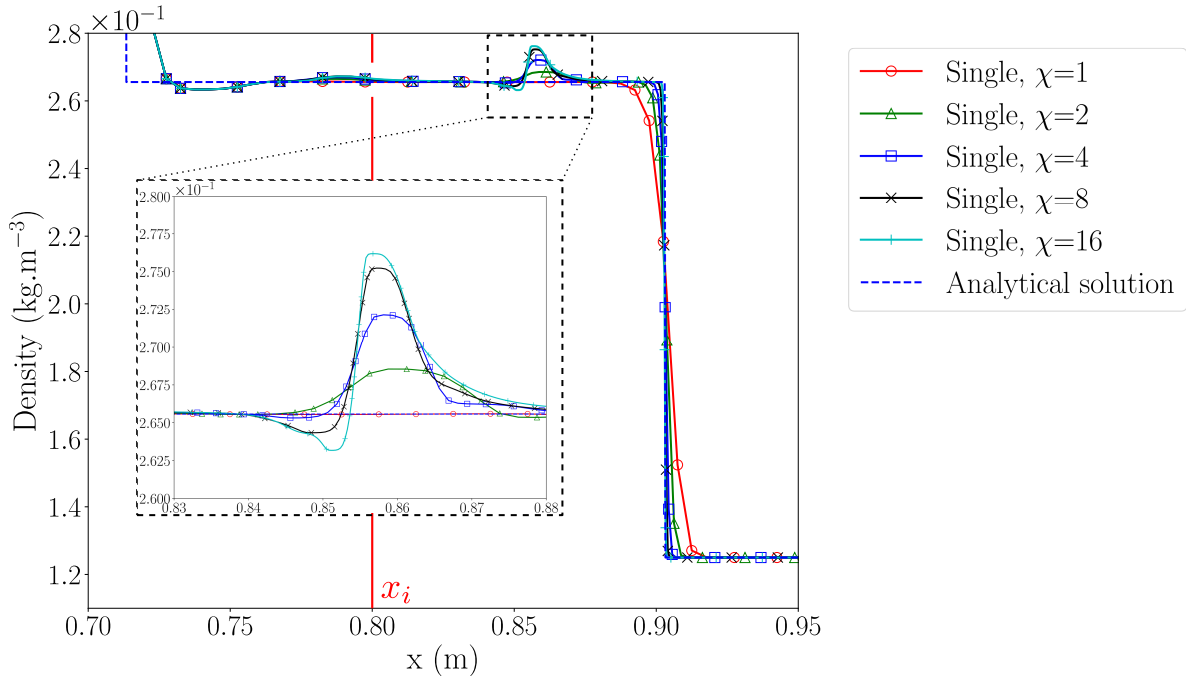


Figure 2.34: Shocktube test case - focus on the shock wave: density profile at $t = t_f$ for single grid configurations with $N_{cells} = 200$ and different values of χ . The markers on the plots are not representative of the number of points of the numerical solution.

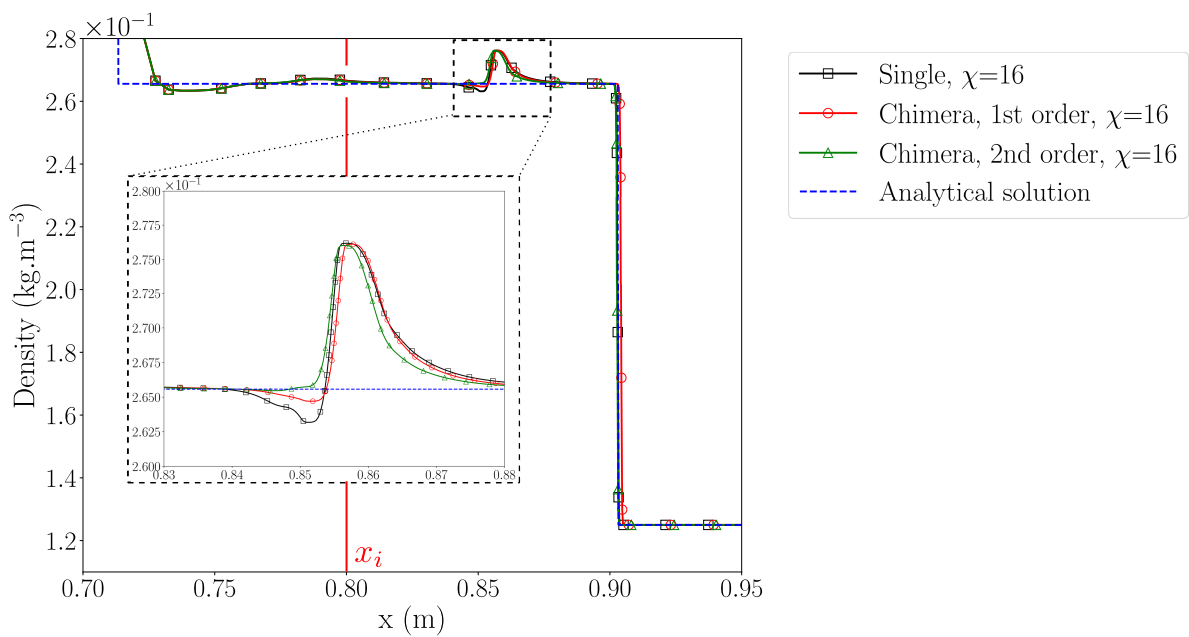


Figure 2.35: Shocktube test case - focus on the shock wave: density profile at $t = t_f$ for single grid and Chimera configurations with $N_{\text{cells}} = 200$, $\chi = 16$ and $\delta_S = 0.6 h_{\gamma}$. The markers on the plots are not representative of the number of points of the numerical solution.

C . Summary of the findings on the Sod shocktube case

With the Sod shocktube test case, we have been able to assess the behavior of the different Chimera configurations transferring an expansion wave or a shock wave from the substrate to the patch. These waves result from the non-linearity of the Euler equations which was not present with the advection test case. Various configurations have been tested in order to assess key aspects of the different versions of the Chimera method:

- A split domain configuration with Chimera interface located at $x_i = 0.6$ m and inverted left and right initial states have been used in order to review the impact of the Chimera method on the solution when an expansion wave crosses the exchange zone. Both first and second order Chimera methods have a negligible impact on the order of convergence compared to a single grid approach. When refining the patch while maintaining N_{cells} constant, the second order Chimera method with the standard detection procedure provides the more accurate solution compared to the other configurations. However, the refinement slightly deteriorates the solution even for the single grid case because of a small oscillation generated near the brutal refinement region.
- A split domain configuration with a Chimera interface located at $x_i = 0.6$ m has been used in order to assess the impact of the Chimera method on the solution when a shock wave crosses the exchange zone. At an equivalent cell size between the patch and the substrate, both first and second order Chimera methods do not generate visible oscillations and the Chimera error reduces with refinement. When refining the patch at a constant N_{cells} , an oscillation is generated near the brutal refinement zone. This oscillation also appears with the single grid configuration and prevent the error from decreasing when using a finer patch. The second order extended detection procedure does not bring significant improvements compared to the standard detection procedure which remains the best compromise between shock wave propagation speed estimation, overall accuracy and number of ghost cells.

2.4.4 - Conservation properties of the present Chimera method

Although our local conservation hypothesis is not sufficient to ensure global conservation of the system [184, 185, 133], we verify in this section that the Chimera method does not introduce conservation error with coincident grid interfaces. Then, we verify that the conservation error due to the Chimera exchange with non-coincident grid interfaces and variable cell ratios meet acceptable levels for industrial requirements.

To this end, we study the behavior of the finite volume Chimera formulation when a steady shock wave is located at the patch interface. This one-dimensional test case is taken from [183] and [148].

The full computational domain $x \in [-5, 5]$ m, is discretized in two regions of $N_{cells} = 25$ each for the single grid configuration. The interface between the two regions is located at $x = 0$ and the Chimera configurations are depicted in Figure 2.36 with coincident grid interfaces ($\delta_S = 0$) and non-coincident grid interfaces ($\delta_S = 0.3 h_W$) with $\chi = 2$. For every Chimera grid configuration, the patch interface is fixed and coincides with the shock wave discontinuity at $x = 0$. The variable N_{cells} corresponds to the number of cells on the substrate while the number of cells on the patch is defined by the cell ratio (χ). The Chimera cases are tested for both the first and the second order Chimera method with the standard detection procedure. The flow states on each side of the discontinuity are the following:

$$\begin{pmatrix} \rho_L \\ u_L \\ p_L \end{pmatrix} = \begin{pmatrix} 1 \text{ kg.m}^{-3} \\ 1.5 \text{ m.s}^{-1} \\ 0.71429 \text{ Pa} \end{pmatrix}, \quad \begin{pmatrix} \rho_R \\ u_R \\ p_R \end{pmatrix} = \begin{pmatrix} 1.8621 \text{ kg.m}^{-3} \\ 0.8055 \text{ m.s}^{-1} \\ 1.7559 \text{ Pa} \end{pmatrix}, \quad (2.25)$$

As the shock wave discontinuity coincides with the patch interface, the patch contains exclusively the right state of the shock wave. All simulations are performed up to a dimensionless time $t^* = t u_L / L = 100$, using a prescribed CFL = 0.9 on both the single grid configuration and the Chimera grids. This time ensures a converged solution with residuals of density, momentum and total energy lower than 10^{-9} on every case. The relative error on system conservation is computed for each conservative variable as the following:

$$\begin{aligned} \varepsilon(\rho(t^*)) &= \frac{\left| \int \rho(t^*, \underline{x}) dV - \int \rho(0, \underline{x}) dV \right|}{\int \rho(0, \underline{x}) dV} \\ \varepsilon((\rho u)(t^*)) &= \frac{\left| \int (\rho u)(t^*, \underline{x}) dV - \int (\rho u)(0, \underline{x}) dV \right|}{\int (\rho u)(0, \underline{x}) dV} \\ \varepsilon(\rho E(t^*)) &= \frac{\left| \int (\rho E)(t^*, \underline{x}) dV - \int (\rho E)(0, \underline{x}) dV \right|}{\int (\rho E)(0, \underline{x}) dV} \end{aligned} \quad (2.26)$$

In Figure 2.37, we show the results of the Chimera configurations (first and second order) with coincident grid interfaces ($\delta_S = 0$) and non-coincident grid interfaces ($\delta_S = 0.3 h_W$) with equivalent cell size compared to the single mesh configuration ($N_{cells} = 25$, $\chi = 1$) and the analytical solution.

As highlighted by Table 2.13, system mass, momentum and total energy are conserved for both Chimera methods with the coincident grid interface configuration ($\delta_S = 0$) as seen in Figure 2.37 with identical errors compared to the single mesh case.

The Chimera method with non-coincident grid interfaces ($\delta_S = 0.3 h_W$) introduces conservation error since a maximum of respectively 0.5% and 0.6% is recorded on the conservation error of mass for the first order Chimera method and on the conservation error of momentum for the second order Chimera method. In fact, the shock wave is still located at the patch interface but at the same time, is also diffused upstream, in a coarse cell of the substrate that induces higher error levels.

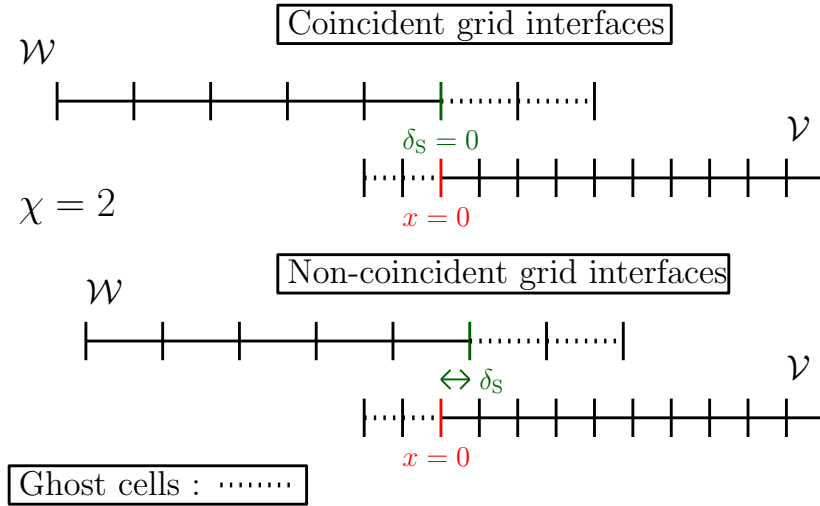


Figure 2.36: Stationary shock wave grid configuration for coincident grids and non-coincident grids with the shock wave located at $x = 0$.

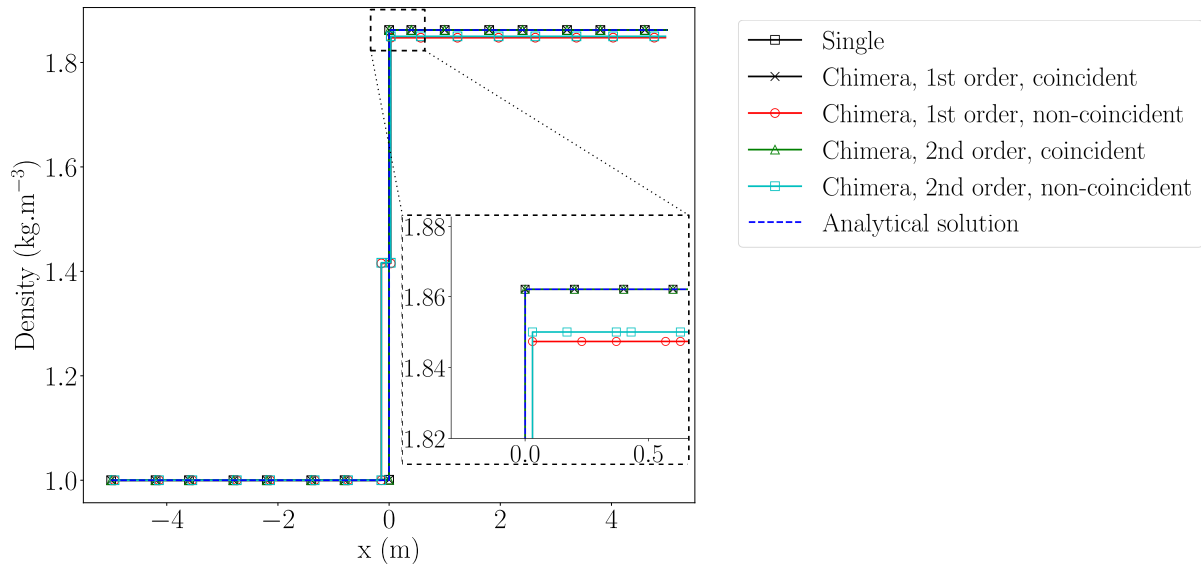


Figure 2.37: Density profile of the stationary shock wave converged solution in a single grid configuration with $N_{cells} = 25$ and Chimera configurations (first and second order exchanges) with coincident and non-coincident grids for $N_{cells} = 25$ and $\chi = 1$ compared to the reference solution. The markers on the plots are not representative of the number of points of the numerical solution.

Table 2.13: System mass, momentum and energy relative error computed on the converged solution with a single grid configuration as well as with the present Chimera approach using a patch with the same grid spacing as the substrate ($N_{cells} = 25$, $\chi = 1$) with a stationary shock wave matching the patch boundary.

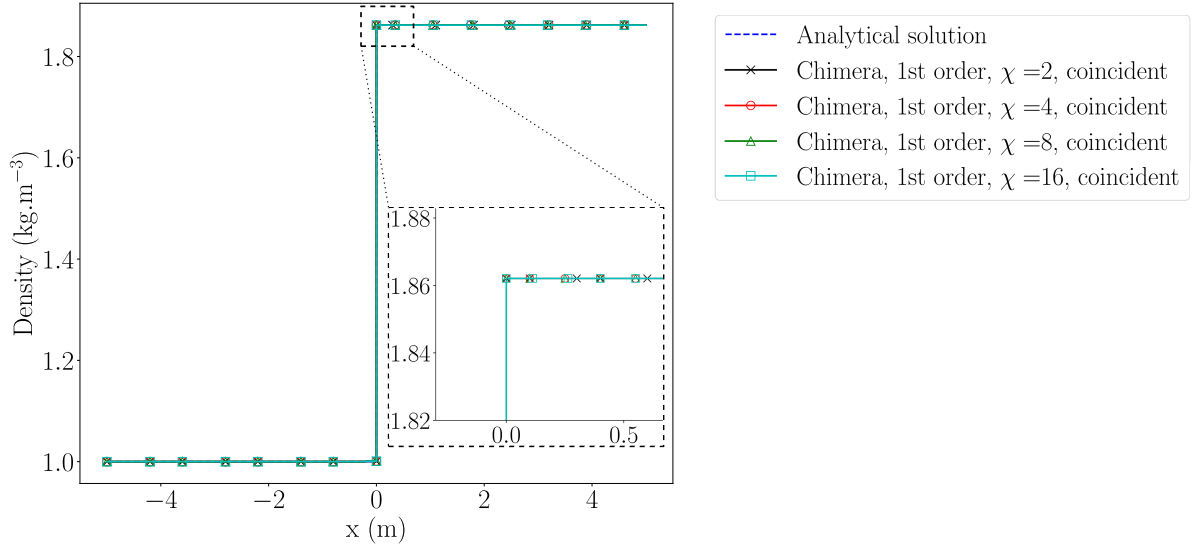
	Single	Chimera			
		Coincident interfaces		Non-coincident interfaces	
		First order	Second order	First order	Second order
$\varepsilon(\rho(t^*))$ in %	5.971e-4	5.971e-4	5.971e-4	5.276e-1	4.359e-1
$\varepsilon((\rho u)(t^*))$ in %	2.449e-3	2.449e-3	2.449e-3	4.996e-1	6.336e-1
$\varepsilon((\rho E)(t^*))$ in %	4.463e-3	4.463e-3	4.463e-3	1.904e-1	4.608e-1

When refining the patch ($\chi = 2, 4, 8$ and 16) with coincident grids ($\delta_S = 0$), we can observe

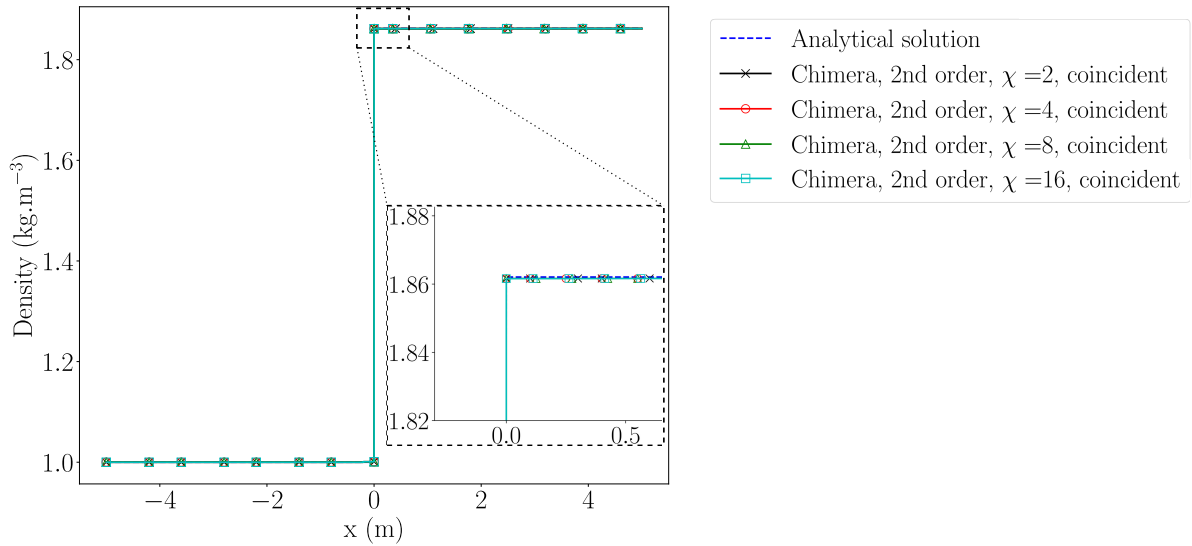
from Table 2.14 and Figure 2.38a, that system mass, momentum and total energy are preserved with the first order Chimera method with an error of the same order of magnitude as the single grid configuration which is $10^{-4}\%$. On the other hand, the second order method has more impact on conservation with a jump of two orders of magnitude when refining the patch. This is caused by the linear reconstruction of the solution that blunts the shock wave interface which translates into a difference in system mass, momentum and total energy. As seen in Figure 2.38b, the error is relatively low as it does not exceed 0.02% .

With non-coincident grid interfaces ($\delta_S = 0.3 h_{\mathcal{V}}$), the shock wave diffuses upstream in the substrate grid. As a result, refining the patch has only a weak effect on error levels for both the first order and second order Chimera methods (see Table 2.15). The error magnitude is however relatively low since it does not exceed 1% . To put those results in perspective, Figure 2.38c and Figure 2.38d show the impact of the Chimera method on the post-shock state with non-matching grids. The loss on the density jump is at most 0.39% of the reference post-shock state for the first order Chimera method and 0.4% for the second order Chimera method which is acceptable for industrial applications.

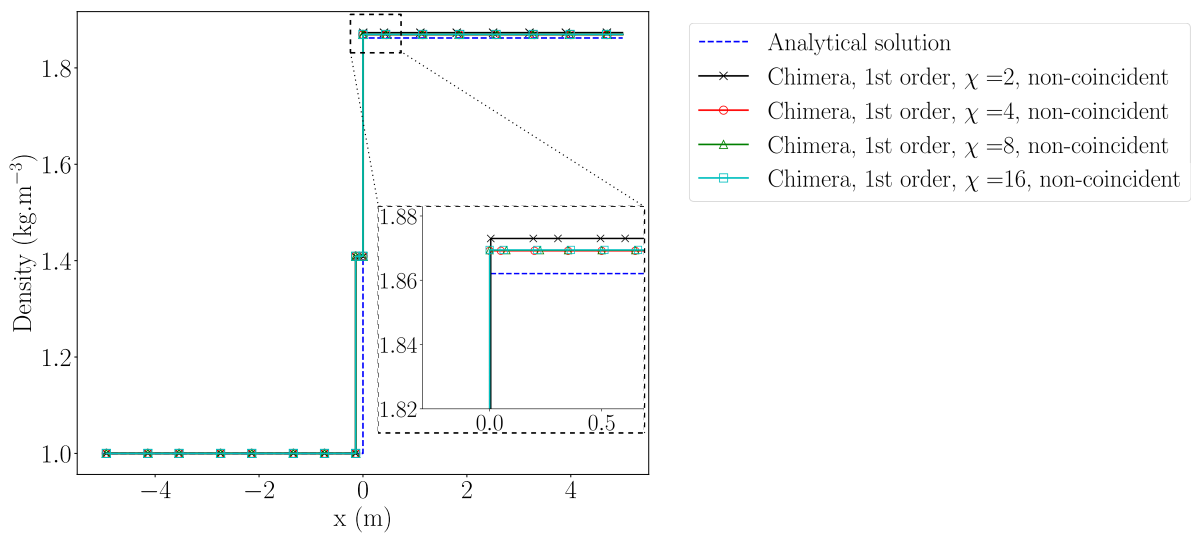
As a result, the first and second order Chimera methods have a very similar behavior with non-coincident grid interfaces with a small advantage for the second order method. This was expected from the Sod shocktube study as the second order Chimera method captures correctly the shock wave speed compared to the first order method.



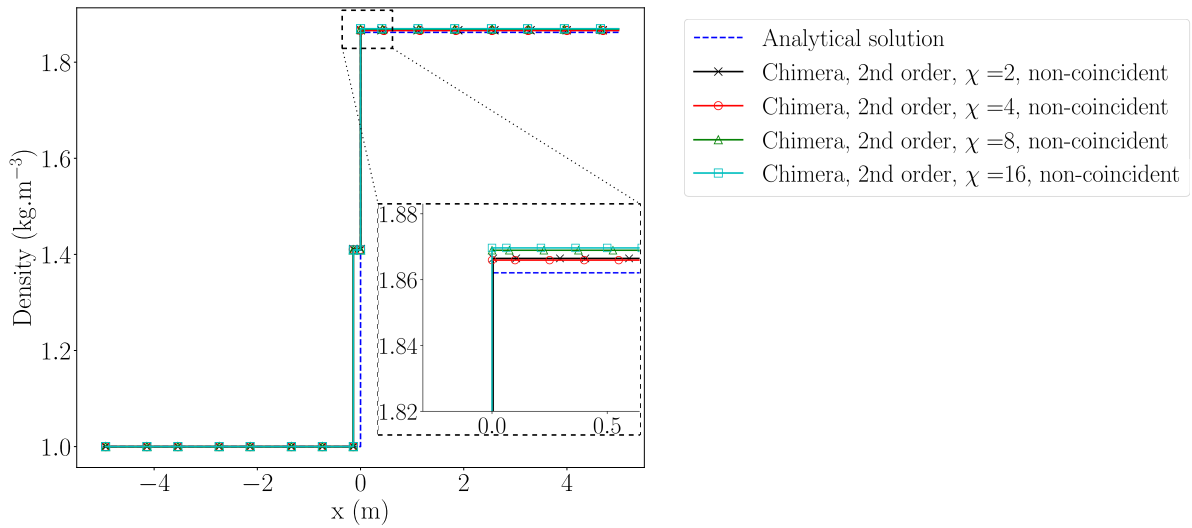
(a) Chimera first order, $\delta_S = 0$



(b) Chimera second order, $\delta_S = 0$



(c) Chimera first order, $\delta_S = 0.3 h_W$



(d) Chimera second order, $\delta_S = 0.3 h_W$

Figure 2.38: Density profile of the stationary shock wave converged solution of Chimera configurations with coincident ($\delta_S = 0$) and non-coincident ($\delta_S = 0.3 h_W$) grids for $N_{cells} = 25$ and χ varying from 2 to 16 compared to the reference solution. The markers on the plots are not representative of the number of points of the numerical solution.

Table 2.14: System mass, momentum and energy relative error computed on the converged solution with a single grid configuration as well as with the present Chimera approach using a patch with different grid spacings and a stationary shock wave matching the patch boundary and coincident interfaces ($\delta_S = 0$).

χ	Chimera (Coincident interfaces)					
	First order			Second order		
	$\varepsilon(\rho(t^*))$ in %	$\varepsilon((\rho u)(t^*))$ in %	$\varepsilon((\rho E)(t^*))$ in %	$\varepsilon(\rho(t^*))$ in %	$\varepsilon((\rho u)(t^*))$ in %	$\varepsilon((\rho E)(t^*))$ in %
1	5.970e-4	2.449e-3	4.463e-3	5.970e-4	2.449e-3	4.463e-3
2	4.171e-4	2.271e-3	4.375e-3	1.111e-2	1.113e-2	3.345e-3
4	5.583e-4	2.421e-3	4.446e-3	1.154e-2	1.175e-2	3.815e-3
8	6.254e-4	2.491e-3	4.480e-3	1.177e-2	1.209e-2	4.062e-3
16	6.582e-4	2.526e-3	4.497e-3	1.118e-2	1.226e-2	4.189e-3

Table 2.15: System mass, momentum and energy relative error computed on the converged solution with a single grid configuration as well as with the present Chimera approach using a patch with different grid spacings and a stationary shock wave matching the patch boundary and non-coincident interfaces ($\delta_S = 0.3 h_{\mathcal{V}}$).

χ	Chimera (Non-coincident interfaces)					
	First order			Second order		
	$\varepsilon(\rho(t^*))$ in %	$\varepsilon((\rho u)(t^*))$ in %	$\varepsilon((\rho E)(t^*))$ in %	$\varepsilon(\rho(t^*))$ in %	$\varepsilon((\rho u)(t^*))$ in %	$\varepsilon((\rho E)(t^*))$ in %
1	5.276e-1	4.996e-1	1.904e-1	4.359e-1	6.336e-1	4.608e-1
2	3.609e-1	5.685e-1	4.397e-1	1.330e-1	3.218e-1	3.179e-1
4	2.253e-1	5.591e-1	5.564e-1	1.131e-1	3.894e-1	4.284e-1
8	2.319e-1	5.647e-1	5.573e-1	2.173e-1	5.590e-1	5.639e-1
16	2.352e-1	5.674e-1	5.578e-1	2.418e-1	5.988e-1	5.955e-1

2.5 - Advection of an isentropic vortex

The last test case of this chapter is an isentropic vortex which is one of the exact solutions for the compressible Euler equations [192]. This test involves convection of an isentropic vortex throughout an inviscid flow. It is often used to illustrate the ability of numerical schemes to capture vortical flows. The mean flow velocities u_∞ and v_∞ , pressure p_∞ and density ρ_∞ are considered to be free stream. This test is a diagonally convecting vortex with $(u_\infty, v_\infty) = (1 \text{ m.s}^{-1}, 1 \text{ m.s}^{-1})$ and $p_\infty = 1 \text{ Pa}$, $\rho_\infty = 1 \text{ kg.m}^{-3}$. As an initial condition, an isentropic vortex is added to the mean flow field. The perturbation values are given by:

$$\begin{cases} (\delta u, \delta v) = \frac{\beta}{2\pi} e^{\frac{1}{2}(1-r^2)} (-\bar{y}, \bar{x}), \\ \delta T = -\frac{(\gamma-1)\beta^2}{8\gamma\pi^2} e^{(1-r^2)}, \end{cases} \quad (2.27)$$

where β is the vortex strength and $\gamma = 1.4$. Here, $T = \frac{p}{\rho}$, $T_\infty = 1.0$, $(\bar{x}, \bar{y}) = (x - x_c, y - y_c)$, where (x_c, y_c) are the coordinates of the initial vortex center equal to $(0, 0)$ and $r^2 = \bar{x}^2 + \bar{y}^2$. The entire flow is assumed to be isentropic, so for a perfect gas, $p/\rho^\gamma = \text{constant}$. From the relations,

$$\begin{cases} \rho = \rho_\infty + \delta\rho, \\ u = u_\infty + \delta u, \\ v = v_\infty + \delta v, \\ T = T_\infty + \delta T, \end{cases} \quad (2.28)$$

and the isentropic relation, the resulting state for conservative variables is given by:

$$\begin{pmatrix} \rho \\ \rho u \\ \rho v \\ \rho E \end{pmatrix} = \begin{pmatrix} \left[1 - \frac{(\gamma-1)\beta^2}{8\gamma\pi^2} e^{(1-r^2)}\right]^{1/(\gamma-1)} \\ \rho \left[1 - \frac{\beta}{2\pi} e^{\frac{1}{2}(1-r^2)}\right] \\ \rho \left[1 + \frac{\beta}{2\pi} e^{\frac{1}{2}(1-r^2)}\right] \\ \frac{p}{\gamma-1} + \frac{1}{2}\rho(u^2 + v^2) \end{pmatrix}. \quad (2.29)$$

The exact solution with the given initial state is a convection of the vortex with the mean velocity comparable to the results shown in Figure 2.39. Therefore, it provides a good measure of the accuracy of the schemes for relatively smooth solutions of the Euler equations. The computational domain for the vortex is a centered square $(x \times y) \in [-5, 5]^2$ m \times m. Periodic boundary conditions are used at the boundary of the domain. The single mesh simulation uses a uniform cartesian grid with N_{cells} cells on the side. The same grid is used as the substrate in the Chimera configuration. The patch is a centered rotated square of a side 5 m at a 45° angle as shown in Figure 2.40. The grid resolution of the patch is set using the cell ratio (χ).

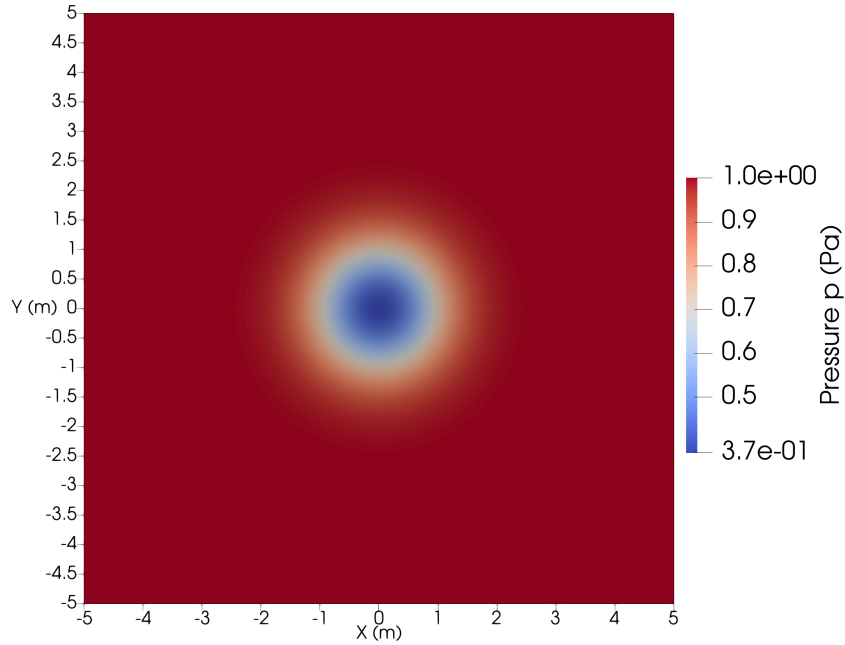


Figure 2.39: Resulting pressure field of the isentropic vortex case at $t^* = t_f^*$ for the single grid configuration with $N_{cells} = 640$.

All simulations are performed up to a dimensionless time $t_f^* = t \frac{\sqrt{u_\infty^2 + v_\infty^2}}{L\sqrt{2}} = 1$, using a prescribed CFL number of 0.6 on both the single grid configuration and the Chimera configurations. The finite volume method is identical to the one-dimensional test cases presented in the previous section and corresponds to a MUSCL-Hancock scheme with an HLLC Riemann solver and the K-Dubois limiter with $k = 0.75$.

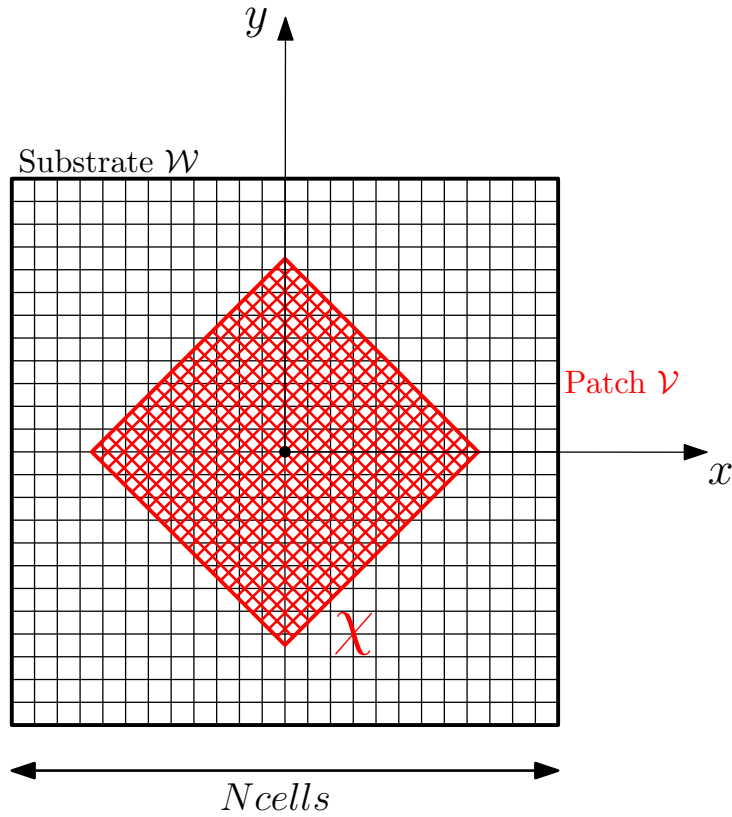


Figure 2.40: Isentropic vortex grid configuration for the Chimera case with $\chi = 2$.

2.5.1 - Impact of the Chimera sending on the order of convergence

First, the cell ratio (χ) is kept constant and equal to 1. Several grid resolutions are employed from $N_{cells} = 50$ to $N_{cells} = 400$, to study grid convergence of the Chimera method compared to the single grid approach. At the final dimensionless time t_f^* , we compare numerical solutions obtained on both the single grid configuration and the Chimera configuration, to the analytical solution. To measure numerical errors, we calculate the L_1 norm of the pressure error written $L_1(\varepsilon_p)$, computed as shown in equation 2.23

Figure 2.41 illustrates the grid convergence results over the 5 grids for both the single grid and the Chimera configurations. Even though the orders of convergence are higher than 1, the single grid solution error does not decrease as expected with smooth solutions. The Chimera configurations follow the same trend.

On a two-dimensional case such as the isentropic vortex, the first order Chimera method slightly deflects from the single grid results and the difference between the latter and the second order Chimera method is invisible to the naked eye. Using the pressure profile over the centerline $y = 0$ shown in Figure 2.42, we can see that the second order Chimera method and the single grid results are matching but the vortex is no longer symmetrical compared to the analytical solution. This explains why the first order Chimera method gives, in some configurations, a lower error compared to the single grid configuration and the second order Chimera method.

This is confirmed by Table 2.16 where both the first order Chimera and the second order Chimera methods have a lower error compared to the single grid case for $N_{cells} = 320$ and $N_{cells} = 160$. At this level of accuracy, the difference is negligible and can be attributed to a grid combination that better fits the solution. Nonetheless, the second order Chimera method seems the better choice here as it remains the closest to the single grid solution across refinement.

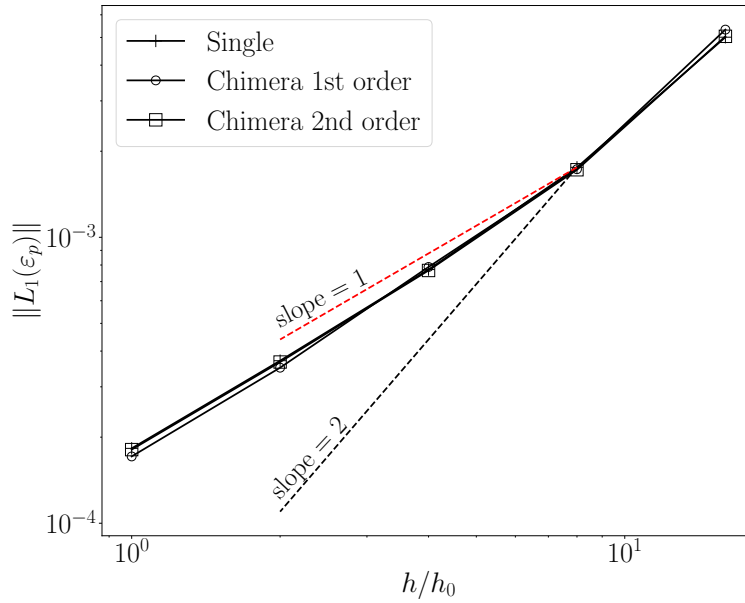


Figure 2.41: Grid convergence analysis of the isentropic vortex case with equivalent cell sizes between the patch and the substrate ($\chi = 1$). $h = h_{\mathcal{V}} = h_{\mathcal{Y}}$ and h_0 corresponds to $N_{cells} = 640$.

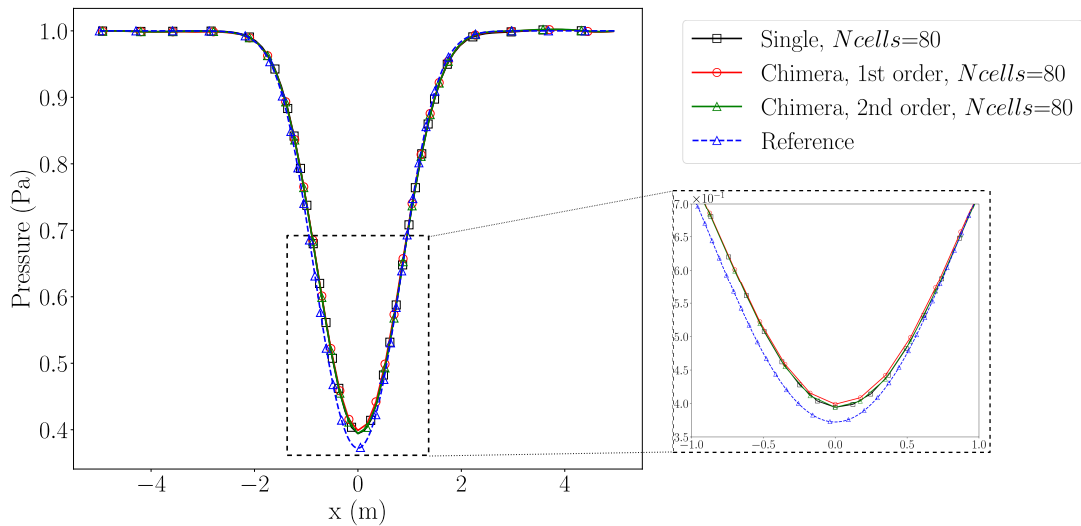


Figure 2.42: Pressure profile at $t^* = t_f^*$ along $y = 0$ for the single grid configuration as well as the Chimera cases with $N_{cells} = 80$ and $\chi = 1$. The markers on the plots are not representative of the number of points of the numerical solution.

Table 2.16: Grid convergence analysis of the vortex case: results on pressure (p) errors obtained with a single grid configuration as well as with the present Chimera approach using a patch with same grid spacing as the substrate ($\chi = 1$).

Ncells	$L_1(\varepsilon_\rho)(\times 10^4)$			Order of convergence p		
	Single	Chimera		Single	Chimera	
		First order	Second order		First order	Second order
40	5.010	5.325	5.046	1.51	1.62	1.55
80	1.757	1.730	1.722	1.18	1.14	1.17
160	7.713e-1	7.874e-1	7.656e-1	1.06	1.17	1.06
320	3.702e-1	3.500e-1	3.662e-1	1.02	1.03	1.02
640	1.828e-1	1.713e-1	1.809e-1	-	-	-

2.5.2 - Impact of the cell ratio (χ) on the solution

In the following, N_{cells} is set to 40 and χ varies. The two detection procedures (standard and extended) are tested for both the first order and the second order Chimera methods. The results are reported on Table 2.17. For both Chimera methods, refining the patch does not improve the overall accuracy but deteriorates it. This deterioration is due to oscillations caused by the transfer from the coarse substrate to the fine patch as shown in Figure 2.43. These oscillations are exacerbated with high values of χ as shown in Figure 2.44. However, this deterioration is reduced when using the second order Chimera method compared to the first order method (see Fig. 2.43a and Fig. 2.43b). Overall, the extended detection does not seem to improve the solution. Therefore, the most accurate configuration is the second order Chimera method with the standard detection procedure.

Table 2.17: Cell ratio analysis of the vortex case: results on pressure (p) errors obtained with with the present Chimera approach using a variable cell ratios (χ) and $N_{cells} = 80$. Equivalent N_{cells} on the patch are reported for equivalent fine single mesh (EFSM) comparison.

χ	$L_1(\varepsilon_p)(\times 10^3)$				Equivalent N_{cells} on the patch (for EFSM comparison)
	First order		Second order		
	Standard detection	Extended detection	Standard detection	Extended detection	
1	5.325	5.325	5.046	5.046	40
2	5.426	5.487	5.073	5.157	80
4	5.806	6.791	5.482	5.573	160
8	6.188	7.623	5.698	5.889	320
16	6.457	8.116	5.812	6.078	640

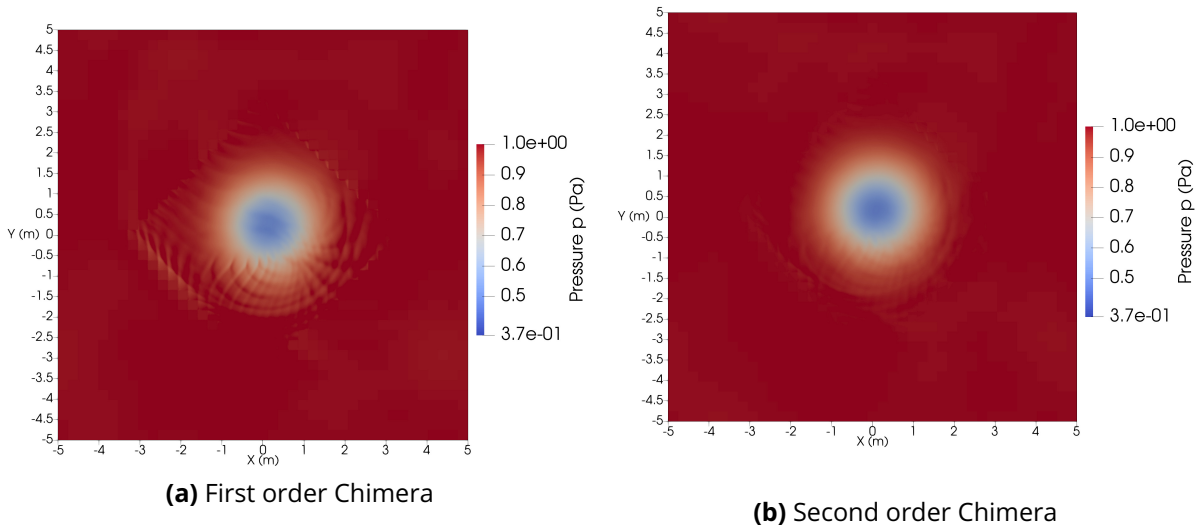


Figure 2.43: Resulting pressure field of the isentropic vortex case at $t^* = t_f^*$ for the Chimera case using the first order sending (a) and the second order sending (b) with $N_{cells} = 40$ and $\chi = 16$ both using the standard detection procedure.

Table 2.18 contains the ratio of the CPU times and memory cost of each equivalent fine single grid configuration to the CPU times and memory of the corresponding Chimera configurations. If $\chi \geq 1$, the equivalent fine single grid of a Chimera configuration is a single grid configuration with the same grid resolution as the patch. Therefore, if the time ratio is higher than 1, it means that the Chimera case takes less time than its equivalent fine single mesh. Similarly, a memory ratio higher than 1, means that the Chimera configuration memory footprint is lower than its equivalent fine single mesh.

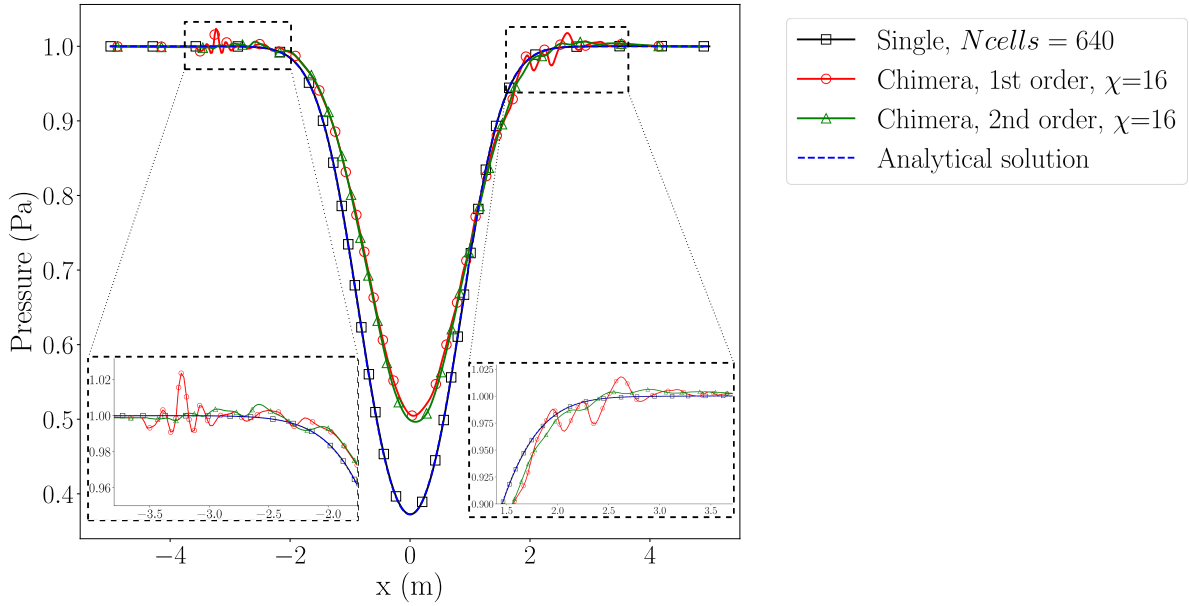


Figure 2.44: Pressure profile at $t^* = t_f^*$ along $y = 0$ for the single grid configuration as well as the Chimera cases with $N_{cells} = 40$ and $\chi = 16$. The markers on the plots are not representative of the number of points of the numerical solution.

Overall, the Chimera method is very interesting using cell ratios as it divides the CPU time by more than 4 in some cases and divide the memory requirements by more than 3. As expected, the first order method is the fastest Chimera configuration and the second order Chimera method with the extended detection procedure is the slowest. Even though the second order Chimera method is not as fast as the first order method, it brings significant gains with up to 3.8 less CPU time than the equivalent single grid configuration. For the second order Chimera method, even though, the extended detection procedure does not significantly deteriorate the CPU time, the gains on the accuracy of the solution are not important enough to justify its utilization compared to the standard detection.

Table 2.18: Time and memory cost of the Chimera method: time and memory ratio of the present Chimera approach using a variable cell ratios (χ) compared to the equivalent fine single mesh (EFSM). The higher the better. Equivalent N_{cells} on the patch are reported for equivalent fine single mesh (EFSM) comparison.

χ	CPU Time Ratio				Memory Ratio	Equivalent N_{cells} on the patch (for EFSM comparison)
	First order		Second order			
	Standard detection	Extended detection	Standard detection	Extended detection		
1	0.81	0.79	0.69	0.63	0.79	40
2	2.43	2.40	1.98	1.67	1.90	80
4	4.47	4.26	3.61	3.26	3.08	160
8	4.83	4.75	3.80	3.73	3.61	320
16	4.48	4.42	3.62	3.61	3.76	640

2.6 - Chapter conclusion

In this chapter, we have detailed the development of a Chimera method based on a finite volume approach using two grids respectively named substrate and patch. The method uses ghost cells as receiving containers and relies on a local conservation hypothesis from which we derived a first order and a second order interpolation formulas of the conservative variables. The geometrical identification procedures have been detailed along with the dependency of the ghost cell layer number upon the order of numerical scheme such as the MUSCL-Hancock scheme. A modified version of the K-Dubois limiter [162] has been presented in order to prevent the appearance of local extrema when using the second order Chimera method. In order to minimize the appearance of unstabilities, a unique time step is chosen for the both domains based on the finest grid. A solution reconstruction from composite domains is proposed in order to compare Chimera configurations to single grid ones.

The developed Chimera method with the two interpolation formulas and the two detection procedures has been tested on reference one-dimensional and two-dimensional test cases from the literature like a sinus perturbation advection, the well known Sod shocktube, a stationary shock wave and an isentropic vortex advection. The first and second order Chimera sendings do not alter the order of convergence of linear one-dimensional solutions like advectations or non-linear, continuous one-dimensional solutions like expansion fans. Using high cell ratios allow an increase in the global accuracy of the solution due to the use of finer grids on localized regions. This improvement is limited by the coarsest grid.

When a discontinuous solution like a shock wave is transferred from a substrate to a patch, the second order Chimera method is able to correctly capture shock wave speeds but oscillations are generated due to abrupt refinements which deteriorates the quality of the solution. These oscillations appear with a coarse-to-fine transfer as well as single grids with abrupt refinement and remain local phenomena as the overall profile is preserved which must but be pointed out. This type of oscillations is also observed when using high cell ratios with solutions sensitive to conservation like the isentropic vortex. However, the second order Chimera method tends to mitigate the perturbations which could potentially be blent in larger cases for industrial applications. Also, the objective of the developed Chimera method is to add local geometrical details that can alter the flow locally which would then impact the larger scale. Therefore, even though the fine-to-coarse perturbations must be taken into account, they do not prevent the developed Chimera method to be used for industrial applications.

Finally, The extended detection procedure does not seem relevant in any of the cases tested with no relevant gains in accuracy and slight additional cost in CPU time and memory. The second order Chimera method with a standard detection procedure is an interesting compromise which combined with a reasonable cell ratio (up to $\chi = 8$), can bring relevant CPU time optimizations while improving the accuracy of the global solution.

In the following, the first order Chimera method is no longer considered and we focus on the second order method. The standard detection is the default configuration and if the extended detection procedure is used, it will be explicitly specified.

3 - Numerical study of the finite volume Chimera method ability to transfer compressible flow structures based on reference test cases

Contents

3.1	Flow around a circular cylinder at Mach = 3	86
3.1.1	Presentation of the case	86
3.1.2	Steady state horizontal pressure force analysis	87
3.1.3	Shock standoff measurements	92
3.2	Interaction of a shock wave moving in air with a bubble . . .	93
3.2.1	Presentation of the case	93
3.2.2	Helium bubble-shock wave interaction	94
3.2.3	R22 bubble-shock wave interaction	97
3.2.4	Summary of the findings on the behavior of the Chimera method with multicomponent flows	100
3.3	Double Mach Reflection problem	101
3.3.1	Presentation of the case	101
3.3.2	Comparison of the Chimera case with the single grid case ($\chi = 1$)	103
3.3.3	Comparison of the Chimera case with the equivalent fine single mesh (EFSM) for various values of χ	103
3.4	Chapter conclusion	108

The second order Chimera method has been assessed on one-dimensional and two-dimensional, reference but relatively simple test cases. In this chapter, we extend the assessment of the method with the standard detection procedure as a default configuration. To evaluate the present approach, we select three well-known two-dimensional test cases from the literature. Each test case is chosen to stress the method on one particular aspect in order to highlight capabilities and limitations of the present Chimera method. The finite volume method set-up is kept constant across all the cases tested which corresponds to a MUSCL-Hancock scheme with an HLLC Riemann solver and the K-Dubois limiter with $k = 0.75$ (see section 1.2 for details on the scheme configuration). The scheme is second order accurate in both time and space. By default the CFL number is set to 0.6. A supersonic flow around a 2D cylinder is undertaken with an overlapping grid in the vicinity of the cylinder. This allows us to check that the present Chimera method is able to transfer a shock wave from the global grid to a patch containing a geometrical detail that will alter the global solution of the flow before reaching a steady state. The second test case concerns the interaction of a shock wave in Air with a bubble initially cylindrical with two variants. In the first one, the bubble is filled with Helium while in the second one, the bubble is filled with R22. This allows us to stress the behavior of the present method to deal with moving interfaces between components in multicomponent flows. At last, the well known test case of the double Mach reflection is undertaken with overlapping grids. We can thus check the ability of the method to account for multiple interactions between discontinuities even if they move across overlapping grid boundaries.

3.1 - Flow around a circular cylinder at Mach = 3

3.1.1 - Presentation of the case

A circular cylinder with a radius $D = 1$ m, is initially placed in Air ($\gamma = 1.4$) which is assumed as a perfect gas. A shock wave is initially located 8 cylinder diameters in front of the cylinder with a flow at Mach $M_\infty = 3$ upstream of the shock wave. Upstream pressure and density are prescribed, respectively at $P_\infty = 96774$ Pa, and $\rho_\infty = 0.519$ kg.m⁻³ upstream of the shock wave. Initial conditions downstream this shock wave, around the cylinder, are prescribed by using the Rankine-Hugoniot relationships assuming that the front shock wave moves towards the cylinder with a Mach number equal to $M_{sh} = 1$. The initial state of this test case is shown in Figure 3.1 where we see the computational domain $(x \times y) \in [-10, 10]^2$ m \times m.

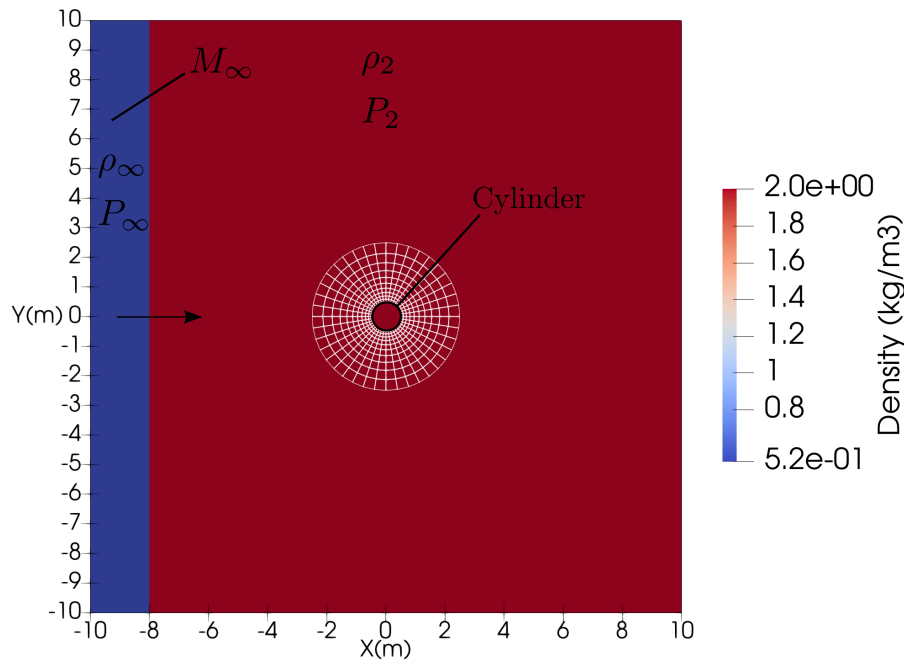


Figure 3.1: Circular cylinder test case: computational domain and initial solution.

A grid that fits both the body and external domain boundaries is first built to serve as a single grid configuration. A zoom-in view in the vicinity of the cylinder is provided in Figure 3.2a, where we see the transition between an O-grid very close to the cylinder towards an H-grid far away. In the followings, we use the number of grid cells (N_{cells}) distributed along the cylinder perimeter as the parameter to refer as refinement. We then built the grid of the patch, attached to the cylinder with an O-grid that at most coincides with the single grid configuration very close to the cylinder to facilitate comparisons with the single grid model (see in Fig. 3.2b the grid in red superimposed to the single grid configuration). Then the substrate model employed in the Chimera computation is a Cartesian grid that fits the external boundaries of the computational domain, as we can see in Figure 3.2b, where a zoom-in close to the cylinder is presented showing the patch grid superimposed to the substrate model. Let us remark that, when considering the problem with overlapping domains, the cylinder only belongs to the patch domain and does not explicitly appears in the substrate model.

All simulations are performed up to a dimensionless time $t^* = t u_\infty / L = 52.5$ (where u_∞ is the infinite velocity), using a prescribed CFL number $CFL = 0.6$ on both the single grid configuration and the overlapping grids.

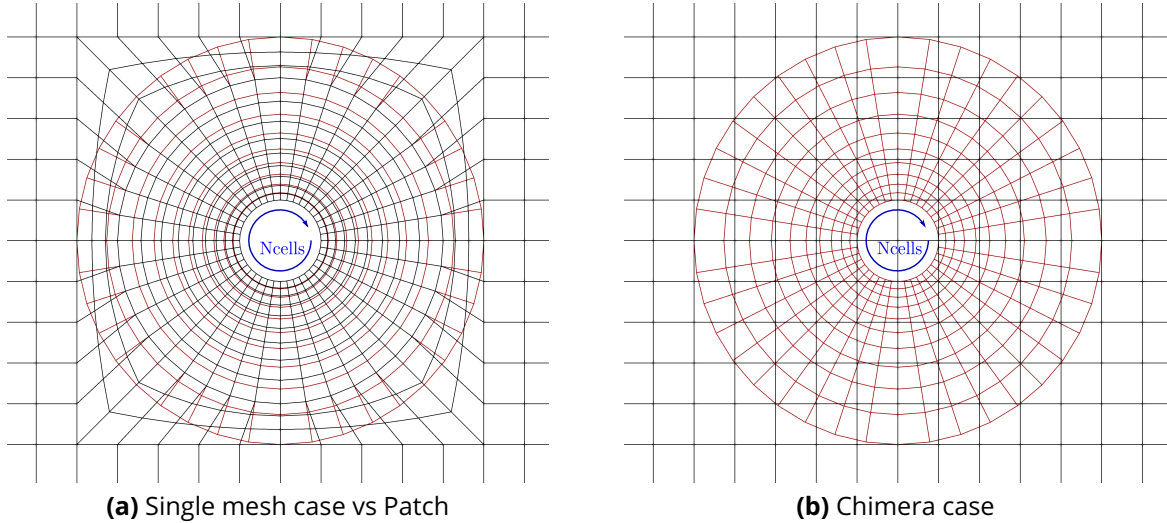


Figure 3.2: Grid configuration for the single mesh case and the Chimera case.

At first, we keep the cell ratio between the patch and the substrate close to unity, meaning that the minimum grid spacing used in the patch (along the cylinder perimeter) is the same as the one used in the substrate although meshes are not coincident away from the cylinder, as we can see in Figure 3.2b. Several grid resolutions are employed from $N_{cells} = 50$ along the cylinder perimeter to $N_{cells} = 400$, to study grid convergence.

Steady state solutions are presented in Figure 3.3, with the comparison of density contours obtained at a dimensionless time $t^* = 52$ for $N_{cells} = 200$ grid cells along the cylinder perimeter, between the single grid configuration (see Fig. 3.3b), and the overlapping grids (see Fig. 3.3a). As we can see, results seem to be similar, and it is hard to differentiate them following the density contours. Let us first remark that in the Chimera case, when the front shock wave passes through the interface from the substrate to the patch, no spurious reflection is generated, meaning that the present Chimera method is able to deal with wave propagation across grid interfaces.

To get a better validation of results obtained with the Chimera method, we use an integral quantity based on the pressure drag force exerted by the flow on the cylinder, calculated at each time step. Time history of this pressure drag force is plotted in Figure 3.4.

3.1.2 - Steady state horizontal pressure force analysis

When the moving front shock wave interacts with the cylinder, a peak on the pressure drag force occurs, followed by a relaxation period during which the front shock wave becomes established as a bow shock in front of the cylinder. Then a steady state solution occurs. The initial peak is well captured by the Chimera method which gives equivalent results compared to the single grid case (see Fig. 3.4). Whatever the grid spacing is, a statistically converged steady state solution is achieved from at most a dimensionless time $t^* = 35$. When the grid becomes finer, this time increases. As we can see, for the coarsest grids the drag force converges towards a constant value while for the finer grids oscillations around a converged value appear due to the high resolution of the cylinder wake. Compared to the single grid computations, the Chimera method gives comparable results on the drag force while some weak discrepancies can be recorded for the coarsest grids. Very similar results have however been recovered for the finest grid tested with the Chimera method. By zooming in on the steady state region between dimensionless times 40 and 52.5 as shown in Figure 3.5, we can see that the average force seems to converge toward the value $F \approx 202 \times 10^3 \text{ N}$. We can observe that the Chimera case captures oscillations around the cylinder with a coarser grid refinement than the

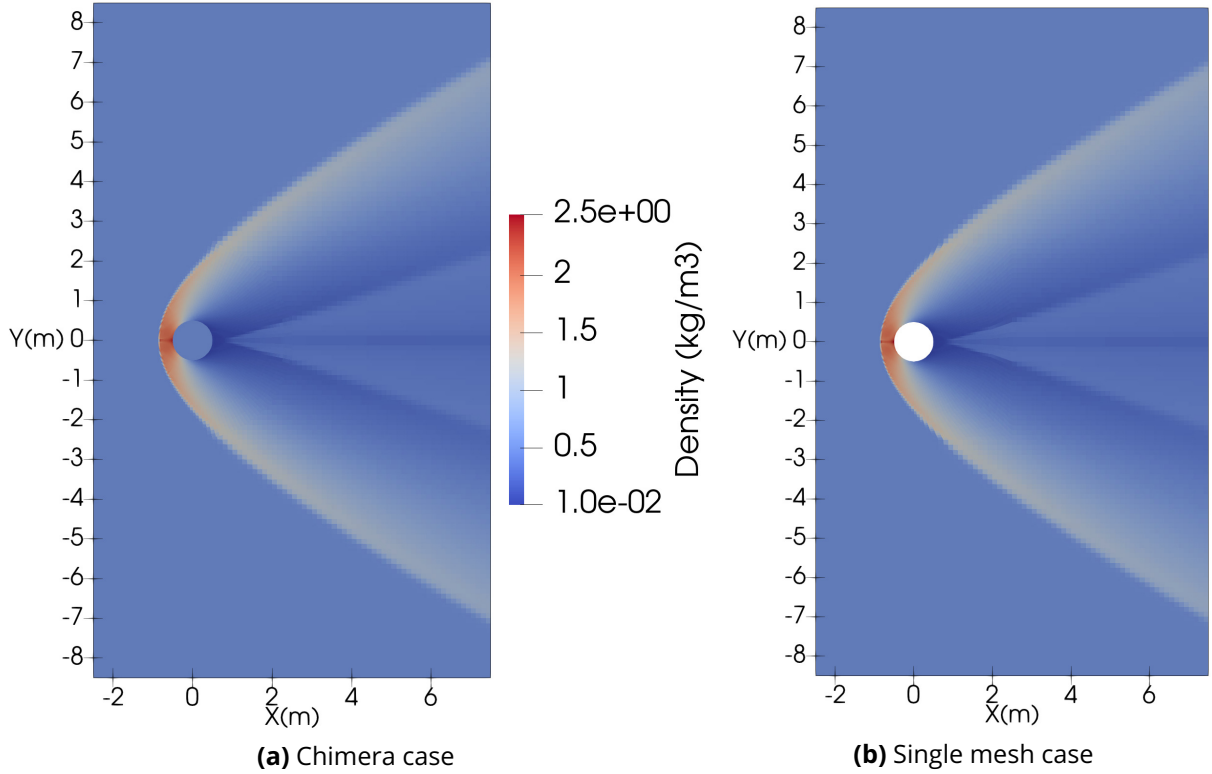


Figure 3.3: Steady state density field for both Chimera case (on the left), and the single grid case (on the right) with a cell ratio of unity ($\chi = 1$), obtained at a dimensionless time $t^* = 52$ and for $N_{cells} = 200$ grid cells along the cylinder perimeter.

single grid configuration. Considering that grids between the single mesh case and the Chimera case are similar but not identical, differences might be caused by a difference in the grid resolution as well as a better grid regularity of the mesh in the Chimera case.

On Table 3.1, we have reported the averaged force calculated for several number of cells over the cylinder perimeter (N_{cells}), over the time interval $t^* \in [40, 52.5]$ for both the single mesh case and the Chimera case. Relative differences, w.r.t. the single grid case, between the Chimera case and the single grid configuration are reported in the last column as percentages. Discrepancies between the single mesh case and the Chimera case do not exceed 2% and the Chimera case converges monotonously as the grids are refined.

Table 3.1: Average resulting pressure force over $t^* \in [40, 52.5]$ for the first study cases ($\chi = 1$).

N_{cells}	$\frac{1}{t_2 - t_1} \int_{t_1}^{t_2} F(t) dt$ (N)		% difference with Single
	Single	Chimera	
50	207728	211312	1.7 %
100	203404	203120	0.14 %
200	201719	202204	0.24 %
400	203059	202161	0.44 %

Secondly, we set the resolution on the substrate model equivalent to $N_{cells} = 100$ and the patch is refined ($\chi = 1, 2$, and 4) with respectively $N_{cells} = 100, 200$, and 400 along the cylinder perimeter. It corresponds to a patch refinement over a constant grid spacing on the substrate. With the definition of the parameters N_{cells} and χ provided for this case, we get the following Chimera configurations: ($N_{cells} = 100, \chi = 1$), ($N_{cells} = 200, \chi = 2$) and ($N_{cells} = 400, \chi = 4$). In

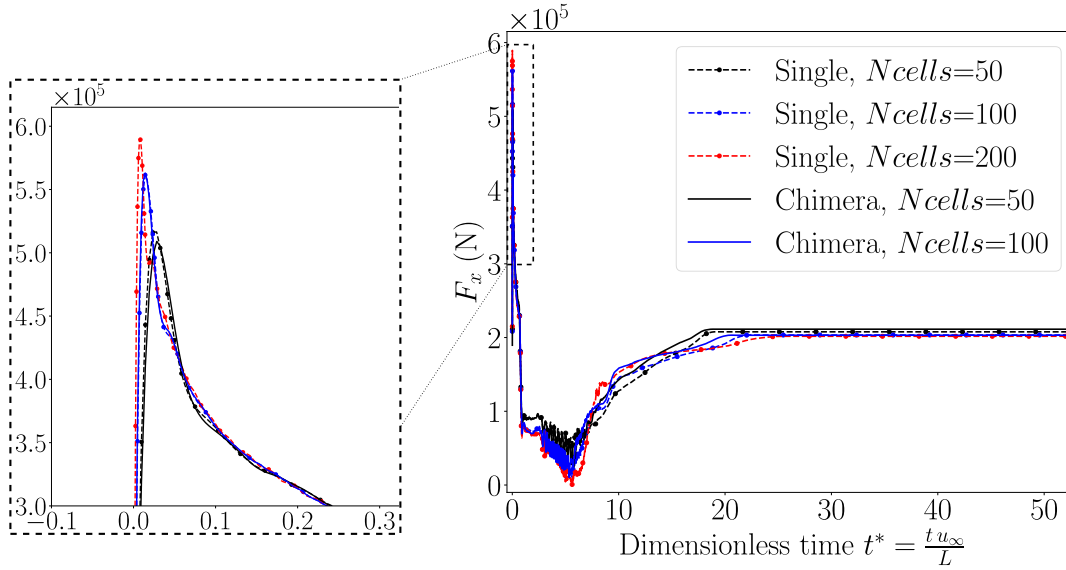
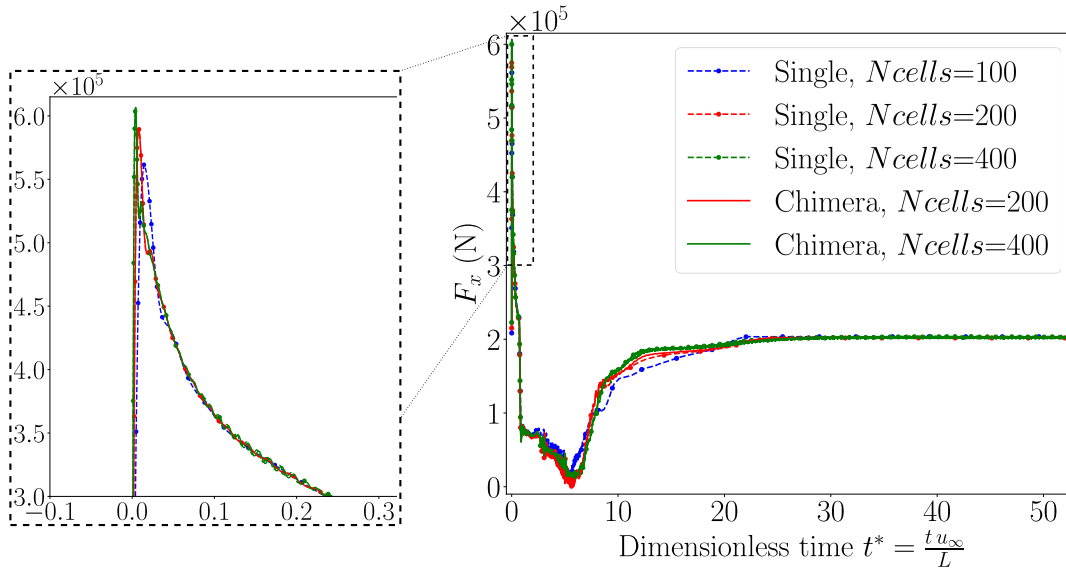

 (a) $N_{cells} = 50, 100$

 (b) $N_{cells} = 200, 400$

Figure 3.4: Time history of the pressure drag force for several number of grid cells (N_{cells}) obtained on both the single grid configuration, and the overlapping grids with however similar grid spacings ($\chi = 1$). The markers on the plots are not representative of the number of points of the numerical solution.

Figure 3.6, we plot histories of the drag force on the cylinder obtained on several refined overlapping grids compared with the equivalent fine single mesh (EFSM) with the same number of cells along the cylinder perimeter. Refining the patch does not introduce local perturbation but instead increases the accuracy of the resulting force as the regularity of the mesh is better ensured than in a single case for the same N_{cells} (see Fig. 3.2).

To better examine predicted converged values of the drag force, we plot a zoom in of histories in between $t^* \in [45, 52.5]$ obtained with both the overlapping grids with cell several ratios and the equivalent fine single mesh (Fig. 3.7). Similar results as with the Chimera case with $\chi = 1$ are obtained that compare very well with the equivalent fine single grid cases. In fact, as reported in Table 3.2, comparable discrepancies with respect to the equivalent single grid computations are recorded by the refined Chimera case ($\chi \neq 1$) compared to the results obtained with $\chi = 1$. Nevertheless, the force

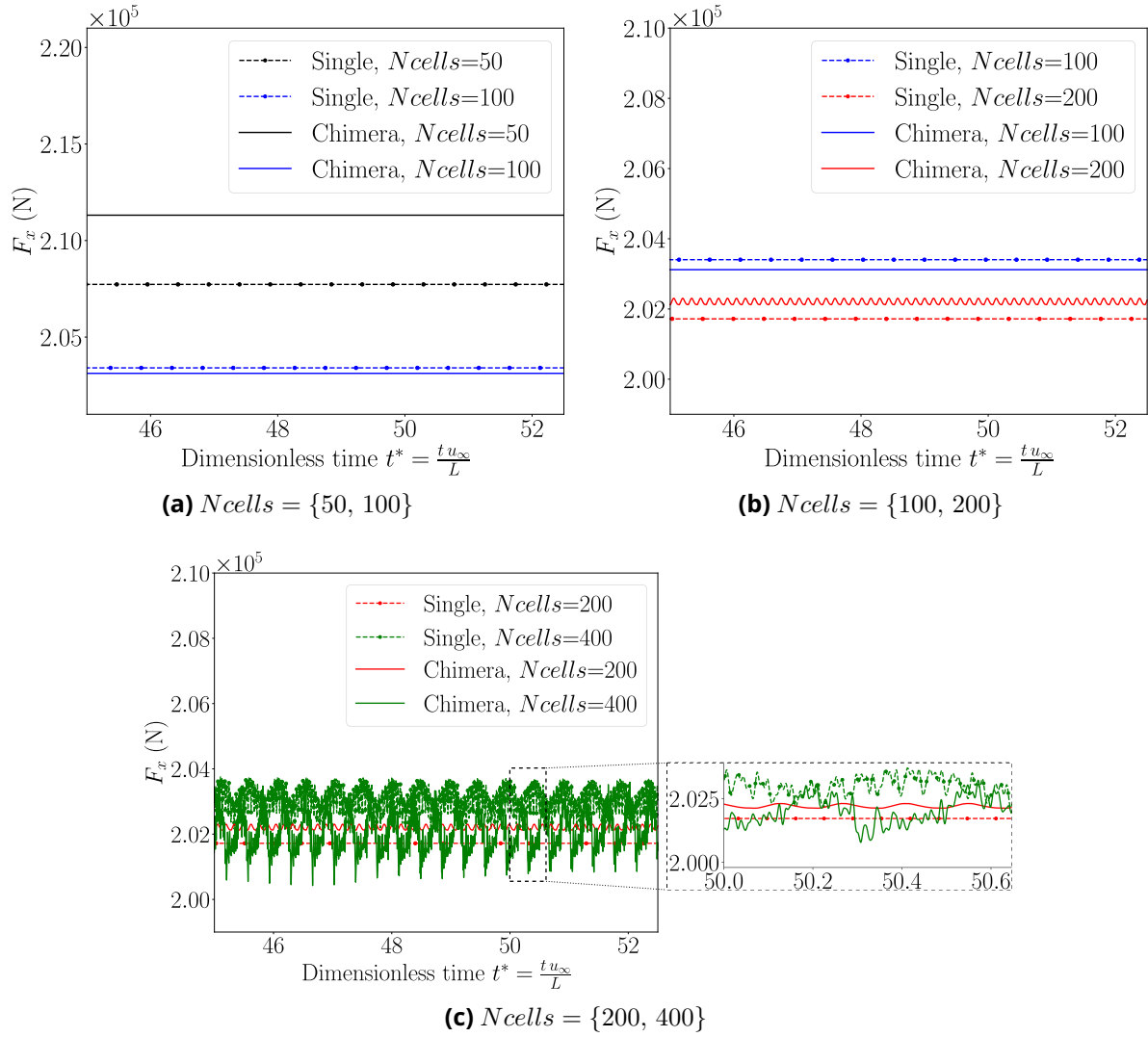


Figure 3.5: Zoom in the interval dimensionless times $t^* \in [45, 52.5]$ of the pressure drag force history for several number of grid cells (N_{cells}), obtained on both the single grid configuration and the overlapping grids with however similar grid spacings ($\chi = 1$). The markers on the plots are not representative of the number of points of the solution.

of the Chimera method allows to predict results with the similar accuracy at however a much less computational cost since less grid points are necessary for the same grid spacing. This is confirmed in

Table 3.2: Results obtained with the Chimera cases when the patch is refined and the substrate resolution is fixed (equivalent to $N_{cells} = 100$), compared with their equivalent fine single mesh computations (EFSM).

χ	Chimera Average F	N_{cells} EFSM	Error (%) compared to EFSM	CPU time ratio	CPU memory ratio
1	203120	100	1.47 %	0.97	0.97
2	202204	200	0.24 %	2.3	2.41
4	202180	400	0.43 %	3.5	3.8

Table 3.2, where we report the ratios of the CPU times for the equivalent fine single grid to the CPU time of the corresponding Chimera configuration when χ varies. The ratios of the memory usage for the equivalent fine single grid to the memory usage of the corresponding Chimera configuration

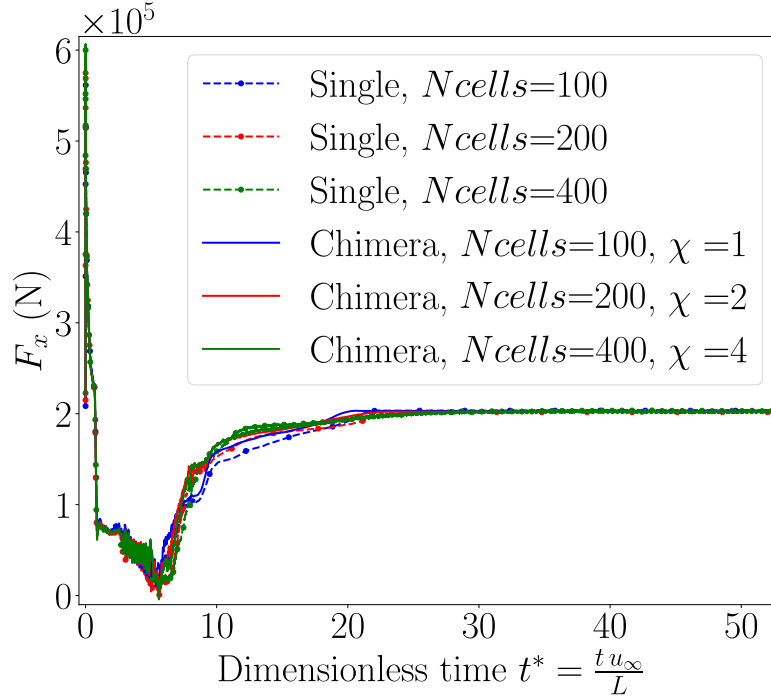


Figure 3.6: Resulting pressure force over time for the second study cases ($N_{cells} = 100$, $\chi = 1$), ($N_{cells} = 200$, $\chi = 2$) and ($N_{cells} = 400$, $\chi = 4$). The markers on the plots are not representative of the number of points of the numerical solution.

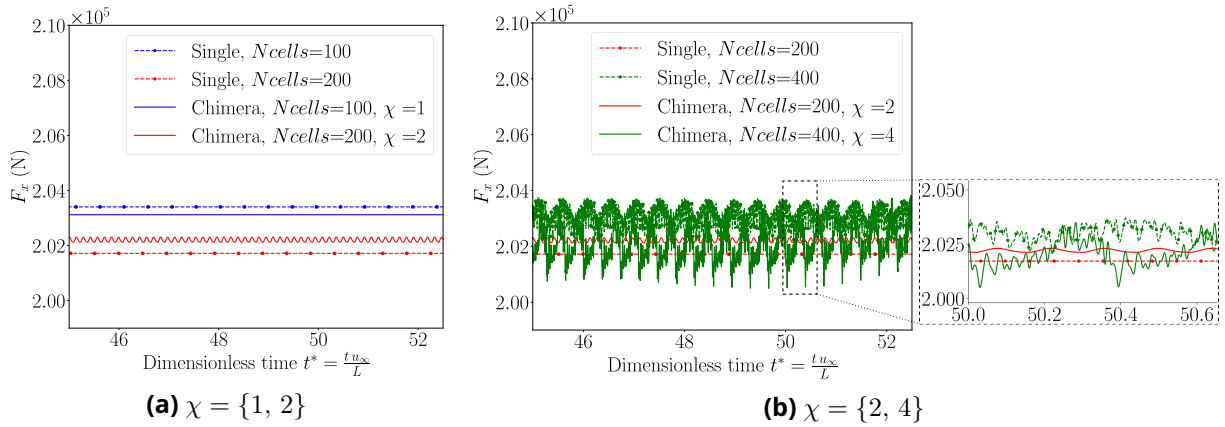


Figure 3.7: Resulting pressure force over time for the second study cases ($N_{cells} = 100$, $\chi = 1$), ($N_{cells} = 200$, $\chi = 2$) and ($N_{cells} = 400$, $\chi = 4$) zoomed in the time interval $[45, 52.5]$. The markers on the plots are not representative of the number of points of the numerical solution.

when χ varies are also reported. When $\chi = 1$, the CPU time ratio is less than 1 expressing that the Chimera method costs more than the single grid computation because of a higher number of grid cells, interpolation and transfer of ghost cell solutions. However, compared to single mesh computations with same grid resolutions, once we increase χ , equivalent results are obtained at a much lower cost, mainly coming from the gain in the number of cells since the time step is equivalent because the grid spacing is the same. Even though the present Chimera method is not intended for grid optimization, the method allows significant gains in time and memory without impacting the resulting solution.

3.1.3 - Shock standoff measurements

To have a better local insight in present results, we measure the detachment distance of the bow shock wave in front of the cylinder. A sketch of the flow structure in front of the cylinder is proposed in Figure 3.8, where the detachment distance (δ) of the bow shock wave is defined. An analytical measurement of the shock wave standoff distance has been proposed by Sinclair and Cui [159], which provides $\delta = 0.3649D$ at an upstream Mach number $M_\infty = 3$.

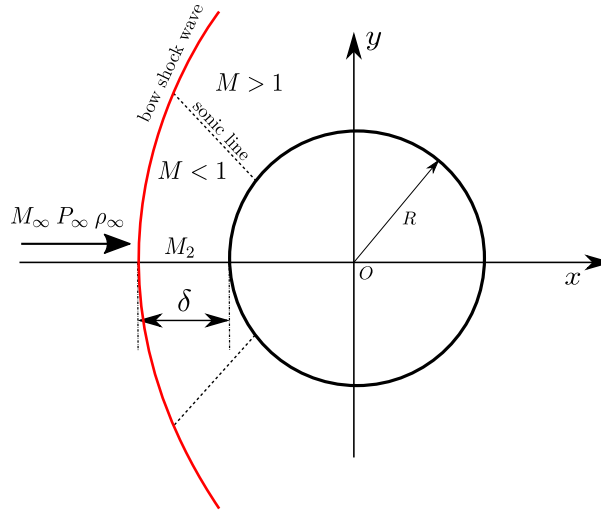


Figure 3.8: Geometric illustration of the flow structure in front of the cylinder.

From our results, we measured the detachment distance (δ) along the horizontal axis of symmetry ($y = 0$) as the first point encountered from infinity where the pressure rise exceeds 50 % of the theoretical pressure jump across the shock wave. Detachment values (δ) recorded on Chimera results are reported in Table 3.3. The left side of the table refers to overlapping grids with similar cell ratio ($\chi = 1$) while the right side relates on results obtained by increasing the cell ratio (χ) while maintaining the substrate resolution fixed and equivalent to $N_{cells} = 100$ resulting in the following Chimera configurations: ($N_{cells} = 100, \chi = 1$), ($N_{cells} = 200, \chi = 2$) and ($N_{cells} = 400, \chi = 4$).

Table 3.3: Detachment distance of the bow shock wave in front of the cylinder: overlapping grids with the proposed Chimera cases. On the left side, number of cells are increased keeping the cell ratio ($\chi = 1$) constant. On the right side, cell ratio (χ) is varied with a prescribed number of cells in the substrate model (equivalent to $N_{cells} = 100$).

Overlapping grids with $\chi = 1$, and N_{cells} is varied:			Substrate resolution fixed and χ is varied (patch refined):			
N_{cells}	δ/D	relative error E (%) w.r.t. analytical value	χ	N_{cells}	δ/D	relative error E (%) w.r.t. analytical value
50	0.433	18.66	1	100	0.428	17.29
100	0.428	17.29	2	200	0.395	8.25
200	0.398	9.07	4	400	0.372	1.95
400	0.372	1.95				

Numerical values of δ converge towards the analytical value $\delta = 0.3649$ [159] as grids are progressively refined with a discrepancy close to 2% of the analytical value obtained for the finest grid. It is important to underline that, compared to overlapping grids with equivalent cell ratio ($\chi = 1$), same δ values have been recorded by using a refined patch model keeping a rather coarse substrate grid at a much smaller computational cost which is promising for target applications.

3.2 - Interaction of a shock wave moving in air with a bubble

3.2.1 - Presentation of the case

In order to assess the Chimera method with two-component flow interfaces, we have numerically reproduced one of the emblematic experiments originally proposed by *Haas and Sturtevant* [75] and more recently conducted by *Layes et al.* [106], where a shock wave moving at a Mach number $M_a = 1.22$ in Air interacts with a cylindrical bubble initially filled of Helium or chlorodifluoromethane also known as R22. The interaction between the shock and the bubble is different depending on the bubble composition as Helium is less dense than air while R22 is denser resulting on different bubble deformation. The problem is modelled using the compressible version of the reduced five-equation two-component flow model proposed by *Allaire et al.* [2] presented in section 1.1.1.B. The initial configuration is depicted in Figure 3.9. The computational domain is defined as $(x \times y) \in$

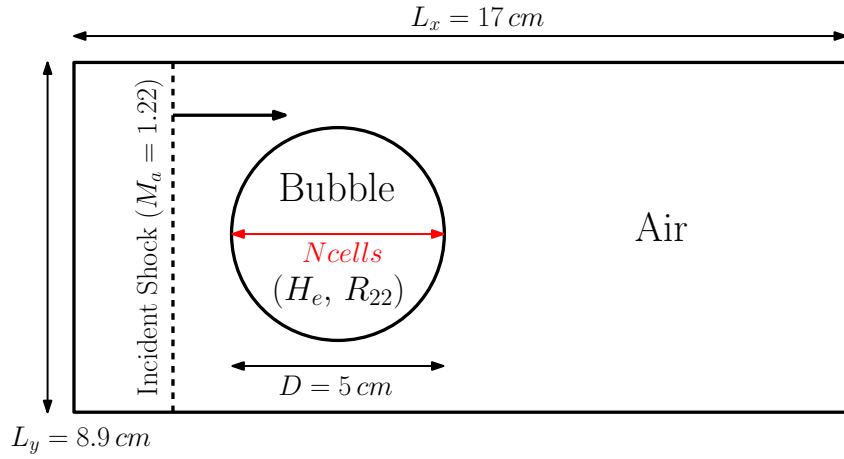


Figure 3.9: Shock wave / Bubble interaction: initial conditions taken from Layes *et al.* experiments [106] and computational domain.

$[0, 170 \times 10^{-3}] \times [-44.5 \times 10^{-3}, 44.5 \times 10^{-3}] \text{ m}^2$. The initial center of the bubble, having an initial diameter of $D = 50 \times 10^{-3} \text{ m}$, is located at $x_b = 52.5 \times 10^{-3} \text{ m}$, and $y_b = 0 \text{ m}$. The shock wave is initially positioned at $x_s = 10 \times 10^{-3} \text{ m}$ and moves to the right towards the bubble with a Mach number $M_a = 1.22$. Flow is then initialized by using the Rankine-Hugoniot relationships, and the corresponding initial conditions [28] on density, streamwise velocity, pressure, and heat capacity ratio are:

$$(\rho_0, u_0, p_0, \gamma) = \begin{cases} (1.66 \text{ kg.m}^{-3}, 114 \text{ m.s}^{-1}, 159080 \text{ Pa}, 1.4) & \text{in air, for } x \leq x_s, \\ (1.2062 \text{ kg.m}^{-3}, 0, 101325 \text{ Pa}, 1.4) & \text{in air, for } x > x_s, \\ (0.2204 \text{ kg.m}^{-3}, 0, 101325 \text{ Pa}, 1.6451) & \text{inside the He bubble,} \\ (3.5965 \text{ kg.m}^{-3}, 0, 101325 \text{ Pa}, 1.1847) & \text{inside the R22 bubble.} \end{cases} \quad (3.1)$$

Helium, R22 and air are all considered as perfect gases. Cartesian grids are employed in these simulations. The arrangements for the overlapping grids is presented in Figure 3.10. In the followings, meshes are dimensioned with the parameter N_{cells} that is the number of cells along the bubble diameter (D). The patch model is a $6 \times 10^{-3} \text{ m}$ side square grid, centered on the initial bubble location, and deliberately rotated at $\theta = 45^\circ$ (w.r.t. the horizontal axis) in order to stress the geometrical intersections of the Chimera exchange. Let us note that the single grid configuration is equivalent to the substrate model used in the Chimera case.

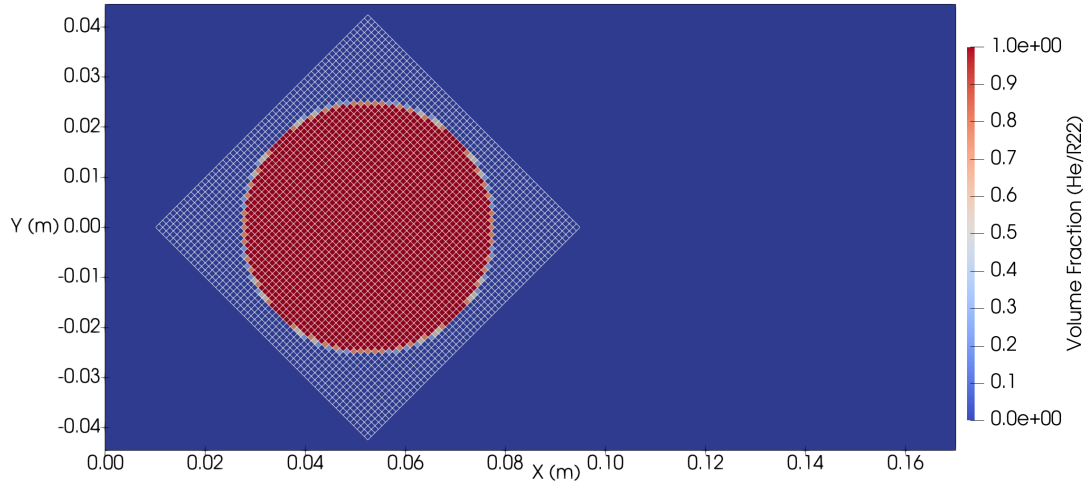


Figure 3.10: Bubble shock test case numerical configuration.

Simulations are performed on both the single grid configuration and the overlapping grid case, using a constant CFL number $CFL = 0.4$, over a dimensionless time of $t_f^* = t u_0/D = 1.6$, with $u_0 = 114 \text{ m.s}^{-1}$. Three grids are considered with respectively $N_{cells} = 50, 100$, and 200 .

3.2.2 - Helium bubble-shock wave interaction

When the shock wave interacts with the Helium bubble, the bubble is severely deformed and globally moves downstream as we can see in Figure 3.11 where the Helium volume fraction field is plotted at two dimensionless times $t^* = 0.24$, and $t^* = 1.6$ for the single grid configuration with $N_{cells} = 200$. As Helium is less dense than the surrounding Air, the bubble acts as a divergent acoustic lens explaining deformations. In fact, as the gradient of pressure induced by the shock wave is not always aligned with the gradient of density imposed by the Air/Helium interface, vorticity is locally produced by baroclinic effect explaining the deformation and the interface coiling. This

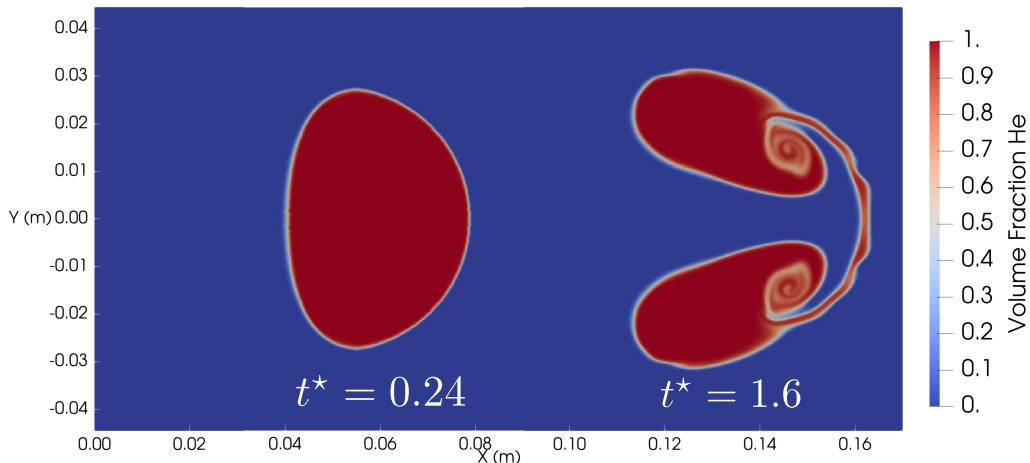


Figure 3.11: Helium volume fraction field obtained with a single grid configuration with $N_{cells} = 200$ at two different dimensionless times $t^* = 0.24$ and $t^* = 1.6$.

present single mesh solution using the finest grid ($N_{cells} = 200$) fits experimental results from [106]. This grid resolution allows the capture of anti-symmetrical vortices as well as oscillations of the interface on the bubble front. Although vortices are locally produced by baroclinic effect, perfectly anti-symmetrical vortices are produced since the integral of vorticity must stay to zero as no vorticity

is present at the initial state. The present single grid simulation allows to account for this physical aspect.

Regarding the Chimera configuration, let us notice that the bubble is only prescribed inside the patch grid and so, does not initially exist in the substrate model. As the patch grid is kept fixed, the bubble moves away from the patch to the substrate during simulations, and at the final time, the bubble is completely located on the right hand side of the substrate mesh and is no longer inside the patch. This allows us to study the robustness of the present Chimera method to deal with a moving two-component interface through the external patch boundary where the local grid spacing may change abruptly. That way, a particular attention will be devoted to examine the field of the Helium volume fraction over time.

In a first step, we keep the ratio $\chi = 1$ while grids in both the patch and the substrate models are refined using the three resolutions previously considered $N_{cells} = 50, 100,$ and 200 . The Helium volume fraction field is plotted, at a dimensionless time $t^* = 1.6$, for both the single grid configuration (see Fig. 3.12), and the overlapping grid configuration (see Fig. 3.13) with $\chi = 1$. Very good agreement is achieved by the present Chimera method on overlapping grids with the same cell ratio ($\chi = 1$), compared to the single grid configuration. The Chimera exchange does not alter the shape of the bubble nor induces sensible perturbations but provides a better description of the bubble curvature. This means that with the coarser grids ($N_{cells} = 50$ and 100), the Chimera impact is minimal and on the finest grid ($N_{cells} = 200$), it helps capturing the bubble front. We can conclude that the impact of the Chimera exchange on the two-component interface can help improving the solution with a better fitted grid when $\chi = 1$, fulfilling our requirements.

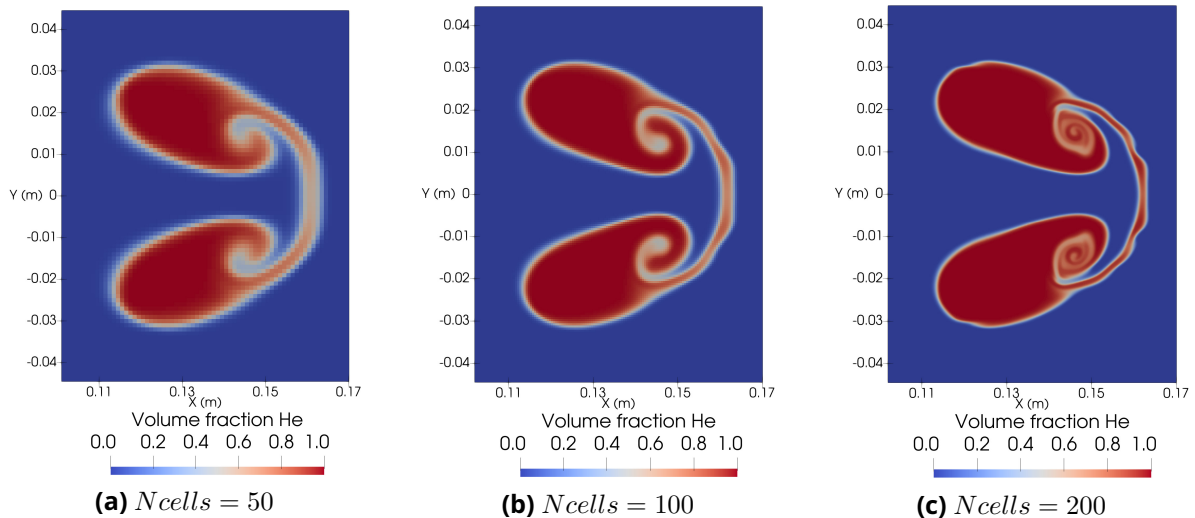


Figure 3.12: Helium volume fraction field obtained in the single mesh case at $t^* = 1.6$, for a number of cells along the bubble diameter of $N_{cells} = 50$ (on the left), 100 (in the middle), and 200 (on the right).

Secondly, we keep the number of grid cells (along the bubble diameter) $N_{cells} = 50$ constant in the substrate model and increase the ratio $\chi = 1, 2, 4,$ and 8 , which respectively correspond to an equivalent mesh refinement of $N_{cells} = 50, 100, 200,$ and 400 in the patch model. We plot results in Figure 3.14 obtained by using these refinements in the patch, at a dimensionless time $t^* = 1.6$, after the bubble has crossed the external patch boundary and is fully embedded in the substrate. By using cell ratios greater than 1, we can see that the solution has been improved compared to the single grid solution with the same resolution as the one used in the substrate ($N_{cells} = 50$). However, although the higher the cell ratio (χ) the better the quality of the final solution, the quality of the solution is mainly impacted by the resolution used in the substrate, and it is obviously impossible and

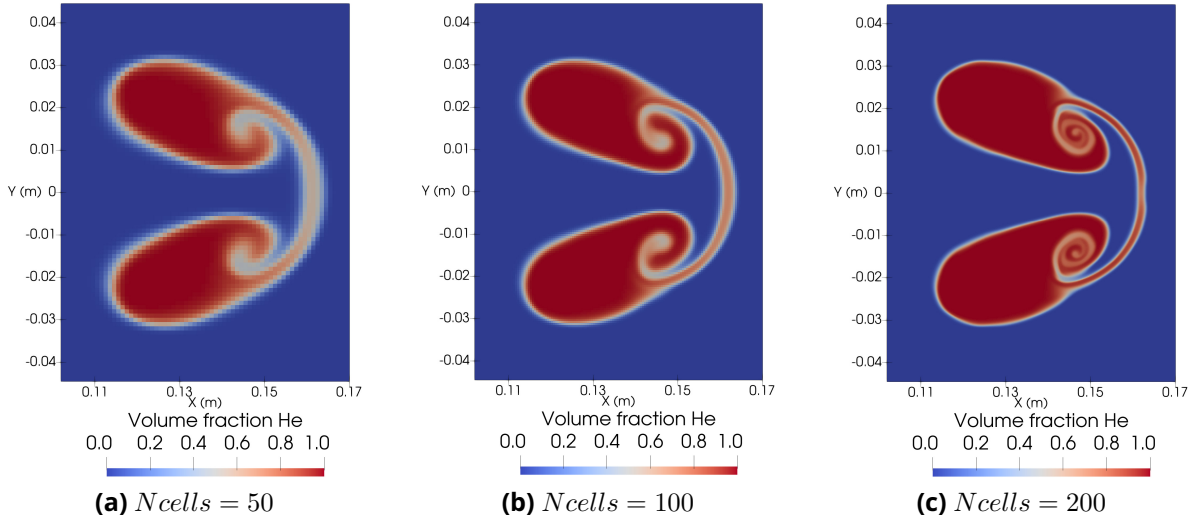


Figure 3.13: Helium volume fraction field obtained with the present Chimera method with overlapping grids with the same cell ratio ($\chi = 1$) at $t^* = 1.6$, for a number of cells along the bubble diameter of $N_{cells} = 50$ (on the left), 100 (in the middle), and 200 (on the right).

irrelevant to recover the quality obtained with the equivalent grid refinement. What it is important to note is that the use of high cell ratios does not introduce numerical artifact but on the contrary improves the quality thanks to the increased grid resolution in the patch. Unlike what Pärt-Enander and Sjögreen [133] observed, we show that refining a patch model in a overlapping grid strategy improves the quality of the solution without any discernable numerical damage on the solution.

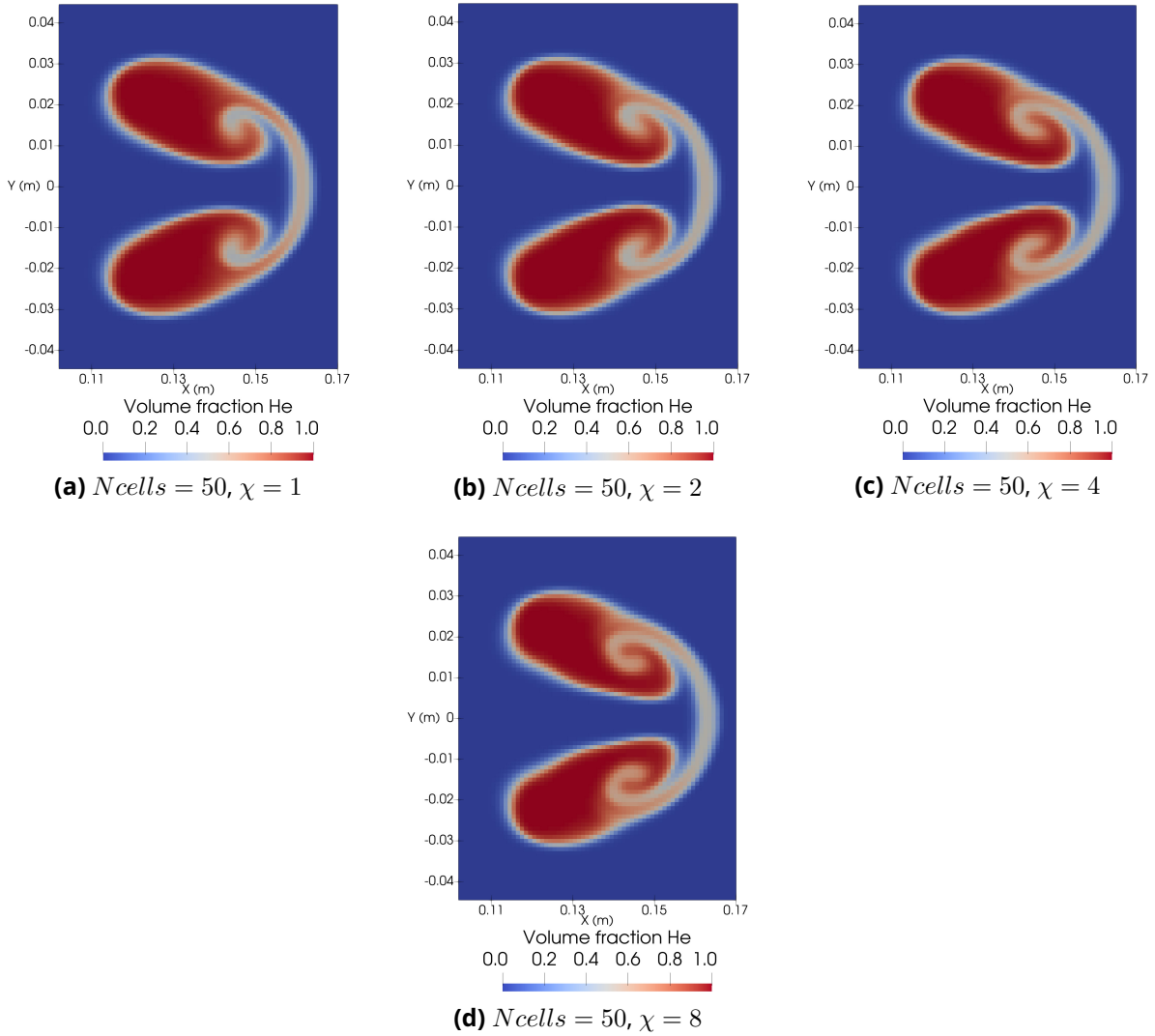


Figure 3.14: Helium volume fraction field obtained with the present Chimera approach, at a dimensionless time $t^* = 1.6$, by using several cell ratios ($\chi = 1, 2, 4, 8$).

3.2.3 - R22 bubble-shock wave interaction

Moving on to the R22 bubble, when the shock wave interacts with the R22 bubble, the latter is severely deformed and globally moves downstream as we can see in Figure 3.15 where the R22 volume fraction field is plotted at two dimensionless times $t^* = 0.23$, and $t^* = 2.28$ for the single grid configuration with $N_{cells} = 200$. As R22 is denser than the surrounding Air, the bubble acts as a convergent acoustic lens explaining deformations. Like the Helium bubble, the gradient of pressure induced by the shock is not always aligned with the gradient of density imposed by the Air/R22 interface. Unlike the Helium bubble, the upstream interface of the R22 bubble remains almost unaltered while the downstream interface presents a spike at the center of the downstream interface. This shape is due to a reverted vorticity field compared to the Helium bubble. This present single mesh solution using the finest grid ($N_{cells} = 200$) fits numerical results from [190]. This grid resolution allows the capture of anti-symmetrical vortices as well as oscillations of the interface on the bubble front.

Regarding the Chimera configuration, the patch grid is still kept fixed and the bubble moves away from the patch to the substrate during simulations, and at the final time, the bubble is completely located on the right hand side of the substrate mesh and is no longer inside the patch.

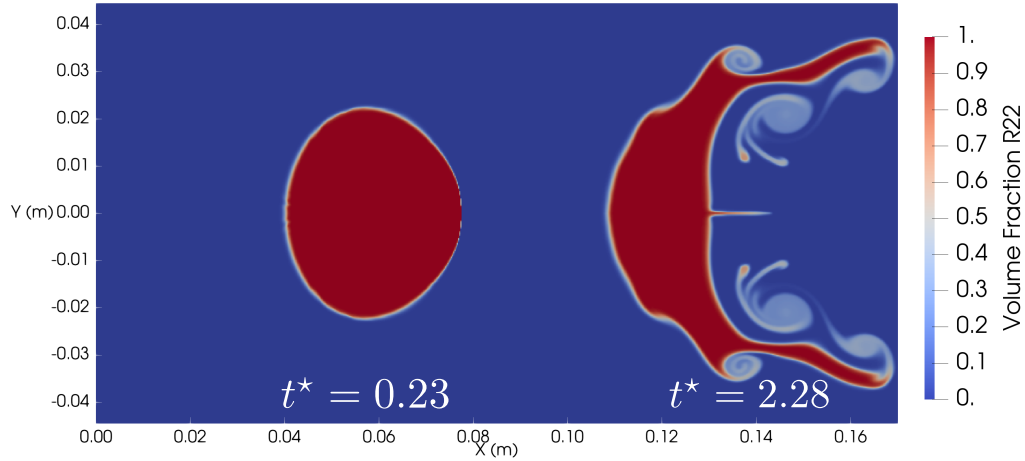


Figure 3.15: R22 volume fraction field obtained with a single grid configuration with $N_{cells} = 200$ at two different dimensionless times $t^* = 0.23$ and $t^* = 2.28$.

In a first step, we keep the ratio $\chi = 1$ while grids in both the patch and the substrate models are refined using the three resolutions previously considered $N_{cells} = 50, 100$, and 200 . The R22 volume fraction field is plotted, at a dimensionless time $t^* = 2.28$, for both the single grid configuration (see Fig. 3.16), and the overlapping grids (see Fig. 3.17) with $\chi = 1$. A good agreement is achieved by the present Chimera method on overlapping grids with the same cell ratio ($\chi = 1$), compared to the single grid configuration for $N_{cells} = 50$ and 100 . The Chimera exchange does not alter the shape of the bubble nor induces sensible perturbations but provides an equivalent description of the bubble curvature. On the finest grid however, the Chimera transfer seems to alter the vorticity field quite significantly with more described upstream bubble interface but generates a splitting of the bubble tails. However, symmetry is preserved and although vortices are locally produced by baroclinic effect, perfectly anti-symmetrical vortices are produced to preserve the integral of vorticity at zero.

With the coarser grids ($N_{cells} = 50$ and 100), the Chimera impact is minimal and on the finest grid ($N_{cells} = 200$), the different grid configuration associated to the Chimera transfer alter the shape of the bubble compared to the single grid solution as it induces additional vorticity.

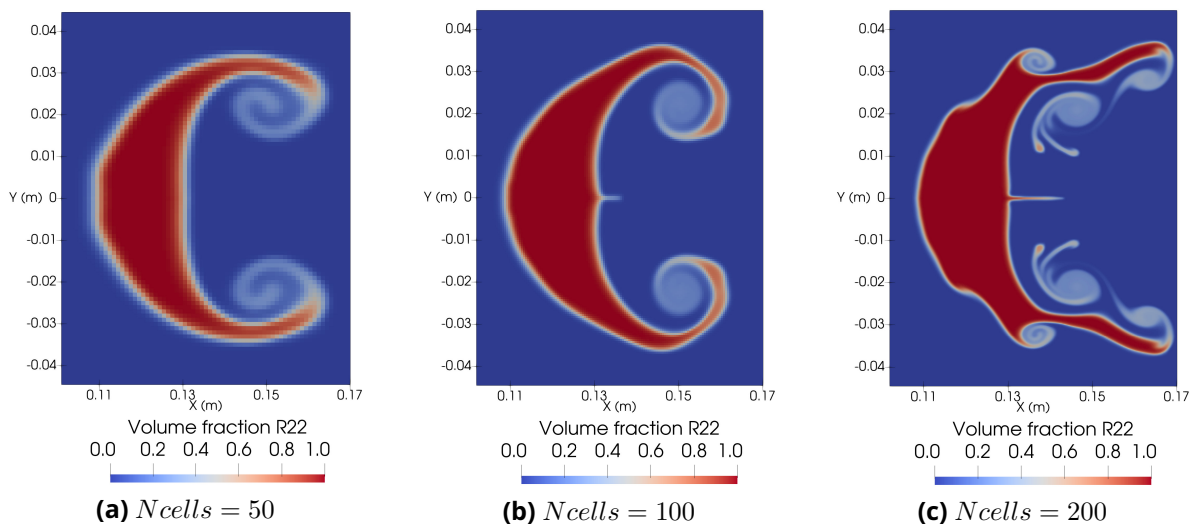


Figure 3.16: R22 volume fraction field obtained in the single mesh case at $t^* = 2.28$, for a number of cells along the bubble diameter of $N_{cells} = 50$ (on the left), 100 (in the middle), and 200 (on the right).

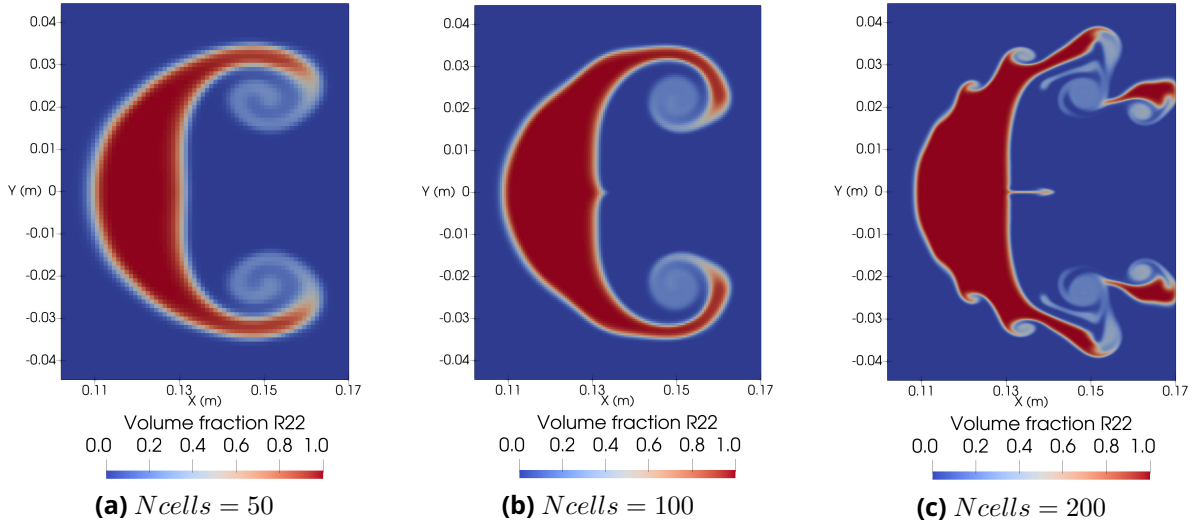


Figure 3.17: R22 volume fraction field obtained with the present Chimera method with overlapping grids with the same cell ratio ($\chi = 1$) at $t^* = 2.28$, for a number of cells along the bubble diameter of $N_{cells} = 50$ (on the left), 100 (in the middle), and 200 (on the right).

Secondly, we keep the number of grid cells (along the bubble diameter) $N_{cells} = 50$ constant in the substrate model and increase the ratio $\chi = 1, 2, 4$, and 8, which respectively corresponds to an equivalent mesh refinement of $N_{cells} = 50, 100, 200$, and 400 in the patch model. We plot results in Figure 3.18 obtained by using these refinements in the patch, at a dimensionless time $t^* = 2.28$ after the bubble has crossed the external patch boundary and is fully embedded in the substrate. By using cell ratio greater than 1, we can see that the solution has been improved regarding the complexity of the bubble shape compared to the single grid solution with the same resolution as the one used in the substrate ($N_{cells} = 50$). As for the Helium bubble, the quality of the solution is mainly impacted by the resolution used in the substrate, and it is obviously hard to recover the quality obtained with the equivalent grid refinement. Nonetheless, the spike of the downstream interface located along the x -axis is improved when using a refined patch.

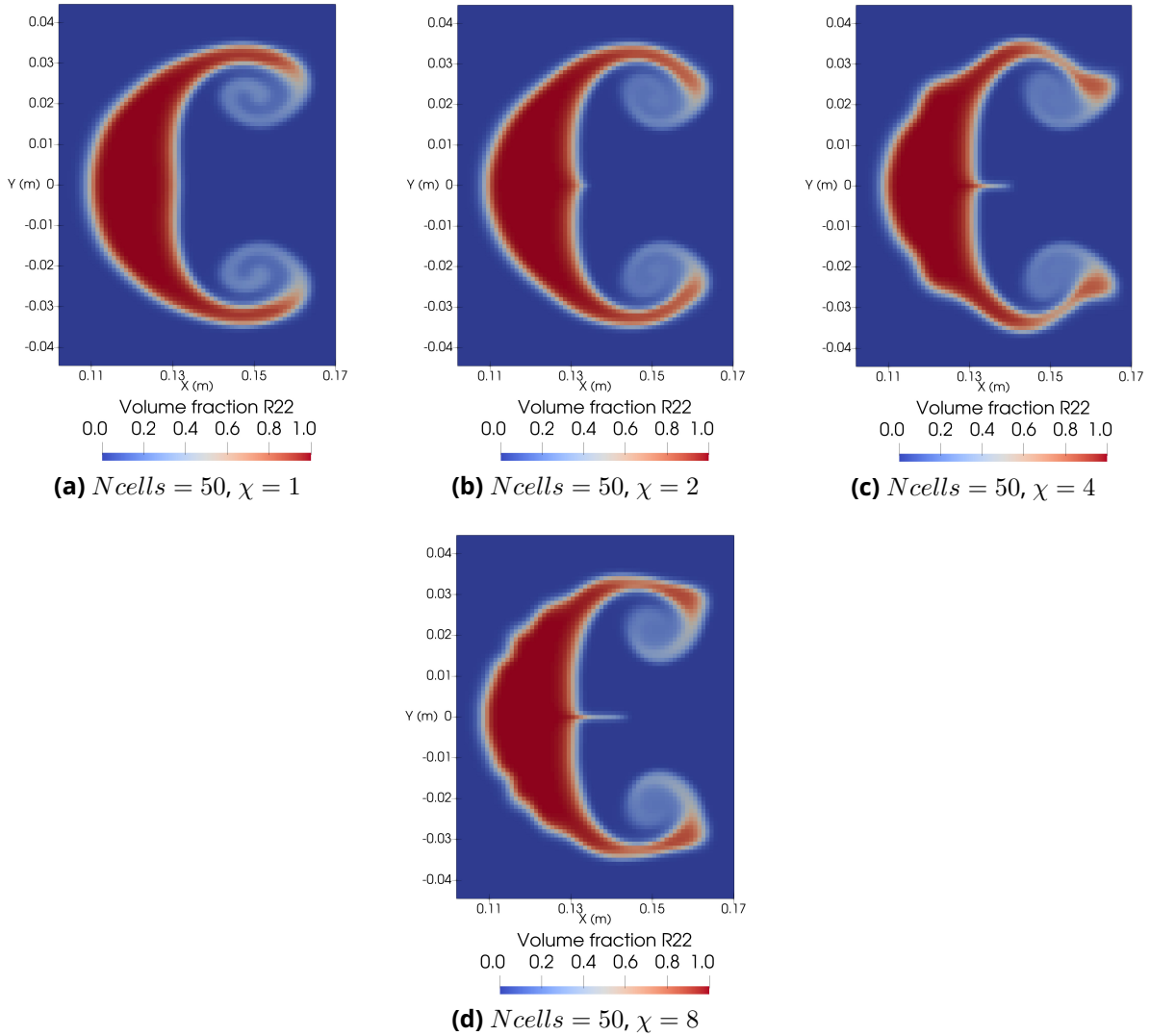


Figure 3.18: R22 volume fraction field obtained with the present Chimera approach, at a dimensionless time $t^* = 2.28$, by using several cell ratios ($\chi = 1, 2, 4, 8$).

3.2.4 - Summary of the findings on the behavior of the Chimera method with multicomponent flows

The shock wave interaction with an Helium/R22 bubble test case allowed us to assess the behavior of the Chimera method when a multicomponent interface crosses the Chimera exchange zone. The Helium bubble configuration has shown, that the Chimera method does not impact the solution when $\chi = 1$ and even allows to use finer patches in order to improve the accuracy of the overall solution. The R22 bubble case has shown that the impact of the Chimera exchange on the two-component interface is minimal with coarse and medium grid but can induce additional vorticity on sensitive cases with fine grids. Using finer patches does not notably alter the global solution while capturing local key features of the flow like a spike.

3.3 - Double Mach Reflection problem

3.3.1 - Presentation of the case

The last problem concerns the emblematic test case of the Double Mach Reflection (DMR) originally proposed by Woodward and Colella [134] as a benchmark for assessing Euler codes that contains vortical flows. The problem consists in a front shock wave that hits a 30 degree inclined ramp. Going up the ramp, a self similar structure with two triple points develops. A sketch of the flow structure is displayed in Figure 3.19. More detailed explanations of the flow structure can be found in [134, 179]. It is a difficult test case, involving both strong shocks and multiple stems. This case is thus relevant to assess the present Chimera method to deal with complex transient flow structures where multiple shock waves and their interactions creating slip lines occur over time (see Fig. 3.19). The idea here is to check the ability of the present method to account for multiple discontinuities and their interactions to pass through the external patch boundary where a drastic change of grid spacings can occur.

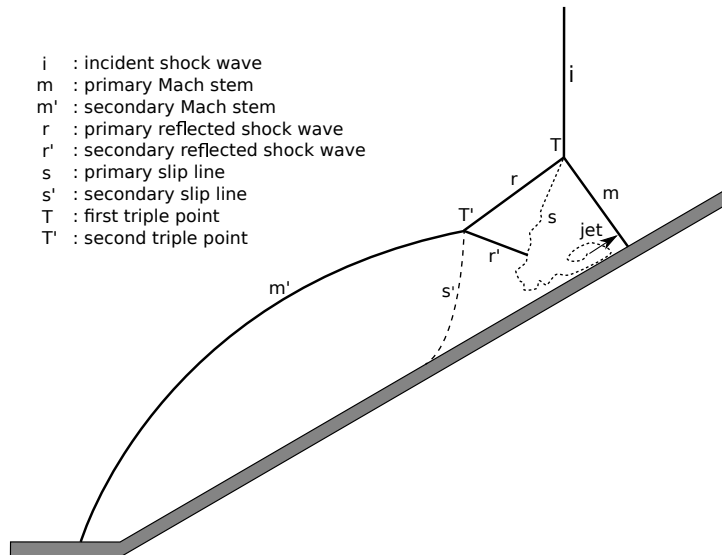


Figure 3.19: Sketch of the self-similar structure of the Double Mach Reflexion (DMR) problem

The numerical configuration of the single mesh case is shown in Figure 3.20a, where the 30° ramp starts at $x_i = 1/6$ m with an overall computational domain length $L_x = 4$ m, and height $L_y = 1$ m. The number of cells in the single mesh configuration is parametrized by N_{cells} which is the number of cells in the height of the domain. Let us say that the single grid case uses $4N_{cells} \times N_{cells}$ grid points in the $(x \times y)$ directions. The shock wave is initially located at $x_s = 1/10$ m. Initial conditions are defined with a driven shock wave moving at a high mach number $M_S = 10$ in Air ($\gamma = 1.4$) initially at rest. Thanks to the Rankine-Hugoniot relationships, initial conditions on primitive variables are:

$$\begin{cases} (\rho, u, v, p)_0 = (1.4 \text{ kg.m}^{-3}, 0, 0, 1 \text{ Pa}), \\ (\rho, u, v, p)_1 = (8 \text{ kg.m}^{-3}, 8.25 \text{ m.s}^{-1}, 0, 116.5 \text{ Pa}). \end{cases} \quad (3.2)$$

As we know in such configuration, the driven shock wave (i, in Fig. 3.19) reflects on the wall of the ramp leading to a diffracted bow shock wave (m') that stays ahead of the ramp. This interaction also creates several Mach stems (m, m') with reflected shock waves (r, r'), triple points (T, T') and subsequent slip lines (s, s'). Issued from the contact discontinuity flow (s), a jet forms along the wall, which is also very difficult to properly predict.

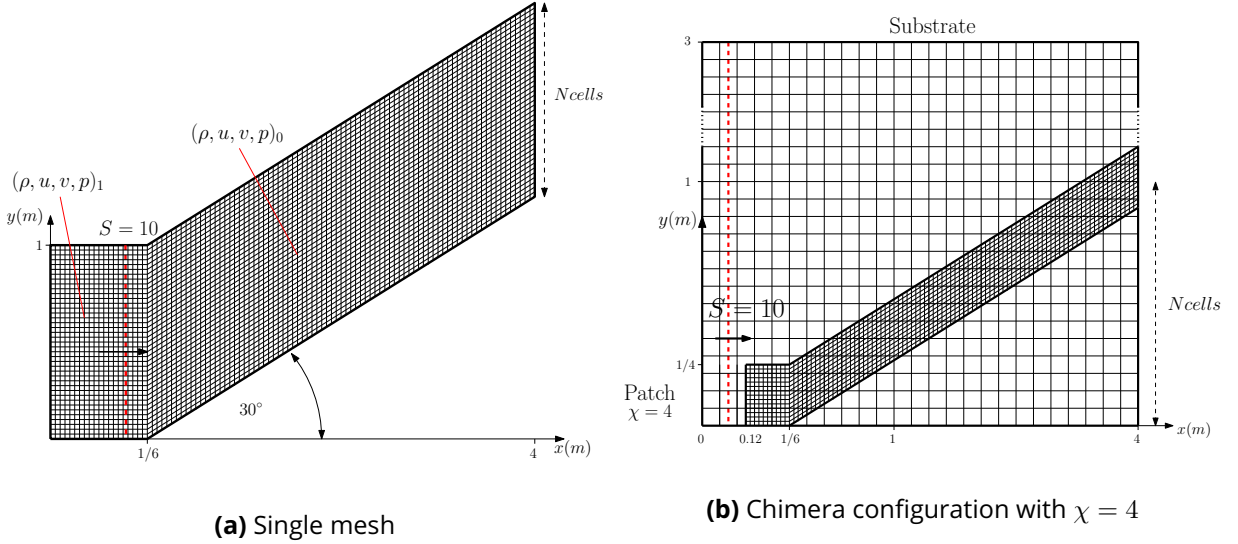


Figure 3.20: Computational domains and initial conditions: configurations of the single mesh case (a), and the Chimera case (b) displayed with a cell ratio $\chi = 4$.

Regarding the Chimera configuration as shown in the Figure 3.20b, the substrate is a standard Cartesian H-grid ($L_x = 4$ m long and $L_y = 3$ m high) configured with the parameter N_{cells} in order to respect the same grid resolution as the single mesh case. Let us notice that the substrate comprises N_{cells} grid points over 1 meter. The patch uses the same geometry as the one of the single grid configuration, that is however positioned so that the bottom surface coincides with that of the substrate. The patch model can be refined using the parameter χ measuring the cell ratio between grid spacings from the substrate and the patch models. As we can see in Figure 3.20b, the driven shock wave is initially located ahead of the patch grid, unlike the original test case of [134]. The dimension of the patch is then chosen so as to allow multiple strong shock waves and the related triple points and slip lines to pass through the external boundary of the patch to study the robustness of the present Chimera method when grid spacings abruptly change. Therefore, the patch extends from $x = 0.12$ m to the end of the substrate, and is $1/4$ m high. This grid configuration has been chosen in order to assess the impact of the proposed Chimera method on flow structures generated inside the patch that cross the overlapping grid interface. The single mesh configuration has then been adapted to be as close as possible to the Chimera configuration.

Simulations are performed on the overlapping grid configuration as well as the single mesh case to allow validation. The Chimera configurations are based on the second order Chimera exchange with the standard detection procedure. The CFL number is constant and equal to 0.4. At first, we keep the cell ratio between the patch and the substrate at $\chi = 1$ and use $N_{cells} = 160$ grid points over 1 meter. We consider the initial time $t_0^* \approx 8.081 \cdot 10^{-3}$ which is the dimensionless time needed for the shock to go from $x_s = 0.1$ m to $x = 1/6$ m. Results obtained at the dimensionless time $t^* - t_0^* = 0.2$ are plotted in Figure 3.21 where the Chimera case (black iso-contour lines) is compared to the single grid configuration (red iso-contour lines). The patch boundary is materialized with the dashed white line.

3.3.2 - Comparison of the Chimera case with the single grid case ($\chi = 1$)

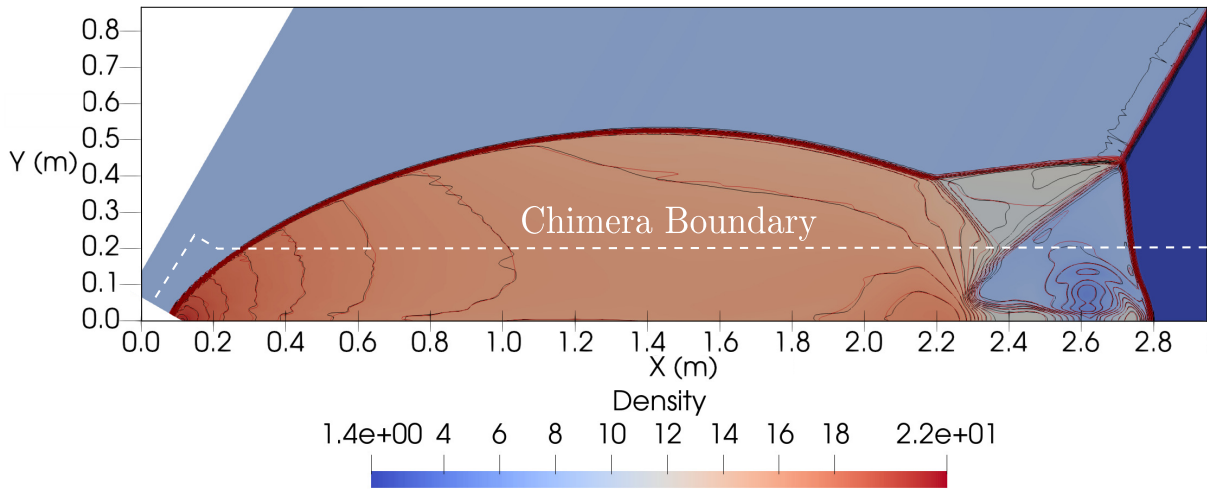


Figure 3.21: Density contours obtained with the present Chimera approach (black iso-contour lines) with the standard detection compared to the single mesh case (red iso-contour lines) at an equivalent dimensionless time $t^* - t_0^* = 0.2$ for $N_{cells} = 160$ and $\chi = 1$. 30 density contours from $\rho = 1.4$ to 21.4. Dashed white line materializes the patch boundary.

Compared to the single grid configuration, a very good agreement is achieved by the present Chimera method since Mach stems, reflected shock waves as well as slip lines are coincident. The jet located at the end of the ramp is also similarly described with the Chimera method since it is always located inside the patch. These results can also be compared to results from Stone *et al.* [167] (Fig. 16) obtained using a second order accurate scheme in both time and space, that can be taken as reference solutions. Concerning the Chimera case, few oscillations can be observed in the substrate part that may result from solution transfers between overlapping grids that might interfere with acoustic waves.

3.3.3 - Comparison of the Chimera case with the equivalent fine single mesh (EFSM) for various values of χ

Secondly, we check the influence of the cell ratio parameter (χ) as well as the detection procedure. The number of grid cells in the substrate is kept constant and equal to $N_{cells} = 80$ cells over 1 meter. The cell ratio is varied using four values $\chi = 2, 4, 8$ and 16 which correspond to an equivalent single mesh resolution respectively using $N_{cells} = 160, 320, 640$ and 1280 grid cells over 1 meter. Results on the density contours (black iso-contour lines) obtained with the present Chimera method with the standard detection procedure and the extended detection procedure are presented in Figure 3.22 for $\chi = 2$, Figure 3.23 for $\chi = 4$, Figure 3.24 for $\chi = 8$, and Figure 3.25 for $\chi = 16$ compared to their equivalent fine single grid solution (red iso-contour lines) obtained with respectively $N_{cells} = 160, 320$ and 640. The Chimera case with $\chi = 16$ is compared to the single grid case with $N_{cells} = 640$ which already gives a good representation of the numerical solution.

At moderate cell ratio values ($\chi = 2, 4$), the overall comparison is very good, although oscillations present inside the substrate are slightly accentuated when the refinement increases but these oscillations do not seem to interfere with what occurs in the patch. In contrast, flow patterns inside the patch are better predicted as the cell ratio has been increased, mainly the jet that forms at the end of the ramps that has an equivalent description to the equivalent fine single mesh solution. The jet is better depicted with the extended procedure than the standard detection. However, when increasing

the ratio to higher values like $\chi = 8$ (see Fig. 3.24) and $\chi = 16$ (see Fig. 3.25), the abrupt change in grid spacing at the external boundary of the patch induces perturbations. As shear layers are likely to develop instabilities, oscillations are mainly visible in the slip line that also alter the jet flow structure. Nonetheless, the extended detection procedure tends to limit these oscillations maintaining a certain level of quality of the solution.

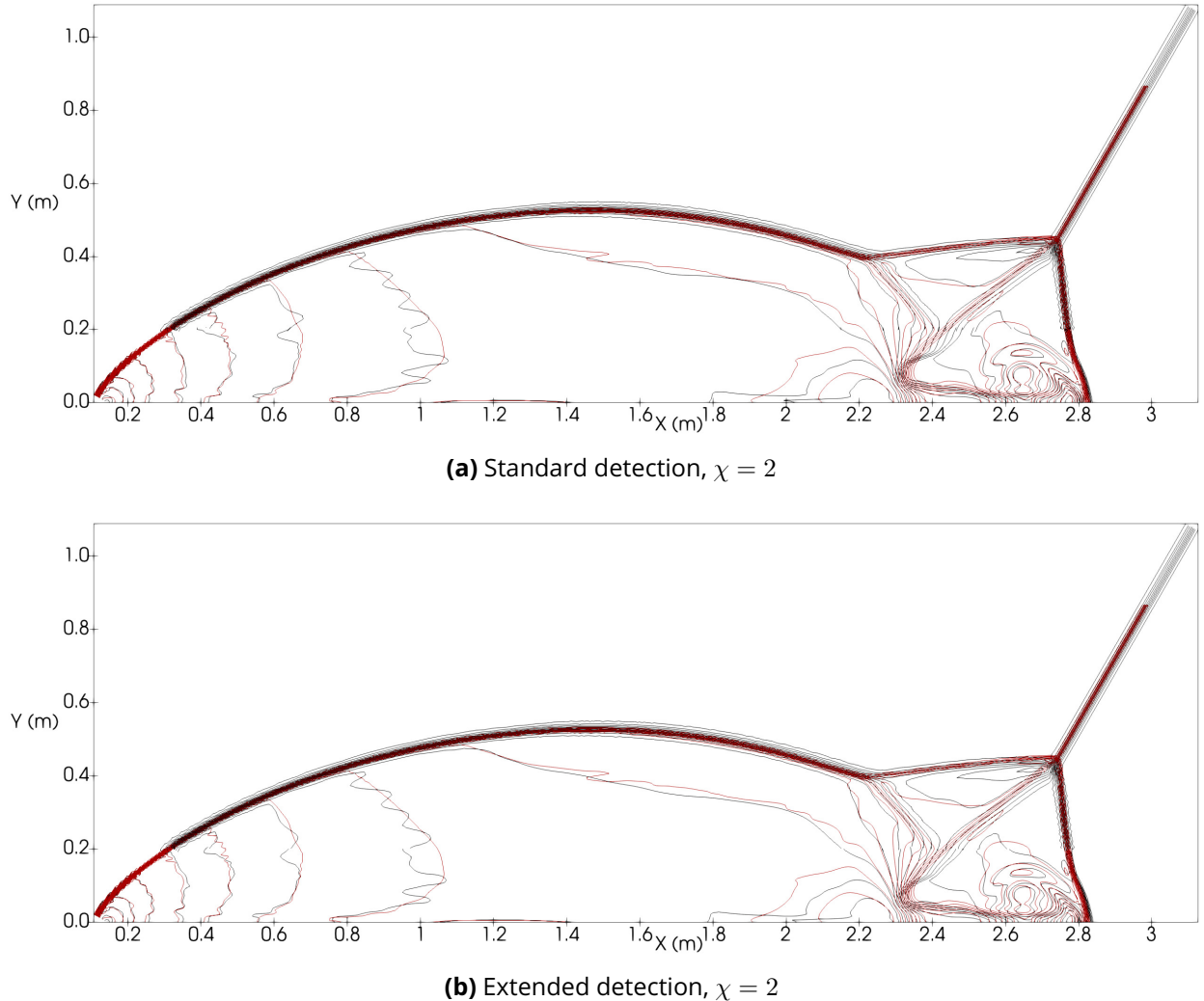


Figure 3.22: Density contours obtained with the present Chimera approach (black iso-contour lines) by using $N_{cells} = 80$ cells on the substrate and a cell ratio $\chi = 2$ on the patch, compared to the single mesh case (red iso-contour lines) with $N_{cells} = 160$, at an equivalent dimensionless time $t^* - t_0^* = 0.2$. 30 density contours from $\rho = 1.4$ to 21.4. Standard detection procedure (a) compared to the extended detection procedure (b).

In Table 3.4, we report the ratios of the CPU times for the equivalent fine single grid to the CPU time of the corresponding Chimera configuration when χ varies. The ratios of the memory usage for the equivalent fine single grid to the memory usage of the corresponding Chimera configuration when χ varies are also reported. When $\chi = 1$, the CPU time ratio is lower than 1 expressing that the Chimera method costs more compared to the single grid approach because of a higher number of grid cells, interpolation procedures and the transfer of ghost cell solutions. However, once we increase χ , equivalent results are obtained at a much lower cost compared to single mesh computations with equivalent grid resolutions. These gains mainly come from the smaller number of cells for the Chimera configuration since the time step is equivalent between the fine single grid and the Chimera case with a fine patch.

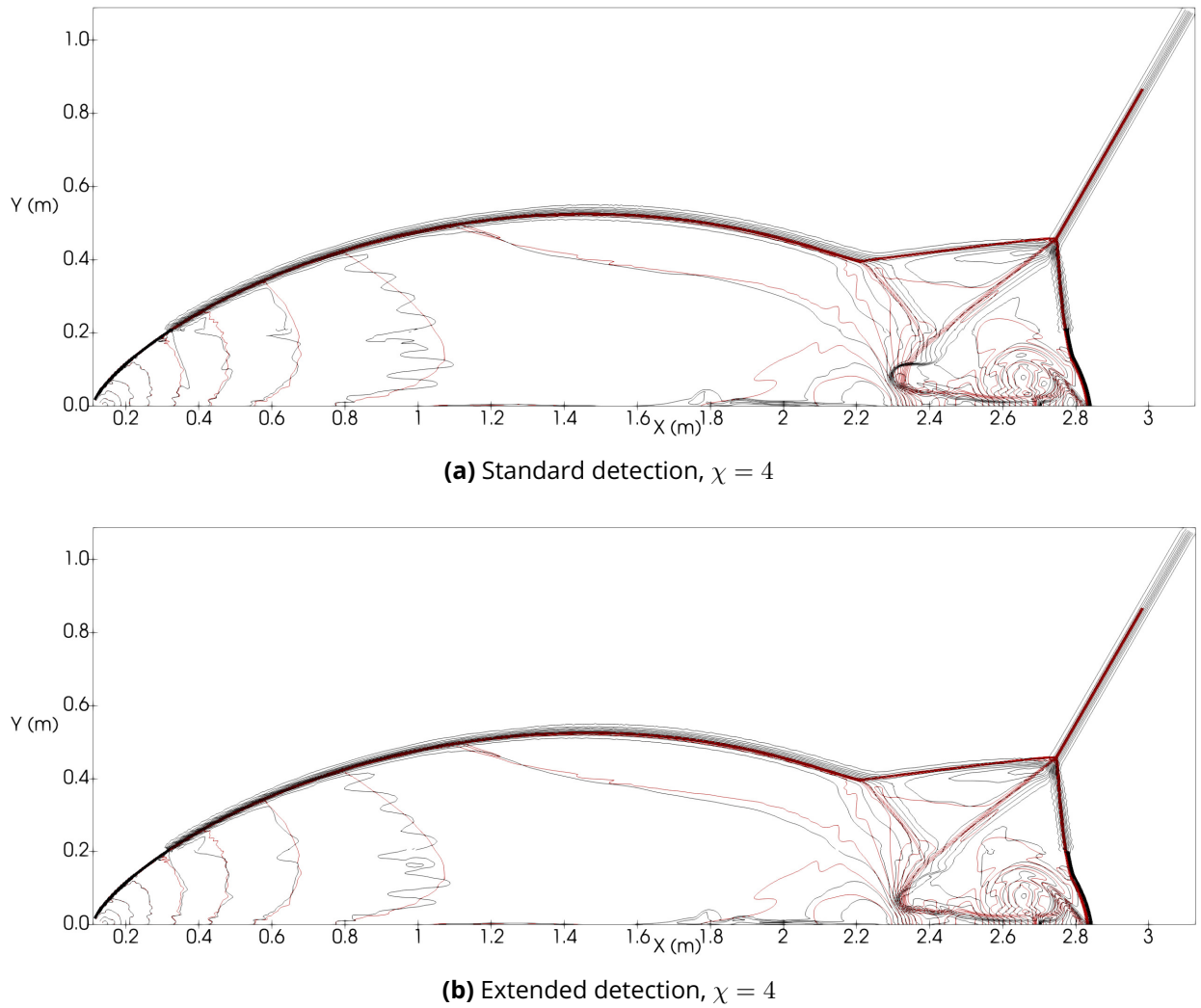
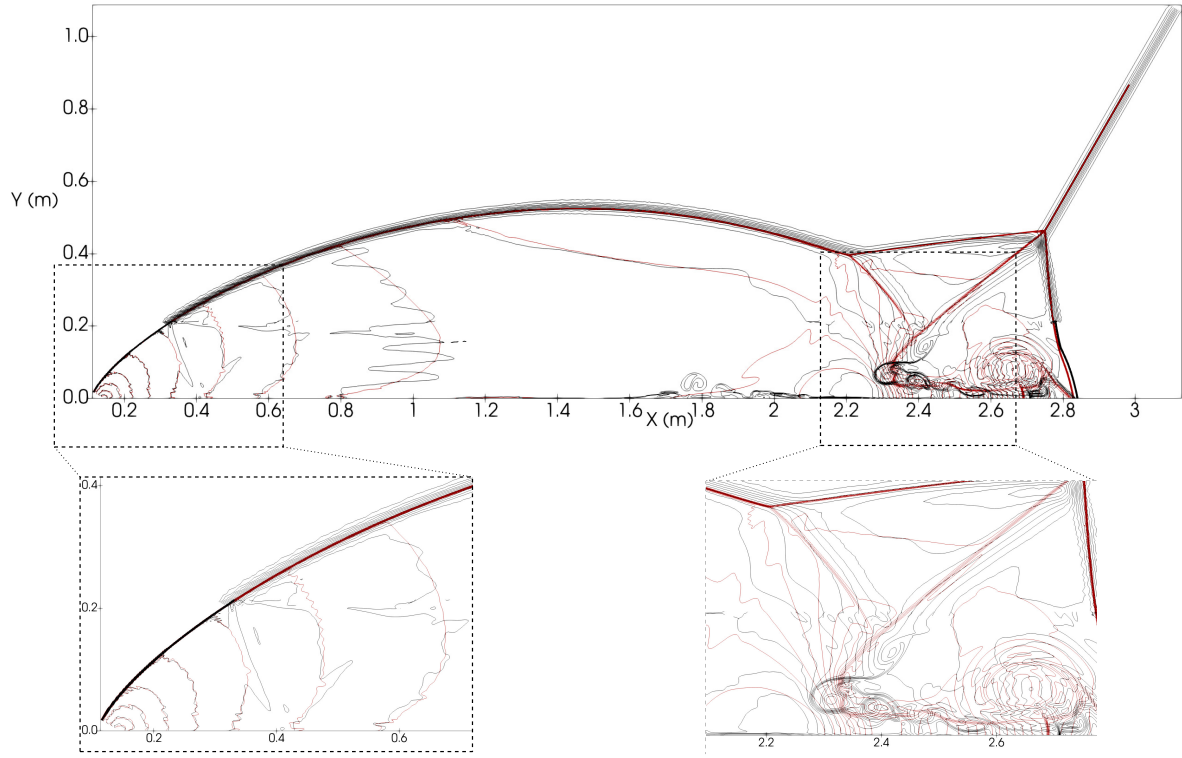
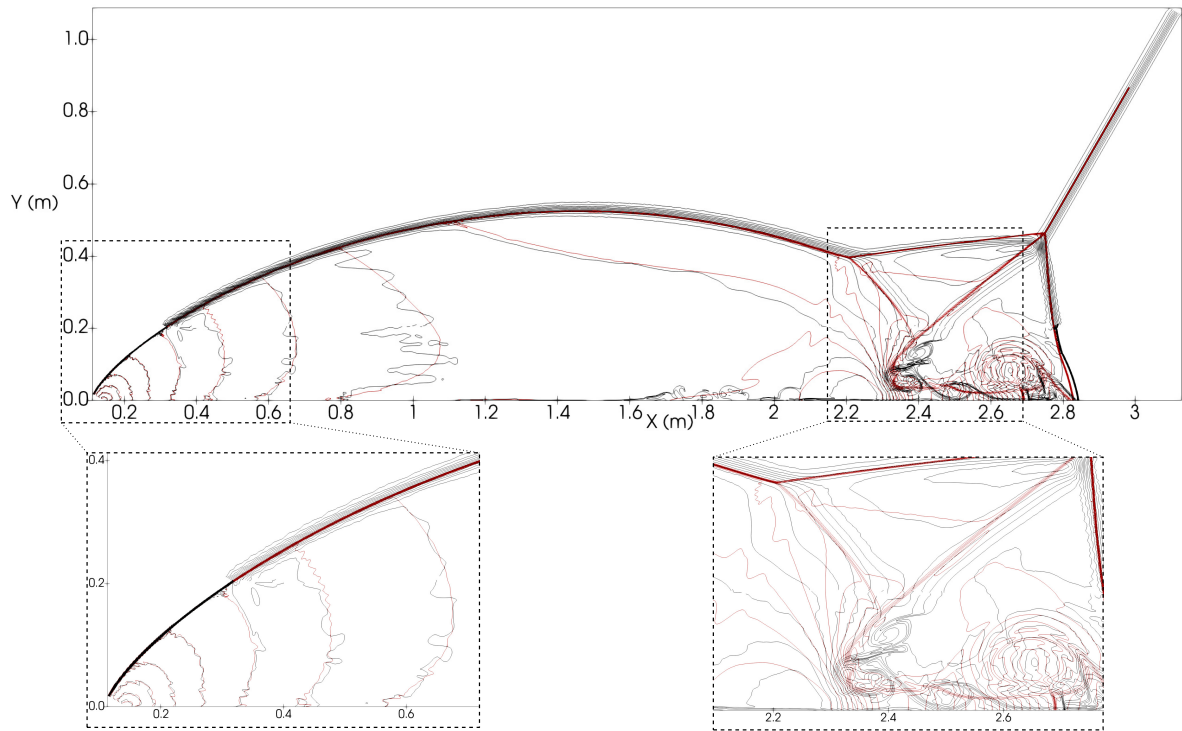


Figure 3.23: Density contours obtained with the present Chimera approach (black iso-contour lines) by using $N_{cells} = 80$ cells on the substrate and a cell ratio $\chi = 4$ on the patch, compared to the single mesh case (red iso-contour lines) with $N_{cells} = 320$, at an equivalent dimensionless time $t^* - t_0^* = 0.2$. 30 density contours from $\rho = 1.4$ to 21.4. Standard detection procedure (a) compared to the extended detection procedure (b).

Even though the present Chimera method is not intended to grid optimization, the method allows significant gains in time and memory without impacting the resulting solution. When the cell ratio is lower than 4, the gains in quality of the solution are worth the cost in CPU time as it remains negligible compared to the equivalent single grid cost. Nevertheless, when strong waves pass through the patch/substrate interface some numerical artifacts can be recorded when the value of the cell ratio (χ) is greater than 4 which imposes an abrupt grid spacing change.



(a) Standard detection, $\chi = 8$



(b) Extended detection, $\chi = 8$

Figure 3.24: Density contours obtained with the present Chimera approach (black iso-contour lines) by using $N_{cells} = 80$ cells on the substrate and a cell ratio $\chi = 8$ on the patch, compared to the single mesh case (red iso-contour lines) with $N_{cells} = 640$, at an equivalent dimensionless time $t^* - t_0^* = 0.2$. 30 density contours from $\rho = 1.4$ to 21.4. Standard detection procedure (a) compared to the extended detection procedure (b).

3.3. DOUBLE MACH REFLECTION PROBLEM

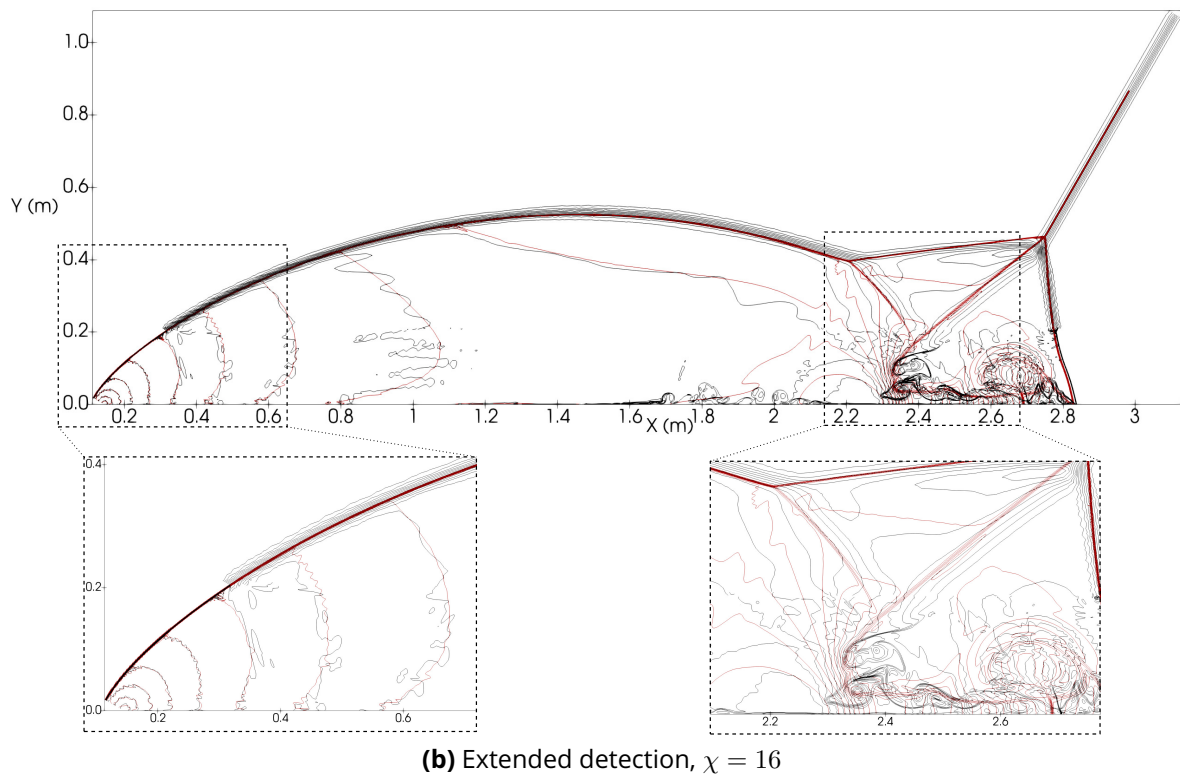
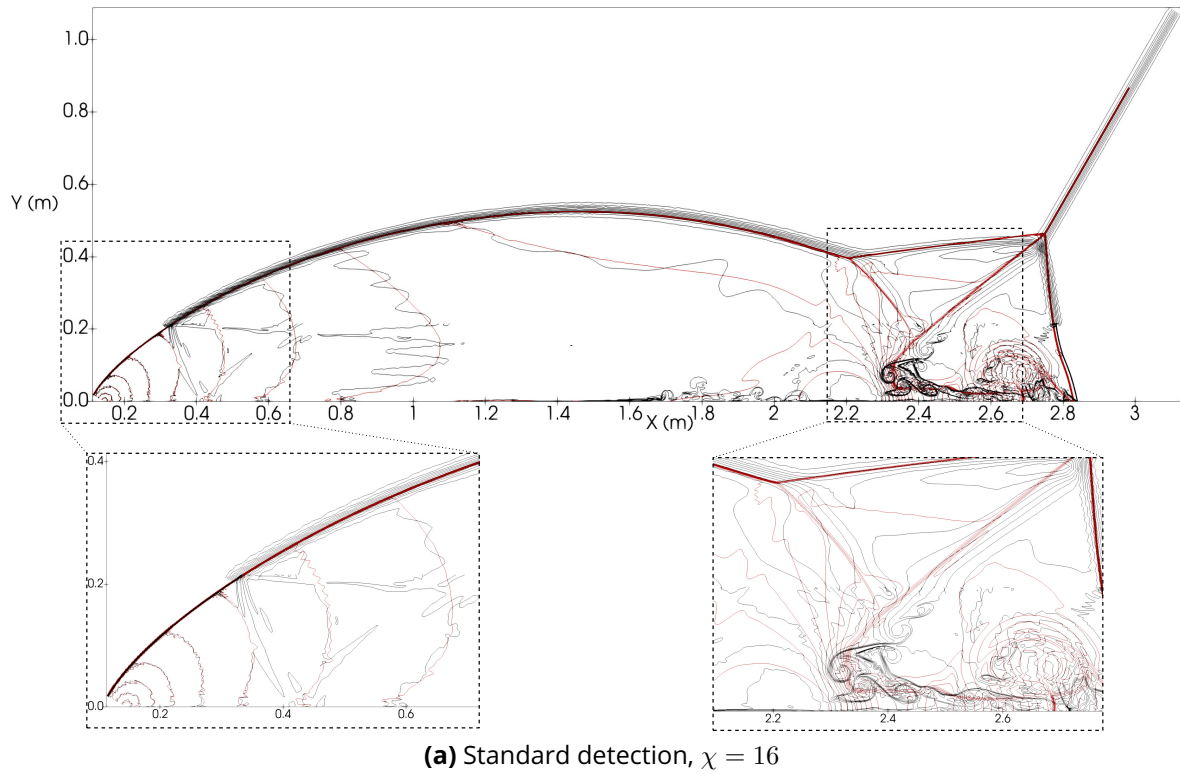


Figure 3.25: Density contours obtained with the present Chimera approach (black iso-contour lines) by using $N_{cells} = 80$ cells on the substrate and a cell ratio $\chi = 16$ on the patch, compared to the single mesh case (red iso-contour lines) with $N_{cells} = 640$, at an equivalent dimensionless time $t^* - t_0^* = 0.2$. 30 density contours from $\rho = 1.4$ to 21.4. Standard detection procedure (a) compared to the extended detection procedure (b).

Table 3.4: Results obtained with the Chimera cases ($N_{cells} = 80$) for different values of χ , compared with their equivalent fine single mesh (EFSM) computations.

χ	Equivalent N_{cells} on the patch (for EFSM comparison)	CPU Time Ratio		Memory Ratio
		Extended detection	Standard detection	
1	80	0.45	-	0.43
2	160	1.15	1.13	1.30
4	320	2.51	2.49	2.67
8	640	3.38	3.20	3.62

3.4 - Chapter conclusion

In this chapter, the second order Chimera method with the standard detection procedure has been assessed on reference two-dimensional test cases.

A supersonic flow around a circular cylinder has shown that the proposed Chimera method allows inclusion of a geometrical detail inside a global calculation. The Chimera method favorably affects the final results compared to the single mesh case as it uses local grids more adapted to the solution. Also, equivalent results are obtained at a much lower computational cost when high cell ratios in the patch are employed because of the gain realized on the number of cells.

The interaction of a shock wave with an Helium/R22 bubble has demonstrated the ability of the proposed Chimera method to account for multi-component flows where a shock wave interacts with a two-fluid interface. We demonstrated that refining patch cells in an overlapping grid strategy improves the quality of the solution without any discernable numerical damage on the solution on the coarsest grids. When the flow involves a more sensitive vorticity field, the impact of the Chimera method is visible but the method is still able to capture key details of the flow.

The Double Mach Reflection, showed that the proposed Chimera method, with reasonable cell ratios ($\chi \leq 4$), improves the quality of the solution compared to a single grid computation, with useful gains in the CPU time and memory usage. Last but not least, the extended detection procedure has shown to be able to smooth oscillations caused by high cell ratios when the triple point and the diffracted bow shock wave cross the Chimera interface, without a major impact on CPU time.

The validation of the method has been made on reference two-dimensional cases but the grid intersections are already 3D compatible for industrial applications. Until now, we only studied the ability of the present Chimera method to deal with fast transient dynamics with wave propagations in compressible flows as well as contact discontinuities usually present in multi-component flows. However, interactions of moving strong discontinuities with flexible structures often occur in accidental configurations involving explosions. Therefore, if one wants to include geometrical details that could influence the Fluid-Structure Interaction (FSI), we must extent the Chimera method to deal with moving deformable structures which is the objective of the next chapter.

4 - An overlapping grid embedded boundary method for compressible flows coupled to deformable thin structures: the Chimera Mediating Body Method

Contents

4.1	Governing equations and discretization of the problem	110
4.1.1	Structural system of equations	110
4.1.2	Coupling conditions	110
4.1.3	Structure discretization : the finite element method	111
4.1.4	Explicit time integration of the structure	111
4.2	Discretization of the coupling conditions: the Chimera-MBM	112
4.2.1	Presentation of the Mediating Body Method	112
4.2.2	Coupling of the Mediating Body Method with the Chimera method: the Chimera-MBM	121
4.3	Numerical validation of the method and applications	134
4.3.1	One-dimensional free piston	134
4.3.2	Three-dimensional separated chambers with a perforated plate	154
4.4	Chapter conclusion	166

In the previous chapter, we showed strong capabilities of the Chimera method to transfer information over two separated domains. In large scale transient computations, one must take into account local interactions between the fluid and structural components. In the case of accidental situations, deformable structural parts can undergo large displacements at the local scale generated by local scale flow phenomena. In this context, having an overlapping grid method like the developed Chimera method compatible with immersed boundary methods like the Mediating Body Method [92] can help composing a large scale model with local additions of structural parts and adapted local grids. In this chapter, we extend the presented Chimera method in order to work with the Mediating Body Method presented in [92]. The resulting method is referred as Chimera-Mediating Body Method (Chimera-MBM) and is assessed using one-dimensional and three-dimensional test cases.

4.1 - Governing equations, discretization and integration of the problem

As the hypothesis on the flow in the fluid-structure interaction framework remain the same as in the fluid only problems, the equation model for the fluid has been given in chapter 1. The same notations are kept in the following.

4.1.1 - Structural system of equations

We consider an isentropic thin wall structure of a thickness h that is immersed in a fluid \mathcal{T} . The structure occupies a moving open set $\mathcal{T}_s \subset \mathcal{T}$. The evolution of the structure is given by the following equilibrium equation, written in local form:

$$\rho_s \frac{D\dot{\underline{\mathbf{u}}}}{Dt} + \nabla \cdot \underline{\underline{\underline{\underline{\sigma}}}} = \underline{\underline{\underline{\underline{f}}}}, \quad (4.1)$$

where ρ_s is the density of the structure material, $\underline{\mathbf{u}}$ is the displacement of the structure, $\dot{\underline{\mathbf{u}}}$ its velocity, $\underline{\underline{\underline{\underline{\sigma}}}}$ is the Cauchy stress tensor and $\underline{\underline{\underline{\underline{f}}}}$ is the density of body forces.

The equilibrium equation is completed by nonlinear constitutive equations. In this work, we assume the structure undergoing finite displacements to be elastic using the Saint Venant-Kirchhoff model [24]. The second Piola-Kirchhoff stress tensor $\underline{\underline{\underline{\underline{S}}}}$ is given by:

$$\underline{\underline{\underline{\underline{S}}}} = \underline{\underline{\underline{\underline{C}}}} : \underline{\underline{\underline{\underline{E}}}}, \quad (4.2)$$

where $\underline{\underline{\underline{\underline{C}}}}$ is the fourth order stiffness tensor and $\underline{\underline{\underline{\underline{E}}}}$ is the Green-Lagrangian strain given by,

$$\underline{\underline{\underline{\underline{E}}}} = \frac{1}{2} \left[(\nabla_{\underline{\mathbf{X}}}\underline{\mathbf{u}})^t + (\nabla_{\underline{\mathbf{X}}}\underline{\mathbf{u}}) + (\nabla_{\underline{\mathbf{X}}}\underline{\mathbf{u}})^t \cdot (\nabla_{\underline{\mathbf{X}}}\underline{\mathbf{u}}) \right], \quad (4.3)$$

with $\nabla_{\underline{\mathbf{X}}}\underline{\mathbf{u}}$, the material displacement gradient tensor.

The Cauchy stress tensor ($\underline{\underline{\underline{\underline{\sigma}}}}$) can be expressed using the second Piola-Kirchhoff stress tensor ($\underline{\underline{\underline{\underline{S}}}}$) as:

$$\underline{\underline{\underline{\underline{\sigma}}}} = J^{-1} \underline{\underline{\underline{\underline{G}}}} \underline{\underline{\underline{\underline{S}}}} \underline{\underline{\underline{\underline{G}}}}^t, \quad (4.4)$$

where $\underline{\underline{\underline{\underline{G}}}}$ is the material deformation gradient tensor and J its determinant (see [77] for additional details).

Remark. *The finite displacement elastic model is a hypothesis from this work but other nonlinear constitutive laws such as plasticity models could have been used with the developed method.*

The structure mid-surface is denoted Γ_S and corresponds to the mediane plane of the structure. The structure being thin, its outer boundary is assimilated to its mid-surface (Γ_S) and the structure is considered as a nonlinear geometrically exact shell [158, 194]. Therefore, the structure is modelled as a curved plane (2D), corresponding to its mid-surface (Γ_S), with a virtual thickness h . This curved plane can undergo finite displacements and elastic deformations in a three-dimensional space.

4.1.2 - Coupling conditions

The Rankine-Hugoniot conditions are applied at the inviscid fluid-structure interface in the direction normal to this interface. The first coupling condition ensures equality between the velocity of the flow ($\underline{\mathbf{u}}$) normal to the structure (Γ_S) and the normal velocity of the structure denoted $\dot{\underline{\mathbf{u}}} \cdot \underline{\mathbf{n}}_{\Gamma_S}$, where $\underline{\mathbf{n}}_{\Gamma_S}$ is the unit normal to the structure (Γ_S). The second coupling condition ensures equality between the pressure exerted by the flow on the structure and the resulting structure stresses. The set of conditions writes:

$$\text{On } \Gamma_S, \begin{cases} (\dot{\underline{\mathbf{u}}} - \underline{\mathbf{u}}) \cdot \underline{\mathbf{n}}_{\Gamma_S} = 0, \\ (\underline{\underline{\underline{\underline{\sigma}}}} - p \underline{\underline{\underline{\underline{I}}}}_d) \cdot \underline{\mathbf{n}}_{\Gamma_S} = 0. \end{cases} \quad (4.5)$$

4.1.3 - Structure discretization : the finite element method

A Lagrangian unstructured conformal mesh \mathcal{S} of the mid-surface (Γ_s) is constructed using 4-node quadrilateral elements. We denote by $\Omega_{\mathcal{S}}$ the number of cells of the set \mathcal{S} . The element indexed i of this mesh is written C_i . The structure equilibrium presented in equation 4.1, is treated using MITC4 shell finite elements [49] (Mixed Interpolation of Tensorial Components). The finite element discretization of the equation 4.1 leads to :

$$\underline{\underline{M}} \ddot{\underline{U}} = \underline{F}_{\text{ext}} + \underline{F}_f + \underline{F}_{\text{int}}, \quad (4.6)$$

where $\underline{\underline{M}}$ is the mass matrix of the global system. \underline{U} and $\ddot{\underline{U}}$ are respectively the vector of generalized displacements of the finite element system and the acceleration vector. $\underline{F}_{\text{int}}$ is the vector of nonlinear internal forces computed according to [49]. $\underline{F}_{\text{ext}}$ is the force vector due to the other external forces applied to the structure and \underline{F}_f is the force vector exerted by the fluid on the structure. The global system vectors contain known quantities at the nodes of the structure grid (\mathcal{S}).

4.1.4 - Explicit time integration of the structure

Like for the fluid, the structure equation set is integrated using an explicit time integration scheme. The fluid is integrated using the second order MUSCL-Hancock integration scheme [170] whereas the structure equation 4.1 is integrated using a central difference scheme:

$$\begin{aligned} \text{Explicit velocity prediction at half time step: } \quad \underline{\dot{U}}^{n+\frac{1}{2}} &= \underline{\dot{U}}^n + \frac{\Delta t_n}{2} \ddot{\underline{U}}^n, \\ \text{Explicit displacement prediction:} \quad \underline{U}^{n+1} &= \underline{U}^n + \Delta t_n \underline{\dot{U}}^{n+\frac{1}{2}}, \\ \text{Implicit velocity correction:} \quad \underline{\dot{U}}^{n+1} &= \underline{\dot{U}}^{n+\frac{1}{2}} + \frac{\Delta t_n}{2} \ddot{\underline{U}}^{n+1}, \end{aligned} \quad (4.7)$$

where indices n and $n + \frac{1}{2}$ indicate time step increments and Δt_n is the variable time step. The time step is the same for the fluid and the structure. It is defined as:

$$\Delta t_n = \min(\Delta t_n^{\mathcal{V}}, \Delta t_n^{\mathcal{W}}, \Delta t^{\mathcal{S}}), \quad (4.8)$$

where $\Delta t_n^{\mathcal{V}}$ and $\Delta t_n^{\mathcal{W}}$ are the stability time steps of the patch and the substrate model at the n -th time step while $\Delta t^{\mathcal{S}}$ is the critical time step of the structure model. The critical time steps for the fluid are defined by the CFL condition given in equation 1.20. The structure stability condition for the time step writes:

$$\Delta t^{\mathcal{S}} < \min_{i \in \Omega_{\mathcal{S}}} \frac{h_i}{c_{\mathcal{S}}}, \quad (4.9)$$

where $c_{\mathcal{S}}$ is the maximum speed of sound of the structure computed as follows:

$$c_{\mathcal{S}} = \sqrt{\frac{E}{\rho_s}}, \quad (4.10)$$

with E the Young modulus of the structure.

4.2 - Discretization of the coupling conditions: the Chimera Mediating Body Method (Chimera-MBM)

The coupling procedure proposed in this work is based on a mediating entity between the fluid and the structure discrete models [92]. The main objective of our work is to combine the previously developed finite-volume Chimera method with the Mediating Body Method (MBM).

In this section, we first present the Mediating Body Method with a single fluid grid $\mathcal{U} \in \mathcal{T}$ as in [92] from the construction of the mediating entity to the time integration scheme. Then we detail the improvements that have been applied in order to couple the Mediating Body Method with the second order developed Chimera method. A new time integration scheme is presented to make the MBM compatible with overlapping grids.

4.2.1 - Presentation of the Mediating Body Method

In the Mediating Body Method (MBM), the coupling is based on the construction of a mediating entity between the fluid and the structure discrete models. This mediating entity is called the mediating body in the following. For the time integration, a staggered scheme is used. At each time step, the structure imposes its normal velocity to the fluid (through the mediating body), fulfilling the first condition in equation 4.5 whereas the fluid imposes the normal flux momentum (also through the mediating body), fulfilling the second condition in equation 4.5. A simplified version of the coupling algorithm is illustrated in Figure 4.1.

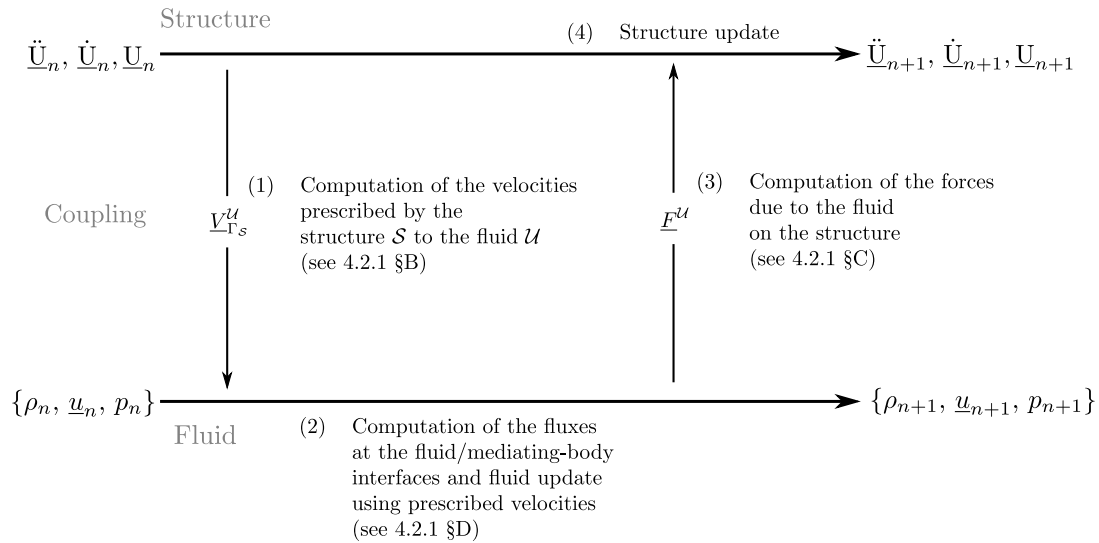


Figure 4.1: Simplified flow chart of the coupling algorithm.

A . Construction of the mediating body

The mediating body is made of fluid cells intersected by the structure. It occupies a volume which approximates the geometry of the structure midsurface (Γ_S). The mediating body volume is defined as the union of all the cells of the fluid (\mathcal{U}) intersected by the structure cells (\mathcal{S}) (see Fig. 4.2). The mediating body cell set is denoted :

$$\mathcal{U}_{\Gamma_S} = \{K_i \in \mathcal{U}, K_i \cap \mathcal{S} \neq \emptyset\}. \quad (4.11)$$

If the structure undergoes large displacement, the set of fluid cells composing the mediating body changes over time and needs to be indexed by the time step n , which writes $\mathcal{U}_{\Gamma_S}^n$. However, for the sake of brevity, the time step reference is willingly omitted referring to an arbitrary time step.

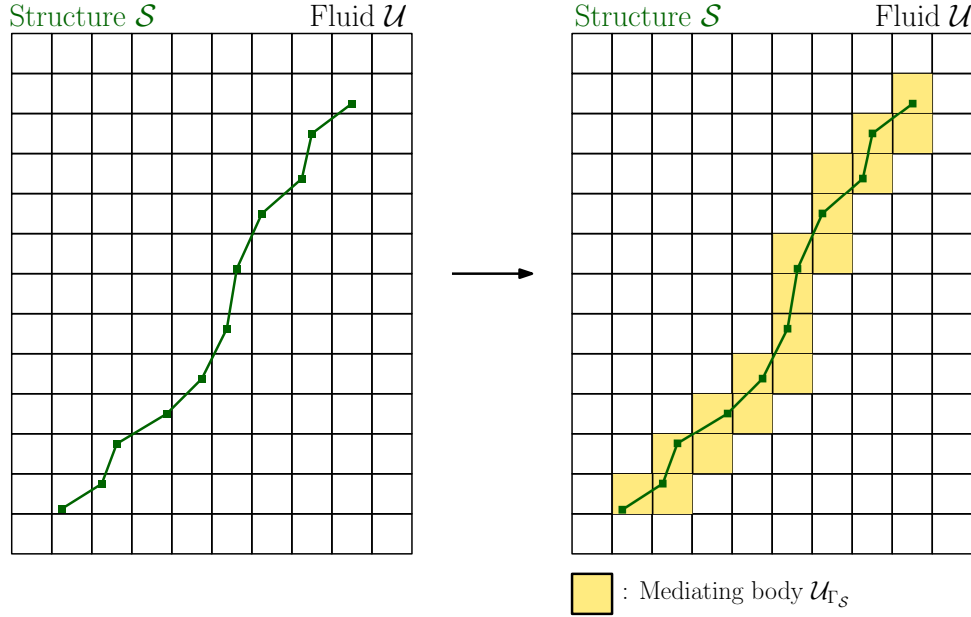


Figure 4.2: mediating body construction for a single grid.

For the i -th cell K_i of the mediating body (\mathcal{U}_{Γ_S}), an averaged normal pseudo-projection operator to the structure written $\underline{\pi}_{\Gamma_S i}^{\mathcal{U}}$ is computed:

$$\underline{\pi}_{\Gamma_S i}^{\mathcal{U}} = \frac{\int_{K_i \cap \mathcal{S}} \underline{n}_{\Gamma_S} \otimes \underline{n}_{\Gamma_S} dx}{|K_i \cap \mathcal{S}|}, \quad (4.12)$$

with \underline{n}_{Γ_S} the unit normal to Γ_S .

The normal pseudo-projection operator ($\underline{\pi}_{\Gamma_S i}^{\mathcal{U}}$) is averaged instead of the normal itself not to depend on an arbitrary choice of the normal for non-manifold structures (see [92] for additional details). In the following, the set of fluid cells, which do not belong to the mediating body is called *active fluid* and is denoted:

$$\mathcal{U}_* = \{K_i \in \mathcal{U}, K_i \notin \mathcal{U}_{\Gamma_S}\} \quad (4.13)$$

With the Mediating Body Method, only the cells in the active fluid (\mathcal{U}_*) contribute to the fluid calculation.

Remark. For the sake of clarity, the figures represent two-dimensional fluid meshes. However, the method is designed for three-dimensional unstructured meshes.

Remark. At a given time step, values of the state vector of the cells composing the mediating body cannot be used as they are bypassed by the fluid computation functions. The values inside the mediating body cells are not used at all. The Riemann problems at the interface of the mediating body are detailed in [92].

B . Velocity exchanges

In the Mediating Body Method, the structure imposes at each time steps its normal velocity to the fluid through the mediating body. Each face $\mathcal{F}_{ij}^{\mathcal{U}}$ shared by the cells $K_i \in \mathcal{U}_{\Gamma_S}$ and $K_j \in \mathcal{U}_*$ i.e.,

at the interface between the active fluid (\mathcal{U}_*) and the mediating body (\mathcal{U}_{Γ_s}), is partially treated as a moving wall boundary condition for the active fluid. An averaged normal velocity of the structure inside the cell K_j denoted $\underline{u}_{\Gamma_s j}^{\mathcal{U}}$ is computed:

$$\underline{u}_{\Gamma_s j}^{\mathcal{U}} = \frac{\int_{K_j \cap \mathcal{S}} (\dot{\mathbf{u}} \cdot \underline{n}_{\Gamma_s}) \underline{n}_{\Gamma_s} dx}{|K_j \cap \mathcal{S}|}, \quad (4.14)$$

with $|K_j \cap \mathcal{S}|$ the surface of the intersection between K_j and \mathcal{S} as illustrated in Figure 4.3.

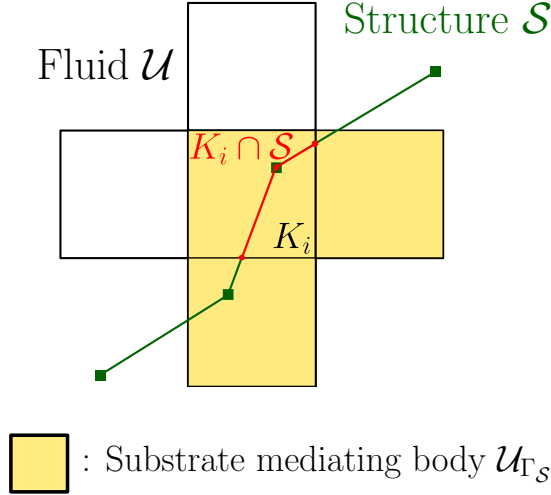


Figure 4.3: Fluid cell intersection with the structure.

The vector $\underline{V}_{\Gamma_s}^{\mathcal{U}}$ denotes the vector in which the $\{\underline{u}_{\Gamma_s j}^{\mathcal{U}}\}_{K_j \in \mathcal{U}_{\Gamma_s}}$ are stacked, $\underline{N}_s(\underline{x})$ the matrix of finite element shape functions such that $\dot{\mathbf{u}} = \underline{N}_s(\underline{x}) \cdot \dot{\mathbf{U}}$, and $\underline{\chi}^{\mathcal{U}}(\underline{x})$ the matrix such that,

$$\underline{\chi}^{\mathcal{U}}(\underline{x}) \cdot \underline{V}_{\Gamma_s}^{\mathcal{U}} = \frac{\underline{u}_{\Gamma_s j}^{\mathcal{U}}}{|K_j \cap \mathcal{S}|}, \text{ if } \underline{x} \in K_j. \quad (4.15)$$

As a more generalized expression, one can write

$$\begin{aligned} \underline{V}_{\Gamma_s}^{\mathcal{U}} &= \left[\int_{\mathcal{S}} \underline{\chi}^{\mathcal{U}t} (\underline{n}_{\Gamma_s} \otimes \underline{n}_{\Gamma_s}) \underline{N}_s dx \right] \cdot \dot{\mathbf{U}}, \\ &= \underline{M}_s^{\mathcal{U}} \cdot \dot{\mathbf{U}}. \end{aligned} \quad (4.16)$$

The integrand of 4.16 is polynomial only on the intersections $\mathcal{J}_{ij}^{\mathcal{U}} = C_i \cap K_j$, $C_i \in \mathcal{S}$, $K_j \in \mathcal{U}_{\Gamma_s}$ (surfaces in 3D, segments in 2D). Then, in order to use standard Gauss quadratures, the integral is computed in the following way:

$$\underline{M}_s^{\mathcal{U}} = \sum_{\{i,j\}, \mathcal{J}_{ij}^{\mathcal{U}} \neq \{\emptyset\}} \int_{\mathcal{J}_{ij}^{\mathcal{U}}} \underline{\chi}^{\mathcal{U}t} (\underline{n}_{\Gamma_s} \otimes \underline{n}_{\Gamma_s}) \underline{N}_s dx. \quad (4.17)$$

Remark. For a 3D problem, the matrix $\underline{\chi}^{\mathcal{U}}(\underline{x})$ writes:

$$\underline{\chi}^{\mathcal{U}}(\underline{x}) = \left[\frac{\chi_1(\underline{x})}{|K_1 \cap \mathcal{S}|} I_3, \frac{\chi_2(\underline{x})}{|K_2 \cap \mathcal{S}|} I_3, \frac{\chi_3(\underline{x})}{|K_3 \cap \mathcal{S}|} I_3, \dots \right], \quad (4.18)$$

where \underline{I}_3 is the 3×3 identity matrix and χ_j the indicator function of the cell K_j , i.e.

$$\chi_j(\underline{x}) = \begin{cases} 1 & \text{if } \underline{x} \in K_j \\ 0 & \text{elsewhere.} \end{cases} \quad (4.19)$$

C . Momentum exchanges

At each time step, the fluid imposes a flux momentum to the structure through the mediating body (\mathcal{U}_{Γ_S}). Each mediating body cell $K_j \in \mathcal{U}_{\Gamma_S}$, gathers the momentum flow rates passing through its faces shared with the active fluid (\mathcal{U}_*). Then, it applies the normal component of this flux to the structure on the section of \mathcal{S} that it intersects. This way, the second equation of 4.5 is fulfilled.

In the following, the momentum ($\rho \underline{u}$) is written \underline{q} for the sake of clarity in the equations. The gathered momentum flow rate between the times t and $t + \Delta t$ for the cell $K_j \in \mathcal{U}_{\Gamma_S}$ of the substrate mediating body writes :

$$\underline{\Phi}_j^{\mathcal{U}^q} = \sum_{i \in \gamma(j), \exists K_i \in \mathcal{U}_*} \underline{\Phi}_{ij}^{\mathcal{U}^q}, \quad (4.20)$$

where $\underline{\Phi}_{ij}^{\mathcal{U}^q}$ is the momentum flow rate at the face $\mathcal{F}_{ij}^{\mathcal{U}}$. The gathered momentum flow rate is projected onto the unit normal to Γ_S , denoted \underline{n}_{Γ_S} , and turned into a force density $\underline{f}^{\mathcal{U}}$ applied to the structure,

$$\begin{aligned} \underline{f}^{\mathcal{U}} &= \frac{(\underline{\Phi}_j^{\mathcal{U}^q} \cdot \underline{n}_{\Gamma_S}) \underline{n}_{\Gamma_S}}{|K_j \cap \mathcal{S}|}, \text{ on } K_j \cap \mathcal{S}, \\ &= (\underline{n}_{\Gamma_S} \otimes \underline{n}_{\Gamma_S}) \underline{\chi}^{\mathcal{U}} \cdot \underline{\Phi}^{\mathcal{U}^q}, \end{aligned} \quad (4.21)$$

where $\underline{\Phi}^{\mathcal{U}^q}$ is a vector in which the $\{\underline{\Phi}_{ij}^{\mathcal{U}^q}\}_{K_j \in \mathcal{U}_{\Gamma_S}}$ are stacked and $\underline{\chi}^{\mathcal{U}}(\underline{x})$, is the matrix such that,

$$\underline{\chi}^{\mathcal{U}}(\underline{x}) \cdot \underline{\Phi}^{\mathcal{U}^q} = \frac{\underline{\Phi}_j^{\mathcal{U}^q}}{|K_j \cap \mathcal{S}|}, \text{ if } \underline{x} \in K_j. \quad (4.22)$$

This force density is then multiplied by the finite element shape function of the structure discrete model, integrated over the surface \mathcal{S} ,

$$\begin{aligned} \underline{F}^{\mathcal{U}} &= \int_{\mathcal{S}} \underline{N}_s^t \cdot \underline{f}^{\mathcal{U}} \, dx, \\ &= \sum_{\{i,j\}, \mathcal{J}_{ij}^{\mathcal{U}} \neq \emptyset} \int_{\mathcal{J}_{ij}^{\mathcal{U}}} \underline{N}_s^t \cdot \underline{f}^{\mathcal{U}} \, dx, \\ &= \left(\int_{\mathcal{S}} \underline{N}_s^t (\underline{n}_{\Gamma_S} \otimes \underline{n}_{\Gamma_S}) \underline{\chi}^{\mathcal{U}} \, dx \right) \cdot \underline{\Phi}^{\mathcal{U}^q}, \\ &= \underline{M}_S^{\mathcal{U}^t} \cdot \underline{\Phi}^{\mathcal{U}^q}. \end{aligned} \quad (4.23)$$

D . Computations at the mediating body/active fluid interface

In this paragraph, we focus on a face $\mathcal{F}_{ij}^{\mathcal{U}} = \mathcal{F}_{ji}^{\mathcal{U}}$, $K_j \in \mathcal{U}_{\Gamma_S}$, $K_i \in \mathcal{U}_*$. Between the times t and $t + \Delta t$, $\mathcal{F}_{ij}^{\mathcal{U}}$ acts as a boundary condition for the active fluid domain (\mathcal{U}_*). We consider the normal \underline{n}_{ij} of the face $\mathcal{F}_{ij}^{\mathcal{U}}$ belonging to the cell $K_j \in \mathcal{U}_{\Gamma_S}$. If \underline{n}_{ij} is parallel to the local averaged normal to the thin structure, the interface is impermeable and the fluid cannot cross it. If these vectors are perpendicular, this interface is permeable and the flow is not affected by the structure.

D.1 - Virtual remeshing of the face

We apply the averaged normal pseudo-projection operator 4.12 to the normal \underline{n}_{ij} of the face $\mathcal{F}_{ij}^{\mathcal{U}}$ inside the cell K_j . As shown in [92], $\|\underline{\pi}_{\Gamma_S}^{\mathcal{U}} \underline{n}_{ij}^{\mathcal{U}}\|$ is zero if \underline{n}_{Γ_S} is orthogonal to the constant vector \underline{n}_{ij} everywhere within the cell K_j . If the value of $\|\underline{\pi}_{\Gamma_S}^{\mathcal{U}} \underline{n}_{ij}^{\mathcal{U}}\|$ is smaller than a given tolerance ϵ (10^{-12}

for instance), the treatment of the face \mathcal{F}_{ij}^u is fully permeable. Otherwise, a unit normal vector to the structure denoted $\underline{n}_{\Gamma s_{ij}}^u$ is defined as follows:

$$\underline{n}_{\Gamma s_{ij}}^u = \frac{\underline{\pi}_{\Gamma s_i}^u \underline{n}_{ij}^u}{\|\underline{\pi}_{\Gamma s_i}^u \underline{n}_{ij}^u\|}. \quad (4.24)$$

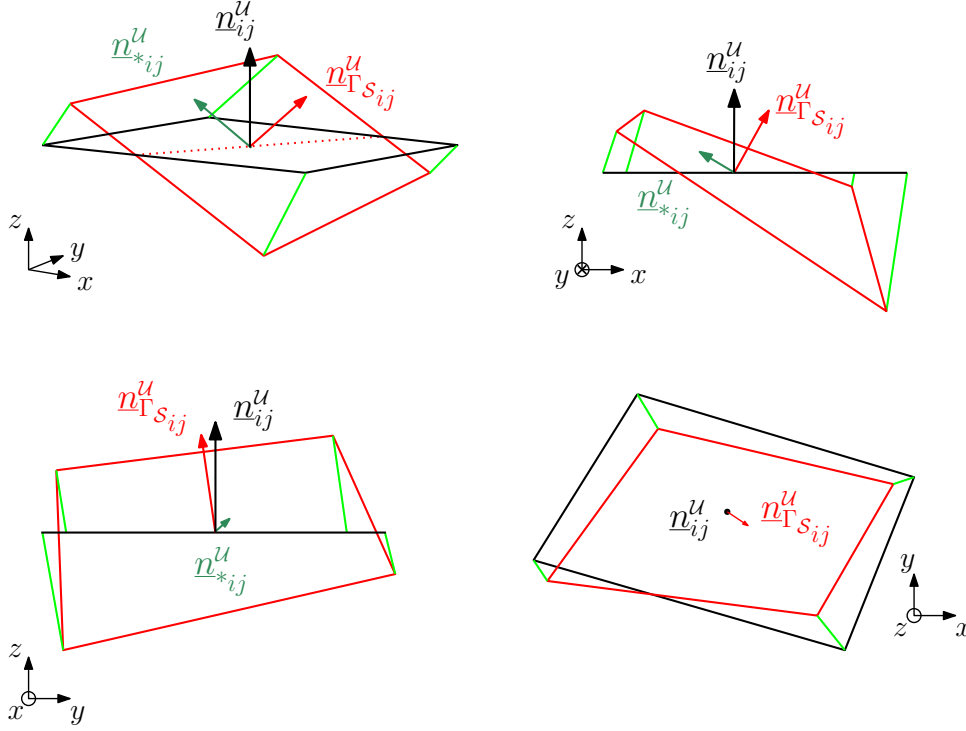


Figure 4.4: Example of virtual remeshing of a two-dimensional face.

In this case, the face \mathcal{F}_{ij}^u is virtually remeshed into two parts, shown in Figure 4.4:

- The first part of the face is denoted $\mathcal{F}_{\Gamma s_{ij}}^u$ and acts as a moving wall in the direction $\underline{n}_{\Gamma s_{ij}}^u$ (red in Fig. 4.4). Geometrically, $\mathcal{F}_{\Gamma s_{ij}}^u$ is the orthogonal projection of \mathcal{F}_{ij}^u onto the plane defined by the normal $\underline{n}_{\Gamma s_{ij}}^u$ and containing the center of the face \mathcal{F}_{ij}^u . The area of $\mathcal{F}_{\Gamma s_{ij}}^u$ is defined as:

$$|\mathcal{F}_{\Gamma s_{ij}}^u| = (\underline{n}_{\Gamma s_{ij}}^u \cdot \underline{n}_{ij}^u) |\mathcal{F}_{ij}^u|, \quad (4.25)$$

where $|\mathcal{F}_{ij}^u|$ is the area of \mathcal{F}_{ij}^u .

- The second part is denoted \mathcal{F}_{*ij}^u and acts as a set of permeable faces orthogonal to $\underline{n}_{\Gamma s_{ij}}^u$ (green in Fig. 4.4). The geometrical support of \mathcal{F}_{*ij}^u is the set of lateral faces of the crossed truncated prism whose bases are \mathcal{F}_{*ij}^u and $\mathcal{F}_{\Gamma s_{ij}}^u$.

Figure 4.5 illustrates the virtual remeshing for two-dimensional simple meshes. Denoting $\{\mathcal{L}_{ik}^u\}$ the set of lateral faces and $\{\underline{n}_{ik}^u\}$ their unit normal vectors, the divergence theorem applied to the crossed truncated prism gives:

$$|\mathcal{F}_{*ij}^u| \underline{n}_{*ij}^u = \sum_{\{\mathcal{L}_{ik}^u\}} |\mathcal{L}_{ik}^u| \underline{n}_{ik}^u = |\mathcal{F}_{ij}^u| \underline{n}_{ij}^u - |\mathcal{F}_{\Gamma s_{ij}}^u| \underline{n}_{\Gamma s_{ij}}^u. \quad (4.26)$$

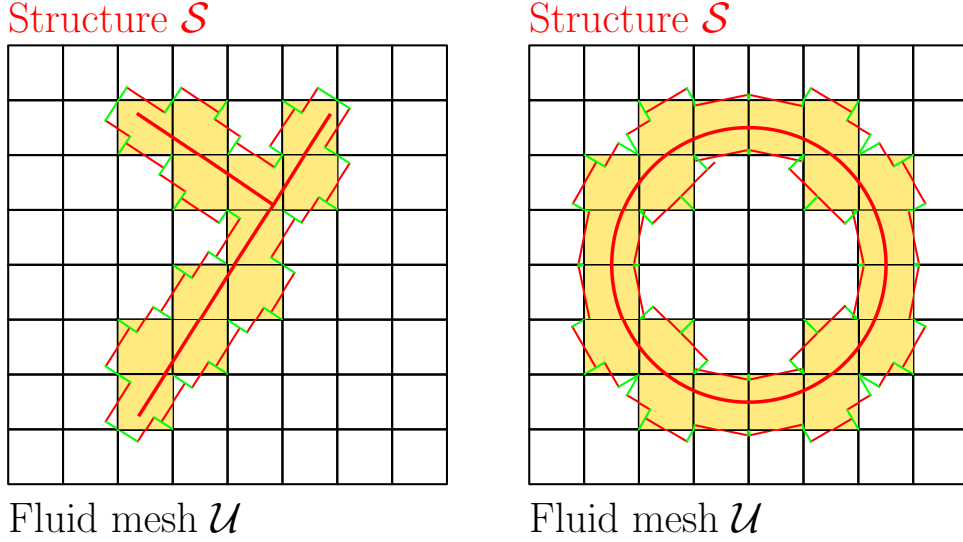


Figure 4.5: Examples of virtual remeshing of the faces at the interface between the active fluid (\mathcal{U}_*) and the mediating body (\mathcal{U}_{Γ_s}), whose cells are represented in yellow shade, for two-dimensional simple meshes. The permeable interfaces are represented by thin green lines while the moving walls are represented by thin red lines.

D.2 - Flux computation

In the following, we consider that the fluid domain is solved using the second order MUSCL reconstruction detailed in section 1.2.4. The interface states are reconstructed based on the primitive variables \overline{W}^u , $\mathcal{U} = \{\mathcal{W}, \mathcal{V}\}$. We note the interface states resulting from the reconstruction at the face \mathcal{F}_{ij}^u , $\overline{W}_{ij}^u / \overline{W}_{ji}^u$ and the corresponding conservative states $\overline{U}_{ij}^u / \overline{U}_{ji}^u$. As the fluid time integration uses a second order MUSCL-Hancock integration, the Riemann problems are solved using half time step interface states $\overline{U}_{ij}^{u, n+\frac{1}{2}} / \overline{U}_{ji}^{u, n+\frac{1}{2}}$ (see section 1.2.5). In the following the time step reference is willingly omitted for clarity as the states used in the flux computation are unequivocal.

Remark. All the flux computations presented in section 4.2.1 D.2 are performed during the fourth step of the MUSCL-Hancock method (see section 1.2.5). The objective is to overload the HLLC flux fonction presented in section 1.2.3 at the mediating body interface.

The part $\mathcal{F}_{\Gamma_{s_{ij}}}^u$ of the face \mathcal{F}_{ij}^u acts as a moving wall translating at velocity $u_{w_{ij}}^u = \underline{u}_{\Gamma_{s_j}}^u \cdot \underline{n}_{\Gamma_{s_{ij}}}^u$ in the direction $\underline{n}_{\Gamma_{s_{ij}}}^u$. This boundary condition is enforced using a virtual cell technique. We consider the Riemann problem between the interface state \overline{U}_{ij}^u and the virtual state \tilde{U}_{ji}^u in the local frame of the face \mathcal{F}_{ij}^u :

$$\underline{U}(\underline{\eta}) = \begin{cases} \overline{U}_{ij}^u, & \text{if } \underline{\eta} \cdot \underline{n}_{\Gamma_{s_{ij}}}^u < 0 \\ \tilde{U}_{ji}^u, & \text{if } \underline{\eta} \cdot \underline{n}_{\Gamma_{s_{ij}}}^u > 0, \end{cases} \quad (4.27)$$

where $\overline{U}_{ij}^u = \left[\rho_{ij}^u, \underline{q}_{ij}^u, \rho_{ij}^u e_{ij}^u + \frac{(\underline{q}_{ij}^u)^2}{2\rho_{ij}^u} \right]$, $\tilde{U}_{ji}^u = \left[\rho_{ij}^u, \tilde{\underline{q}}_{ij}^u, \rho_{ij}^u e_{ij}^u + \frac{(\tilde{\underline{q}}_{ij}^u)^2}{2\rho_{ij}^u} \right]$, $\underline{q}_{ij}^u = (\rho \underline{u})_{ij}^u$ and $\tilde{\underline{q}}_{ij}^u = \underline{q}_{ij}^u - 2(\underline{q}_{ij}^u \cdot \underline{n}_{\Gamma_{s_{ij}}}^u - \rho_{ij}^u u_{w_{ij}}^u) \underline{n}_{\Gamma_{s_{ij}}}^u$. The flux related to this Riemann problem on the characteristic line $\eta/t = \zeta$ is denoted $\Phi_{ij}^{uR}(\zeta)$.

The remainder of the face \mathcal{F}_{ij}^u (\mathcal{F}_{*ij}^u), acts as a permeable interface with an area $|\mathcal{F}_{*ij}^u|$ and a unit normal vector \underline{n}_{*ij}^u , defined as in equation 4.26. On \mathcal{F}_{*ij}^u , the flux is simply the flux related to the reconstructed state \overline{U}_{ij}^u .

Finally, the flux at the face \mathcal{F}_{ij}^u is given by:

$$|\mathcal{F}_{ij}^u| \hat{F}(\bar{U}_{ij}^u, \tilde{U}_{ji}^u, n_{ij}^u) = \Phi_{ij}^u(\zeta) = |\mathcal{F}_{\Gamma_{s_{ij}}}^u| \Phi_{ij}^{uR}(\zeta) \cdot n_{\Gamma_{s_{ij}}}^u + |\mathcal{F}_{*ij}^u| \underline{F}(\bar{U}_{ij}^u) \cdot n_{*ij}^u, \quad (4.28)$$

where $\underline{F}(\bar{U}_{ij}^u)$ is the flux related to the interface state \bar{U}_{ij}^u .

Note that conservation is lost at the faces \mathcal{F}_{*ij}^u as the fluid contribution is not transmitted to the fluid nor the structure. The impact of this loss of conservation is negligible and does not affect significantly the accuracy of the solution according to the numerical experiments in [92].

Additional treatments at the mediating body/active fluid interface are detailed in [92] and provide values for the Riemann solver parameter ζ depending on the structure displacements:

- First, in order to prevent the MBM from generating motion in the case of a structure at rest, immersed in a still fluid, a corrective pressure term is added during the computation of the momentum flow rate Φ_{ij}^{uq} at the face \mathcal{F}_{ij}^u from the transmitted flux $\Phi_{ij}^{uR}(u_{w_{ij}}^u)$.
- Finally, an ALE emulation is developed in order to take into account small displacements of the structure that does not involves changes in the mediating body definition during the computations of the fluxes.

These treatments are not detailed in this work for the sake of clarity as they do not impact the coupling between the Chimera method and the Mediating Body Method.

E . Large structure displacement: handling of the indefinite active cells

When the structure undergoes large displacements, the mediating body set (\mathcal{U}_{Γ_s}) changes. Therefore, some cells belonging to the mediating body at the time step $n - 1$ become part of the active fluid at time step n . At $t = t^n$, we call these cells *indefinite active cells* and their set is denoted \mathcal{U}_{*indef} , omitting the time step reference:

$$\mathcal{U}_{*indef} \equiv \mathcal{U}_{*indef}^n = \{K_i \in \mathcal{U}_{\Gamma_s}^{n-1}, K_i \in \mathcal{U}_*^n\}, \quad (4.29)$$

where the exponents n and $n - 1$ refer to time steps.

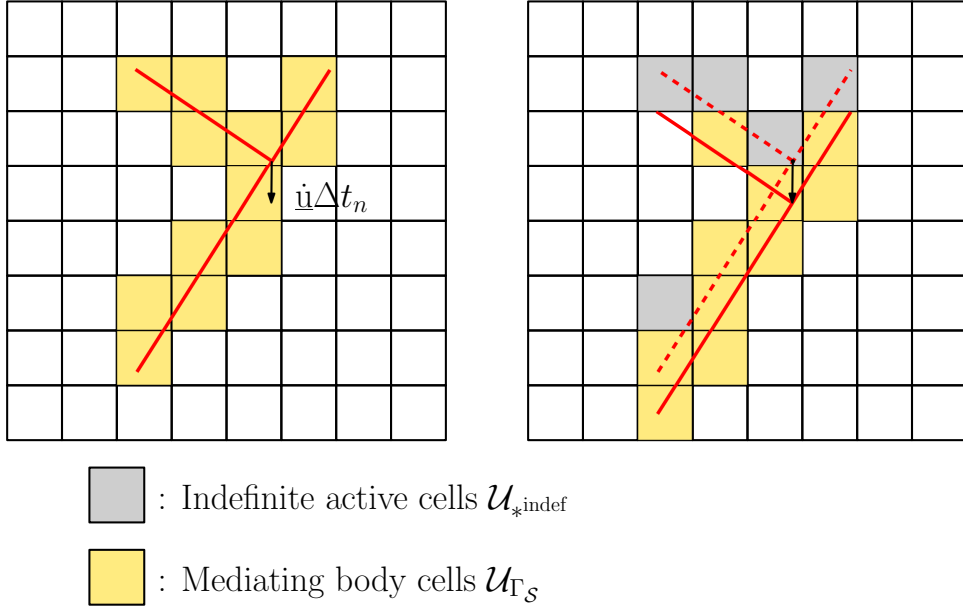
Figure 4.6 provides an illustration of the indefinite active cells. At a given time t^n , before any flux computations, a state vector must be attributed to these indefinite cells. For a given indefinite active cell $K_i \in \mathcal{U}_{*indef}$, an extrapolated state is computed using the definite cells adjacent to it which contain a valid solution. To do so, we define for each cell $K_i \in \mathcal{U}_{*indef}$ another set of cells \mathcal{L}_i^u defined as:

$$\mathcal{L}_i^u = \{K_j, j \in \gamma(i), K_j \notin \mathcal{U}_{*indef}\}. \quad (4.30)$$

Then, the indefinite active cell K_i is attributed the extrapolated state:

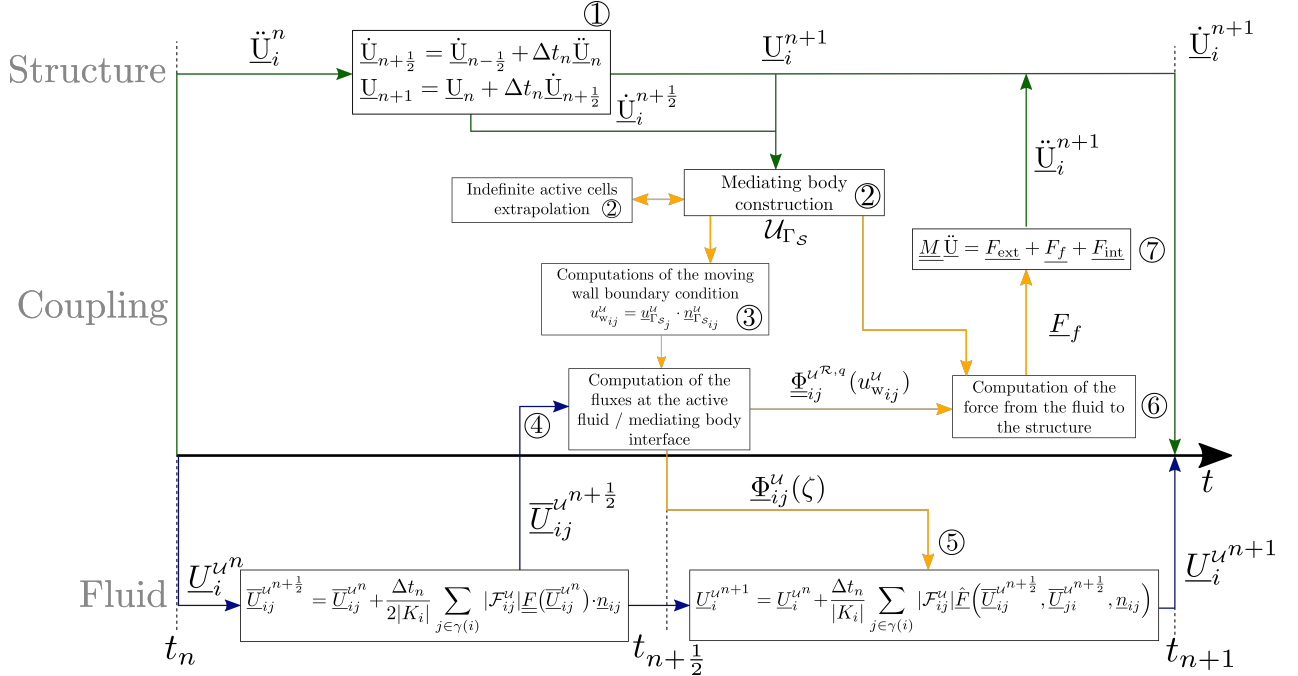
$$\underline{U}_i^u = \frac{\sum_{j \in \Omega_{\mathcal{L}_i^u}} |K_j| \underline{U}_j^u}{\sum_{j \in \Omega_{\mathcal{L}_i^u}} |K_j|}. \quad (4.31)$$

It can occur, as in Figure 4.6, that the set \mathcal{L}_i^u is empty. In this case, the indefinite cells are attributed a state in successive passes until all the indefinite cells are attributed a state: the indefinite cells, for which \mathcal{L}_i^u is not empty, are attributed a state and removed from the list of indefinite cells. Then a new attribution pass is done and so forth until all the indefinite cells requiring an extrapolation are attributed a state.


Figure 4.6: Indefinite active cells in grey shade

F . Time integration scheme for the MBM

A staggered time integration scheme is used in the MBM with a single fluid grid: regarding the fluid-structure coupling, at each time step, the structure imposes its velocity to the fluid interface and the fluid exerts a force on the structure. This detailed scheme is depicted in Figure 4.7.


Figure 4.7: Time integration scheme for the Mediating Body Method with a MUSCL-Hancock integration for the fluid and a central difference scheme for the structure.

At a given discrete time t^n , every quantity on every grid is known and indexed by its time step n . In order to advance from t^n to t^{n+1} the following steps are done:

1. The structure velocity $\dot{\underline{U}}^{n+\frac{1}{2}}$ at $t^{n+\frac{1}{2}}$ and its position \underline{U}^{n+1} at t^{n+1} are computed explicitly

from its acceleration $\ddot{\mathbf{U}}^n$ at t^n using the central difference scheme presented in section 4.1.4.

2. The mediating body $\mathcal{U}_{\Gamma_s}^{n+1}$ is computed using the structure position \mathbf{U}^{n+1} following the procedure described in section 4.2.1.A. If needed, the indefinite active cells are extrapolated as detailed in section 4.2.1.E.
3. The velocities at the interfaces of the mediating body are computed from the structure velocity $\dot{\mathbf{U}}^{n+\frac{1}{2}}$ following the procedure described in section 4.2.1.B.
4. The fluid interface states $\overline{\mathbf{U}}_{ji}^n$, $(i, j) \in \Omega_{\mathcal{U}_*} \times \gamma(i)$, are reconstructed and updated by half a time step $\frac{\Delta t_n}{2}$ using the first two steps of the MUSCL-Hancock time integration *i.e.* the steps 1 and 2 presented in section 1.2.5.
5. The fluid variables $\underline{\mathbf{U}}^n$ are updated to the time t^{n+1} from the interface states $\underline{\mathbf{U}}^{n+\frac{1}{2}}$ using the fluxes presented in section 4.2.1.D.2, the HLLC solver presented in section 1.2.3 and the ALE emulation detailed in [92].
6. The force vector $\underline{\mathbf{F}}_f$ imposed by the fluid to the structure is computed from the flux momentum of the fluid problem between t^n and t^{n+1} following the procedure detailed in section 4.2.1.C.
7. Finally, the structure acceleration $\ddot{\mathbf{U}}^{n+1}$ is computed using the finite element equilibrium equation presented in section 4.1.3 (see equation 4.6).

4.2.2 - Coupling of the Mediating Body Method with the Chimera method: the Chimera-MBM

The MBM has been presented for a unique fluid grid $\mathcal{U} \subset \mathcal{T}$. We now consider, a set of two overlapping grids: a global grid referred as the substrate denoted $\mathcal{W} \subset \mathcal{T}$ and a local superimposed grid referred as patch denoted \mathcal{V} , fully immersed inside the substrate. In this section, we detail the numerical strategy that we have developed to couple the presented MBM and the developed Chimera method. Therefore, we use the notations and the terminology introduced in section 2 and in section 4.2.1.

At each time step, the structure imposes its normal velocity to the fluid through the mediating body whereas the fluid imposes the normal flux momentum also through the mediating body. Simultaneously, the sending cells $\{\mathcal{W}^s, \mathcal{V}^s\}$ and ghost cells $\{\widetilde{\mathcal{W}}, \widetilde{\mathcal{V}}\}$ of both the patch and the substrate exchange information in order to ensure up-to-date fluid information across the grids.

To present the coupling of the MBM with the Chimera method, we detail the aspects of the MBM that are modified by the presence of overlapping grids starting from the mediating body construction.

A . Construction of the mediating body in an overlapping grid framework

With overlapping grids, the construction of the mediating body is distributed between the patch grid (\mathcal{V}) and the substrate grid (\mathcal{W}) as seen in Figure 4.8.

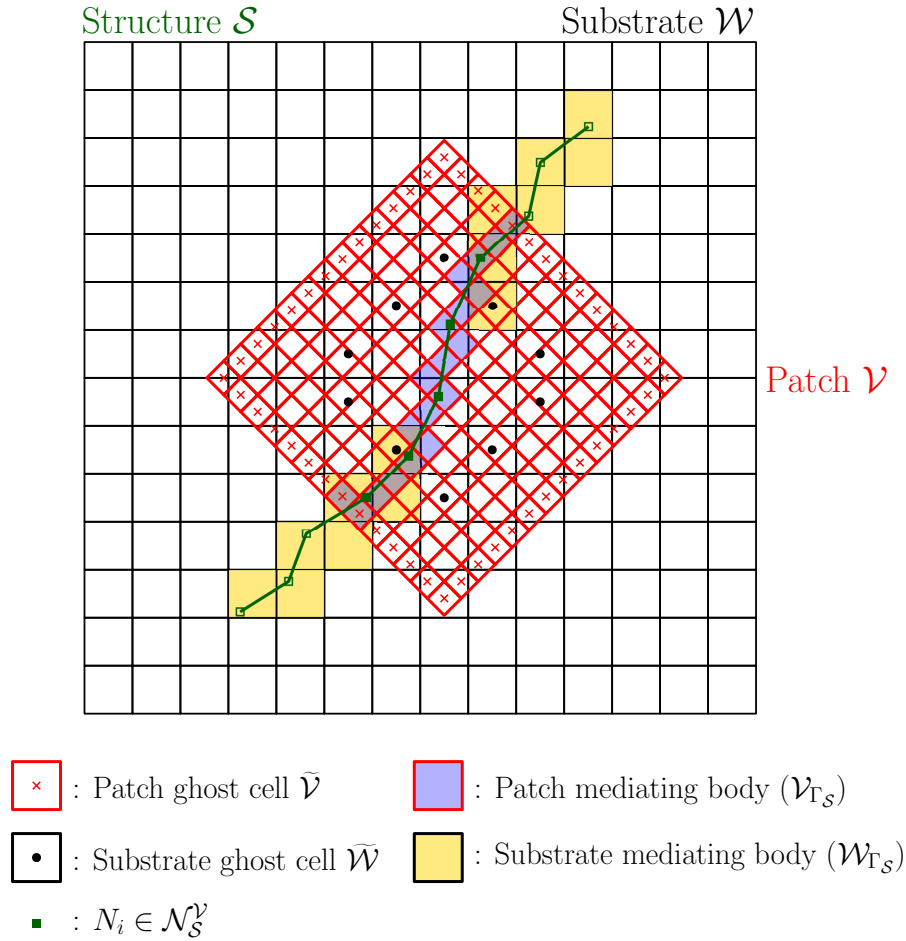


Figure 4.8: Mediating body construction with an overlapping grid configuration.

In order to surround the structure and to avoid redundancy in the overlapped regions, the priority is given to the patch grid which means that the mediating body will be constructed using patch cells

in priority before using substrate cells while minimizing overlapped cells in the mediating body. To do so, we recall the following set of cells : $\mathcal{V}_c = \mathcal{V} \setminus \tilde{\mathcal{V}}$ and $\mathcal{W}_c = \mathcal{W} \setminus \mathcal{W}_p$, where

$$\mathcal{W}_p = \{K_i, i \in \Omega_{\mathcal{W}} / \sum_{j \in \Omega_{\mathcal{V}_c}} |K_i \cap K_j| = |K_i|\}. \quad (4.32)$$

\mathcal{V}_c corresponds to the set of cells of the patch \mathcal{V} deprived of its ghost cells $\tilde{\mathcal{V}}$ also called *cleaned patch* and \mathcal{W}_c corresponds to the set of cells of the substrate deprived of its cells fully covered by the cleaned patch \mathcal{W}_p . \mathcal{W}_c is called *cleaned substrate*. These different sets of cells are represented in Figure 4.9. It is worth noting that $\tilde{\mathcal{W}} \subset \mathcal{W}_p$, and therefore, \mathcal{W}_c does not contain any substrate ghost cell. If \mathcal{W} and \mathcal{V} are non-matching grids, $\mathcal{V}_c \cup \mathcal{W}_c$ covers the entirety of the fluid domain \mathcal{T} with minimized overlapped regions.

We also define the set of cells $\mathcal{W}_c^{\text{wGC}} = \mathcal{W}_c \cup \tilde{\mathcal{W}}$ which comprises the cleaned substrate cells (\mathcal{W}_c) with the addition of the substrate ghost cells ($\tilde{\mathcal{W}}$). $\mathcal{W}_c^{\text{wGC}}$ is referred as *cleaned substrate with ghost cells*. The definition of an equivalent set for the patch is not relevant as $\mathcal{V}_c \cup \tilde{\mathcal{V}} = \mathcal{V}$.

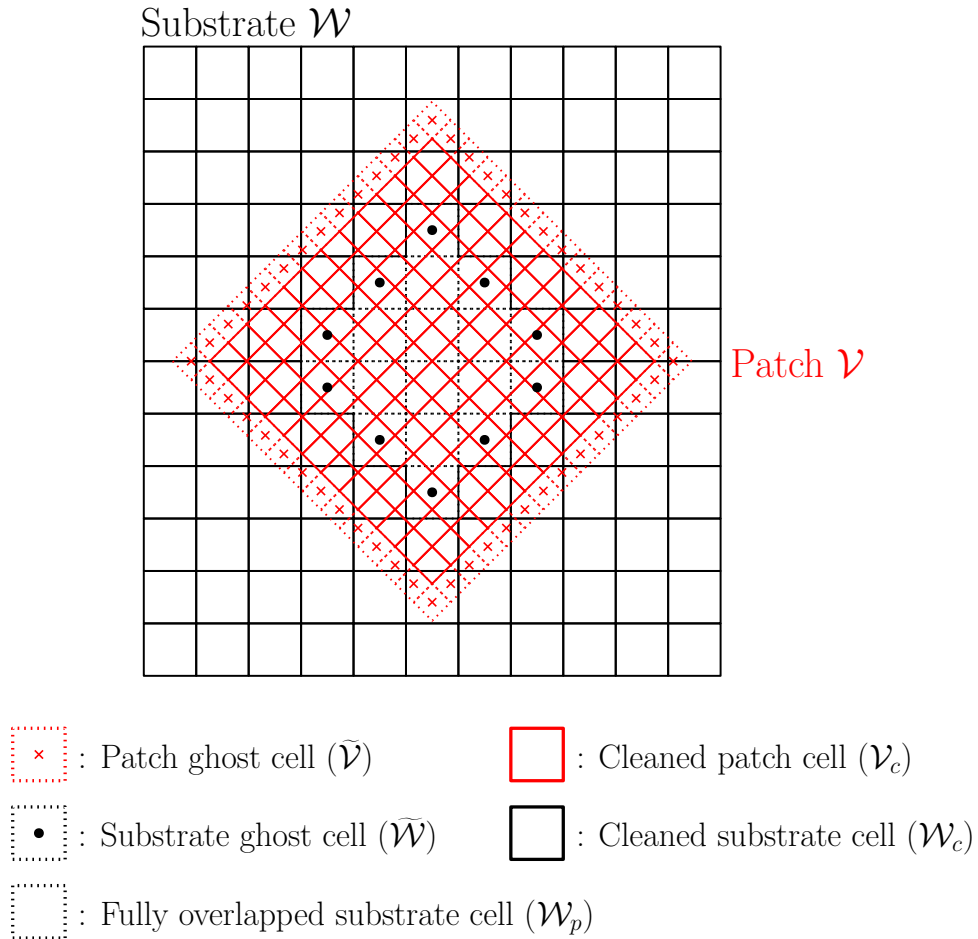


Figure 4.9: Cleaned patch (\mathcal{V}_c) and cleaned substrate (\mathcal{W}_c) sets of cells.

The structure cell set \mathcal{S} , is intersected with the cleaned patch in order to define the following set of cells:

$$\mathcal{S}_{\mathcal{V}} = \{C_i, i \in \Omega_{\mathcal{S}}, |C_i \cap \mathcal{V}_c| = |C_i|\}. \quad (4.33)$$

$\mathcal{S}_{\mathcal{V}}$ corresponds to the structure cells that are fully included inside the cleaned patch (\mathcal{V}_c). We note $\mathcal{N}_{\mathcal{S}} = \{N_i\}_{i \in \Omega_{\mathcal{N}_{\mathcal{S}}}}$, the node set of the structure grid (\mathcal{S}). For each element $C_i, i \in \Omega_{\mathcal{S}}$, we note

$\mathcal{N}(i) = \{N_j\}_{j \in \Omega_{\mathcal{N}(i)}}$ its node set. From $\mathcal{S}_{\mathcal{V}}$, we extract the nodes composing each cell avoiding duplications:

$$\mathcal{N}_{\mathcal{S}}^{\mathcal{V}} = \{N_j, j \in \Omega_{\mathcal{N}(i)}, i \in \Omega_{\mathcal{S}_{\mathcal{V}}}\}, \quad (4.34)$$

which corresponds to the nodes of the structure \mathcal{S} located inside the cleaned patch (\mathcal{V}_c).

The mediating body cell set, denoted $\mathcal{M}_{\Gamma_{\mathcal{S}}}$, is defined as the union of all the cells of the fluid from the patch grid (\mathcal{V}) and cleaned substrated grid with ghost cells ($\mathcal{W}_c^{\text{wGC}}$) intersected by the structure cell set (\mathcal{S}) as represented in Figure 4.8. The set of these intersected cells can be seen as the union of two separate mediating bodies written $\mathcal{W}_{\Gamma_{\mathcal{S}}}$ and $\mathcal{V}_{\Gamma_{\mathcal{S}}}$:

$$\mathcal{M}_{\Gamma_{\mathcal{S}}} = \mathcal{V}_{\Gamma_{\mathcal{S}}} \cup \mathcal{W}_{\Gamma_{\mathcal{S}}} \quad (4.35)$$

$$= \{K_i \in \mathcal{W}_c^{\text{wGC}}, K_i \cap \mathcal{S} \neq \emptyset\} \cup \{K'_i \in \mathcal{V}, K'_i \cap \mathcal{S} \neq \emptyset\}. \quad (4.36)$$

If the structure undergoes large displacements, the set of fluid cells composing the mediating body $\mathcal{M}_{\Gamma_{\mathcal{S}}}$ changes over time and needs to be indexed by the time step n , referred as $\mathcal{M}_{\Gamma_{\mathcal{S}}}^n$. For the sake of clarity, the time step reference is willingly omitted corresponding to an arbitrary time step.

As the mediating body for overlapping grids ($\mathcal{M}_{\Gamma_{\mathcal{S}}}$) is composed of two distinct mediating bodies namely $\mathcal{V}_{\Gamma_{\mathcal{S}}}$ and $\mathcal{W}_{\Gamma_{\mathcal{S}}}$, the single grid MBM is applied independently to both entities. For each cell $K'_i \in \mathcal{V}_{\Gamma_{\mathcal{S}}}$ and $K'_j \in \mathcal{W}_{\Gamma_{\mathcal{S}}}$, with $(i, j) \in \Omega_{\mathcal{V}_{\Gamma_{\mathcal{S}}}} \times \Omega_{\mathcal{W}_{\Gamma_{\mathcal{S}}}}$, averaged normal pseudo-projection operators to the structure denoted $\underline{\underline{\pi}}_{\Gamma_{\mathcal{S}i}}^{\mathcal{V}}$ and $\underline{\underline{\pi}}_{\Gamma_{\mathcal{S}j}}^{\mathcal{W}}$ are computed according to equation 4.12. Also the active fluid cell sets \mathcal{V}_* and \mathcal{W}_* are defined using equation 4.13.

B . Impact of overlapping grids on the Mediating Body Method numerical functions

As the mediating bodies $\mathcal{V}_{\Gamma_{\mathcal{S}}}$ and $\mathcal{W}_{\Gamma_{\mathcal{S}}}$ are independent cell sets, the coupling conditions 4.5 are applied independently. Starting with the first coupling condition, velocity exchanges for the fluid moving wall boundary condition are treated with structure velocity vectors $\underline{\underline{V}}_{\Gamma_{\mathcal{S}}}^{\mathcal{V}}$, $\underline{\underline{V}}_{\Gamma_{\mathcal{S}}}^{\mathcal{W}}$ computed for each grid using equation 4.16. Similarly, the operators $\underline{\underline{\chi}}^{\mathcal{W}}$, $\underline{\underline{\chi}}^{\mathcal{V}}$ are computed using equation 4.15 and the operators $\underline{\underline{M}}_{\mathcal{S}}^{\mathcal{V}}$, $\underline{\underline{M}}_{\mathcal{S}}^{\mathcal{W}}$ are computed using equation 4.17.

For the second coupling condition, the quantities $\underline{\underline{\Phi}}^{\mathcal{V}^q}$ and $\underline{\underline{F}}^{\mathcal{V}}$ are computed for the patch using equation 4.20 and equation 4.23. Similarly the quantities $\underline{\underline{\Phi}}^{\mathcal{W}^q}$ and $\underline{\underline{F}}^{\mathcal{W}}$ are computed for the substrate. Then the two force vectors $\underline{\underline{F}}^{\mathcal{W}}$ and $\underline{\underline{F}}^{\mathcal{V}}$ are summed up with an overlapping ponderation matrix to form the finite element force vector $\underline{\underline{F}}_f$ exerted by the fluid to the structure,

$$\underline{\underline{F}}_f = \underline{\underline{P}} \cdot \underline{\underline{F}}^{\mathcal{W}} + (\underline{\underline{I}}_{N_{\text{dof}}} - \underline{\underline{P}}) \cdot \underline{\underline{F}}^{\mathcal{V}}, \quad (4.37)$$

where $\underline{\underline{I}}_{N_{\text{dof}}}$ is the $N_{\text{dof}} \times N_{\text{dof}}$ identity matrix with $N_{\text{dof}} = \Omega_{\mathcal{S}} \times k$, the number of degrees of freedom of the structural system and k the number of unknown per node. $\underline{\underline{P}}$ is a diagonal matrix defined as:

$$\underline{\underline{P}} = \begin{pmatrix} \underline{\underline{P}}_1 & \underline{\underline{0}} & \cdots & \underline{\underline{0}} \\ \underline{\underline{0}} & \underline{\underline{P}}_2 & \ddots & \vdots \\ \vdots & \ddots & \ddots & \underline{\underline{0}} \\ \underline{\underline{0}} & \cdots & \underline{\underline{0}} & \underline{\underline{P}}_{\Omega_{\mathcal{S}}} \end{pmatrix}, \quad \text{where } \underline{\underline{P}}_i = \begin{pmatrix} p_{i1} & 0 & \cdots & 0 \\ 0 & p_{i2} & \ddots & \vdots \\ \vdots & \ddots & \ddots & 0 \\ 0 & \cdots & 0 & p_{ik} \end{pmatrix}, \quad (4.38)$$

and $p_{ij} = 1$, if the i -th node of the structure \mathcal{S} denoted $N_i \in \mathcal{N}_{\mathcal{S}}^{\mathcal{V}}$, 0 otherwise, $(i, j) \in \Omega_{\mathcal{S}} \times k$.

Remark. As illustrated in Figure 4.10, this approach can lead to an underestimation of the fluid force exerted on the structural elements partially immersed inside the patch \mathcal{V} . The mediating

body definitions of \mathcal{V}_{Γ_s} and \mathcal{W}_{Γ_s} , respectively include the ghost cell sets $\tilde{\mathcal{V}}$ and $\tilde{\mathcal{W}}$. The fluid pressure force is integrated over the intersections between the structure and the mediating bodies. On the structural elements straddling the patch \mathcal{V} and the cleaned substrate with ghost cells $\mathcal{W}_c^{\text{wGC}}$, the fluid integration is performed for the patch mediating body \mathcal{V}_{Γ_s} as well as for the substrate mediating body \mathcal{W}_{Γ_s} . Then the ponderation matrix \underline{P} prevents redundancy by favorising the nodes fully included inside the cleaned patch \mathcal{V}_c using the node set $\mathcal{S}_\mathcal{V}$.

If a structural element $C_i, i \in \Omega_s$ protrudes from the cleaned patch \mathcal{V}_c but is still immersed inside the patch \mathcal{V} , the value inside the ghost cells $\tilde{\mathcal{V}}$ ensures a fluid force integration over the entire element C_i . However, if the element C_i protrudes from the patch \mathcal{V} (see Figure 4.10), the fluid force integration is partially carried out over the element C_i as it is not completely immersed inside the patch fluid domain. As a result, the fluid force $\underline{F}^\mathcal{V}$ can be underestimated if the structural cell characteristic size h_i is much higher the characteristic cell size of the patch $h_\mathcal{V}$ ($h_i \gg h_\mathcal{V}$).

If $k_{\text{GC}} = n$, it is recommended to use $h_i < nh_\mathcal{V}$ to ensure that the fluid force is integrated on the entire element C_i . This underestimation can also happen favorising nodes fully included inside the cleaned substrate with ghost cells $\mathcal{W}_c^{\text{wGC}}$ as seen in Figure 4.10. In this case, if $k_{\text{GC}} = n$, it is recommended to use $h_i < nh^\mathcal{W}$ to ensure that the fluid force is integrated on the entire element C_i .

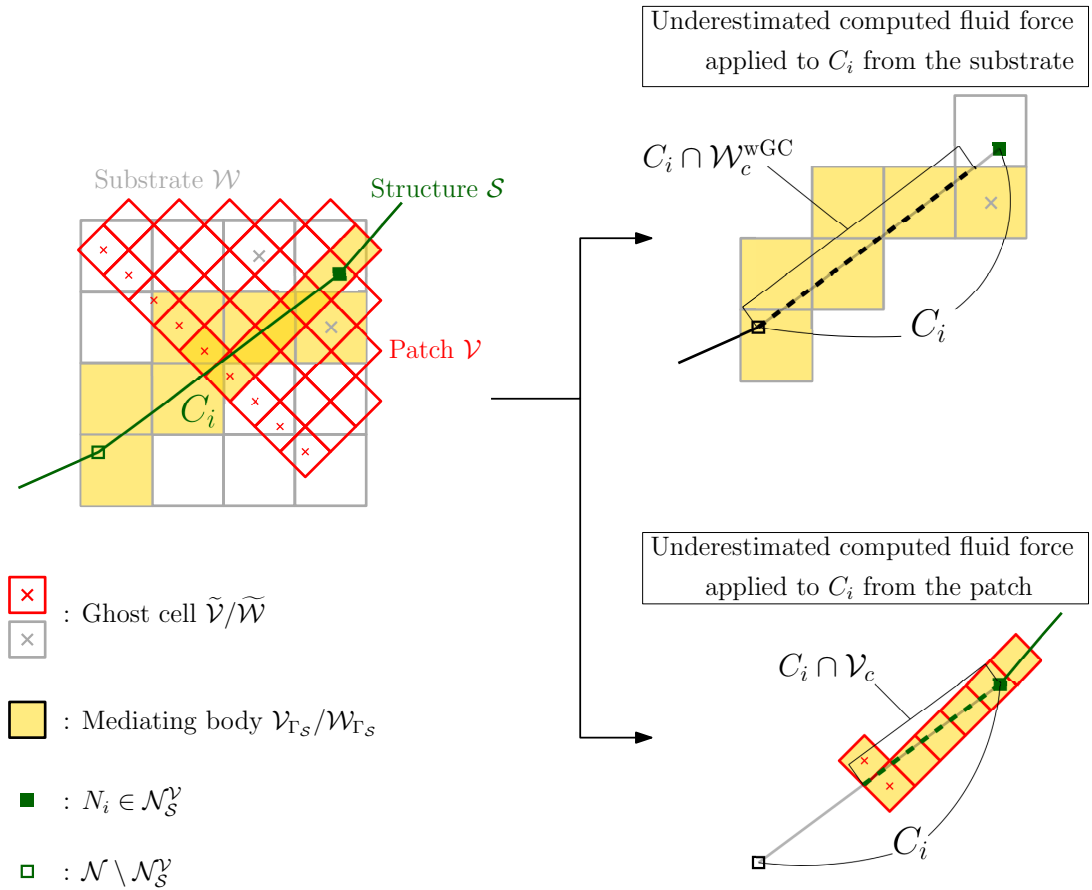


Figure 4.10: Underestimation of the fluid forces computed using the mediating bodies \mathcal{W}_{Γ_s} and \mathcal{V}_{Γ_s} .

Regarding the conservation improvements, the ALE emulation is performed like for the single grid MBM (see [92]) as the value inside the ghost cell sets $\tilde{\mathcal{W}}$ and $\tilde{\mathcal{V}}$ is supposed to be valid at the beginning of each time iteration. Finally, the indefinite resolved cell sets $\mathcal{V}_{*\text{indef}}$ and $\mathcal{W}_{*\text{indef}}$ are defined by equation 4.29 without any change coming from the overlapping grids.

C . Impact of the Mediating Body Method on the Chimera method

In the following, we focus on a patch (\mathcal{V}) for the sake of simplicity. The Chimera method involves two categories of cells: the ghost cells ($\tilde{\mathcal{V}}$) and the sending cells (\mathcal{V}^s). On the other hand, the MBM involves two main categories of cells: the mediating body cells (\mathcal{V}_{Γ_s}) and the active fluid cells (\mathcal{V}_*). As the Chimera method and the MBM coexist in the overlapping grid context, a patch cell can be simultaneously a ghost cell for the Chimera method and an active cell for the MBM.

Four types of cells are reviewed in order to identify potential conflicts between the MBM and the Chimera method. These cell type combinations are summarized in Table 4.1:

- **Ghost cell and mediating body cell:** A ghost cell receives information at the beginning of every iteration to ensure a valid flux at its interfaces. A mediating body cell is used to compute particular fluxes at its interfaces resulting from the structure displacements and not depending on the mediating body cell solution. In the case of a ghost cell that is also a mediating body cell, the ghost cell does not need to receive information as the value inside a mediating body cell does not matter. This type of cell is referred as *indefinite ghost cell* and is reviewed later on.
- **Ghost cell and active cell:** A ghost cell that is also an active cell does not impact the Chimera method as the value inside the active cell will be overwritten by the Chimera method. Therefore, an active cell that is also a ghost cell is referred as ghost cell because the behavior of the ghost cell remains unaltered compared to the standard Chimera method (without the MBM).
- **Sending cell and mediating body cell:** The solution inside a mediating body cell is not physically valid and cannot be used for a sending cell. Therefore, a sending cell that is also a mediating body cell cannot send any information which impact the Chimera method. This type of cell is referred as *indefinite sending cell* and a strategy to reconstruct a solution inside this type of cell is detailed in the next section.
- **Sending cell and active cell:** The solution of an active cell is computed by the numerical scheme (MUSCL-Hancock in our case). The resulting solution is physically valid and can be used for a sending cell. Therefore, a sending cell that is also an active cell does not cause any problem for the Chimera method. This type of cell is referred as *valid cell*.

Table 4.1: Cell type combinations for the coupling of the Chimera method with the MBM.

$K_i \in \mathcal{V}$	Ghost cell ($\tilde{\mathcal{V}}$)	Sending cell (\mathcal{V}^s)
Mediating body cell (\mathcal{V}_{Γ_s})	Indefinite ghost cell	Indefinite sending cell
Active cell (\mathcal{V}_*)	Ghost cell	Valid cell

Among the identified types of cells, only two require a particular attention: the indefinite sending cells and the indefinite ghost cells. The first one requires a numerical strategy to recover a usable solution that can be sent to the other grid through the Chimera method. The second type of cell needs to be considered in order to assess the impact of the Mediating Body Method on ghost cells. The two types of cells are represented in Figure 4.11.

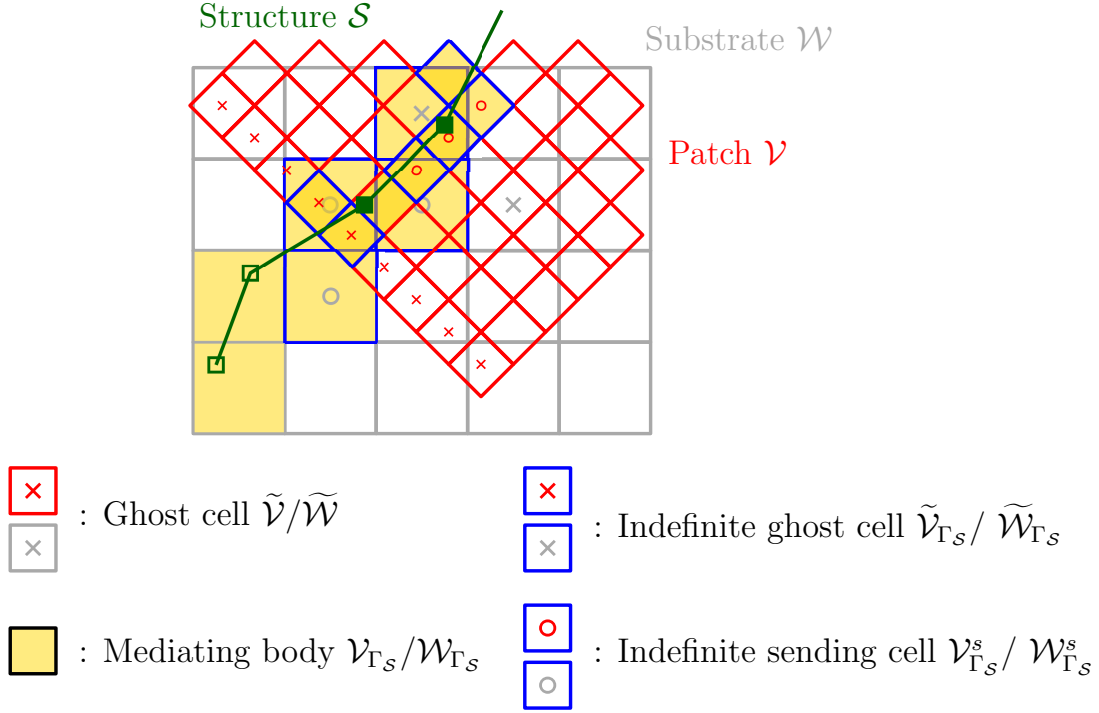


Figure 4.11: Indefinite sending cells and indefinite ghost cells when using the Mediating Body Method combined with the Chimera method with a number of ghost cell layers $k_{GC} = 1$ and a Chimera cell ratio $\chi = 2$.

C.1 - Handling of indefinite sending cells: the $+/-$ extrapolation

We consider a substrate indefinite sending cell $K_i \in \mathcal{W}^s$ belonging to the mediating body ($K_i \in \mathcal{W}_{\Gamma_S}$), therefore, $K_i \in \mathcal{W}^s \cap \mathcal{W}_{\Gamma_S}$. The same reasoning applies to any patch cell $K'_j \in \mathcal{V}^s \cap \mathcal{V}_{\Gamma_S}$. As K_i belongs to the substrate mediating body (\mathcal{W}_{Γ_S}), it does not contain a usable solution. Because of the Chimera method, K_i has to transfer information to the patch. As $K_i \in \mathcal{W}_{\Gamma_S}$, the structure crosses K_i . Therefore, K_i can be split into two subcells K_i^+ and K_i^- located on either side of the structure as shown in Figure 4.12. The objective is to reconstruct two solutions for the cell K_i , one for K_i^+ and one for K_i^- , using different sets of neighboring cells located on either side of the structure. This method is referred as $+/-$ extrapolation in the following.

In order to extrapolate a value for the subcells K_i^+ and K_i^- , we need to explore the neighboring cells of K_i . We define the $+/-$ adjacent crossed cell index sets:

$$\mathcal{L}_{i_{\Gamma_S}^s}^s \mathcal{W}^+ (0) = \left\{ j \in \gamma(i), K_j \in \mathcal{W}_{\Gamma_S}, d(\mathcal{S}, \underline{x}_j) > 0 \right\}, \quad (4.39)$$

$$\mathcal{L}_{i_{\Gamma_S}^s}^s \mathcal{W}^- (0) = \left\{ j \in \gamma(i), K_j \in \mathcal{W}_{\Gamma_S}, d(\mathcal{S}, \underline{x}_j) \leq 0 \right\}. \quad (4.40)$$

where $d(\underline{x}_j, \mathcal{S})$ is the signed distance between the structure \mathcal{S} and the barycenter \underline{x}_j of the cell K_j . $\gamma(i)$ is the index set of the cells adjacent to K_i . $\mathcal{L}_{i_{\Gamma_S}^s}^s \mathcal{W}^+ (0)$ and $\mathcal{L}_{i_{\Gamma_S}^s}^s \mathcal{W}^- (0)$ contain the indices of the cells adjacent to K_i that are crossed by the structure with respectively a positive signed distance to the structure and a negative signed distance to the structure. Those two sets contain the indices of mediating body cells.

As a mediating body cell do not contain a usable solution, we define the $+/-$ adjacent active cell index sets:

$$\mathcal{L}_{i_*^s}^s \mathcal{W}^+ (0) = \left\{ j \in \gamma(i), K_j \in \mathcal{W}_*, d(\mathcal{S}, \underline{x}_j) > 0 \right\} \quad (4.41)$$

$$\mathcal{L}_{i_*^s}^s \mathcal{W}^- (0) = \left\{ j \in \gamma(i), K_j \in \mathcal{W}_*, d(\mathcal{S}, \underline{x}_j) \leq 0 \right\}, \quad (4.42)$$

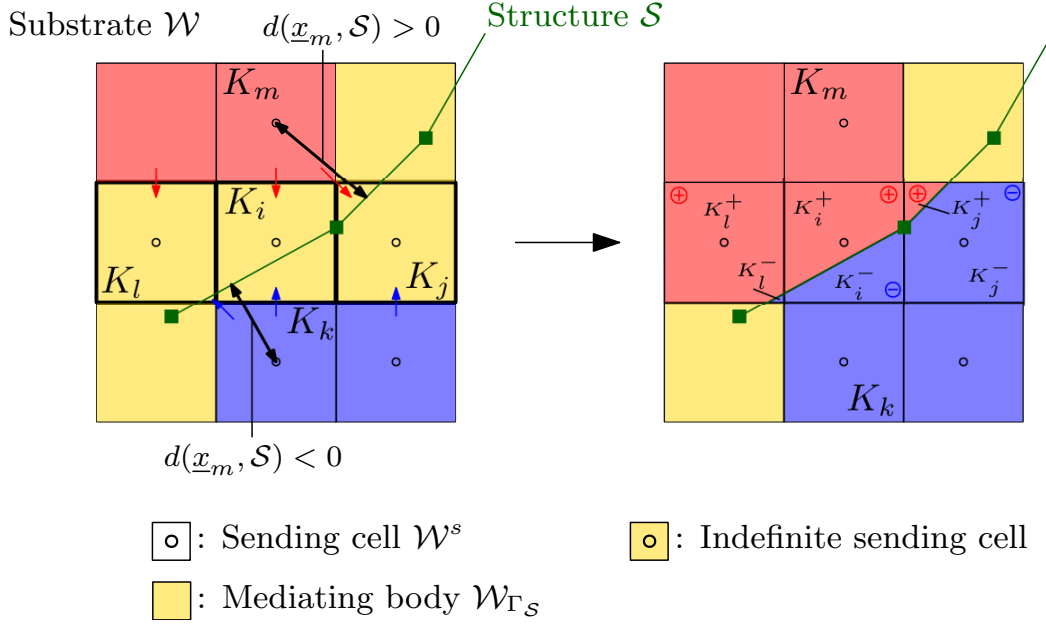


Figure 4.12: Indefinite sending cells subcell decomposition and extrapolation

$\mathcal{L}_{i_*}^{s\mathcal{W}^+}(0)$ and $\mathcal{L}_{i_*}^{s\mathcal{W}^-}(0)$ correspond to the indices of the active fluid cells adjacent to K_i with respectively a positive signed distance to the structure \mathcal{S} .

The $+/-$ extrapolation relies on the solution of the active cells sets $\mathcal{L}_{i_*}^{s\mathcal{W}^+}(0)$ and $\mathcal{L}_{i_*}^{s\mathcal{W}^-}(0)$. However, it can occur, that the set $\mathcal{L}_{i_*}^{s\mathcal{W}^+}(0)$ (or the set $\mathcal{L}_{i_*}^{s\mathcal{W}^-}(0)$) is empty, meaning that no adjacent cells to K_i with a positive (or negative) signed distance to the structure (\mathcal{S}) is an active cell.

In this case, successive exploration passes are performed until active neighboring cells with a positive (or negative) signed distance to the structure (\mathcal{S}) are found. Starting from, $\mathcal{L}_{i_*}^{s\mathcal{W}^+}(0)$ and $\mathcal{L}_{i_*}^{s\mathcal{W}^-}(0)$, these passes are performed avoiding repetitions in the neighboring cells explored. To do so, we define the crossed cell sets of the n -th pass ($n \in \mathbb{N}^*$) as:

$$\mathcal{L}_{i_*}^{s\mathcal{W}^+}(n) = \left\{ k \in \gamma(j), j \in \mathcal{L}_{i_*}^{s\mathcal{W}^+}(n-1), k \notin \mathcal{L}_{i_*}^{s\mathcal{W}^+}(n-1), K_k \in \mathcal{W}_{\Gamma_S}, d(\mathcal{S}, \underline{x}_j) > 0 \right\}, \quad (4.43)$$

$$\mathcal{L}_{i_*}^{s\mathcal{W}^-}(n) = \left\{ k \in \gamma(j), j \in \mathcal{L}_{i_*}^{s\mathcal{W}^-}(n-1), k \notin \mathcal{L}_{i_*}^{s\mathcal{W}^-}(n-1), K_k \in \mathcal{W}_{\Gamma_S}, d(\mathcal{S}, \underline{x}_j) \leq 0 \right\}. \quad (4.44)$$

which correspond to the indices of the cells adjacent to K_j that are mediating body cells with a positive (or negative) signed distance to the structure whose index dot not belong to $\mathcal{L}_{i_*}^{s\mathcal{W}^+}(n-1)$ (or $\mathcal{L}_{i_*}^{s\mathcal{W}^-}(n-1)$). In this definition, K_j is a mediating body cell neighboring K_i detected during the $n-1$ -th pass ($j \in \mathcal{L}_{i_*}^{s\mathcal{W}^+}(n-1)$, or $j \in \mathcal{L}_{i_*}^{s\mathcal{W}^-}(n-1)$).

Then, the active cell index sets of the n -th pass ($n \in \mathbb{N}^*$) are defined as:

$$\mathcal{L}_{i_*}^{s\mathcal{W}^+}(n) = \left\{ k \in \gamma(j), j \in \mathcal{L}_{i_*}^{s\mathcal{W}^+}(n-1), K_k \in \mathcal{W}_*, d(\mathcal{S}, \underline{x}_j) > 0 \right\}, \quad (4.45)$$

$$\mathcal{L}_{i_*}^{s\mathcal{W}^-}(n) = \left\{ k \in \gamma(j), j \in \mathcal{L}_{i_*}^{s\mathcal{W}^-}(n-1), K_k \in \mathcal{W}_*, d(\mathcal{S}, \underline{x}_j) \leq 0 \right\}, \quad (4.46)$$

which correspond to the indices of the cells adjacent to K_j that are active cells with a positive (or negative) signed distance to the structure. In this definition, K_j is a mediating body cell neighboring K_i detected during the $n-1$ -th pass ($j \in \mathcal{L}_{i_*}^{s\mathcal{W}^+}(n-1)$, or $j \in \mathcal{L}_{i_*}^{s\mathcal{W}^-}(n-1)$). On each side of the

structure, passes are performed independently, until

$$\exists n^+ \in \mathbb{N}, \mathcal{L}_{i_*}^{s\mathcal{W}^+}(n^+) \neq \{\emptyset\} \text{ and, } \forall n \in \mathbb{N}, n < n^+ \Rightarrow \mathcal{L}_{i_*}^{s\mathcal{W}^+}(n) = \{\emptyset\} \quad (4.47)$$

$$\text{and, } \exists n^- \in \mathbb{N}, \mathcal{L}_{i_*}^{s\mathcal{W}^-}(n^-) \neq \{\emptyset\} \text{ and, } \forall n \in \mathbb{N}, n < n^- \Rightarrow \mathcal{L}_{i_*}^{s\mathcal{W}^-}(n) = \{\emptyset\}. \quad (4.48)$$

The independence of the sets reduces the amount of neighbors explored. Indeed, on each side, the exploration stops as soon as at least one active cell is found. At the n -th pass ($n \in \mathbb{N}$), $\mathcal{L}_{i_{\Gamma_S}^s\mathcal{W}^+}(n)$ and $\mathcal{L}_{i_{\Gamma_S}^s\mathcal{W}^-}(n)$ are explored only if an $n + 1$ -th pass is needed.

Figure 4.13, illustrates the different steps of the $+/-$ extrapolation procedure and its contribution to the Chimera sending. Once $\mathcal{L}_{i_*}^{s\mathcal{W}^{+/-}}(n^{+/-})$ are filled, $+/-$ states can be extrapolated for both subcells $K_i^{+/-}$ (see Figure 4.13-3) based on the conservative variables as the following:

$$\underline{U}_i^{\mathcal{W}^+} = \frac{\sum_{j \in \mathcal{L}_{i_*}^{s\mathcal{W}^+}(n^+)} |K_j| \underline{U}_j^{\mathcal{W}}}{\sum_{j \in \mathcal{L}_{i_*}^{s\mathcal{W}^+}(n^+)} |K_j|}, \quad \underline{U}_i^{\mathcal{W}^-} = \frac{\sum_{j \in \mathcal{L}_{i_*}^{s\mathcal{W}^-}(n^-)} |K_j| \underline{U}_j^{\mathcal{W}}}{\sum_{j \in \mathcal{L}_{i_*}^{s\mathcal{W}^-}(n^-)}. \quad (4.49)$$

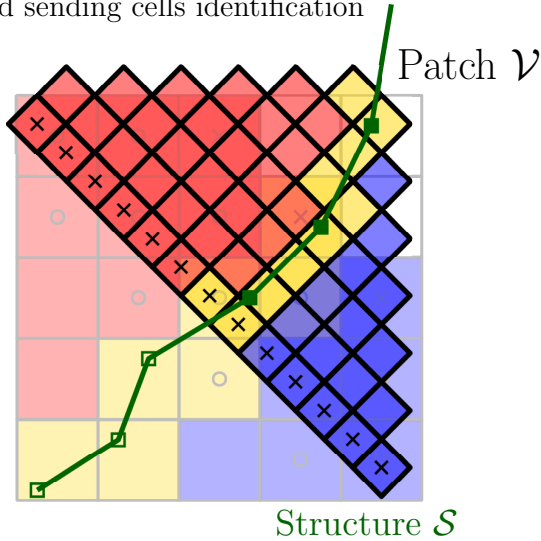
As a result, the indefinite sending cells have two different values that can be sent to their corresponding ghost cells.

Let $\tilde{K}_j' \in \tilde{\mathcal{V}}$ be a ghost cell receiving from K_i . As detailed in section 2.2, the intersection $\tilde{K}_j' \cap K_i$ is computed with the resulting barycenter of the intersection \tilde{x}_{ji} . The signed distance of the center of the intersection to the structure, written $d(\mathcal{S}, \tilde{x}_{ji})$, is computed in order to decide which $+/-$ state K_i will provide to \tilde{K}_j' (see Figure 4.13-4). If $d(\mathcal{S}, \tilde{x}_{ji}) > 0$, then $\underline{U}_i^{\mathcal{W}^+}$ is provided and if $d(\mathcal{S}, \tilde{x}_{ji}) \leq 0$, then $\underline{U}_i^{\mathcal{W}^-}$ is provided. If the mediating body remains constant over time, the $+/-$ neighbor detection does not need to be repeated as the definitions of $\mathcal{L}_{i_*}^{s\mathcal{W}^{+/-}}(n^{+/-})$ are directly dependent from the mediating body definition.

Remark. *The orientation of the normal to the structure \mathcal{S} is arbitrary and needs to be set at the beginning of the computation. As long as the orientations of the surfaces are not inverted during the calculation, the procedure is not impacted by the orientation of the normal to the structure (\mathcal{S}).*

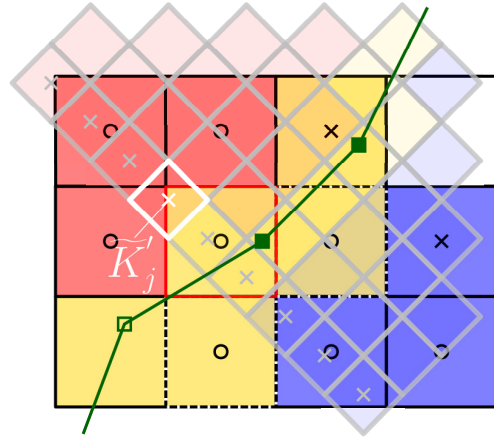
Remark. *While the second order Chimera method and more specifically the gradient reconstruction has been adapted to work with the Mediating Body Method on active sending cells \mathcal{U}_*^s , $\mathcal{U} = \{\mathcal{V}, \mathcal{W}\}$ even near the mediating body region, the extrapolated sending cell contribution is limited to first order due to the complexity of computing a gradient within an undefined area. Also, due to the $+/-$ subcell decomposition, two gradients would be required.*

1) Mediating body construction + ghost cells and sending cells identification



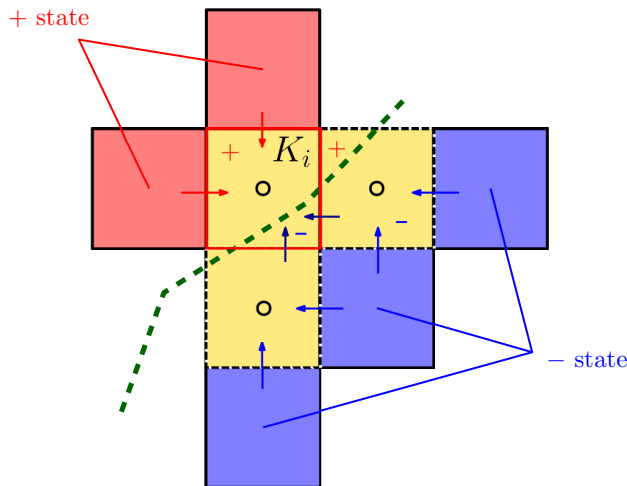
- x : Ghost cell $\tilde{\mathcal{V}}/\tilde{\mathcal{W}}$
- o : Sending cell $\mathcal{V}^s/\mathcal{W}^s$
- : Mediating body $\mathcal{W}_{\Gamma_S}/\mathcal{V}_{\Gamma_S}$

2) Detection of $\mathcal{W}^s \cap \mathcal{W}_{\Gamma_S}$



- : Low pressure state
- : High pressure state

3) +/- state extrapolation for $\mathcal{W}^s \cap \mathcal{W}_{\Gamma_S}$



4) Chimera sending with appropriate +/- state depending on the sign of $d(\tilde{x}_{ji}, \mathcal{S})$

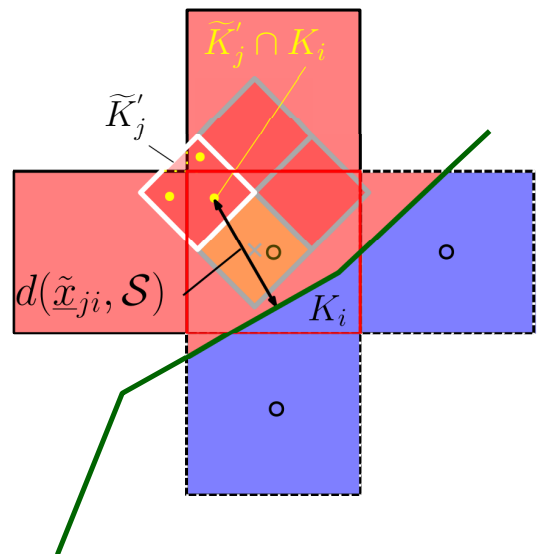


Figure 4.13: Indefinite sending cells complete treatment.

C.2 - Handling of indefinite ghost cells

The next cells that we are interested in are the indefinite ghost cells. In this section, we consider a patch ghost cell $\tilde{K}'_i \in \tilde{\mathcal{V}}$ that also belongs to the patch mediating body (\mathcal{V}_{Γ_s}), therefore, $\tilde{K}'_i \in \tilde{\mathcal{V}} \cap \mathcal{V}_{\Gamma_s}$ is an indefinite ghost cell. The same reasoning applies to any substrate indefinite ghost cell $\tilde{K}'_j \in \tilde{\mathcal{W}} \cap \mathcal{W}_{\Gamma_s}$. We consider $K'_k \in \mathcal{V}_c$ such that $K'_k \in \gamma(i)$ is adjacent to \tilde{K}'_i as shown in Figure 4.14. The ghost cell \tilde{K}'_i is intersected by a sending cell $K_j \in \mathcal{W}^s$. As a ghost cell, \tilde{K}'_i is used to ensure an appropriate flux $F_{ik}^{\mathcal{V}} = \hat{F}(\bar{U}_{ik}^{\mathcal{V}}, \bar{U}_{ki}^{\mathcal{V}}, n_{ik})$ at the interface $\mathcal{F}_{ik}^{\mathcal{V}} \subset \Gamma_{\tilde{\mathcal{V}}}$ of the resolved fluid domain (see Fig. 4.14) which corresponds to the cleaned patch \mathcal{V}_c . As we have $\tilde{K}'_i \in \mathcal{V}_{\Gamma_s}$, the face $\mathcal{F}_{ik}^{\mathcal{V}}$ also acts as a boundary condition of the active fluid domain \mathcal{V}_* as detailed in section 4.2.1.D.

In the Chimera method, the flux computation is carried out by the numerical scheme itself (MUSCL-Hancock in this work, see section 1.2.5). In the MBM, the flux computation at the active fluid/mediating body interface is overloaded by numerical functions. Therefore, the flux at the interface $\mathcal{F}_{ik}^{\mathcal{V}}$ will be computed using the MBM instead of the solution sent by the Chimera method which results in a non-issue.

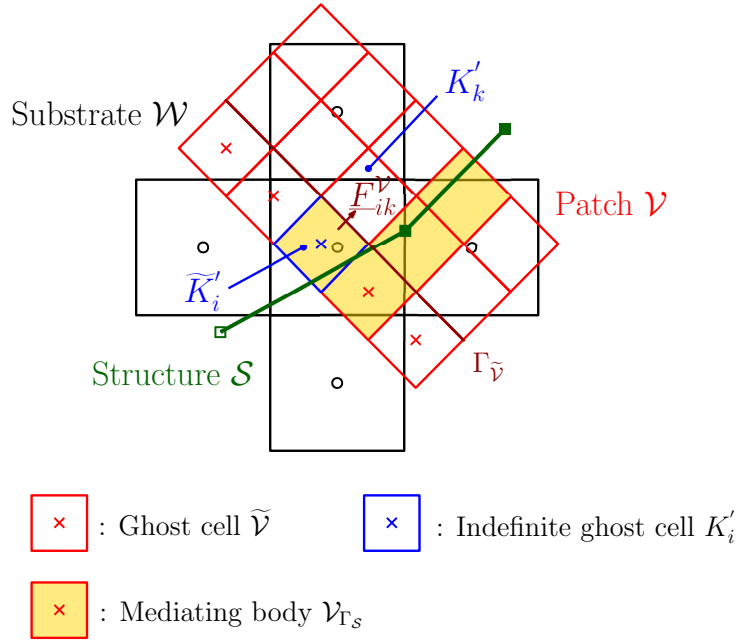


Figure 4.14: Indefinite ghost cell impact on the fluid domain.

One could think about preventing the appearance of indefinite ghost cells by enforcing the condition:

$$\tilde{\mathcal{U}} \cap \mathcal{U}_{\Gamma_s} = \{\emptyset\}, \quad \mathcal{U} = \{\mathcal{V}, \mathcal{W}\}, \quad (4.50)$$

during the construction of the mediating body, which would result in the absence of indefinite ghost cells and would reduce the number of mediating body cells. This solution is considered in the following example (see Fig. 4.15). We suppose that the structure \mathcal{S} separates two fluid cavities at rest in one dimension but with a pressure jump Δp .

If the cell \tilde{K}'_i is treated as a ghost cell instead of a mediating body cell, part or all of its solution comes from an extrapolated sending cell $K_j \in \mathcal{W}^s$. When the structure \mathcal{S} crosses the barycenter \tilde{x}_{ij} of the intersection $\tilde{K}'_i \cap K_j$, the intersection distance to the structure, $d(\tilde{x}_{ij}, \mathcal{S})$ changes sign and therefore the ghost cell \tilde{K}'_i will start receiving the high pressure state whereas the cell K'_k contains the low pressure state. At the interface $\mathcal{F}_{ik}^{\mathcal{V}}$, hermeticity of the system breaks as the high pressure state leaks into the low pressure one. However, if the ghost cell \tilde{K}'_i is treated as a mediating body

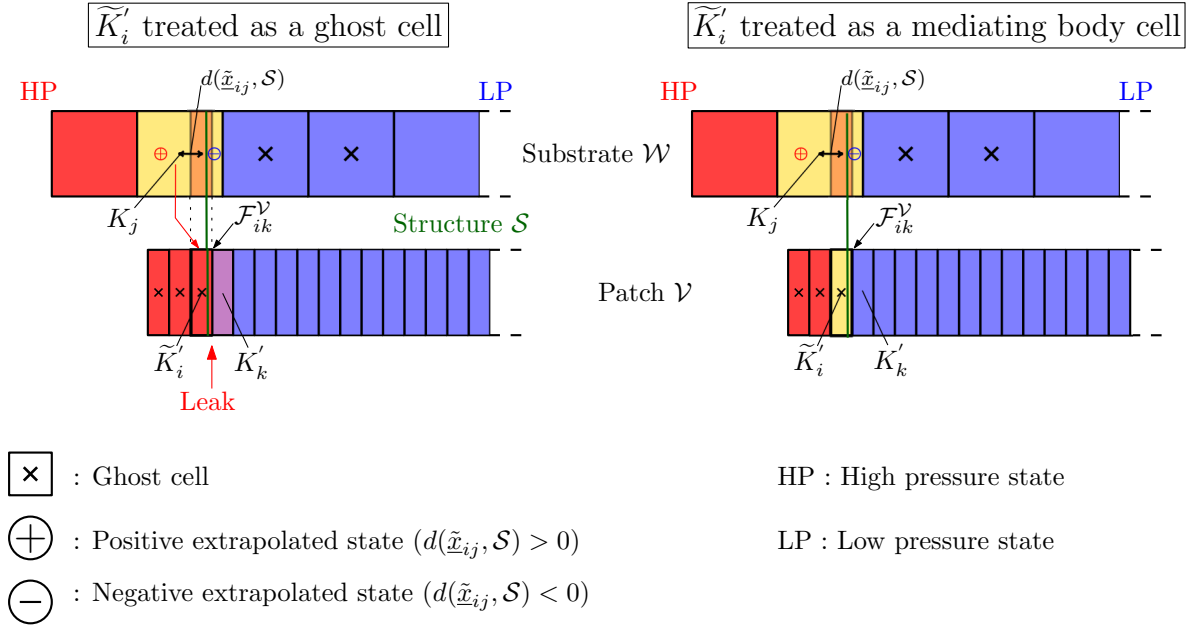


Figure 4.15: Indefinite ghost cell treatment possibilities.

cell, the leak disappears as the face $\mathcal{F}_{ik}^{\mathcal{V}}$ is handled by the mediating body flux functions. As a result, including the ghost cells inside the mediating body ensures that the Chimera-Mediating Body Method preserves hermeticity of overlapping grid system.

D . Time integration scheme of the Chimera-MBM

After introducing the indefinite sending cells and the indefinite ghost cells which result from the coupling of the Chimera method with the MBM, we have provided a numerical strategy to reconstruct a solution inside the sending cells. We also have reviewed the benefit of the indefinite ghost cells which preserve the hermeticity of the Chimera-Mediating Body Method. In this section, we present the modifications made to the integration scheme presented in section 4.2.1.F for the MBM only. We detail the time integration scheme for a pair of fluid grids, a substrate (\mathcal{W}) and a patch (\mathcal{V}). The fluid integration is performed using the second order MUSCL-Hancock integration presented in section 1.2.5. The Chimera sending is based on the second order sending presented in section 2.2.3.B. The time integration scheme of the Chimera-MBM, depicted, in Figure 4.16, is carried out using the following steps:

1. The structure velocity $\dot{\mathbf{U}}^{n+\frac{1}{2}}$ at $t^{n+\frac{1}{2}}$ and its position \mathbf{U}^{n+1} at t^{n+1} are computed explicitly from its acceleration $\ddot{\mathbf{U}}^n$ at t^n , using the central different scheme presented in section 4.1.4.
2. The mediating bodies $\mathcal{W}_{\Gamma_s}^{n+1}$ and $\mathcal{V}_{\Gamma_s}^{n+1}$ are computed using the structure position \mathbf{U}^{n+1} following the procedure described in section 4.2.2.A. If needed, the indefinite active cells are extrapolated as detailed in section 4.2.1.E
3. The velocities at the interfaces of the mediating bodies are computed from the structure velocity $\dot{\mathbf{U}}^{n+\frac{1}{2}}$ following the procedure described in section 4.2.1.B.
4. The ghost cells $\tilde{\mathcal{W}}$ and $\tilde{\mathcal{V}}$ are updated using the first order Chimera exchange detailed in section 2.2.3.A. This step is called *uninformed sending* and allows ghost cells to be part of a $+/-$ neighboring active cell set if these ghost cell receive from active cells (see Appendix C.1).

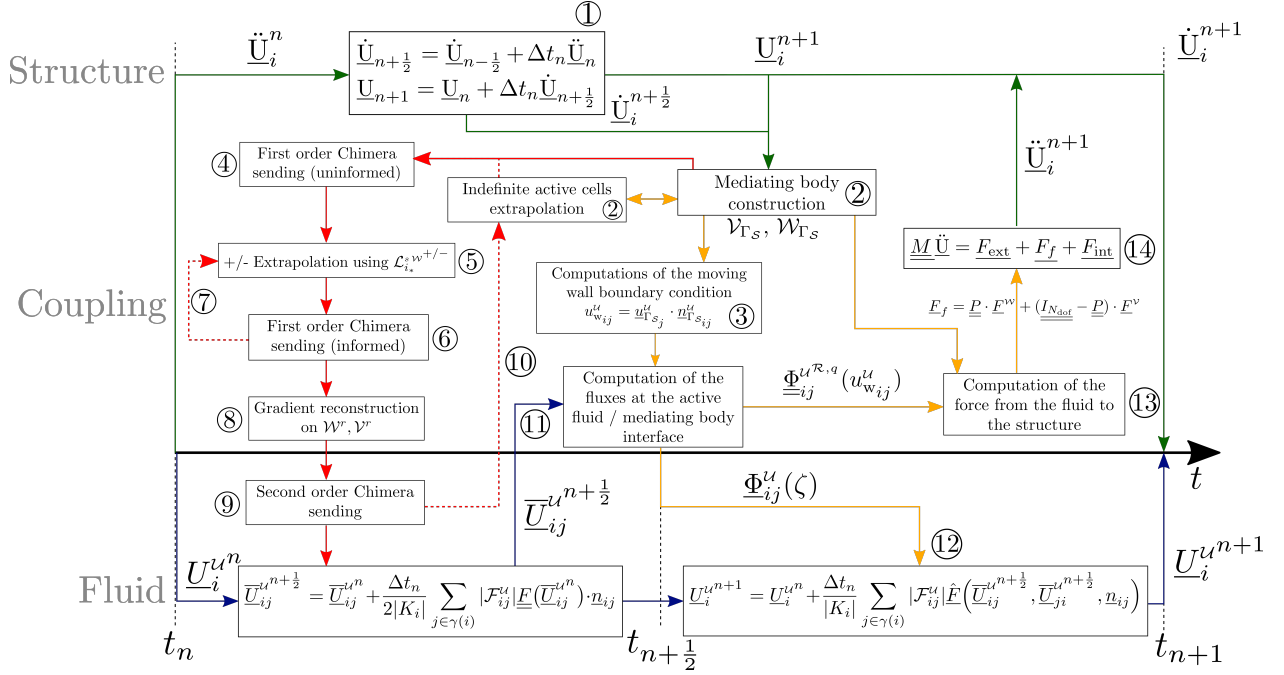


Figure 4.16: Time integration scheme for the Chimera-Mediating Body Method with a MUSCL-Hancock integration for the fluid and a central difference scheme for the structure.

5. The \pm states are extrapolated using the procedure detailed in section 4.2.2.C.1.
6. The ghost cells $\widetilde{\mathcal{W}}$ and $\widetilde{\mathcal{V}}$ are re-updated using the first order Chimera exchange (section 2.2.3.A). It is called *informed sending* (see Appendix C.1).
7. Steps 5 and 6 are performed a second time to allow ghost cells to be part of a \pm neighboring active cell set even if these ghost cells receive from indefinite sending cells as detailed in Appendix C.2.
8. The solution gradient is computed and limited inside \mathcal{V}^r and \mathcal{W}^r for ghost cell solution reconstruction.
9. The ghost cells $\widetilde{\mathcal{W}}$ and $\widetilde{\mathcal{V}}$ are updated using the second order Chimera exchange presented in section 2.2.3.B.
10. The MBM extrapolation as well as steps 3 to 9 are performed a second time as a correction loop in case indefinite active cells use ghost cells for the MBM extrapolation as explained in Appendix C.3.
11. The fluid interface states \underline{U}_{ji}^u , $(i, j) \in \Omega_{\mathcal{U}_*} \times \gamma(i)$, $\mathcal{U} = \{\mathcal{V}, \mathcal{W}\}$, are reconstructed and updated by half a time step $\frac{\Delta t_n}{2}$ using the first two steps of the MUSCL-Hancock time integration *i.e.* the steps 1 and 2 presented in section 1.2.5.
12. The fluid variables \underline{U}^u , $\mathcal{U} = \{\mathcal{V}, \mathcal{W}\}$ are updated to the time t^{n+1} from the interface states $\underline{U}^{u^{n+1/2}}$ using the fluxes presented in section 4.2.1.D.2, the HLLC solver presented in section 1.2.3 and the ALE emulation as detailed in [92].
13. The force vector \underline{F}_f imposed by the fluid to the structure is computed from the patch and substrate flux momentum computed in the fluid problem between t^n and t^{n+1} following the procedure detailed in section 4.2.1.C and section 4.2.2.B.

14. Finally, the structure acceleration \ddot{U}^{n+1} is computed using the finite element equilibrium equation presented in section 4.1.4 (see equation 4.6).

The Chimera-MBM method has been implemented inside the C++ in-house code MANTA. The developed method has the benefit of being flexible as no additional constraints on the grids are added apart from those due to the Chimera method or the MBM which are already designed to be as flexible as possible. In the next section, we assess the method on validation test cases.

4.3 - Numerical validation of the method and applications

In the previous sections, we have presented a coupling of the developed Chimera method in a finite volume context with the Mediating Body Method for large fluid-structure displacements in overlapping grid computations. In the following, the impact of the coupling of the Chimera method with the Mediating Body Method is assessed using two different test cases. Each test case involves a structure crossing the Chimera boundary. The first test is a free piston separating two cavities at rest with a pressure jump. This test allows us to compare the numerical results to an analytical solution for both the piston displacements and the fluid dynamics. The last test is a "large scale" three-dimensional problem involving three fluid grids including two patches and a deformable structure.

For both test cases, the Chimera-MBM configuration is compared to single grid configurations using the Mediating Body Method for fluid-structure interactions. The finite volume method set-up is kept constant across all the cases which corresponds to a MUSCL-Hancock scheme with the HLLC Riemann solver and the K-Dubois limiter with $k = 0.75$ presented in section 1.2. The integration scheme is second order accurate in both time and space and the second order Chimera sending is used with the standard detection as the default configuration.

4.3.1 - One-dimensional free piston

This test is a simple configuration involving fluid-structure interactions with large structure displacements. It consists in a free membrane of thickness $e = 1.35 \cdot 10^{-3}$ m and height $l = 0.2$ m referred as piston separating two fluid chambers initially at rest inside a closed tube of length $L = 60$ m and height l as shown in Figure 4.17. The computational domain extends from $-\frac{L}{2}$ to $\frac{L}{2}$ and the membrane is initially located at $x_s = -1.8$ m. The left and right states of the fluid chambers on each sides of the piston are given by:

$$\begin{pmatrix} \rho_L \\ u_L \\ p_L \end{pmatrix} = \begin{pmatrix} 0.2 \text{ kg.m}^{-3} \\ 0 \\ 0.2 \text{ Pa} \end{pmatrix}, \quad \begin{pmatrix} \rho_R \\ u_R \\ p_R \end{pmatrix} = \begin{pmatrix} 0.125 \text{ kg.m}^{-3} \\ 0 \\ 0.1 \text{ Pa} \end{pmatrix}, \quad (4.51)$$

The chambers have a pressure jump $\Delta p = p_L - p_R = 0.1$ Pa initiating the displacement of the membrane that generates a compression wave on the right-hand side, in the low pressure region and a rarefaction wave on the left-hand side, in the high pressure region of the tube. The pressure values have been chosen in order to keep the flow isentropic in the compression wave region and to prevent the formation of a shock wave (see Appendix D). The membrane parameters are the following: $\rho_s = 2710 \text{ kg} \cdot \text{m}^{-3}$, $E = 10^{-4}$ GPa and $\nu = 0.33$, where ρ_s , E and ν are respectively the piston density, Young modulus and Poisson ratio. The piston is modelled with a single four-node quadrilateral MITC4 shell element as mentioned in section 4.1.3.

In order to measure the impact of the Chimera-MBM locally, the free piston case is assessed using two different grid configurations respectively referred as split configuration and patched configuration like the advection test case presented in section 2.4.2. Computations are performed up to the dimensionless time $t_f^* = t \dot{u}_\infty / L = 0.106$, where $\dot{u}_\infty \approx 0.277 \text{ m.s}^{-1}$ is the asymptotic speed of the piston in an infinite domain. The CFL number is set to 0.9. The analytical solution of the problem is presented in Appendix D. At $t^* = t_f^*$, the piston barycenter is located at $x = x_s \approx 2.04327$ m. The computational domain is long enough so that the boundary conditions of the domain do not impact the solution.

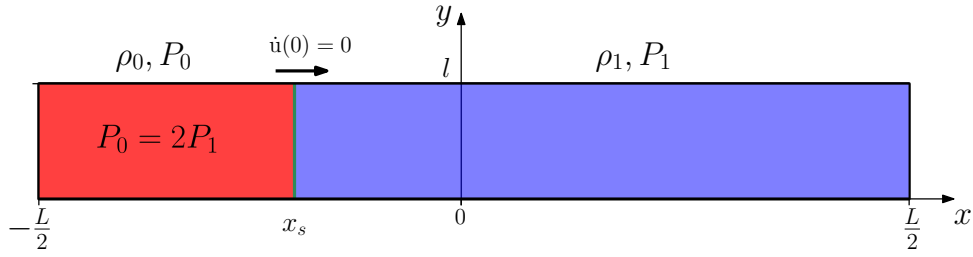


Figure 4.17: Free piston case presentation.

A . Split configuration

The first assessed configuration is the split grid configuration and it is illustrated in Figure 4.18. The computational domain is split at $x_i = 0$ with a substrate on the left-hand side and a patch on the right-hand side. For the Chimera grid configurations, the parameter N_{cells} is used to set the cell size on the substrate ($h_{\mathcal{W}}$) with N_{cells} corresponding to the number of grid cells over the length L . On the patch, the cell size $h_{\mathcal{V}}$ is obtained from $h_{\mathcal{W}}$ with the cell ratio χ . Finally, for the Chimera configurations, the patch is shifted by the value δ_S set to $0.6 h_{\mathcal{W}}$ in order to avoid coincident grids between the patch (\mathcal{V}) and the substrate (\mathcal{W}) as shown in Figure 4.18. In order to monitor potential oscillations caused by a brutal refinement, when χ varies, the single grid configurations are set-up like Chimera configurations with $\delta_S = 0$ (see Fig. 4.18). In the presence of oscillations in the solution, single grid configurations allow us to determine if the perturbations are caused by the Chimera-MBM or by the brutal refinement as we have seen in section 2.4.3.B. As a result, single grid configurations also depend on N_{cells} and χ .

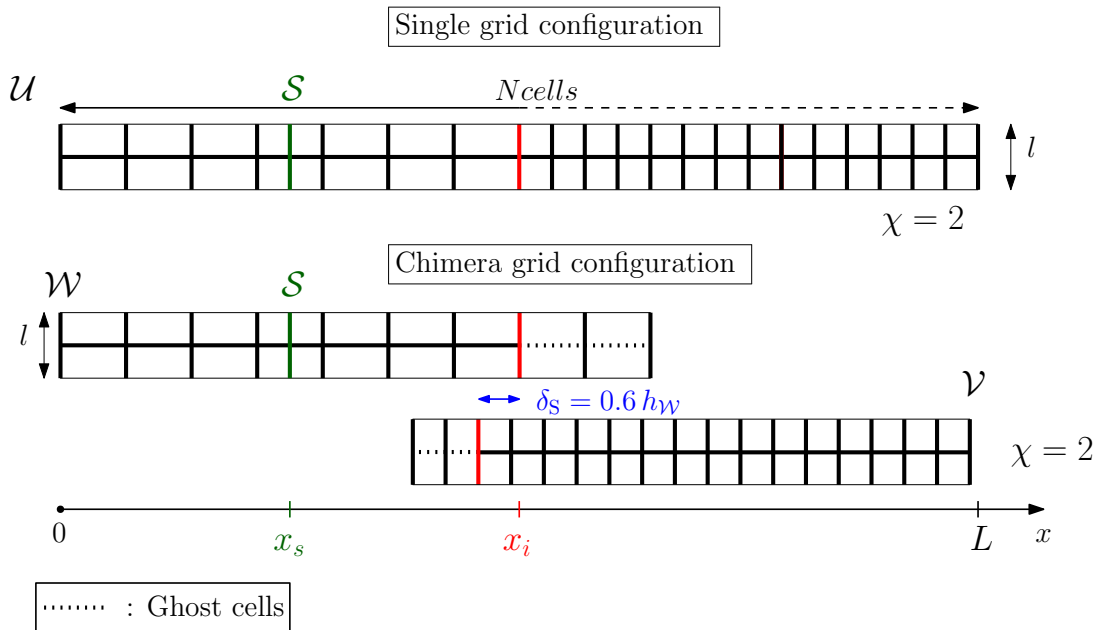


Figure 4.18: Free piston split configuration.

The results are compared to the analytical solution presented in Appendix D and the L_1 norm of the density error is computed as in equation 2.23.

A.1 - Impact of the Chimera-Mediating Body Method on the order of convergence

To begin with, we study the impact of the Chimera-Mediating Body Method (Chimera-MBM) on the order of convergence compared to the standard Mediating Body Method (MBM). Five different grids are used from the coarsest with $N_{cells} = 300$ to the finest with $N_{cells} = 4800$. The cell ratio (χ) is set to 1 meaning that cell sizes between the patch and the substrate are equal ($h_{\mathcal{V}} = h_{\mathcal{V}}$) for the Chimera configurations. For the single grid configurations, $\chi = 1$ means that the cell size is uniform over the domain.

Figure 4.19 and Figure 4.20 represent the fluid density, velocity and pressure profiles over the entire domain with respectively $N_{cells} = 300$ and $N_{cells} = 1200$ for both the Chimera-MBM and the MBM with the split configuration. The Chimera method combined with the Mediating Body Method does not alter the solution profile as the two solutions are superimposed to the naked eye.

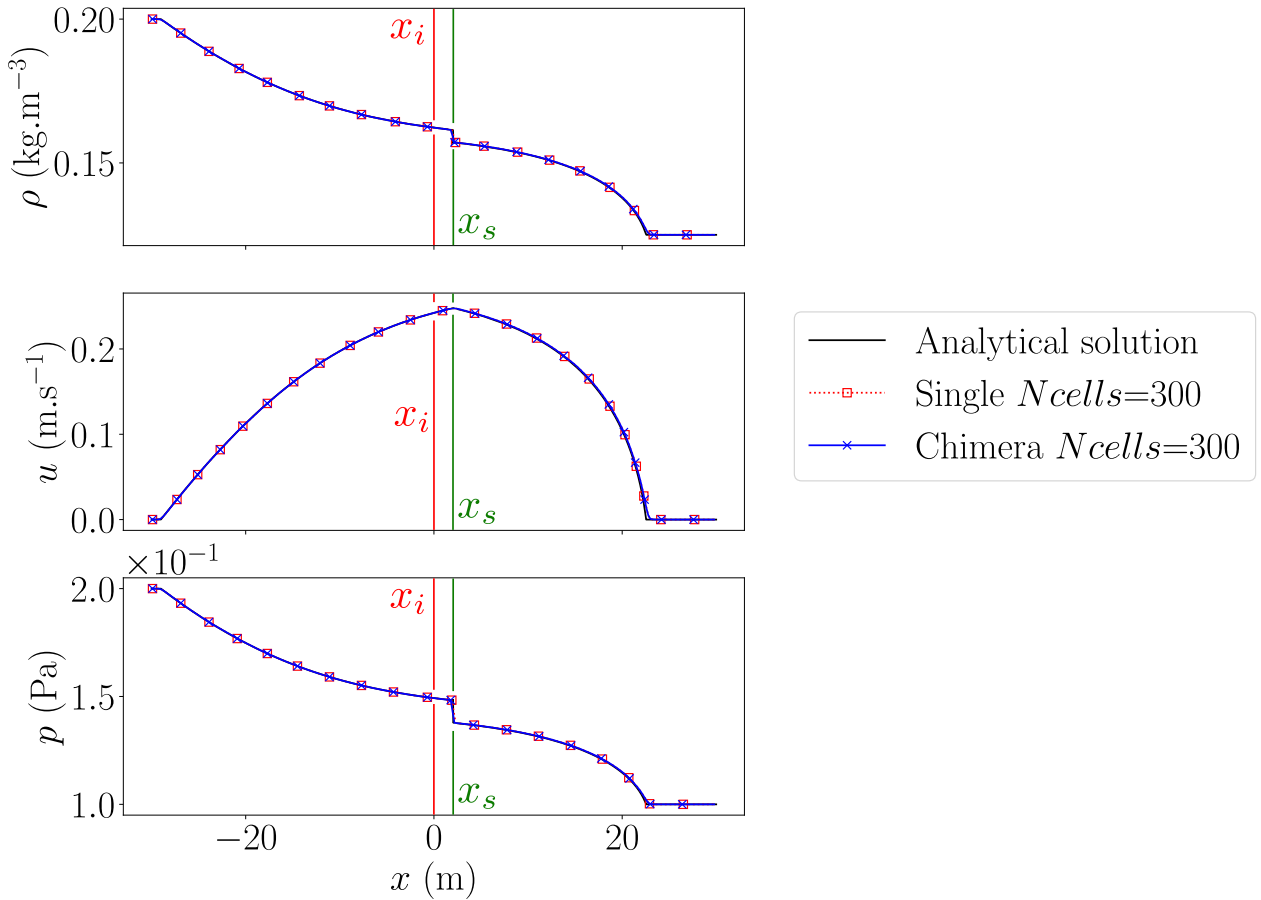


Figure 4.19: Free piston density (ρ), velocity (u) and pressure (p) profiles of the split configuration for the Chimera-MBM case as well as the single grid MBM case when $\chi = 1$ and $N_{cells} = 300$ at $t = t_f^*$. The markers on the plots are not representative of the number of points of the numerical solution.

The grid convergence results for both the MBM and Chimera-MBM are plotted on Figure 4.21. Overall, the use of multiple fluid grids does not seem to affect the order of convergence. This is confirmed by Table 4.2 where the values of $L_1(\varepsilon_\rho)$ are reported. Overall, when $\chi = 1$, the Chimera-MBM is equivalent to the single grid MBM with a difference between the two configurations lower than 1% for every value of N_{cells} tested. As a result, the Chimera-MBM does not alter the order of convergence of the solution compared to the single grid MBM.

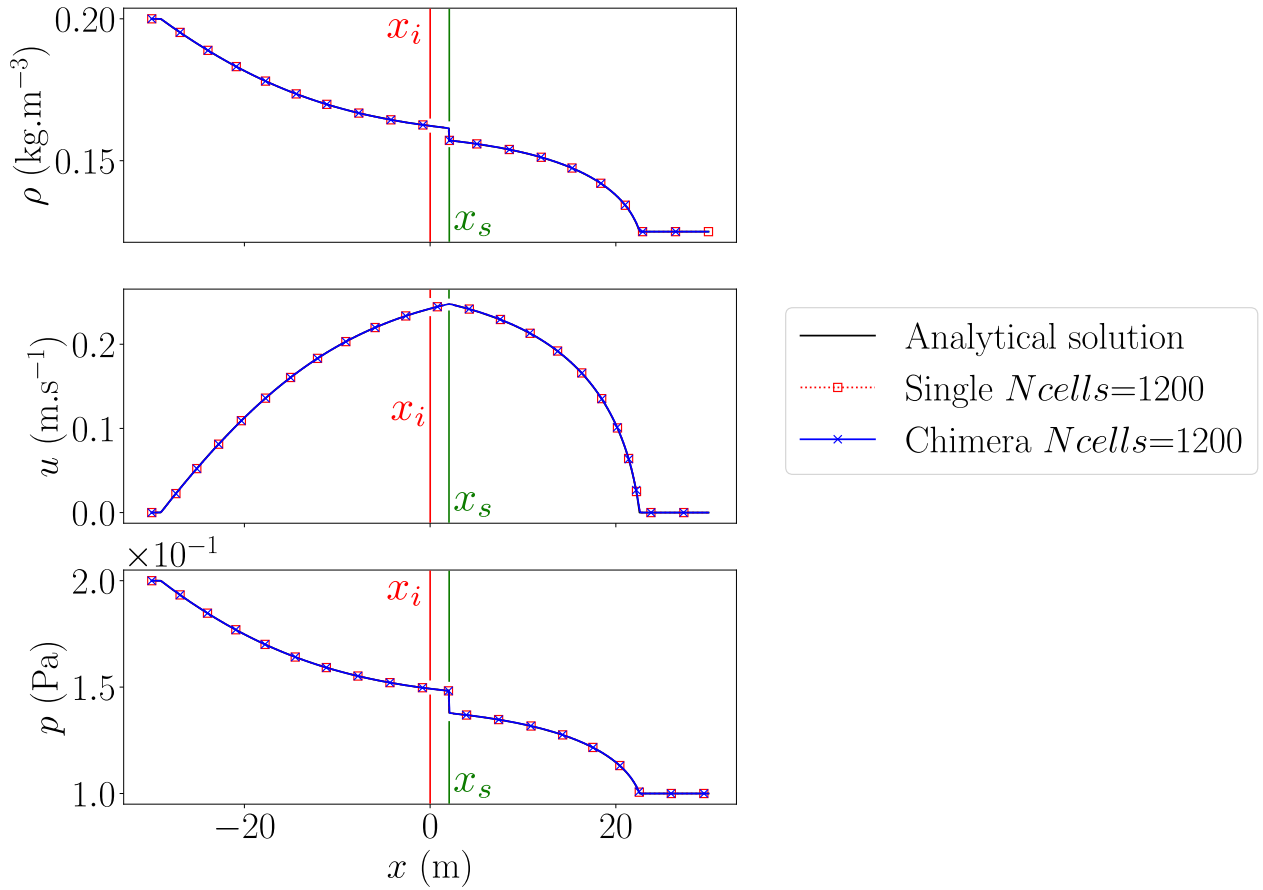


Figure 4.20: Free piston density (ρ), velocity (u) and pressure (p) profiles of the split configuration for the Chimera-MBM case as well as the single grid MBM case when $\chi = 1$ and $N_{cells} = 1200$ at $t = t_f^*$. The markers on the plots are not representative of the number of points of the numerical solution.

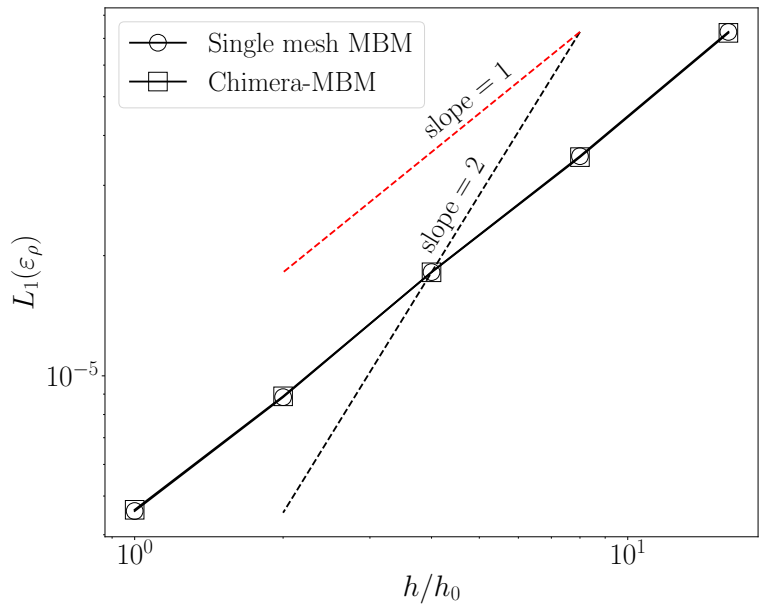


Figure 4.21: Grid convergence analysis of the free piston test case with the split configuration and equivalent cell sizes between the patch and the substrate ($\chi = 1$).

Table 4.2: Grid convergence analysis of the free piston with the split configuration: results on density (ρ) errors obtained with a single grid MBM as well as with the present Chimera-MBM using a patch with same grid spacing as the substrate ($\chi = 1.0$) but with non-coincident grids ($\delta_S = 0.6 h_W$).

Ncells	$L_1(\varepsilon_\rho)$ error ($\times 10^5$)		Order of convergence p	
	Single	Chimera	Single	Chimera
300	7.266	7.226	1.03	1.03
600	3.549	3.530	0.96	0.96
1200	1.819	1.817	1.04	1.03
2400	8.843e-1	8.886e-1	0.95	0.94
4800	4.586e-1	4.619e-1	-	-

A.2 - Impact of the cell ratio (χ)

Now we focus on the impact of cell size discrepancies between the patch and the substrate ($\chi \neq 1$). We review successively configurations where the piston is transferred from a coarse grid to a finer one and when the piston is transferred from a fine grid to a coarser one. In both configurations, the Chimera results are compared to an equivalent single grid one with a brutal refinement or coarsening at $x = x_i$.

A.2.1 - Impact of the Chimera-MBM on a coarse-to-fine transfer

First, we consider a finer patch with $N_{cells} = 300$ and χ goes from 1 up to 16. In Figure 4.22, the density profiles are plotted for $\chi = 1$, $\chi = 2$, and $\chi = 4$ for both the Chimera-MBM and the MBM while Figure 4.22 contains the density profile of both configurations for $\chi = 4$, $\chi = 8$ and $\chi = 16$. We can see that a brutal refinement generates a perturbation that is transported with the flow for both the Chimera-MBM and MBM solutions. This perturbation is generated inside the flow when the piston crosses the Chimera interface (or the refinement interface for the MBM single grid configuration). However, the Chimera-MBM oscillation is more pronounced even though it does not seem to affect the global shape of the density profile.

For the Chimera configuration, this perturbation is generated by indefinite sending cells extrapolating a value using the $+/-$ extrapolation when the piston enters the patch. The perturbation is generated as long as indefinite sending cells are sending the $+/-$ extrapolated solutions to ghost cells. However, once the structure is completely immersed inside the patch, perturbations are no longer emitted but the perturbations already present are transported in the coarse-to-fine direction which corresponds to the positive x -direction in this grid configuration.

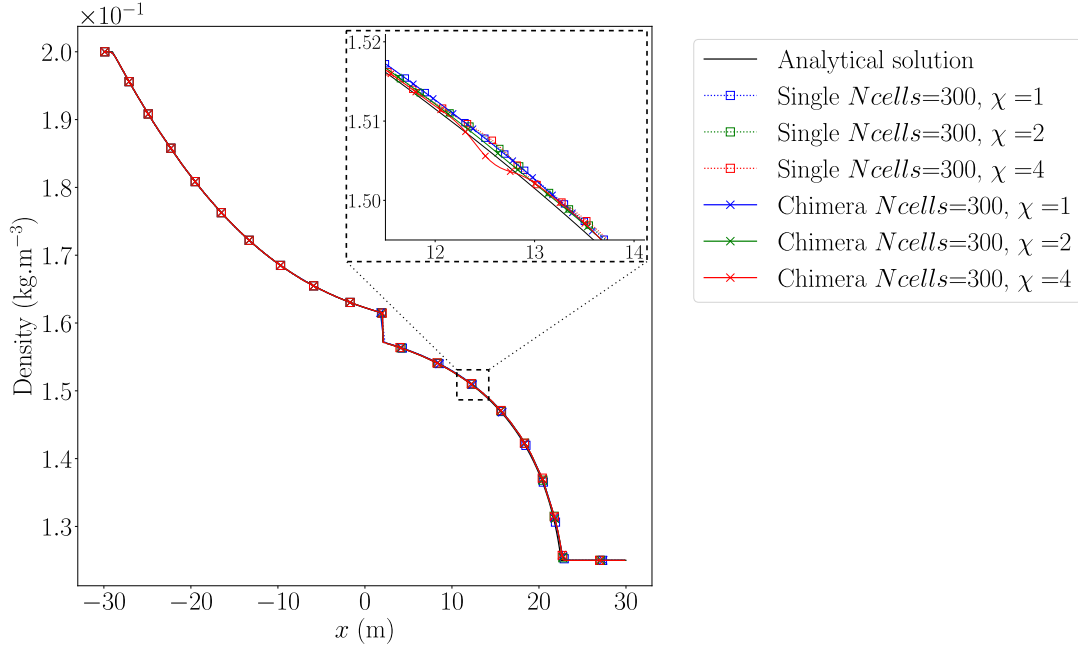


Figure 4.22: Free piston density (ρ) profile of the split configuration for the Chimera-MBM as well as the single grid MBM when $N_{cells} = 300$ and $\chi = 1, 2, 4$ at $t^* = t_f^*$. The markers on the plots are not representative of the number of points of the numerical solution.

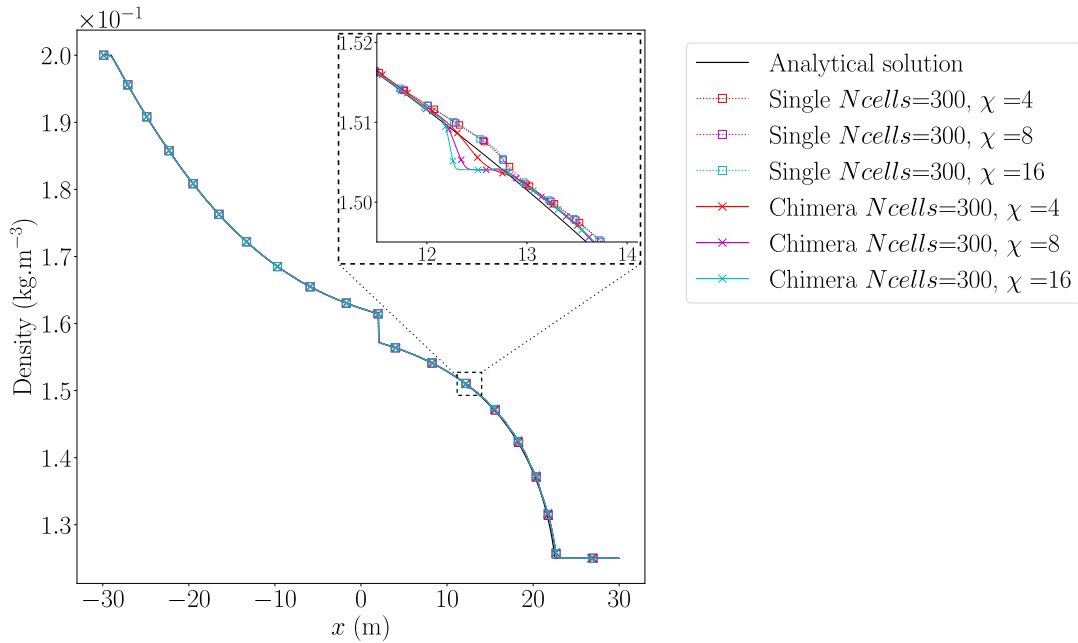


Figure 4.23: Free piston density (ρ) profile of the split configuration for the Chimera-MBM as well as the single grid MBM when $N_{cells} = 300$ and $\chi = 4, 8, 16$ at $t^* = t_f^*$. The markers on the plots are not representative of the number of points of the numerical solution.

In Table 4.3, the values of $L_1(\varepsilon_\rho)$ are reported for both the Chimera-MBM and the MBM with $N_{cells} = 300$ and $\chi = 1 - 16$. Refining the patch does improve the overall solution for the Chimera-MBM as the error decreases when χ increases up to 8. The single grid follows the same trend which means that the Chimera-MBM does not impact the global solution significantly when compared to the single grid MBM. However, the improvement on the solution is limited by the coarse part of the mesh (see Table 4.2 for reference). When $\chi = 16$, the quality of the solution is slightly deteriorated

but remains equivalent to the single grid MBM. It is worth noting that the Chimera-MBM method behaves in a similar way as the second order Chimera method for fluid simulations when refining the patch.

Table 4.3: Cell ratio analysis of the free piston with the split configuration: results on density (ρ) errors obtained with a single grid MBM as well as with the present Chimera-MBM using a finer grid in the patch region ($N_{cells} = 300, \chi \geq 1$).

χ	$L_1(\varepsilon_\rho) (\times 10^5)$		Equivalent N_{cells} on the patch
	Single mesh MBM	Chimera-MBM	
1	7.266	7.226	300
2	6.672	6.420	600
4	6.386	6.104	1200
8	6.126	5.899	2400
16	6.054	6.073	4800

A.2.2 - Impact of the Chimera-MBM on a fine-to-coarse transfer

Finally, we consider a coarser patch by setting $N_{cells} = 4800$ and χ goes from 1 up to 0.0625 (1/16) which corresponds to a patch 16 times coarser than the substrate. In Figure 4.24, we can see that a similar perturbation to the one observed with a finer patch occurs with a coarser patch in the Chimera-MBM configurations. However, the oscillation is located inside the substrate which is finer than the patch and the perturbation is not generated by the single grid MBM. Therefore, the perturbation is generated at the interface of the finest grid and transported in the coarse-to-fine direction which corresponds to the negative x -direction in this grid configuration.

This perturbation impacts the values of $L_1(\varepsilon_\rho)$ reported in Table 4.4 as we can observe a growing difference between the Chimera-MBM results and the MBM results when χ decreases (the patch becomes coarser).

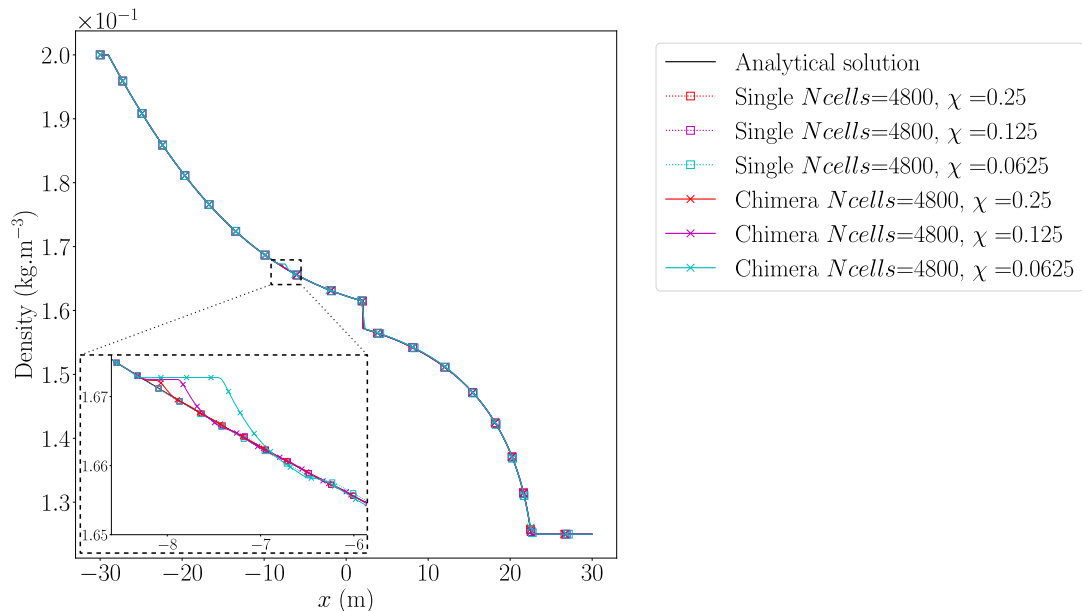


Figure 4.24: Free piston density (ρ) profile of the split configuration for the Chimera-MBM as well as the single grid MBM when $N_{cells} = 4800$ and $\chi = 0.25, 0.125, 0.0625$ at $t^* = t_f^*$. The markers on the plots are not representative of the number of points of the numerical solution.

From the two studies carried out, we can see that a perturbation is generated at the interface of the finest grid between the patch and the substrate and then transported in the coarse-to-fine

Table 4.4: Cell ratio analysis of the free piston case with the split configuration: results on density (ρ) errors obtained with a single grid MBM as well as with the present Chimera-MBM using a coarser grid in the patch region ($N_{cells} = 4800, \chi \leq 1$).

χ	$L_1(\varepsilon_\rho) (\times 10^6)$		Equivalent N_{cells} on the patch
	Single mesh	Chimera	
1	4.586	4.619	40
0.5	5.216	5.197	80
0.25	6.767	7.274	160
0.125	10.662	13.095	320
0.0625	20.599	29.860	640

direction. For the study involving a finer patch, the coarse-to-fine direction is the positive x -direction whereas for the study involving a coarser patch, the coarse-to-fine direction is the negative x -direction.

This indicates that the perturbation results from a coarse-to-fine transfer. As a result, the Chimera-Mediating Body Method can be used with cell ratios higher than 8 but local perturbations will be generated at the interface of the finest of the two grids and transported along the coarse-to-fine direction.

A.3 - Discussion on conservation

We now focus on the impact on mass conservation of the Chimera method coupled with the Mediating Body Method for different values of N_{cells} and cell ratio (χ). The impact on conservation is monitored using the relative error on total mass of the system over time which is computed at each time step as the following:

$$\varepsilon(\rho(t^*)) = \frac{|\int \rho(t^*, \underline{x}) dV - \int \rho(0, \underline{x}) dV|}{\int \rho(0, \underline{x}) dV}. \quad (4.52)$$

Figure 4.25 illustrates the variation of the system mass over time for different mesh resolution from $N_{cells} = 300$ up to $N_{cells} = 4800$ with $\chi = 1$. We can see that mass conservation is not altered compared to the single grid configuration up to $t^* \approx 0.06$ which corresponds to the time the piston enters the patch. When the piston transitions from the substrate to the patch, a drop followed by a peak in the total mass relative error occurs.

This trend is explained by Figure 4.26. As we are reconstructing a merged domain $\mathcal{W} + \mathcal{V}$ from a composite domain with non-matching grids (a patch and a substrate), the last resolved cell on the left side of the substrate is cut by the first resolved cell on the right side of the patch. Therefore, when the structure intersects the last cell of the substrate but not the patch yet, the system mediating body occupies a smaller volume compared to the previous intersected substrate cells and the system mass relative error decreases (left side of Fig. 4.26).

When the structure progresses and enters the first resolved cell of the patch, it is still in the last cell of the substrate, therefore, the perceived system mediating body volume on the merged domain $\mathcal{W} + \mathcal{V}$ is higher compared the previous intersected substrate cells and the system mass relative error increases (right side of Fig. 4.26).

When the piston leaves the Chimera exchange zone, the levels of system mass relative error are equivalent to the corresponding single grid configuration with equal N_{cells} but with a constant shift in the variation due to the grid shift $\delta_S = 0.6 h_{\mathcal{W}}$.

In the end, the grid merging procedure of the Chimera-Mediating Body Method for post processing captures the variations in the total mass of the system induced by structure crossing the Chimera interface. However, these variations are negligible as they disappear once the structure is fully immersed inside the patch (or the substrate) and the system comes back to levels of error equivalent to the single grid configuration.

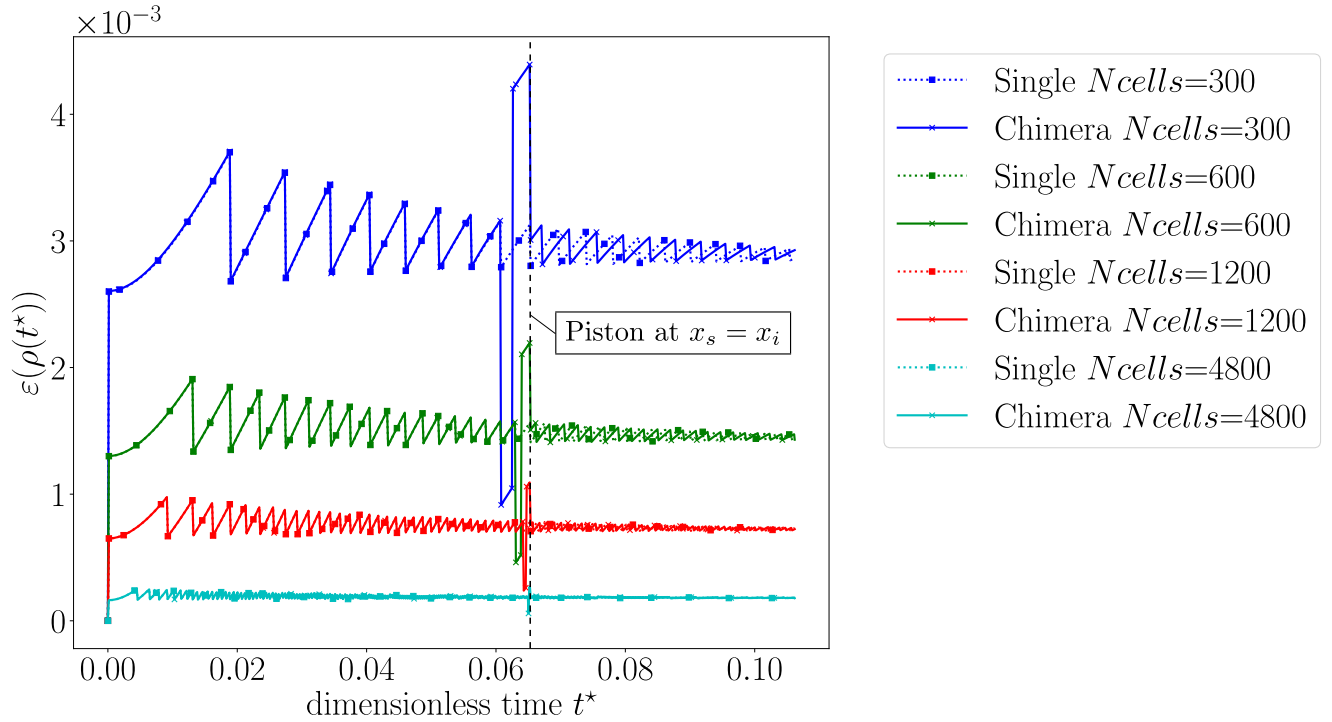


Figure 4.25: Free piston system mass relative error of the split configuration for the Chimera-MBM as well as the single grid MBM when N_{cells} varies and $\chi = 1$ over time. The markers on the plots are not representative of the number of points of the numerical solution.

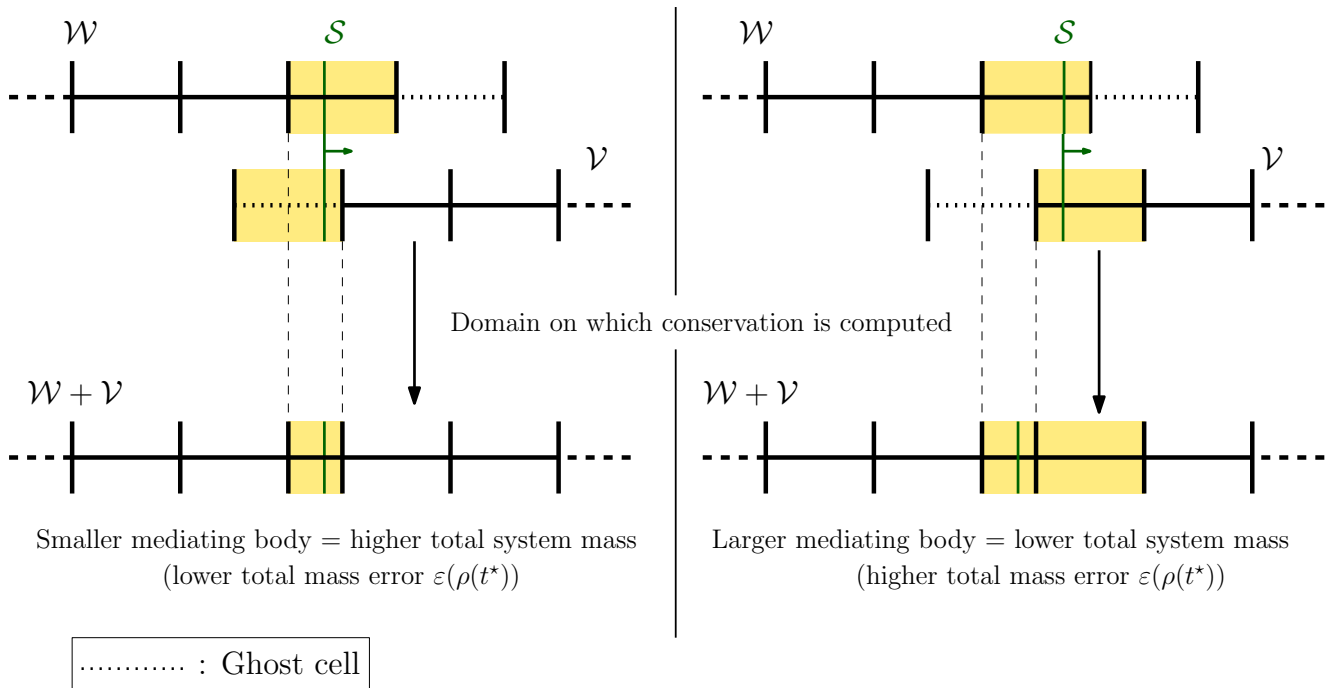


Figure 4.26: Explanation of the variations in system total mass at the patch boundaries when the structure enters the patch.

In the following, N_{cells} is kept fixed at 300 and the patch is refined (χ increases from 1 to 16). Refining the patch allows to lower the mass conservation defect as seen in Figure 4.27 and Figure 4.28 where the variation of the system mass are plotted for both the single grid MBM and the Chimera-MBM with different values of χ . Apart from the transition, no particular impact on

system mass is observed from the Chimera-MBM configuration as it remains equivalent to the single grid MBM case for every value of χ tested.

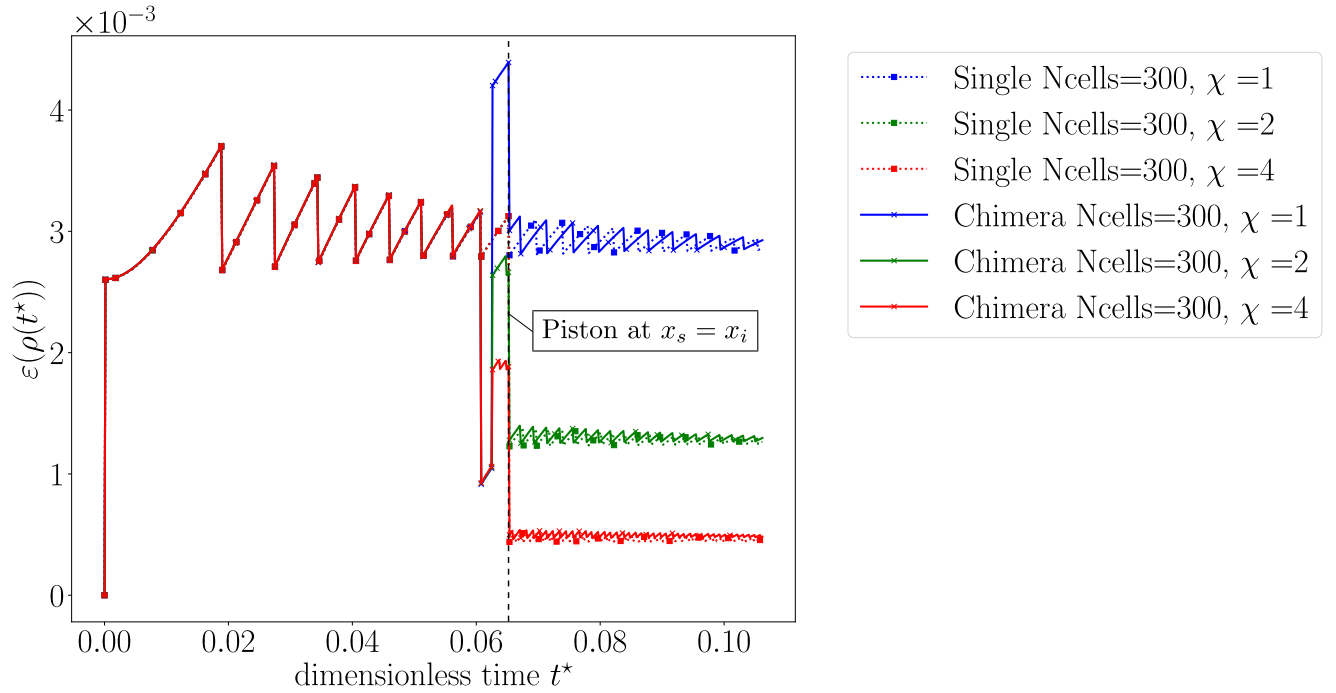


Figure 4.27: Free piston system mass relative error of the split configuration for the Chimera-MBM as well as the single grid MBM when $N_{cells} = 300$ and $\chi = 1, 2$ and 4 (finer patch) over time. The markers on the plots are not representative of the number of points of the numerical solution.

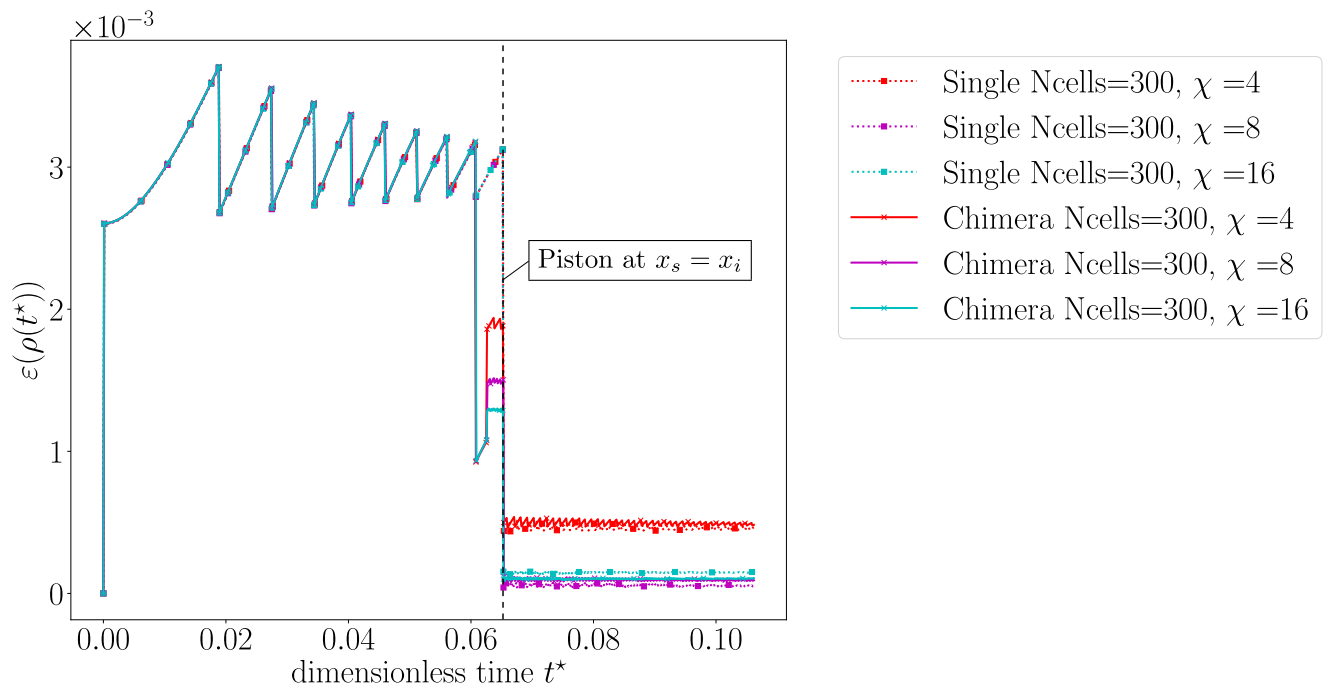


Figure 4.28: Free piston system mass relative error of the split configuration for the Chimera-MBM as well as the single grid MBM when $N_{cells} = 300$ and $\chi = 4, 8$ and 16 (finer patch) over time. The markers on the plots are not representative of the number of points of the numerical solution.

Finally, N_{cells} is kept fixed at 4800 and the patch is coarsened (χ decreases from 1 to $\frac{1}{16}$).

Figure 4.29 and Figure 4.30 represent the relative system mass error over time for both the single grid MBM and the Chimera-MBM configurations when the piston travels from a fine grid to a coarser one. The coarser portion deteriorates the total mass relative error for both the Chimera-MBM and the single grid MBM configurations. Similarly to the coarse-to-fine mass conservation study, the Chimera-Mediating Body Method does not seem to alter mass conservation of the system when a fine-to-coarse grid transition is at play compared to an equivalent single grid configuration.

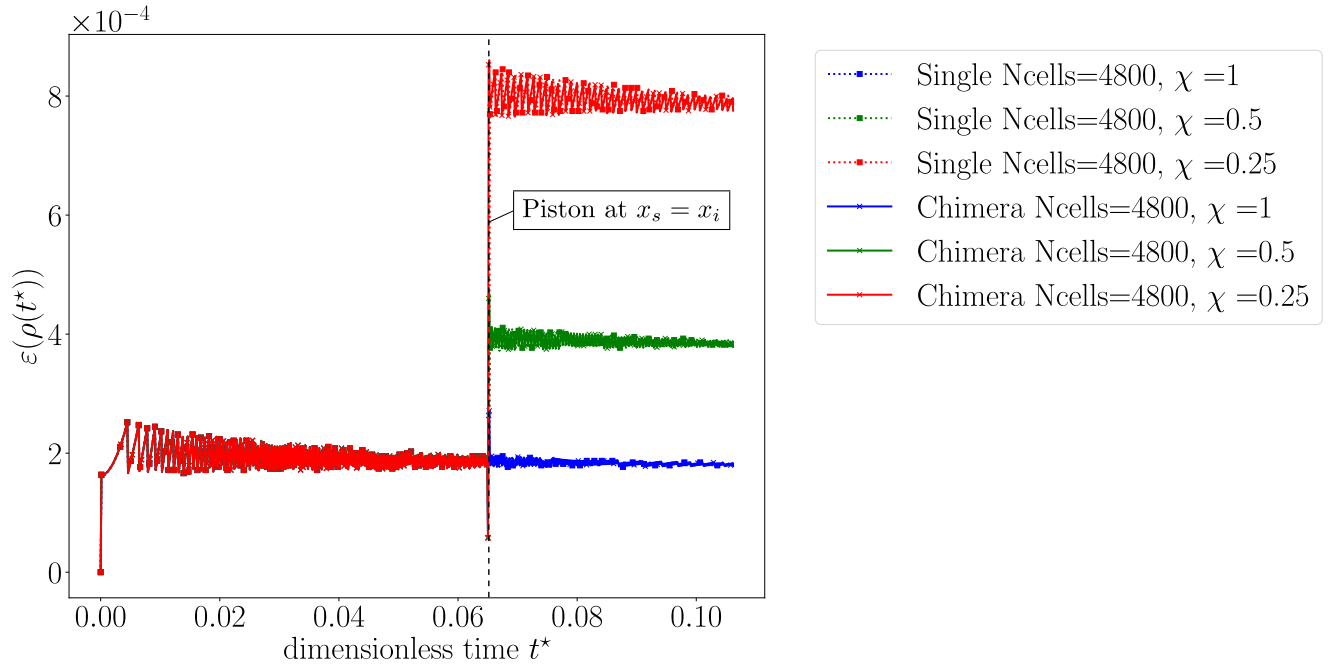


Figure 4.29: Free piston system mass relative error of the split configuration for the Chimera-MBM as well as the single grid MBM when $N_{cells} = 300$ and $\chi = 1, 0.5$ and 0.25 (coarser patch) over time. The markers on the plots are not representative of the number of points of the numerical solution.

As a conclusion, the Chimera-MBM does not add significant additional error on system mass conservation compared to a single grid MBM in a split grid configuration. The system mass errors are equivalent between the Chimera-MBM and the single grid MBM. The system mass error is related to the grid resolution which is lowered when using a finer patch. The Chimera exchange zone can generate temporary perturbations in the system mass but these perturbations do not remain once the piston has crossed the exchange zone.

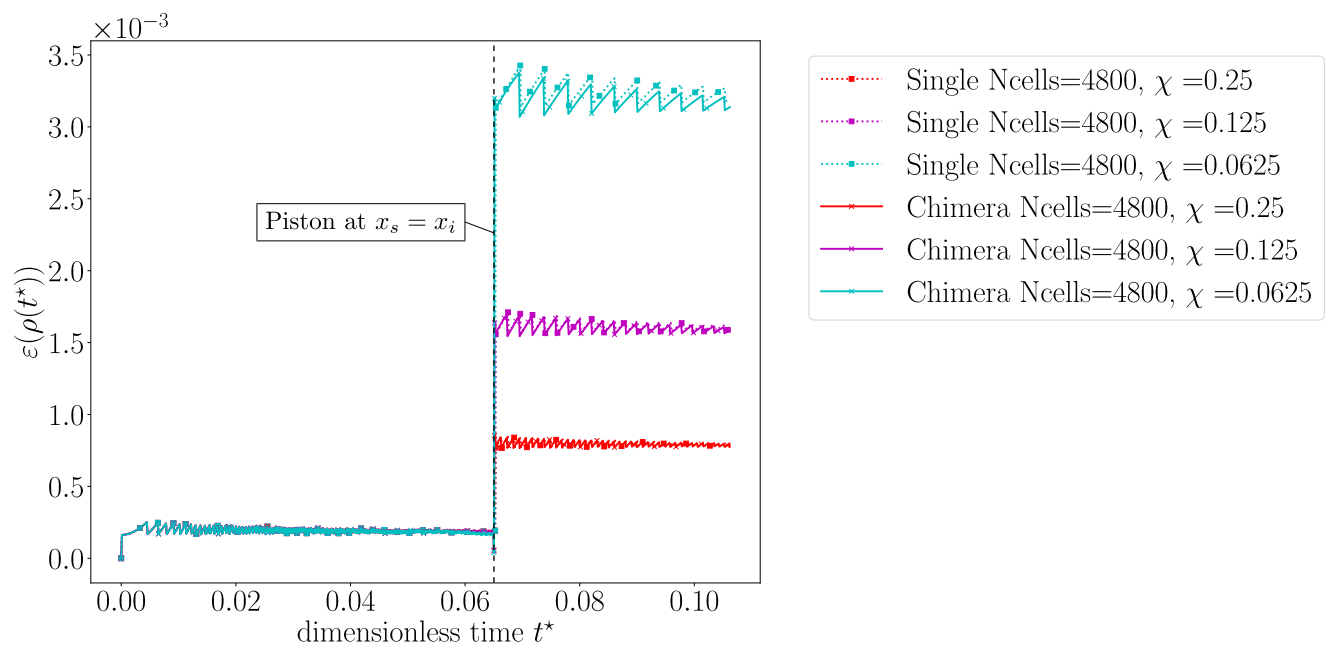


Figure 4.30: Free piston system mass relative error of the split configuration for the Chimera-MBM as well as the single grid MBM when $N_{cells} = 300$ and $\chi = 0.25, 0.125$ and 0.0625 (coarser patch) over time. The markers on the plots are not representative of the number of points of the numerical solution.

B . Patched configuration

The second configuration tested is the patched domain and it is illustrated in Figure 4.31. The computational domain is based on a one-dimensional domain of length L such that $x \in [-\frac{L}{2}, \frac{L}{2}]$. For the single grid configuration, the domain is decomposed into three sections: the left section corresponds to the interval $[-\frac{L}{2}, -\frac{L}{50}]$ and the right section corresponds to the interval $[\frac{L}{50}, \frac{L}{2}]$. The cell size in both sections is set using the parameter N_{cells} which corresponds to the number of cells over the length L . The middle section is located between $x = -\frac{L}{50}$ and $x = \frac{L}{50}$ and is set using the cell ratio (χ). For the Chimera configuration, the substrate (\mathcal{W}) corresponds to a standard one-dimensional domain of length L such that $x \in [-\frac{L}{2}, \frac{L}{2}]$ containing N_{cells} cells. The patch (\mathcal{V}) is built as the middle section of the single grid configuration but two ghost cells are added at each ends of the patched grid. Then the patch is shifted by the value $\delta_S = 0.3 h_{\mathcal{W}}$ in order to ensure non-coincident grids between the patch and the substrate. This Chimera configuration allows us to assess the impact of a moving structure entering and leaving a patched domain.

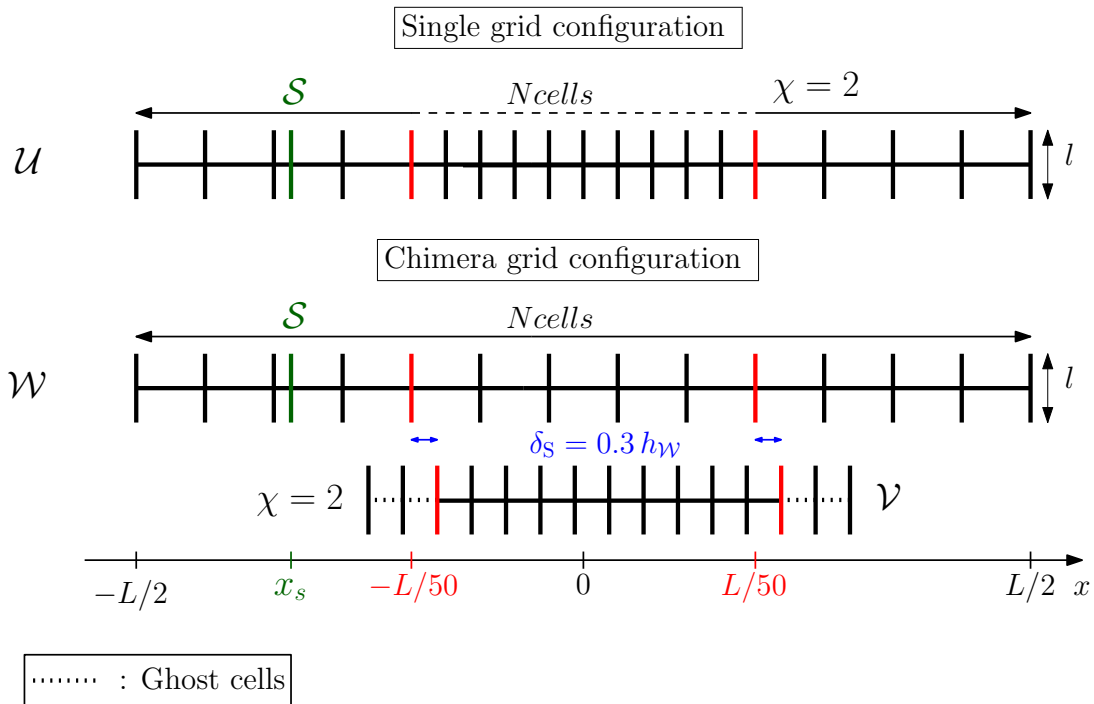


Figure 4.31: Free piston patched configuration.

B.1 - Impact of the Chimera-Mediating Body Method on the order of convergence

Firstly, we focus on the impact of the Chimera-Mediating Body Method on the order of convergence when $\chi = 1$ and we increase N_{cells} . Five different grids are used from the coarsest with $N_{cells} = 300$ to the finest with $N_{cells} = 4800$. The cell ratio (χ) is set to 1. Figure 4.32 represents the fluid density, velocity and pressure profiles over the entire domain with $N_{cells} = 300$ for both the Chimera-MBM and the MBM with the patched grid configuration. The Chimera method combined with the Mediating Body Method does not alter the solution profile as the two solutions remain superimposed to the naked eye.

Figure 4.33 represents the results of the L_1 error on density when the parameter N_{cells} increases for a constant cell ratio $\chi = 1$. The Chimera-Mediating Body Method does not present a significant difference compared to the single grid mediating body case. When the grid resolution increases, the spatial error decreases and the error caused by the Chimera exchange is exhibited. Looking at the

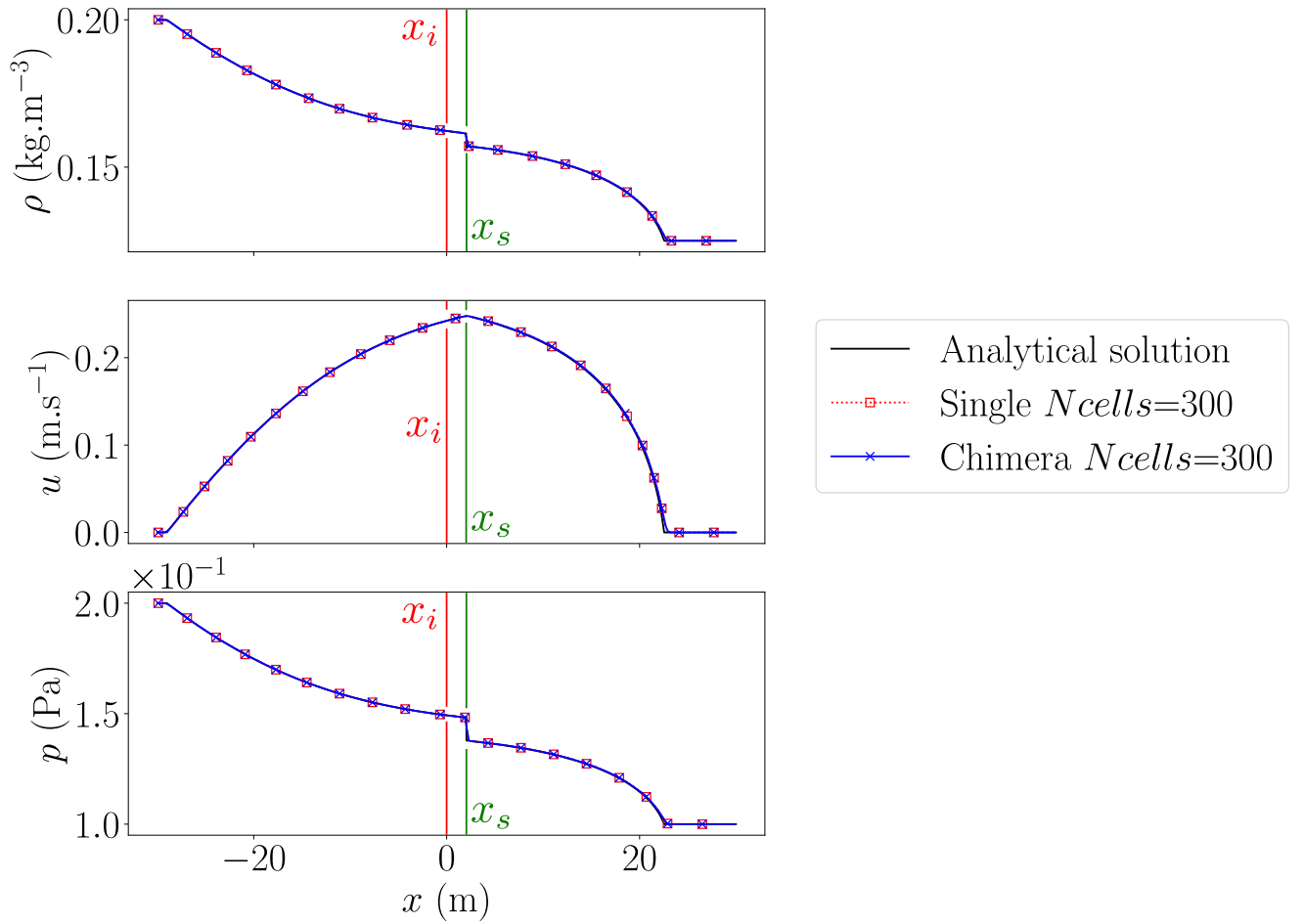


Figure 4.32: Free piston density (ρ), velocity (u) and pressure (p) profiles of the patched configuration for the Chimera-MBM as well as the single grid MBM when $\chi = 1$ and $N_{cells} = 300$ at $t = t_f^*$. The markers on the plots are not representative of the number of points of the numerical solution.

error figures presented in Table 4.5, the Chimera-Mediating Body Method error remains acceptable as it does not exceed $\pm 5\%$ compared to the single grid configuration. Also, it is worth noting that the Chimera-Mediating Body Method does not impact the order of convergence significantly but tends to reduce it by 1 – 2% compared to the single mesh results. Overall the Chimera-MBM provides equivalent results to the single grid MBM when $\chi = 1$.

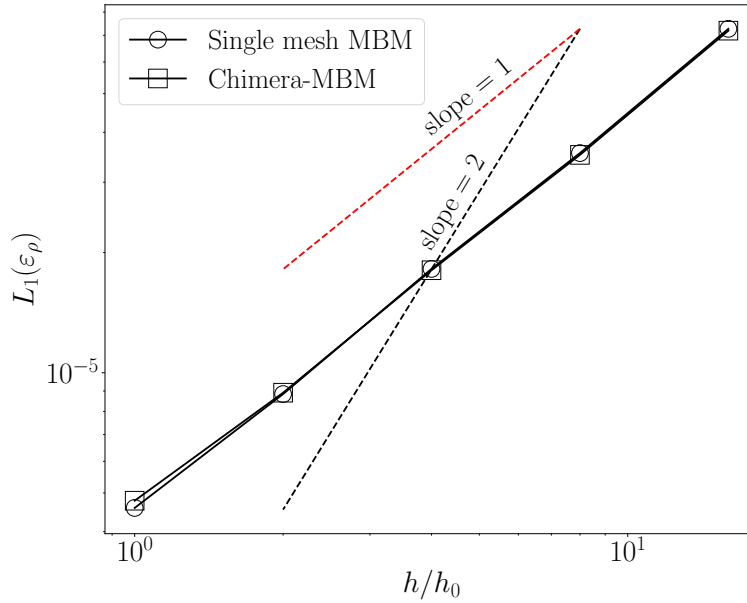


Figure 4.33: Grid convergence analysis of the free piston case with the patched configuration and equivalent cell sizes between the patch and the substrate ($\chi = 1$).

Table 4.5: Grid convergence analysis of the free piston with the patched configuration: results on density (ρ) errors obtained with a single grid MBM as well as with the present Chimera-MBM using a patch with same grid spacing as the substrate ($\chi = 1.0$) but with non-coincident grids ($\delta_S = 0.3 h_{\mathcal{V}}$).

Ncells	$L_1(\varepsilon_\rho)$ error ($\times 10^5$)		Order of convergence p	
	Single	Chimera	Single	Chimera
300	7.266	7.189	1.03	1.03
600	3.549	3.512	0.96	0.96
1200	1.820	1.806	1.04	1.02
2400	8.843e-1	8.913e-1	0.95	0.90
4800	4.586e-1	4.781e-1	-	-

B.2 - Impact of the cell ratio (χ)

We now focus on the impact of the Chimera-Mediating Body Method when the patch is refined. The parameter N_{cells} is set to 300 and the cell ratio (χ) is doubled from 1 up to 16. Figure 4.34 and Figure 4.35 show the density profiles for both the Chimera-MBM and the single grid MBM for different values of χ . The profile is preserved even for the highest values of χ but refining the patch generates two perturbations which have been observed separately with the split configuration study.

In the compression wave region, around $x = 18\text{ m}$ (see right hand side zoom in Fig. 4.34 and Fig. 4.35), a perturbation can be observed and results from the piston entering the patch. This perturbation is equivalent to the perturbation observed in section 4.3.1.A.2.1. It is generated at the left hand side patch interface (near $x = -\frac{L}{50}$) when the piston enters the patch and it is transported in the positive x -direction (which corresponds to the local coarse-to-fine direction for the left hand side patch interface). Then, the perturbation is transferred back to the right hand side portion of the substrate (near $x = \frac{L}{50}$) and it is smoothed out during the transfer due to the coarser substrate. Therefore, the perturbation is difficult to discern in the final global solution which means that structural components entering a finer domain do not significantly impact the global solution.

The second perturbation is located in the expansion wave region at $t^* = t_f^*$. Around $x = -1.1$ m (see left hand side zoom in Fig. 4.34 and Fig. 4.35), a perturbation can be observed and results from the piston leaving the patch. This perturbation is equivalent to the perturbation observed in section 4.3.1.A.2.2. It is generated at the right hand side patch interface (near $x = \frac{L}{50}$) when the piston leaves the patch. This perturbation is transported in the negative x -direction (which corresponds to the local coarse-to-fine direction for the right hand side patch interface). At $t^* = t_f^*$, the perturbation is located at the left hand side patch interface and is being transferred back to the left hand side portion of the substrate (near $x = -\frac{L}{50}$) but it is still partially located inside the patch. For $t^* > t_f^*$, the perturbation is fully transmitted to the substrate and will be smoothed out due to the coarser substrate like the perturbation located in the compression wave.

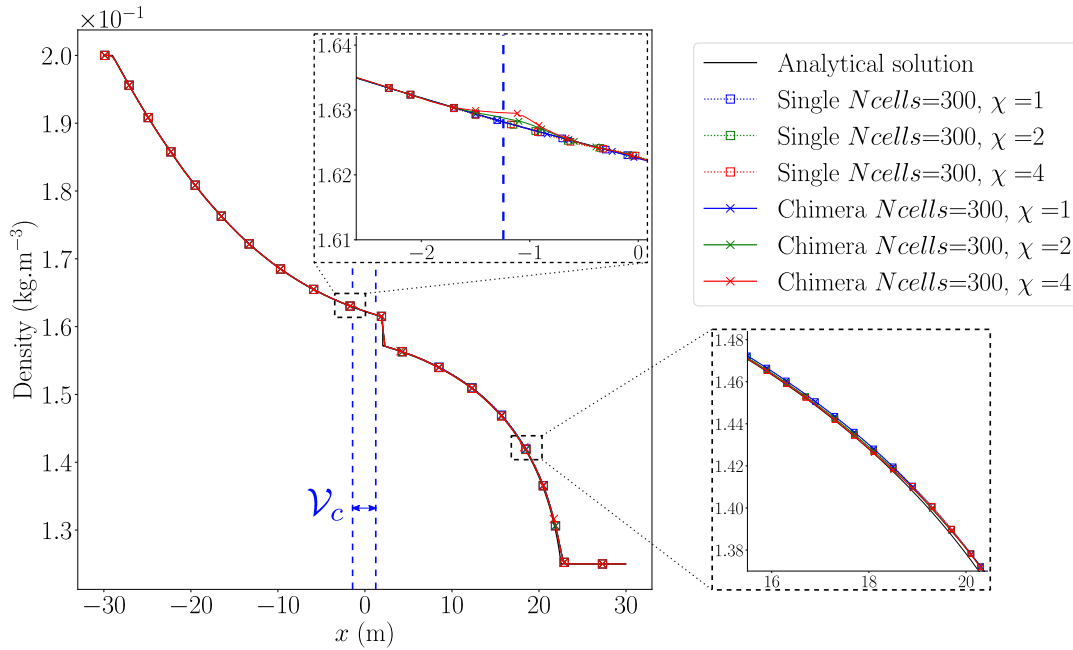


Figure 4.34: Free piston density (ρ) profile of the patched configuration for the Chimera-MBM as well as the single grid MBM when $N_{cells} = 300$ and $\chi = 1, 2, 4$ at $t = t_f^*$. The markers on the plots are not representative of the number of points of the numerical solution.

When looking at the L_1 error values summarized in Table 4.6, we can see that refining the patch helps improving the accuracy of the solution as the error decreases when χ increases up to 8. The single grid MBM follows the same trend but the error keeps decreasing for $\chi > 8$. For the Chimera-MBM, if this value is exceeded, the inherent perturbation deteriorates the accuracy compared to a lower cell ratio while using more grid cells. However, the relative difference between the Chimera-MBM and the single grid MBM does not exceed $\pm 5\%$ for $\chi \leq 8$ and is equal to 6% for $\chi = 16$ which emphasizes the local character of the induced perturbations.

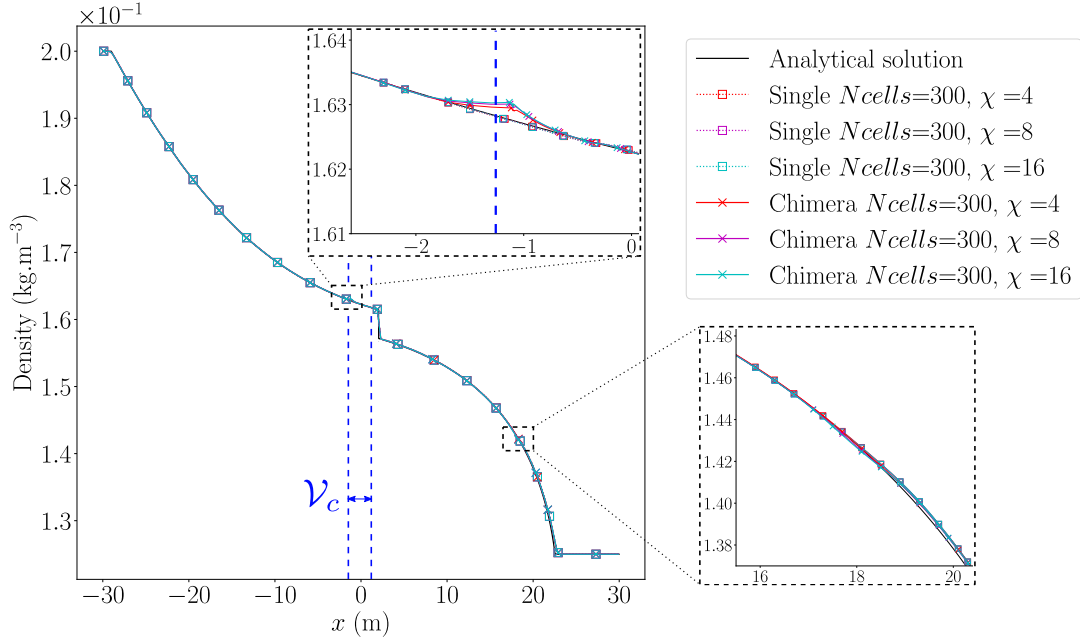


Figure 4.35: Free piston density (ρ) profile of the patched configuration for the Chimera-MBM as well as the single grid MBM when $N_{cells} = 1200$ and $\chi = 4, 8, 16$ at $t^* = t_f^*$. The markers on the plots are not representative of the number of points of the numerical solution. The markers on the plots are not representative of the number of points of the numerical solution.

Table 4.6: Cell ratio analysis of the free piston with the patched configuration: results on density (ρ) errors obtained with the present Chimera-mediating body approach using a finer grid in the patch ($N_{cells} = 300, \chi \geq 1$).

χ	$L_1(\varepsilon_\rho) (\times 10^5)$		Equivalent N_{cells} on the patch
	Single mesh	Chimera	
1	7.266	7.189	300
2	6.016	5.731	600
4	5.394	5.138	1200
8	4.965	4.972	2400
16	4.859	5.166	4800

B.3 - Impact on conservation

As for the split configuration, we are interested in measuring the impact of the Chimera-MBM on mass conservation of the system over time. Using equation 4.52, we have monitored the relative error on system mass over time for $\chi = 1$ with different values of N_{cells} and we have plotted the results in Figure 4.36. When the structure enters the patch (see Fig. 4.36), the relative error on system mass drops and then increases before returning to its "standard" variation mode as explained in Figure 4.26. This trend is inverted when the structure leaves the patch as the relative error on system mass increases and then drops before returning to a more standard variation trend. Overall, the Chimera-MBM provides an equivalent level of mass conservation compared to the single grid MBM. Also, refining the domains helps reducing the system mass variations.

The same conclusion can be drawn when the cell ratio (χ) varies as illustrated in Figure 4.37 and in Figure 4.38. Indeed, using a finer patch helps improving the global conservation when combined with the Mediating Body Method. The finer the patch the lower the system mass varies without visible conservation impact from the Chimera-Mediating Body Method.

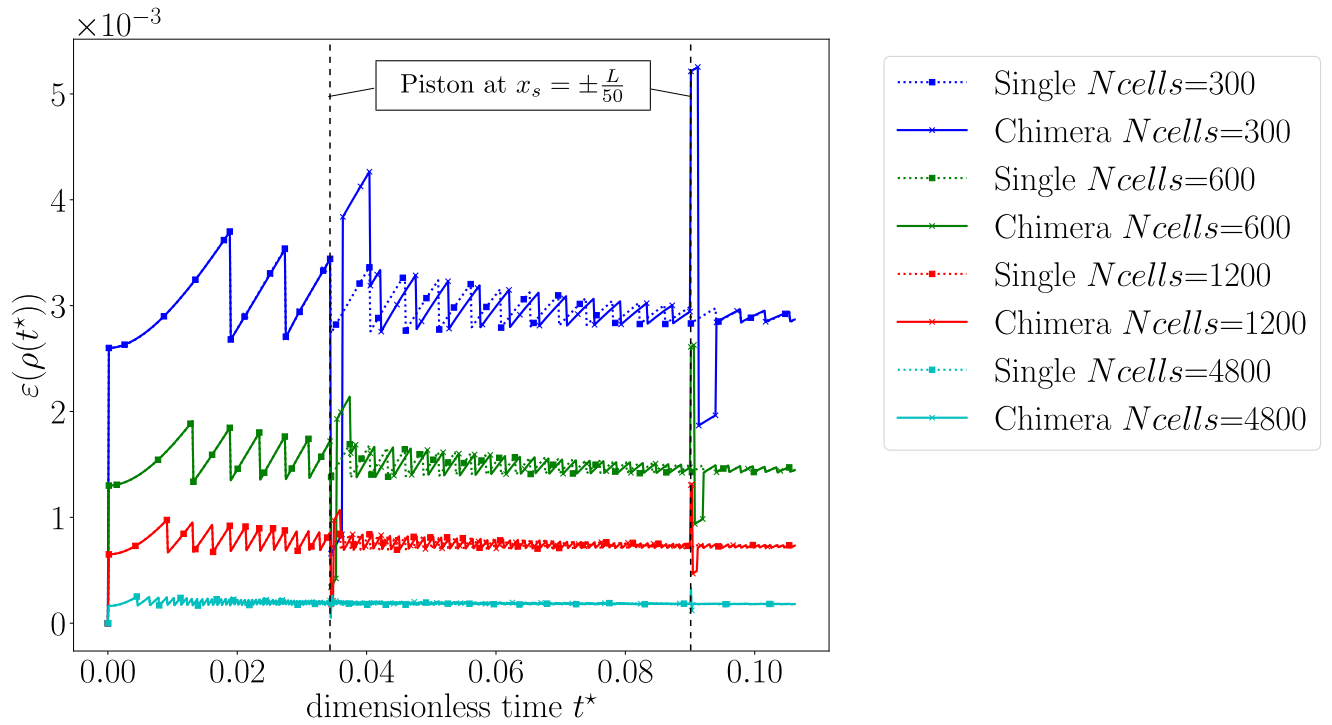


Figure 4.36: Free piston system mass relative error of the patched configuration for the Chimera-MBM case as well as the single grid MBM case when N_{cells} varies and $\chi = 1$ over time. The markers on the plots are not representative of the number of points of the numerical solution.

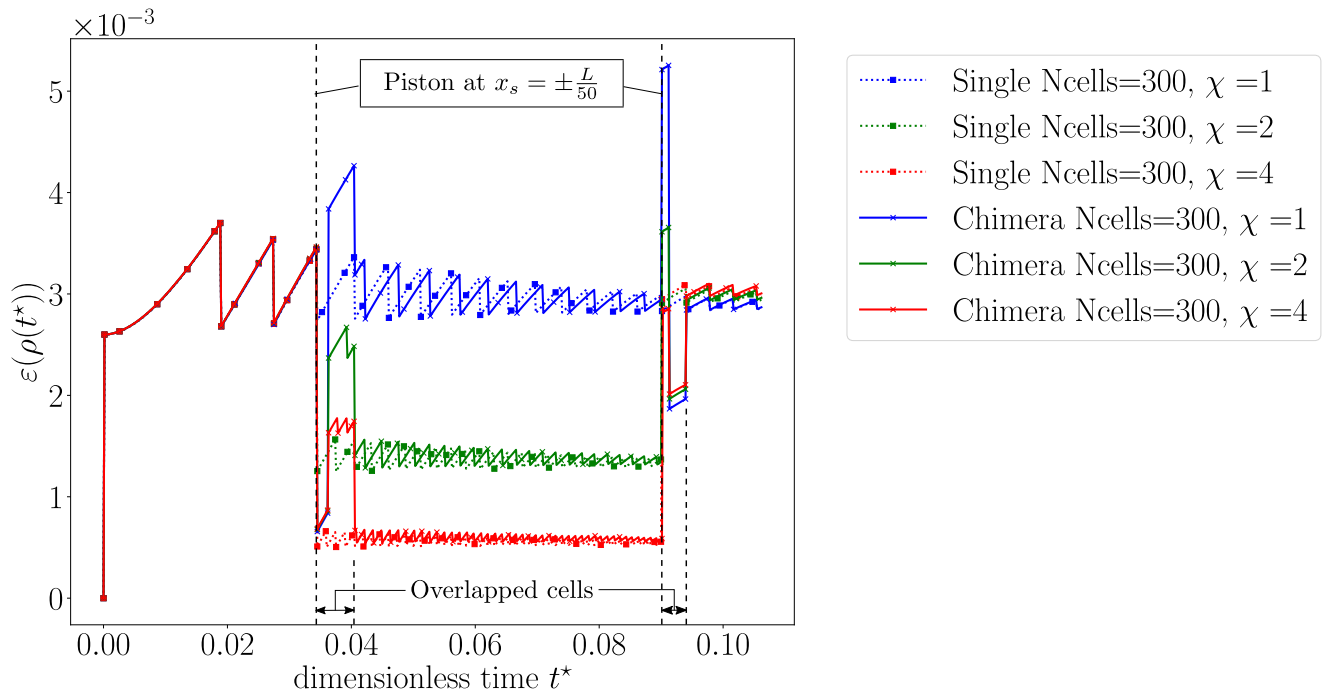


Figure 4.37: Free piston system mass relative error of the patched configuration for the Chimera-MBM case as well as the single grid MBM case when $N_{cells} = 300$ and $\chi = 1, 2$ and 4 (finer patch) over time. The markers on the plots are not representative of the number of points of the numerical solution.

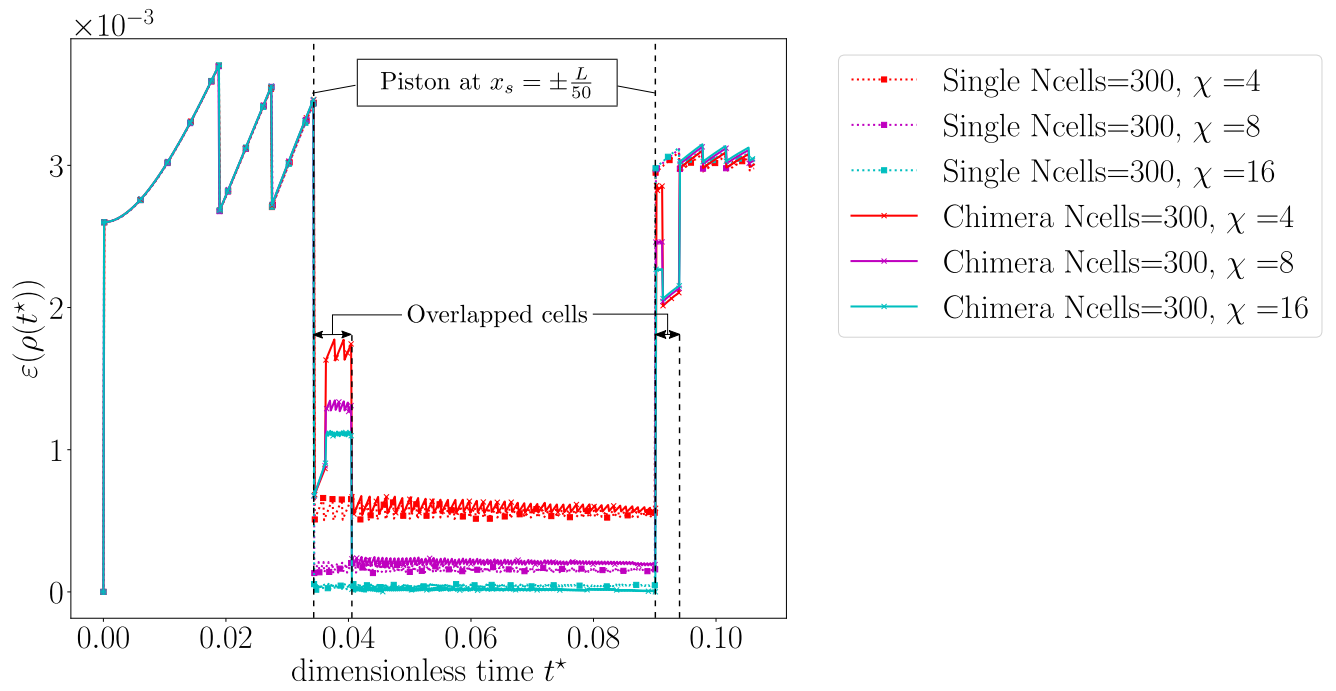


Figure 4.38: Free piston system mass relative error of the patched configuration for the Chimera-MBM case as well as the single grid MBM case when $N_{cells} = 300$ and $\chi = 4, 8$ and 16 (finer patch) over time. The markers on the plots are not representative of the number of points of the numerical solution.

C . Summary of the findings on the one-dimensional free piston test case

The free piston has demonstrated that the developed Chimera-Mediating Body Method provides very comparable results to its single grid counterpart when the cell size are equivalent between the grids. The impact on mass conservation is negligible and the method is fully functional.

When the cell ratio χ increases or decreases, perturbations are generated when the structure crosses the Chimera exchange zone. Equivalent perturbations do not exist in the single grid Mediating Body Method. However, these perturbations remain small and contained with cell ratios up to 8 and we have not observed any stability issues with the computations, even at high cell ratios. The free piston is a one-dimensional test case with moderate stress on the numerical methods with relatively simple flow dynamics. In the following, we propose a more complex test case to demonstrate the capabilities of the method when using larger scale flow phenomena.

4.3.2 - Three-dimensional separated chambers with a perforated plate

As a final test case, we consider a three-dimensional test involving two chambers separated by a perforated membrane (see Fig. 4.39). This test aims to demonstrate an example of application of the Chimera-Mediating Body Method when modelling a three-dimensional problem involving localized geometrical details that heavily impact the physics of the problem. This test also exhibits the flexibility of the implementation that allows the use of multiple patched grids within the same computation. The objective of this test is not to provide a reference solution of the Chimera-Mediating Body Method on a well-known test case but to show the benefits of the Chimera-MBM when used in a large scale simulation involving fluid-structure interactions.

In this test, a square membrane of a side $H = 8$ m is perforated at the center by a circular hole with a radius equal to $r_c = 0.25$ m. The membrane perforation is centered on a parallelepiped fluid domain with the dimensions $(L \times H \times D) = (12$ m, 8 m, 8 m) where L is the length of the domain in the x -direction, H is the height of the domain in the y -direction, D is the width of the domain in the z -direction. As the geometry benefits from symmetry axis, we have decided to model a quarter of the domain as shown in Figure 4.39.

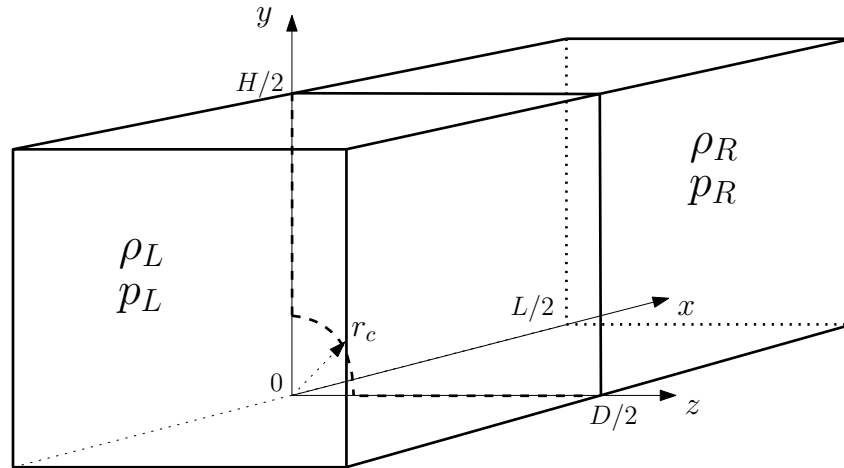


Figure 4.39: 3D chambers case presentation

The membrane separates two chambers filled with fluids at rest with respectively a left state L ($x < 0$) and a right state R ($x > 0$) which are given by:

$$\begin{pmatrix} \rho_L \\ u_L \\ p_L \end{pmatrix} = \begin{pmatrix} 0.125 \text{ kg.m}^{-3} \\ 0 \\ 0.1 \text{ Pa} \end{pmatrix}, \quad \begin{pmatrix} \rho_R \\ u_R \\ p_R \end{pmatrix} = \begin{pmatrix} 0.5 \text{ kg.m}^{-3} \\ 0 \\ 0.5 \text{ Pa} \end{pmatrix}. \quad (4.53)$$

For the single grid configuration, the fluid domain is fully covered by a unique 3D cartesian grid with cubic cells of a side h_U . The single grid configuration is derived in a coarse configuration with $h_U = h_U^{\text{coarse}} = 0.2$ m and a fine configuration with $h_U = h_U^{\text{fine}} = 0.05$ m. The perforated plate grid is set using an O-grid with a first row of square cells of a side $h_U = 0.04$ m around the hole perimeter as shown in Figure 4.40.

The membrane grid configuration does not change between the single grid cases and the Chimera cases in order to focus on the differences between the Chimera-MBM and the single grid MBM. The Chimera case is composed of three distinct grids serving different purposes as shown in Figure 4.41.

A substrate grid, denoted \mathcal{W} , is used as a global large scale model with a coarse resolution. The substrate grid (\mathcal{W}) is equivalent to the single grid case with cubic cells of a side $h_{\mathcal{W}}$ and corresponds to the domain $(x, y, z) = [-\frac{L}{2}, \frac{L}{2}] \times [0, \frac{H}{2}] \times [0, \frac{D}{2}]$.

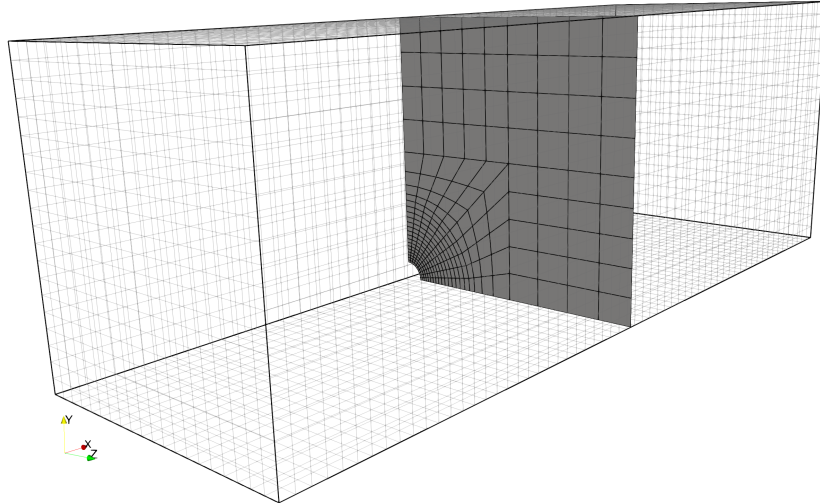


Figure 4.40: 3D chambers grid configuration for the plate. The first row of cells around the perimeter of the hole contains square cells of a side $h_{\mathcal{U}} = 0.04$ m.

A first patch grid, denoted \mathcal{V}_1 , is used to insert the membrane inside the domain. The membrane is assumed to remain contained inside the first patch (\mathcal{V}_1) which is modelled using a 3D cartesian grid with cubic cells of a side $h_{\mathcal{V}_1} = 0.1$ m. \mathcal{V}_1 covers the domain $(x, y, z) = [-\frac{L_1}{2}, \frac{L_1}{2}] \times [0, \frac{H}{2}] \times [0, \frac{D}{2}]$ with $L_1 = 3$ m. The first patch grid (\mathcal{V}_1) is finer than the substrate grid (\mathcal{W}) in order to better capture the flow physics near the membrane.

Around the perforation of the membrane, a second patch grid, denoted \mathcal{V}_2 , is used to better capture the flow interactions between the two chambers. As we are using the MBM as a fluid-structure interaction method, using a finer grid near a structural geometrical detail makes sense as it allows better capturing of the impact of the structure on the flow. The second patch (\mathcal{V}_2) is modelled using a 3D cartesian grid, finer than the first patch grid (\mathcal{V}_1), with cubic cells of a side $h_{\mathcal{V}_2} = 0.05$ m. \mathcal{V}_2 covers the domain $(x, y, z) = [-\frac{L_2}{2}, \frac{L_2}{2}] \times [0, \frac{H_2}{2}] \times [0, \frac{D_2}{2}]$ with $L_2 = 1.2$ m, $H_2 = 1.2$ m and $D_2 = 1.2$ m.

As both the first patch and the second patch are used to improve local accuracy and to bring better fitted fluid grids around structural details, we have $h_{\mathcal{W}} = h_{\mathcal{U}}^{\text{coarse}} > h_{\mathcal{V}_1} > h_{\mathcal{V}_2} = h_{\mathcal{U}}^{\text{fine}}$. The outer boundaries ($y = \frac{H}{2}$ and $z = \frac{D}{2}$) of the membrane are clamped to the fluid domain. The exterior walls of the domain ($x = -\frac{L}{2}$, $x = \frac{L}{2}$, $y = \frac{H}{2}$ and $z = \frac{D}{2}$) are set with slip wall boundary conditions while the interior faces of the domain ($y = 0$ and $z = 0$) are set using symmetry boundary conditions.

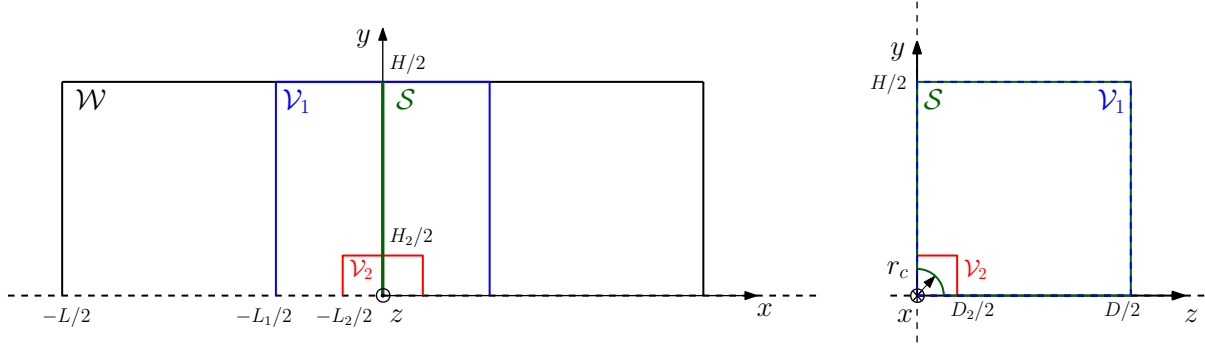


Figure 4.41: Three-dimensional chambers grid configuration for the Chimera-MBM case. The computational domain contains a coarse substrate (in black), a finer first patch (in blue) that contains the perforated membrane (in green) and an even finer second patch (in red) that helps improving the accuracy around the perforation

Computations are performed up to the dimensionless time step $t_f^* = t_f \frac{c_R}{L} = 3.75$ where $c_R = \sqrt{\frac{\gamma p_R}{\rho_R}}$ is the right hand side sound speed ($\gamma = 1.4$). We recall that the plate is modelled using quadrilateral MITC4 shell elements with an elastic Saint Venant-Kirchhoff nonlinear behavior [24]. The membrane parameters are the following: the density is equal to $2710 \text{ kg}\cdot\text{m}^{-3}$, the thickness e is equal to $2 \cdot 10^{-2} \text{ m}$, Young modulus E is equal to 10^{-2} GPa and Poisson coefficient ν is equal to 0.33. The CFL number is taken equal to 0.3.

The first patch (\mathcal{V}_1) and the substrate (\mathcal{W}) exchange information using the second order Chimera method presented in section 2.2.3.B while the second patch (\mathcal{V}_2) and the first patch (\mathcal{V}_1) interact using the Chimera-MBM presented in section 4.2.2.

At $t^* > 0$, the high pressure chamber ($x > 0$) leaks into the low pressure chamber with a shock wave propagating along the x axis, in the negative direction and an expansion wave in the positive direction. Simultaneously, the high pressure chamber pushes the membrane in the negative x -direction. The membrane region around the perimeter of the perforation oscillates between its initial position and its maximum absolute displacement. The high pressure cavity expands into the low pressure cavity and eventually creates Mach diamonds along the x -axis due to the plate acting as a slightly over-expanded nozzle. At $x = -\frac{L}{2}$, the flow is reflected on the wall and is redirected in the positive y -direction and z -direction before being reflected back toward the plate corner located at $(x, y, z) = (0, \frac{H}{2}, \frac{D}{2})$, opposed to the perforation creating a low velocity recirculation region or mixing region in the low pressure cavity.

The displacements of the plate along the x -axis and the y -axis are monitored over time. We focus on one particular node at the edge of the plate perforation with $z = 0$ which corresponds to the node initially located at $(x, y, z) = (0, r_c, 0)$. The x -displacement and the y -displacement of this node are plotted respectively in Figure 4.42 and Figure 4.43 for the coarse and fine single grid MBM cases as well as the Chimera-MBM case.

The Chimera-MBM matches the fine single grid MBM x -displacement and y -displacement profiles very closely. Compared to the coarse single grid MBM, the Chimera-MBM is more accurate from a structural dynamics point of view. These results exhibit the strong capabilities of the Chimera-MBM to improve global computations with localized refined patches around structural components. Over time, the Chimera-MBM and the fine single grid profiles remain superimposed while the coarse single grid starts diverging from the other two due to growing discrepancies in the fluid solution that alter the structural dynamics of the plate.

The fluid solution has been monitored for the three configurations (coarse single grid MBM, Chimera-MBM and fine single grid MBM) and the resulting velocity magnitude fields ($\|\underline{u}\|$) are

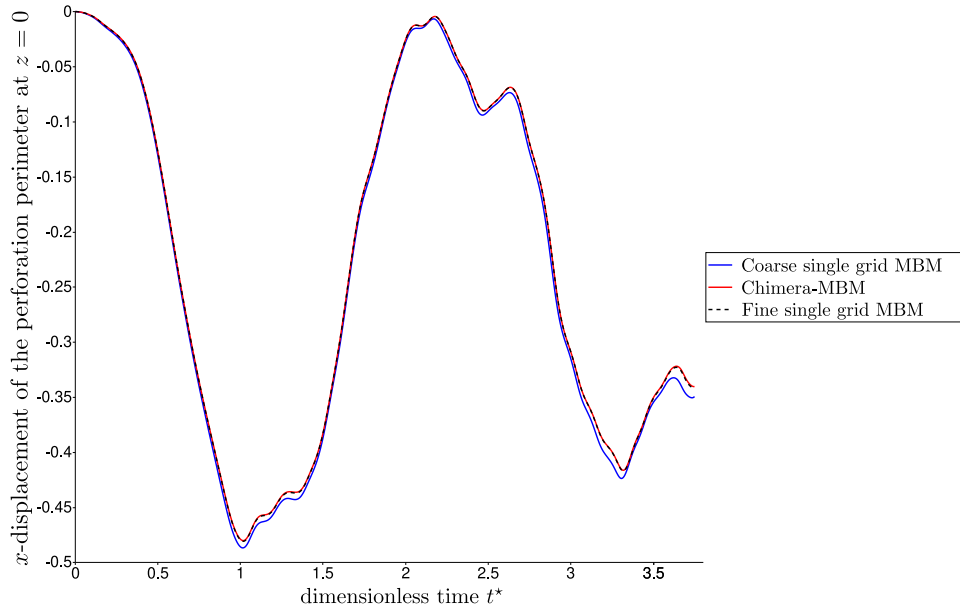


Figure 4.42: x -displacement of the plate extremity around the perforation perimeter at $z = 0$. The monitored node is initially located at $(x, y, z) = (0., r_c, 0.)$

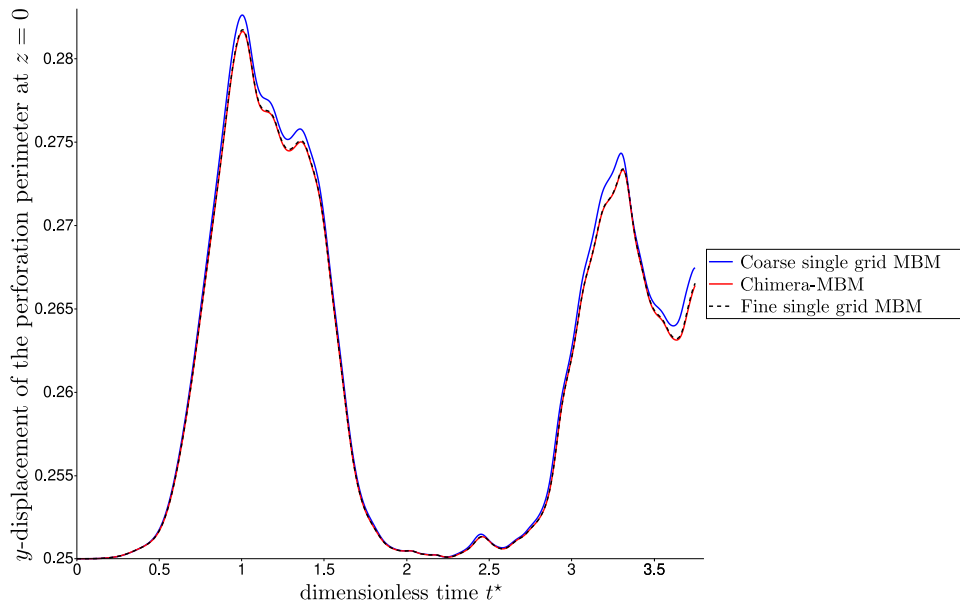
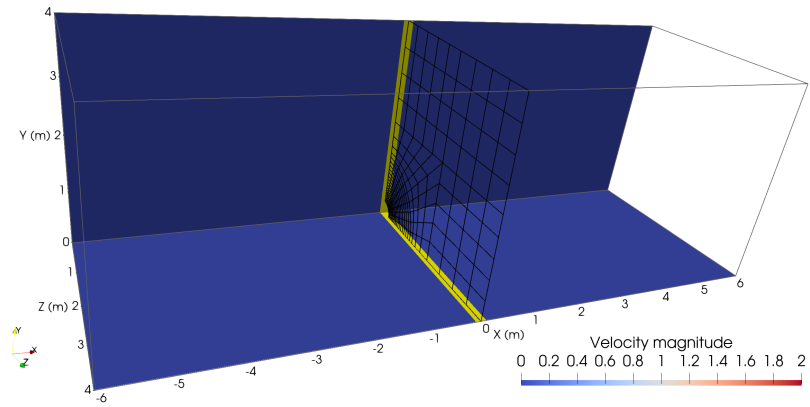


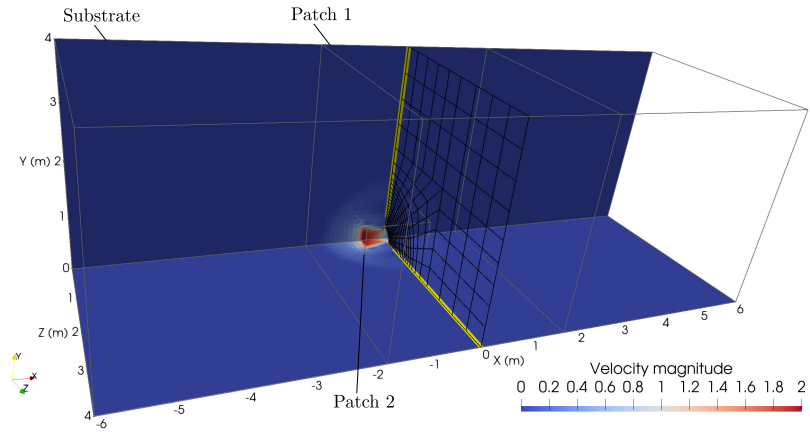
Figure 4.43: y -displacement of the plate extremity around the perforation perimeter at $z = 0$. The monitored node is initially located at $(x, y, z) = (0., r_c, 0.)$

compared at the dimensionless times 0.1, 0.5, 1, 2, 3 and 3.75 in respectively Figure 4.44, Figure 4.45, Figure 4.46, Figure 4.47, Figure 4.48 and Figure 4.49.

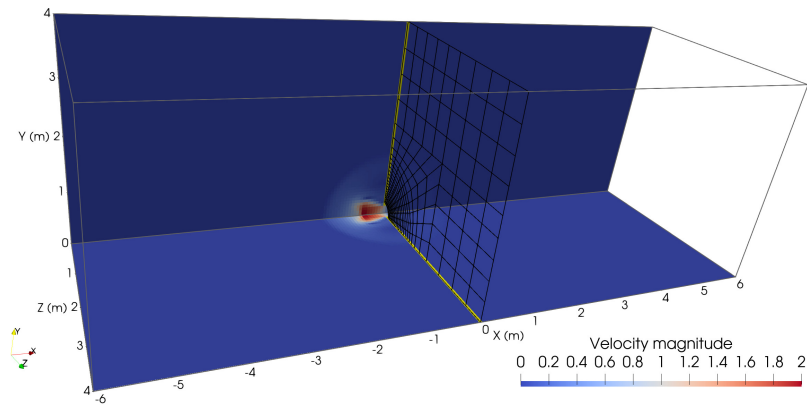
Between $t^* = 0$ and $t^* = 0.5$ (see Fig. 4.44 and Fig. 4.45), the fine single grid MBM captures the perforation and the high pressure cavity starts leaking into the low pressure one. In the coarse single grid MBM configuration, the resolution of the grid does not allow the capture of the perforation and therefore the fluid physics are very different between the two single grid MBM cases. The use of the second patch (\mathcal{V}_2) allows the Chimera-Mediating Body Method to capture the perforation at every instant. Even though the Chimera-MBM configuration is limited by the coarse resolution of the substrate, flow structures equivalent to the fine single grid MBM such as the shock wave propagating inside the low pressure chamber are captured which is not the case for the coarse single grid MBM.



(a) Coarse single grid - MBM

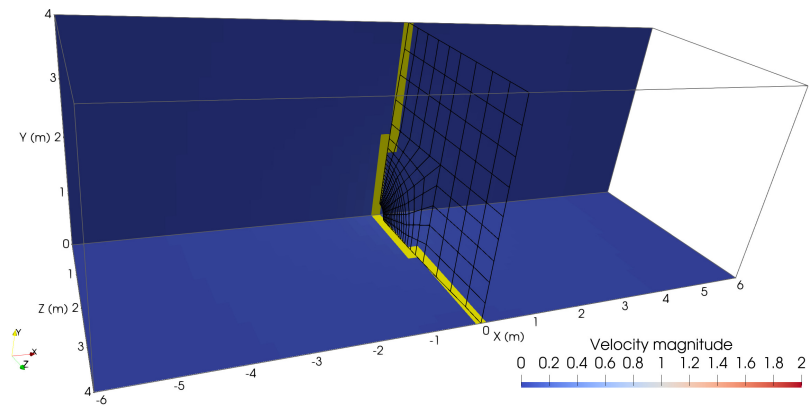


(b) Chimera - MBM

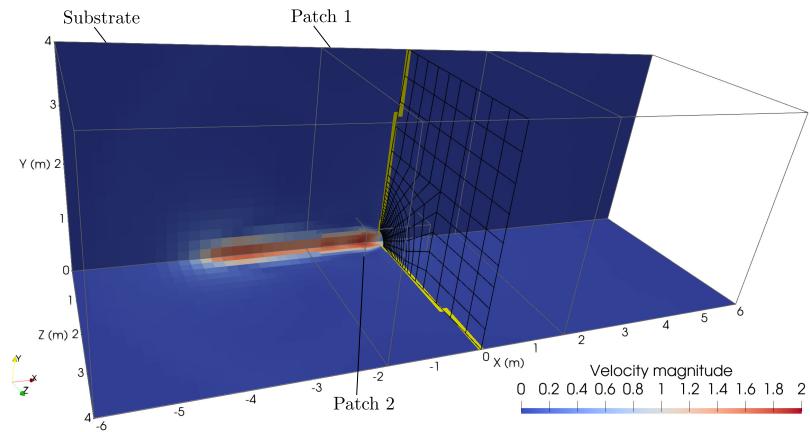


(c) Fine single grid - MBM

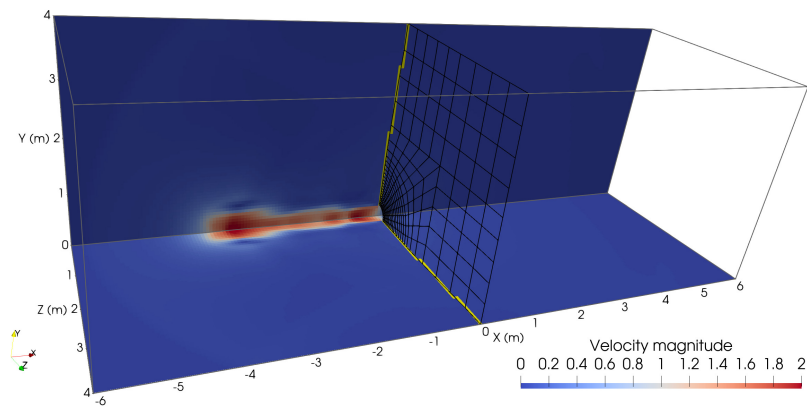
Figure 4.44: Velocity magnitude field ($\|\underline{u}\|$) obtained with the coarse single grid MBM case (a), the Chimera-MBM case (b) and the fine single grid MBM case (c) at the dimensionless time $t^* = 0.1$.



(a) Coarse single grid - MBM



(b) Chimera - MBM

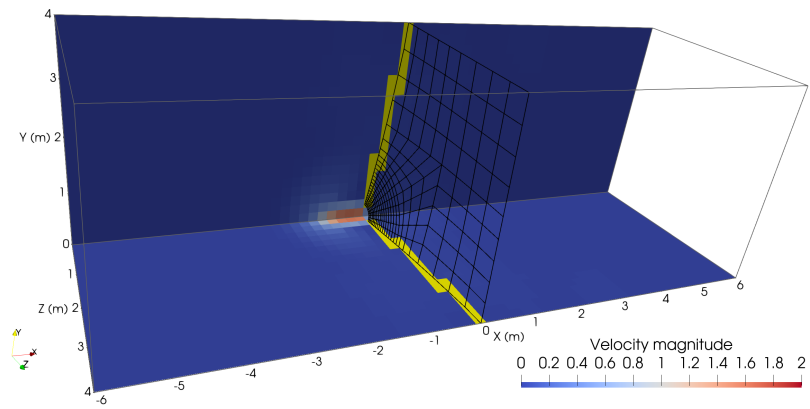


(c) Fine single grid - MBM

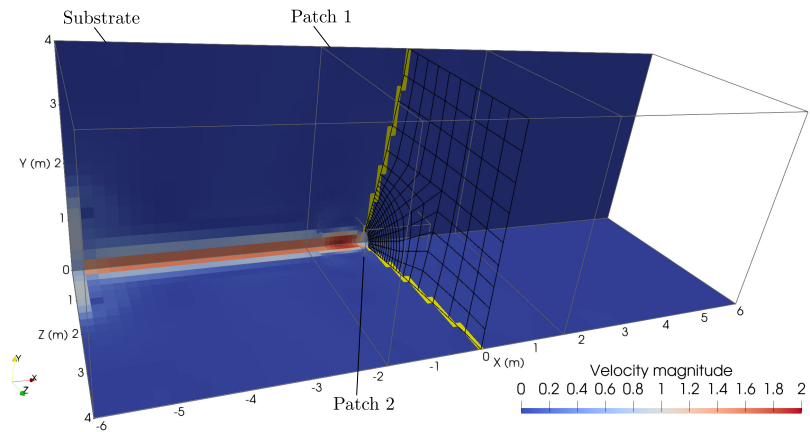
Figure 4.45: Velocity magnitude field ($\|\underline{u}\|$) obtained with the coarse single grid MBM case (a), the Chimera-MBM case (b) and the fine single grid MBM case (c) at the dimensionless time $t^* = 0.5$.

At $t^* = 1$, (see Fig. 4.46), the displacement of the membrane is important enough for the coarse single grid MBM to capture the starting leak whereas in the fine single grid MBM case and in the Chimera-MBM case, the shock front has already reached the boundary of the domain at $x = -12$ m. Around the perforation, due to an equivalent grid resolution between the fine single grid and the second patch (\mathcal{V}_2), the first Mach diamond is captured by the Chimera-MBM and transmitted to the first patch (\mathcal{V}_1). However, the coarse resolution of the substrate does not allow the Chimera-MBM configuration to hold a sufficient level of accuracy to capture Mach diamonds downstream unlike the fine single grid MBM configuration.

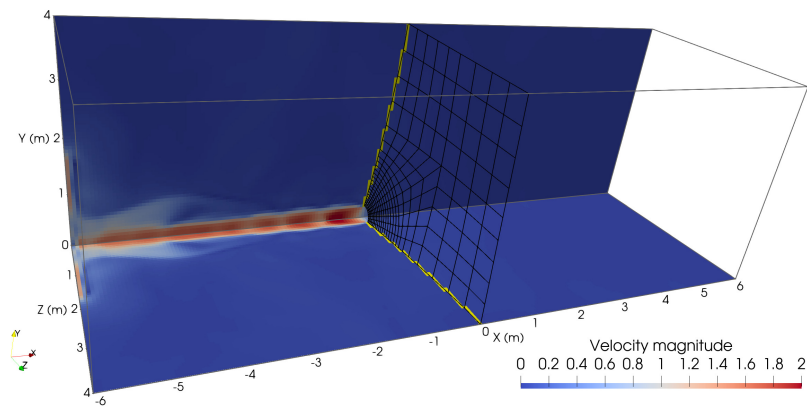
From $t^* = 2$ to $t^* = t_f^* = 3.75$ (see Fig. 4.47, Fig. 4.48 and Fig. 4.49), for both the fine single grid MBM and the Chimera-MBM, the flow is reflected onto the wall normal to the x -axis located at $x = -12$ m. Because of the reflection, the flow becomes perpendicular to the x -axis before recirculating toward the perforated plate which creates a mixing region at a lower velocity compared to the fluid velocity near the perforation. Even though the mixing of the fluid is not as well captured as the fine single grid MBM, the recirculation toward the perforated plate can clearly be identified with the Chimera-MBM. For the coarse single grid MBM configuration, the resolution of the grid does not allow the capture of the perforation and therefore the fluid physics are very different from the fine single grid MBM and the Chimera-MBM.



(a) Coarse single grid - MBM

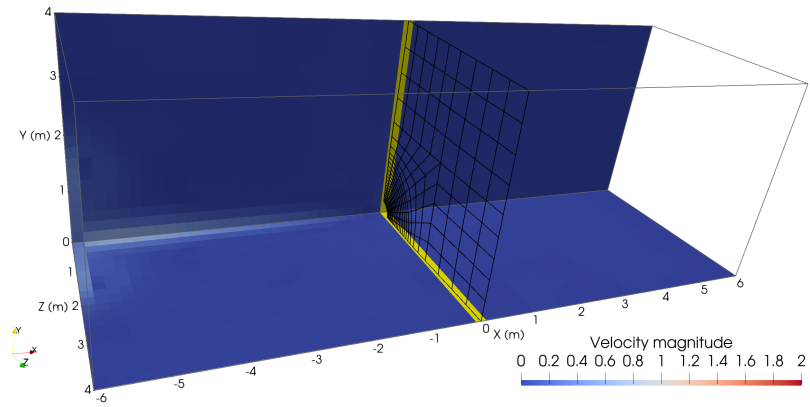


(b) Chimera - MBM

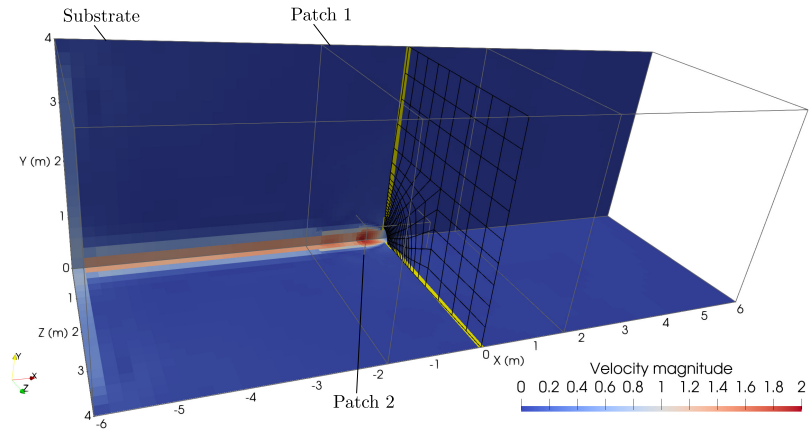


(c) Fine single grid - MBM

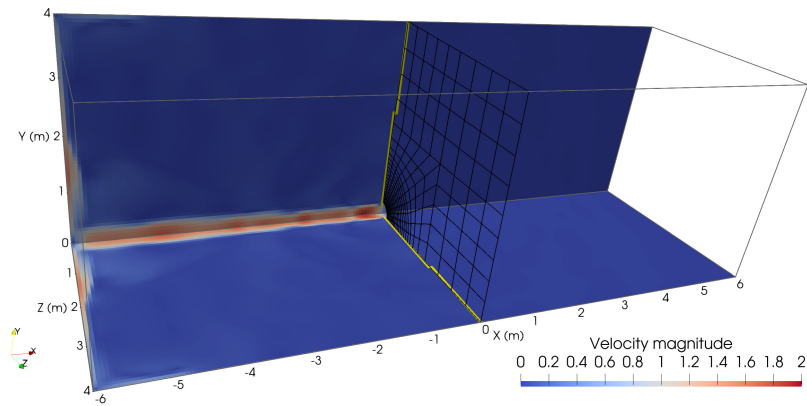
Figure 4.46: Velocity magnitude field ($\|\underline{u}\|$) obtained with the coarse single grid MBM case (a), the Chimera-MBM case (b) and the fine single grid MBM case (c) at the dimensionless time $t^* = 1$.



(a) Coarse single grid - MBM

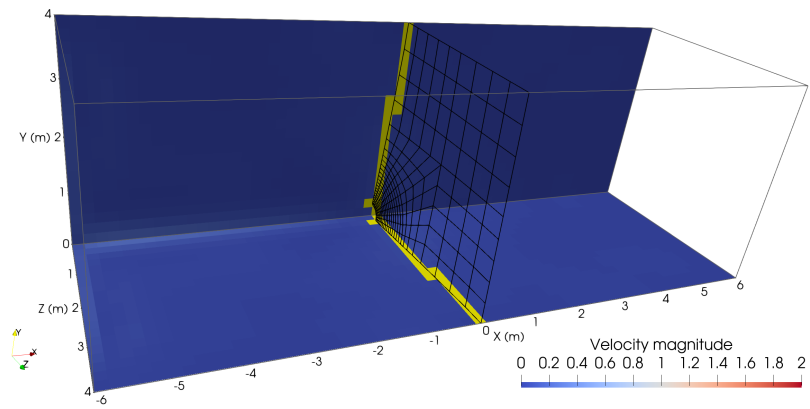


(b) Chimera - MBM

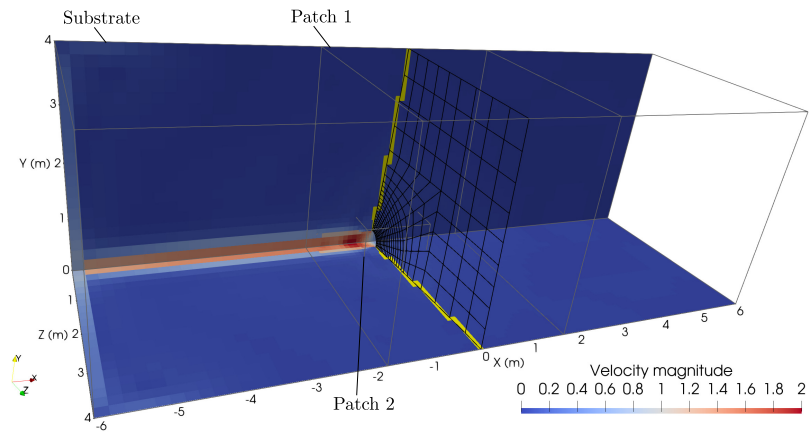


(c) Fine single grid - MBM

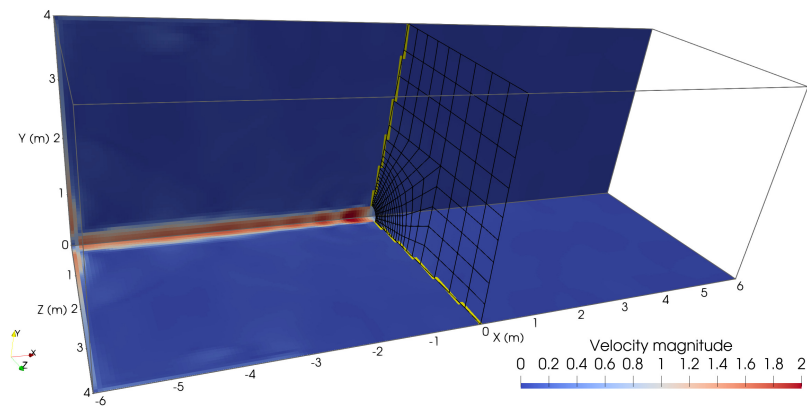
Figure 4.47: Velocity magnitude field ($\|\underline{u}\|$) obtained with the coarse single grid MBM case (a), the Chimera-MBM case (b) and the fine single grid MBM case (c) at the dimensionless time $t^* = 2$.



(a) Coarse single grid - MBM

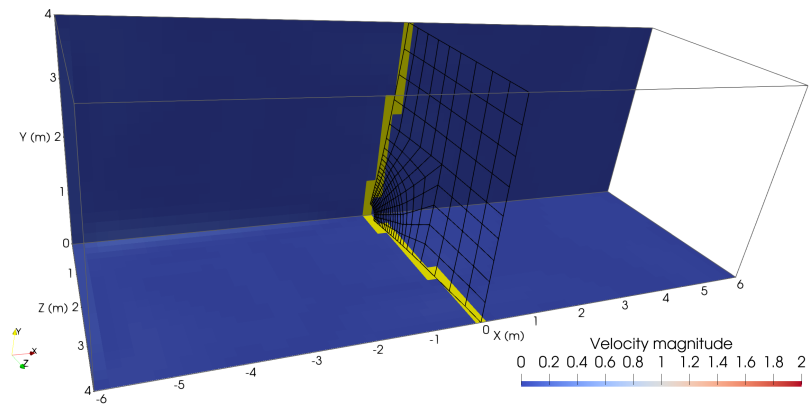


(b) Chimera - MBM

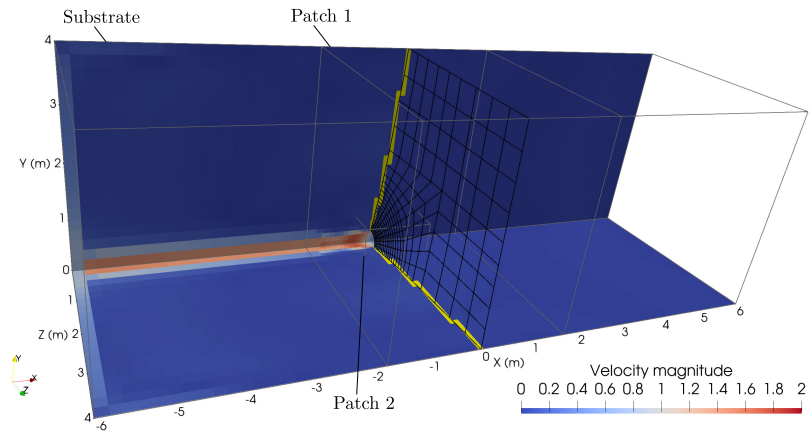


(c) Fine single grid - MBM

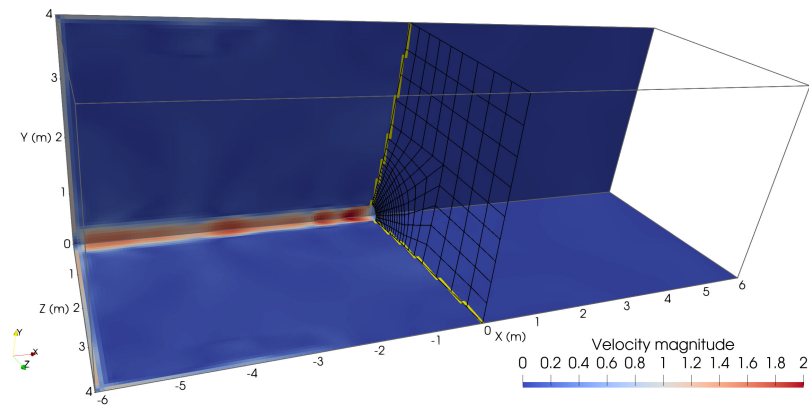
Figure 4.48: Velocity magnitude field ($\|\underline{u}\|$) obtained with the coarse single grid MBM case (a), the Chimera-MBM case (b) and the fine single grid MBM case (c) at the dimensionless time $t^* = 3$.



(a) Coarse single grid - MBM



(b) Chimera - MBM



(c) Fine single grid - MBM

Figure 4.49: Velocity magnitude field ($\|\underline{u}\|$) obtained with the coarse single grid MBM case (a), the Chimera-MBM case (b) and the fine single grid MBM case (c) at the dimensionless time $t^* = t_f^* = 3.75$.

In order to quantify the impact of the capture of the perforation at a larger scale with global quantities, we measure the fluid mass variation of the low pressure chamber between $t^* = 0$ and $t^* = t_f^* = 3.75$. The fluid mass variation of the low pressure chamber at the dimensionless time t^* is denoted $\Delta m_L(t^*)$ and is defined as:

$$\Delta m_L(t^*) = \frac{m_L(t^*) - m_L(0)}{m_L(0)}, \quad (4.54)$$

with,

$$m_L(t^*) = \int_{-L/2}^0 \int_0^{D/2} \int_0^{H/2} \rho(\underline{x}, t^*) \, dx \, dy \, dz. \quad (4.55)$$

$m_L(t^*)$ is the fluid mass of the left hand side chamber ($x < 0$) which corresponds to the low pressure cavity.

Remark. *As the chambers are surrounded by impermeable walls except for the perforated region of the plate. We assume that between $t^* = 0$ and $t^* = t_f^*$, the average pressure in the high pressure chamber does not change significantly resulting in equivalent fluxes between $t^* = 0$ and $t^* = t_f^*$ at the perforation. As a result, the mass variation of the low pressure chamber can be approximated with the integral difference of the density fields between $t^* = 0$ and $t^* = t_f^*$.*

The low pressure chamber mass variations are reported in Table 4.7 for the single grid MBM configurations as well as the Chimera-MBM. As the perforation is not captured by the coarse single grid MBM, the high pressure chamber does not leak immediately into the low pressure one which results in a fluid mass increase in the low pressure cavity of 0.2%. The Chimera-MBM and the fine single grid MBM being able to capture the perforation, the mass of the low pressure cavity increases at an equivalent rate as both provide a gain of $\approx 2.45\%$ of fluid mass inside the low pressure chamber.

Table 4.7: Fluid mass variation of the low pressure chamber between $t^* = 0$ and $t^* = t_f^* = 3.75$.

	Coarse single grid MBM	Chimera-MBM	Fine single grid MBM
$\Delta m_L(t_f^*)$	0.20 %	2.47 %	2.44 %

To put those results in perspective, we compare the computational cost of each configuration including memory footprint and CPU time. To do so, we report the CPU time ratio and memory usage ratio of the single grid MBM case to every configuration tested from the coarse single grid MBM case to the Chimera-MBM case (see Table 4.8). The coarse single grid MBM configuration is 27 times faster than the fine single grid MBM configuration. Part of this is due to 36 times less number of fluid cells. The Chimera-MBM configuration is 7 times faster than the fine single grid MBM configuration with 14 times less fluid cells. This gap will increase with the ratio of the large scale domain size to the small geometrical detail size. Therefore, in a large scale computation, the Chimera-Mediating Body Method is a relevant alternative for capturing flow components generated by small geometrical details without impacting the computational cost of the global calculation. Also, the first patch which brought the structure makes the FSI component of the computation independent from the substrate grid. This flexibility exhibits the advantages of the Chimera-Mediating Body Method compared to a fine single grid configuration as the Chimera-MBM allows to reduce the computational time for an equivalent level of accuracy on the dynamics of structural components.

Table 4.8: CPU time ratio and memory usage ratio of the fine single grid MBM configuration to the coarse single grid MBM configuration and the Chimera-MBM configuration.

CPU Time ratio			Memory ratio		
Coarse single grid MBM	Chimera-MBM	Fine single grid MBM	Coarse single grid MBM	Chimera-MBM	Fine single grid MBM
26.57	7.3	1	35.88	13.99	1

4.4 - Chapter conclusion

In this chapter, we have developed a coupling method between the previously introduced finite volume Chimera method and an immersed boundary method known as the Mediating Body Method [92]. The objective of the resulting method called Chimera-Mediating Body Method is to allow the modelling of large scale fluid-structure interactions involving small structural details that can impact the flow field in a non-negligible way.

The method has been developed in order to be fully compatible with the previously introduced second order finite volume Chimera method. Therefore, the Chimera-Mediating Body Method is compatible with large structural displacements over multiple and independent fluid grids.

Tested on a one-dimensional free piston test case, the Chimera-Mediating Body Method provides equivalent results as a single mesh configuration and remains adequate when using high cell ratios between the fluid grids even though it can introduce local perturbation when the structure crosses the Chimera exchange zone with cell ratios (χ) higher than 8. Therefore, it is not recommended to have structural components mainly located inside the fluid exchange zone for an extended period of time as the quality of the solution will deteriorate locally and propagates over time.

As a conclusion, the method allows to capture local flow phenomena generated by structural components equivalent to fine single grid models at a global scale while preserving a reasonable computational cost compared to a fine grid model. Last but not least, the Chimera-MBM does not deteriorate the dynamics of structural components but is able to reach levels of accuracy equivalent to fine single grid models using localized refined patches.

5 - Conclusion and open prospects

The objective of this thesis was to develop a numerical tool able to add local geometrical details and local refinements in large scale brutal accidental simulations. These numerical simulations often involve complex fast transient and coupled phenomena with different spatial and time scales within the same physical domain such as fluid-structure interaction. Taking into account these different scales with industry standard methods like the finite volume method (FVM) or the finite element method (FEM) often results in a large number of grid points and becomes computationally expensive. The numerical strategy that we have developed aims to capture physical phenomena of interest and/or to add geometrical details that significantly impacts the flow with less computing resources compared to single grid FVM/FEM approaches.

In order to achieve this objective, we focus on fast transient flows in a first place with a finite volume framework and explicit time integration, with the perspective of adding fluid-structure coupling to the developed method. After a thorough study of composite grid methods, we chose an overlapping grid method known as the Chimera method as a basis of our numerical strategy. The Chimera method uses grid cells as a support for the exchange of information and is compatible with a finite volume framework and with explicit time integration by design compared to other overlapping grid methods. As the Chimera method requires few constraints on the superimposed grids, the method is very suitable for coupling with fluid-structure interaction methods. On the topic of FSI, the Chimera method is able to capture local flow phenomena using ALE methods and structures connected to the fluid mesh. In this work, we are interested in structural components undergoing large deformations and displacements, therefore, we chose to couple the Chimera method with FSI methods such as immersed boundary method, more adapted to this type of structural dynamics.

The first step of this work was to develop an overlapping grid technique for fast transient dynamics. A Chimera method has been developed in a finite volume framework with as little constraints on the overlapping grids as possible. Initially, the information sent between overlapping grids is interpolated using a first order method that uses cell intersections to build an average solution. This interpolation is simple and computationally effective but tends to deteriorate the global solution of the flow when the ratio of the sending cell size to the receiving cell size exceeds an order of magnitude (≈ 10). To limit this effect, the first order interpolation method has been extended to a second order method using finite volume reconstruction techniques with a modified limiter to avoid spurious oscillations while using grids with different refinements. The second order Chimera method allows an improvement of the solution using composite domains with finer grids at specific locations and does not deteriorates the solution on one-dimensional reference test cases compared to an equivalent single grid computation.

The second step was to assess the reference configuration of the second order finite volume Chimera method on two-dimensional test cases from the literature involving flow structures crossing the Chimera grid interfaces that cannot be reproduced with one-dimensional configurations. Examples of such structures are bow shocks, shock-bubble interactions, Mach stems, triple points or jets. The developed Chimera method has proven to preserve the solution when grids have an equivalent cell size. Using finer local grids onto a coarser global one can help capturing local flow phenomena up to a certain point as the resolution on the coarser grid is a limiting factor. Finally, using fine patched grids allows global improvement on the solution with largely reduced computational resources compared to an equivalent fine single grid configuration.

The final step of this work was to couple the developed Chimera method with an FSI method compatible with large structure displacements such as the Mediating Body Method (MBM) [92].

The use of an immersed boundary method like the MBM allows the fluid grid and the structure grid to be meshed independently and provides the same flexibility as the Chimera method does. With such methods, the perception of the structure by the fluid is conditioned by the fluid grid resolution. Therefore, small details on the structure require a fine fluid grid around it to have an impact on the fluid. With the developed Chimera-Mediating Body Method, local fine fluid grids can be added around geometrical details present on the structure without overburdening computational costs. The method allows the capture of fluid phenomena that would not be perceived by the fluid with a coarse global grid. Nonetheless, due to limits of the method, perturbations are generated if the structure remains static in the Chimera exchange zone. If the structure only crosses the exchange zone, the error generated is negligible which makes the Chimera-Mediating Body Method fully usable.

With the work carried out in this thesis, a detailed analysis has been provided for the developed Chimera method applied to fast transient flows with variable grid configurations as well as a coupling for FSI with an immersed boundary method. With the developed method the structure is modelled by a single grid. One way to continue this work would be to extend the overlapping grid approach to structural transient dynamics as it has been done in [60] with the Arlequin method. With the Chimera-Mediating Body Method coupled with the Arlequin method, a local geometrical detail could be patched onto the global structure. Both structure grids would be immersed inside a global fluid grid and the local structure patch could be associated with a local fluid grid patched onto the global fluid grid in order to capture the effect of the structural detail on the fluid. To make this work, the Chimera method must be extended to moving local grids as the local fluid grid would be attached to the local structural grid.

As an additional solution to the first prospect but with different applications, one could use the developed Chimera method in order to improve grid dependent FSI methods like the Arbitrary Lagrangian Eulerian (ALE) method. Inside a global fluid grid, small structural components could be added using local moving ALE fluid-structure grids. This application also requires the developed Chimera method to be compatible with moving grids but is more suitable for small moving structural parts. For large moving structures with equivalent sizes as the fluid domain, the first prospect is preferable.

The Chimera-Mediating Body Method extended via the two prospects could provide a complete tool for modeling large and geometrically complex systems involving fluid-structure interactions.

Also, the Chimera-MBM could be coupled with Adaptive Mesh Refinement methods [22, 20] with the idea of using AMR methods on patched grid containing a geometrical detail. The combination of the Chimera-MBM with AMR could allow for a very fine tuning of the grid resolution in localized regions of interest of a global model. Finally, the Chimera-Mediating Body Method could be computationally optimized using decoupled time steps for each fluid grid and for the structure. This improvement could lead to major gains in CPU times as all the results provided in this work were constrained by the finest grid of the domain.

Appendices

A - Ghost cell layer dependency for an advection equation using a second order MUSCL-Hancock scheme

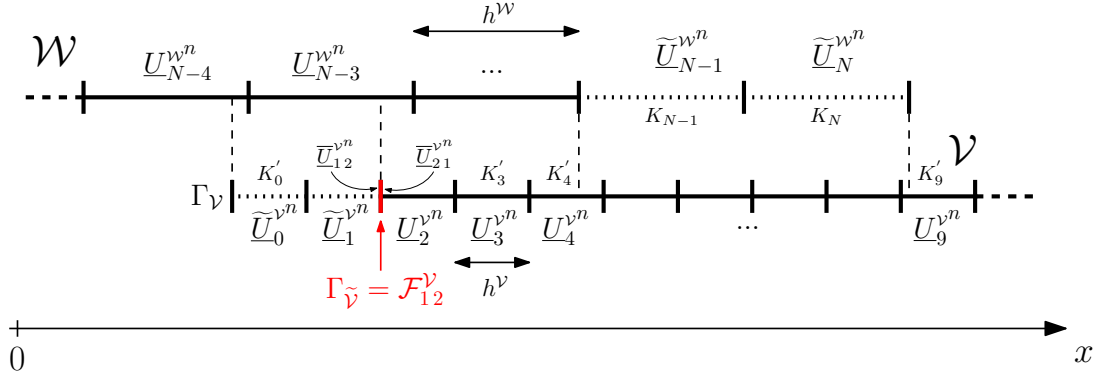


Figure A.1: Chimera boundary condition.

Using the notation introduced in Figure A.1, we demonstrate using a simple numerical example, the ghost cell requirements using a MUSCL Hancock method. To do so, we consider the linear scalar hyperbolic equation of a quantity q :

$$\frac{\partial q}{\partial t} + \nabla F(q) = 0, \quad (\text{A.1})$$

with $F(q) = aq$ where a is the constant advection speed. We discretize this equation on the discrete domain \mathcal{U} using the Godunov first order upwind method and a Rusanov flux [170]:

$$\begin{aligned} q_i^{\mathcal{U}^{n+1}} &= q_i^{\mathcal{U}^n} - C_{\mathcal{U}}^n (u_i^{\mathcal{U}^n} - u_{i-1}^{\mathcal{U}^n}), & \text{if } a > 0, \\ q_i^{\mathcal{U}^{n+1}} &= q_i^{\mathcal{U}^n} - C_{\mathcal{U}}^n (u_{i+1}^{\mathcal{U}^n} - u_i^{\mathcal{U}^n}), & \text{if } a < 0, \end{aligned} \quad (\text{A.2})$$

where $q_i^{\mathcal{U}^n}$ is the numerical approximation of q in the cell K_i , $i \in \Omega_{\mathcal{U}}$, $\mathcal{U} = \{\mathcal{W}, \mathcal{V}\}$, and $C_{\mathcal{U}}^n$ is the CFL number of the discretized domain \mathcal{U} at the discrete time t^n that writes in this case:

$$C_{\mathcal{U}}^n = \frac{a \Delta t_n}{h^{\mathcal{U}}}, \quad \mathcal{U} = \{\mathcal{W}, \mathcal{V}\}. \quad (\text{A.3})$$

As we are using the overlapped grid configuration shown in Figure 2.15 with \mathcal{W} and \mathcal{V} , we note respectively $q_i^{\mathcal{W}^n}$ and $q_i^{\mathcal{V}^n}$, the numerical solutions of q at the discrete time t^n over $K_i \in \mathcal{W}$ and $K'_i \in \mathcal{V}$. For the sake of simplicity, we assume that $a > 0$. This implies that the information comes from \mathcal{W} and needs to be transferred to \mathcal{V} . As a result, we focus on the cell $K'_2 \in \mathcal{V}$ containing the numerical solution $q_2^{\mathcal{V}^n}$ at the time t^n . We apply the MUSCL Hancock scheme to this cell, the objective being to quantify the number of ghost cells k_{GC} required to avoid any impact of the boundary $\Gamma_{\mathcal{V}}$, we use a Rusanov flux instead of the HLLC, for the sake of simplicity. We recall that the gradient computation is performed using the least square method presented in section 1.2.4 B and is centered.

- We first reconstruct the interface states at $\mathcal{F}_{12}^{\mathcal{V}}$ and $\mathcal{F}_{23}^{\mathcal{V}}$:

$$\begin{aligned} \bar{q}_{21}^{\mathcal{V}^n} &= q_2^{\mathcal{V}^n} - \Phi_2^{\mathcal{V}^n} \nabla q_2^{\mathcal{V}^n} \frac{h^{\mathcal{V}}}{2}, & \bar{q}_{23}^{\mathcal{V}^n} &= q_2^{\mathcal{V}^n} + \Phi_2^{\mathcal{V}^n} \nabla q_2^{\mathcal{V}^n} \frac{h^{\mathcal{V}}}{2} \\ \bar{q}_{12}^{\mathcal{V}^n} &= \tilde{q}_1^{\mathcal{V}^n} + \Phi_1^{\mathcal{V}^n} \nabla \tilde{q}_1^{\mathcal{V}^n} \frac{h^{\mathcal{V}}}{2}, & \bar{q}_{32}^{\mathcal{V}^n} &= q_3^{\mathcal{V}^n} - \Phi_3^{\mathcal{V}^n} \nabla q_3^{\mathcal{V}^n} \frac{h^{\mathcal{V}}}{2} \end{aligned} \quad (\text{A.4})$$

with $\nabla q_2^{\nu^n} = \nabla q_2^{\nu^n}(\tilde{q}_1^{\nu^n}, q_2^{\nu^n}, q_3^{\nu^n})$, $\nabla \tilde{q}_1^{\nu^n} = \nabla \tilde{q}_1^{\nu^n}(\tilde{q}_0^{\nu^n}, \tilde{q}_1^{\nu^n}, q_2^{\nu^n})$ and $\nabla q_3^{\nu^n} = \nabla q_3^{\nu^n}(q_2^{\nu^n}, q_3^{\nu^n}, q_4^{\nu^n})$.

- Then we update the interface solutions by half a time step:

$$\begin{aligned} q_{21}^{\nu^{n+\frac{1}{2}}} &= q_2^{\nu^n} - \frac{1}{2}(1 + C_{\mathcal{V}}^n)\Phi_2^{\nu^n}\nabla q_2^{\nu^n}, & q_{23}^{\nu^{n+\frac{1}{2}}} &= q_2^{\nu^n} + \frac{1}{2}(1 - C_{\mathcal{V}}^n)\Phi_2^{\nu^n}\nabla q_2^{\nu^n} \\ q_{12}^{\nu^{n+\frac{1}{2}}} &= \tilde{q}_1^{\nu^n} + \frac{1}{2}(1 - C_{\mathcal{V}}^n)\Phi_1^{\nu^n}\nabla \tilde{q}_1^{\nu^n}, & q_{32}^{\nu^{n+\frac{1}{2}}} &= q_3^{\nu^n} - \frac{1}{2}(1 + C_{\mathcal{V}}^n)\Phi_3^{\nu^n}\nabla q_3^{\nu^n} \end{aligned} \quad (\text{A.5})$$

- Riemann problems are solved at the interfaces \mathcal{F}_{12}^{ν} and \mathcal{F}_{23}^{ν} with the interface states respectively $(q_{12}^{\nu^{n+\frac{1}{2}}}, q_{21}^{\nu^{n+\frac{1}{2}}})$ and $(q_{23}^{\nu^{n+\frac{1}{2}}}, q_{32}^{\nu^{n+\frac{1}{2}}})$. Using a Rusanov flux gives:

$$\begin{aligned} F_{12}^{\nu^{n+\frac{1}{2}}} &= -F_{21}^{\nu^{n+\frac{1}{2}}} = \frac{1}{2}(1 + \text{sign}(a))F(q_{12}^{\nu^{n+\frac{1}{2}}}) + \frac{1}{2}(1 - \text{sign}(a))F(q_{21}^{\nu^{n+\frac{1}{2}}}) = F(q_{12}^{\nu^{n+\frac{1}{2}}}), \\ F_{23}^{\nu^{n+\frac{1}{2}}} &= -F_{32}^{\nu^{n+\frac{1}{2}}} = \frac{1}{2}(1 + \text{sign}(a))F(q_{23}^{\nu^{n+\frac{1}{2}}}) + \frac{1}{2}(1 - \text{sign}(a))F(q_{32}^{\nu^{n+\frac{1}{2}}}) = F(q_{23}^{\nu^{n+\frac{1}{2}}}) \end{aligned} \quad (\text{A.6})$$

where $\text{sign}(a) = 1$ if $a > 0$, and $\text{sign}(a) = -1$ if $a < 0$. We recall that $F(q_j^{\nu^n}) = a q_j^{\nu^n}$ for $j \in \Omega_{\mathcal{V}}$.

- Finally, the solution is updated using the Godunov scheme with the intermediate fluxes:

$$q_2^{\nu^{n+1}} = q_2^{\nu^n} + \frac{\Delta t_n}{h_{\mathcal{V}}} (F_{21}^{\nu^{n+\frac{1}{2}}} - F_{23}^{\nu^{n+\frac{1}{2}}}), \quad (\text{A.7})$$

which can be written explicitly as:

$$q_2^{\nu^{n+1}} = q_2^{\nu^n} + C_{\mathcal{V}}^n [(\tilde{q}_1^{\nu^n} - q_2^{\nu^n}) + \frac{1}{2}(1 - C_{\mathcal{V}}^n)(\Phi_1^{\nu^n}\nabla \tilde{q}_1^{\nu^n} - \Phi_2^{\nu^n}\nabla q_2^{\nu^n})]. \quad (\text{A.8})$$

Knowing that $\nabla \tilde{q}_1^{\nu^n} = \nabla \tilde{q}_1^{\nu^n}(\tilde{q}_0^{\nu^n}, \tilde{q}_1^{\nu^n}, q_2^{\nu^n})$, equation A.8 exhibits the numerical dependency of the cell K'_2 regarding its neighbors.

B - Von Neumann stability analysis of the Chimera method

We carry out a Von Neumann stability analysis [31] for the scalar hyperbolic equation of a quantity q :

$$\frac{\partial q}{\partial t} + \nabla F(q) = 0, \quad (\text{B.1})$$

with $F(q) = aq$ where a is the constant advection speed. Using the configuration illustrated in Figure B.1, we discretize this equation on the discrete domain \mathcal{U} using the Godunov first order upwind method and a Rusanov flux [170]:

$$\begin{aligned} q_i^{\mathcal{U}^{n+1}} &= q_i^{\mathcal{U}^n} - C_{\mathcal{U}}^n (u_i^{\mathcal{U}^n} - u_{i-1}^{\mathcal{U}^{n+1}}), & \text{if } a > 0, \\ q_i^{\mathcal{U}^{n+1}} &= q_i^{\mathcal{U}^n} - C_{\mathcal{U}}^n (u_{i+1}^{\mathcal{U}^n} - u_i^{\mathcal{U}^n}), & \text{if } a < 0, \end{aligned} \quad (\text{B.2})$$

where $q_i^{\mathcal{U}^n}$ is the numerical approximation of q in the cell K_i , $i \in \Omega_{\mathcal{U}}$, $\mathcal{U} = \{\mathcal{W}, \mathcal{V}\}$, and $C_{\mathcal{U}}^n$ is the CFL number of the discretized domain \mathcal{U} at the discrete time t^n that writes in this case:

$$C_{\mathcal{U}}^n = \frac{a\Delta t_n}{h^{\mathcal{U}}}, \quad \mathcal{U} = \{\mathcal{W}, \mathcal{V}\}. \quad (\text{B.3})$$

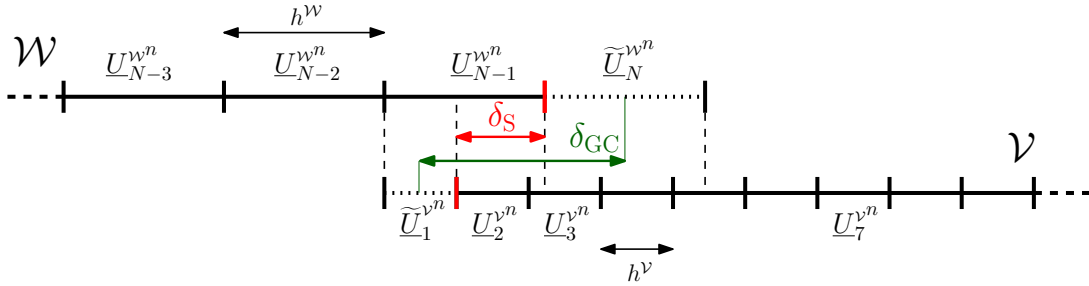


Figure B.1: Chimera configuration with exchange zone gap (δ_{GC}) and exchange zone shift (δ_S).

We focus on the first order Chimera method with a first order upwind Godunov method. We define the rounding error at the cell $K'_j \in \mathcal{V}$ and at the discrete time t^n as:

$$\varepsilon'_j{}^n = v_j^n - \vartheta_j^n, \quad (\text{B.4})$$

where ϑ_j^n is the hypothetical solution of the discretized hyperbolic scalar equation B.1 without rounding error and v_j^n is the numerical approximation of the solution with a finite arithmetic accuracy. The equivalent definition can be made for any cell $K_i \in \mathcal{W}$ and the corresponding rounding error ε_i^n . We assume that $a > 0$. Considering that the solution ϑ_2^n verifies equation B.2, the rounding error also verifies the discretized equation B.2:

$$\varepsilon'_i{}^{n+1} = \varepsilon'_i{}^n - C_{\mathcal{V}}^n [\varepsilon'_i{}^n - \varepsilon'_{i-1}{}^n]. \quad (\text{B.5})$$

Equation B.5 shows that the error and the numerical solution have the same behaviour over time. If we assume periodic boundary conditions at the boundaries of the domain \mathcal{V} , the variation of the spatial error can be decompose using Fourier series on the interval L by:

$$\varepsilon'(x, t) = \sum_{m=1}^M A_m(t) \exp^{ik_m x}, \quad (\text{B.6})$$

where the wave number $k_m = \frac{\pi m}{L_V}$ with $m = 1, 2, \dots, M_V$ and $M_V = L_V/h^V \in \mathbb{N}$. The time dependence is included in the error amplitude A_m . Knowing that the error tends to grow or decrease exponentially over time, it is reasonable to suppose that the amplitude also varies exponentially over time which gives:

$$\varepsilon'(x, t) = \sum_{m=1}^M \exp^{\alpha t} \exp^{ik_m x}, \quad (\text{B.7})$$

where α is a constant. Equation B.1 is linear, so it is possible to study one specific term m :

$$\varepsilon'_m(x, t) = \exp^{\alpha t} \exp^{ik_m x}. \quad (\text{B.8})$$

The same assumptions can be done for \mathcal{W} as it is possible to study one specific term p :

$$\varepsilon_p(x, t) = \exp^{\beta t} \exp^{ik_p x}, \quad (\text{B.9})$$

where β is constant and $k_p = \frac{\pi p}{L_W}$ with $p = 1, 2, \dots, M_W$ and $M_W = L_W/h^W \in \mathbb{N}$. As we are using a first order Chimera interpolation, we have:

$$\tilde{U}_1^{\nu n} = U_{N-1}^{\nu n}. \quad (\text{B.10})$$

As a result, inside the ghost cell K'_1 , we enforce:

$$\varepsilon_1^{\prime n} = \varepsilon_{N-1}^n. \quad (\text{B.11})$$

Given these notations, we focus on the cell K'_2 and rewrite equation B.5 taking into account the Chimera exchange:

$$\exp^{\alpha(t+\Delta t_n)} \exp^{ik_m x} = \exp^{\alpha t} \exp^{ik_m x} - C_V^n \left[\exp^{\alpha t} \exp^{ik_m x} - \exp^{\beta t} \exp^{ik_p(x - \frac{1}{2}(h_W + h_V) + \delta_S)} \right], \quad (\text{B.12})$$

with

$$\delta_S = \delta_{GC} - \frac{h_W + h_V}{2}, \quad (\text{B.13})$$

which can be simplified as:

$$\exp^{\alpha \Delta t_n} = 1 - C_V^n \left[1 - \underbrace{\exp^{(\beta - \alpha)t}}_A \exp^{i \overbrace{\left((k_p - k_m)x + k_p(\delta_S - \frac{1}{2}(h_W + h_V)) \right)}^B} \right]. \quad (\text{B.14})$$

The amplitude factor G_n is defined by :

$$G_n = \frac{\varepsilon_j^{n+1}}{\varepsilon_j^n}. \quad (\text{B.15})$$

The necessary and sufficient condition for the error to be bounded is $|G| \leq 1$. Considering that

$$G_n = \exp^{\alpha \Delta t_n}, \quad (\text{B.16})$$

we have,

$$G_n = 1 - C_V^n [1 - A \exp^{iB}]. \quad (\text{B.17})$$

The modulus of the amplitude factor becomes:

$$|G_n| = \sqrt{1 - 2C_V^n (1 - A \cos(B)) (1 - C_V^n)}. \quad (\text{B.18})$$

As a result, stability is ensured if

$$C_{\mathcal{V}}^n < 1, \quad (\text{B.19})$$

and if,

$$\left| \cos \left((k_p - k_m)x + k_p(\delta_S - \frac{1}{2}(h_{\mathcal{W}} + h_{\mathcal{V}})) \right) \right| < \frac{1}{\exp(\beta - \alpha)t}. \quad (\text{B.20})$$

Condition B.19 is the CFL condition for the grid \mathcal{V} whereas condition B.20 results from the use of overlapping grids and depends on the wavenumbers k_m and k_p , the cell sizes $h_{\mathcal{W}}$ and $h_{\mathcal{V}}$ and the amplitude constants α and β .

In the case of $\alpha > \beta$, $\frac{1}{\exp(\beta - \alpha)t} \xrightarrow{t \rightarrow \infty} \infty$ which means that the Chimera exchange does not alter the stability of the scheme. If $\alpha < \beta$, $\frac{1}{\exp(\beta - \alpha)t} \xrightarrow{t \rightarrow \infty} 0$, therefore, the scheme can become unstable over time. However, the values α and β depend on the grid size as they correspond to the amplitude time variation coefficient of the error.

C - Problematic configurations using the Chimera-MBM

During the implementation of the Chimera-Mediating Body Method with the staggered integration scheme presented in section 4.2.2.D, different problematic configurations have been encountered and have been solved with improvements made to the integration scheme improving the robustness and the flexibility of the Chimera-MBM. These different problematic configurations are reviewed in this section.

C.1 - Ghost cells belonging to a $+/-$ neighboring active cell set and receiving from an active cell

The first problematic configuration is illustrated in Figure C.1 and comes from the fact that ghost cells can be used as a support for the $+/-$ extrapolation due to the minimized size of the Chimera exchange zone. At the beginning of the n -th time step, as the $+/-$ extrapolation provides a value to the indefinite sending cells, it must be carried out before the Chimera sending operations. However, before the Chimera operations, the values inside the ghost cells cannot be used as they result from the fluid integration carried out during the previous time iteration ($n - 1$ -th time step).

Using the grid configuration represented in Figure C.1, if the $+/-$ extrapolation is performed before the Chimera sending, the $-$ extrapolated state of the indefinite sending cell K_j is not usable as the cell K_l does not have received information yet. Therefore, performing the $+/-$ extrapolation followed by the Chimera sending procedure (see section 2.3.2) will result in the propagation of incorrect values within the fluid domains.

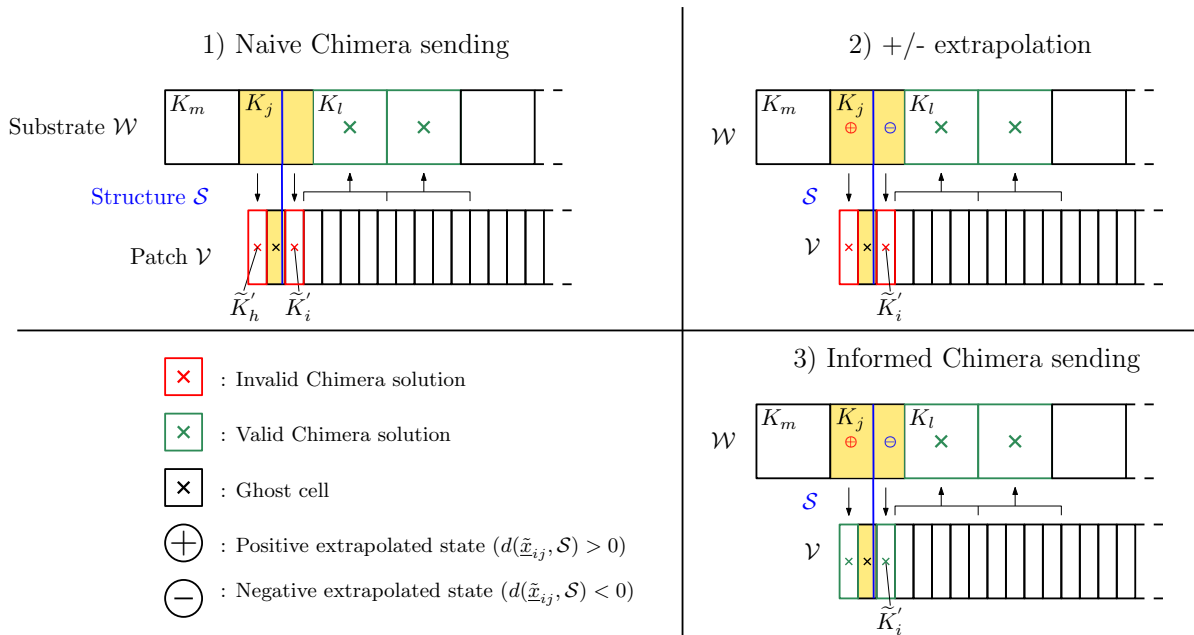


Figure C.1: Problematic configuration where the indefinite sending cell K_j extrapolates from a ghost cell K_l .

To solve this issue, we propose the following solution: before the $+/-$ extrapolation, a first order Chimera sending is performed (first step in Figure C.1). This step is referred as *naive Chimera sending*. A first order naive Chimera sending makes sense considering that the $+/-$ extrapolation is mostly used on the coarsest grid between the patch and the substrate as seen in Figure C.1. Therefore, the naive Chimera sending provides a solution to coarse ghost cells like K_l which, in the case of a high cell ratio $\chi \gg 1$, are not significantly impacted by the order of the Chimera sending (see fine-to-coarse Chimera sendings in section 2.4)

After the $+/-$ extrapolation (second step in Figure C.1), a first order Chimera sending is performed and it corresponds to the first order sending step required in the second order Chimera sending procedure (see section 2.2.3.C). This step is referred as *informed Chimera sending* (third step in Fig. C.1).

C.2 - Ghost cells belonging to a $+/-$ neighboring active cell set and receiving from an indefinite sending cell

The second problematic configuration is an extension of the first problem that can happen with 2D and 3D grids as represented in Figure C.2. It comes from the fact that a ghost cell \tilde{K}_m can belong to the $+/-$ active cell neighboring of a cell K_j ($\tilde{K}_m \in \mathcal{L}_{j*}^{s,w+/-}(0)$) and can propagate an unusable solution. Unlike the situation presented in section C.1, the ghost cell \tilde{K}_m , belonging to a $+/-$ active cell neighboring of K_j receives information from indefinite sending cells K'_m and K'_p .

As Chimera operations like the naive Chimera sending, the $+/-$ extrapolation or the informed Chimera sending are performed by pair (one operation for the patch \mathcal{V} and one for the substrate \mathcal{W}), the order in the pair must not impact the method. In the case of Figure C.2, we see that after the naive Chimera sending (for both the patch \mathcal{V} and substrate \mathcal{W}), \tilde{K}_m has received an invalid value from the indefinite sending cells K'_p and K'_m as the $+/-$ extrapolation has not been performed yet. Then, during the $+/-$ extrapolation (for both the patch \mathcal{V} and substrate \mathcal{W}), the indefinite sending cell K_j uses the solution of the ghost cell \tilde{K}_m to reconstruct a $+$ state or a $-$ state as it is an active cell adjacent to K_j . At this moment, the $+/-$ extrapolated value inside K_j coming from \tilde{K}_m is not usable. Then, the informed Chimera sending will spread the unusable $+/-$ value from K_j to the ghost cells \tilde{K}_j and \tilde{K}_k .

A possible cure to this problem would be to forbid the use of ghost cells as $+/-$ extrapolation neighbors but this would cause problems when a structure enters or leaves the patch. The chosen solution is to perform the $+/-$ extrapolation and the informed Chimera sending steps twice in a row. This way, during the first $+/-$ extrapolation, the indefinite cells K'_p and K'_m extrapolate $+/-$ values that are sent to \tilde{K}_m during the first informed sending. During the second $+/-$ extrapolation, the indefinite sending cell K_j can extrapolate $+/-$ states using \tilde{K}_m which contains a usable solution. This first improvement on the time integration scheme is illustrated in Figure 4.16 by a small dotted-line red loop.

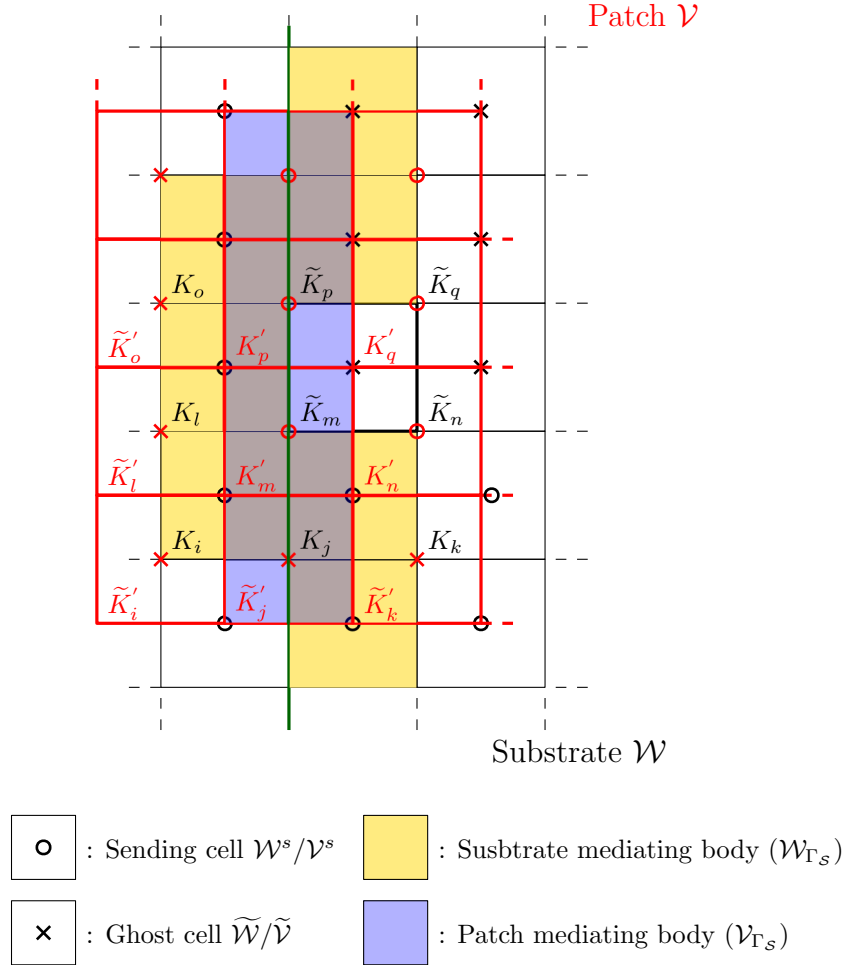


Figure C.2: Problematic configuration where the ghost cell \tilde{K}_m belongs to the $+/-$ neighboring of K_j but receives from indefinite sending cells K'_p and K'_m .

C.3 - Indefinite active cells using ghost cells for the MBM extrapolation

The last configuration, illustrated in Figure C.3, comes from the possibility for the structure to cross fluid grid boundaries in an overlapping grid context (patch boundaries in particular). As we have seen in section 4.2.1.E, when the mediating body changes, indefinite active cells require an extrapolation referred as MBM extrapolation. Because of the Chimera method, ghost cells are used at the borders of the patch. As illustrated in Figure C.3, when the structure enters the patch, indefinite active cells like K'_k can use ghost cells like \tilde{K}'_i as valid MBM extrapolation neighbors ($\mathcal{L}'_k \cap \tilde{\mathcal{V}} \neq \{\emptyset\}$).

However, with the Chimera-MBM time integration scheme presented in section 4.2.2.D, the MBM extrapolation is performed before the update of the ghost cells $\tilde{\mathcal{V}}$ and $\tilde{\mathcal{W}}$ which do not contain a usable solution at this step due to the previous time integration performed over the fluid domain. This problem is addressed with a repetition of the steps 2 to 8 in the Chimera-MBM time integration scheme presented in section 4.2.2.D which will perform a first loop referred as prediction loop from steps 2 to 8 using with the indefinite active cells $\mathcal{U}_{*,\text{indef}}$, $\mathcal{U} = \{\mathcal{W}, \mathcal{V}\}$ not updated correctly. At the end of this loop, the MBM extrapolation is carried out with valid ghost cell solutions. Then a second loop from steps 2 to 8 referred as correction loop is carried out to set the values of the ghost cells that were dependent on indefinite active cells $\mathcal{U}_{*,\text{indef}}$, $\mathcal{U} = \{\mathcal{W}, \mathcal{V}\}$ during the prediction loop. This

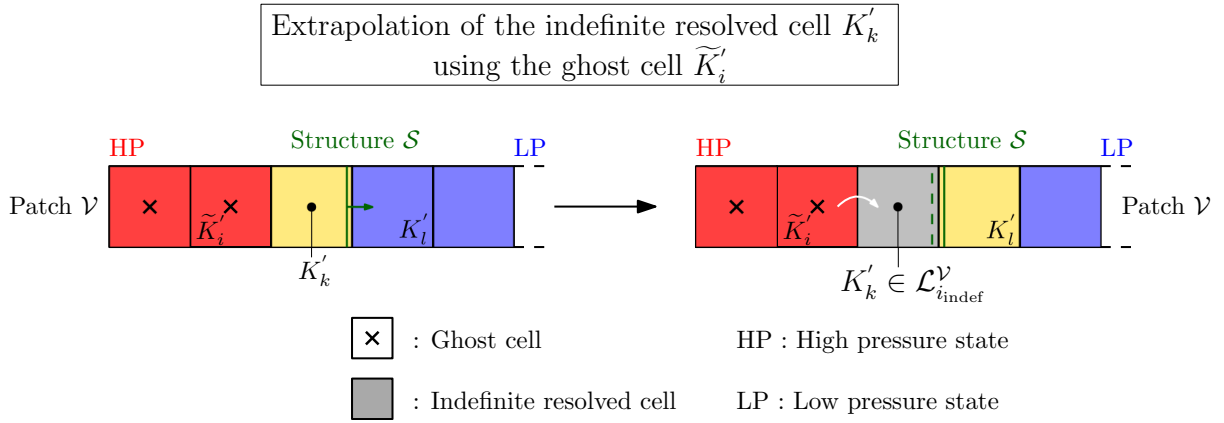


Figure C.3: Problematic configuration where the indefinite active cell K'_k uses the ghost cell \tilde{K}'_i to extrapolate its value.

improvement on the time integration scheme is illustrated in Figure 4.16 by a long dotted-line red loop.

D - Analytical solution for the free piston test case

D.1 - Presentation of the problem

In this section, we detail the steps to derive an analytical solution for a one-dimensional free moving piston used to assess the Chimera-MBM in section 4.3.1. A cuboid non-deformable piston \mathcal{P} initially at rest, with a thickness $e = 1.35 \cdot 10^{-3}$ m and a side $l = 0.2$ m, separates two fluid cavities also at rest inside an infinite tube of height l as shown in Figure D.1. The boundary of the piston is written $\Gamma_{\mathcal{P}}$. The initial fluid states are given by:

$$\begin{pmatrix} \rho_L \\ u_L \\ p_L \end{pmatrix} = \begin{pmatrix} 0.2 \text{ kg.m}^{-3} \\ 0 \\ 0.2 \text{ Pa} \end{pmatrix}, \quad \begin{pmatrix} \rho_R \\ u_R \\ p_R \end{pmatrix} = \begin{pmatrix} 0.125 \text{ kg.m}^{-3} \\ 0 \\ 0.1 \text{ Pa} \end{pmatrix}, \quad (\text{D.1})$$

The cavities have a pressure jump $\Delta P = 0.1$ initiating the displacement of the piston that generates a compression wave on the right-hand side, in the low pressure region and a rarefaction wave on the left-hand side, in the high pressure region of the tube. The pressure values have been chosen in order to keep the flow isentropic in the compression wave region and to prevent the formation of a shock wave. The piston parameters are the following: $\rho_s = 2710 \text{ kg} \cdot \text{m}^{-3}$, $e = 1.35 \cdot 10^{-3}$ m, $l = 0.2$ m.

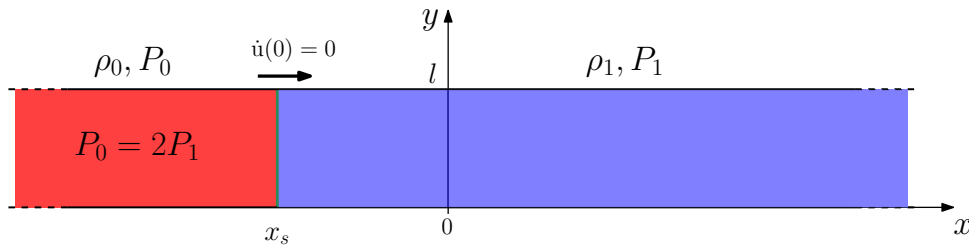


Figure D.1: Free piston case presentation with an infinite domain.

The analytical solution of the free piston problem is computed in two steps: first, the motion of the piston is obtained using the fundamental principle of dynamics applied to the piston combined with the method of characteristics [1] applied to the fluid domain as a one-dimensional system. Finally, knowing the motion of the piston, the fluid solution is computed over the entire domain using the method of characteristics. In this problem, we assume the absence of discontinuities inside each cavity which ensures entropy conservation and we treat the cavities as two separate simple wave regimes. This problem is one-dimensional along the x -axis.

D.2 - Study of the piston dynamics

D.2.1 - Fundamental principle of dynamics applied to the piston

To study piston dynamics, we use the notations already introduced in section 4.1.1 for the structure. The fundamental principle of dynamics applied to the piston at the time t gives:

$$\int_{\mathcal{P}} \rho_s \ddot{\underline{x}}(\underline{x}, t) dV = \int_{\Gamma_{\mathcal{P}}} p(\underline{x}, t) d\underline{S}, \quad (\text{D.2})$$

Considering the piston as a rigid-body and assuming that the pressure exerted on the piston is uniform on each side, we can write equation D.2 as:

$$m_s \ddot{\underline{u}}(t) dV = \left[p(x_s - e/2, t) - p(x_s + e/2, t) \right] \underline{S}, \quad (\text{D.3})$$

with $m_s = \rho_s e S$ the piston total mass, \underline{S} the piston surface, normal to the x -axis, in contact with the fluid on either side of the piston such that $S = \|\underline{S}\| = l^2$ and x_s the piston barycenter position along the x -axis. The thickness of the piston e being negligible compared to the other dimensions of the problem ($e \ll l$), we assume $p(x_s - e/2, t) \approx p(x_s^L, t)$ and $p(x_s + e/2, t) \approx p(x_s^R, t)$. We note the left hand side of the piston, the side such that $x \xrightarrow{x < x_s} x_s$, corresponding to x_s^L . Reciprocally, we note the right hand side of the piston, the side such that $x \xrightarrow{x > x_s} x_s$, corresponding to x_s^R . Also the problem being one-dimensional, we can limit the study to the x -component of Equation D.3, which writes:

$$m_s \ddot{u}(t) = \left[p(x_s^L, t) - p(x_s^R, t) \right] S, \quad (\text{D.4})$$

with \ddot{u} the x -component of the acceleration $\ddot{\underline{u}}$.

Knowing the initial fluid states (ρ_L, u_L, p_L) , (ρ_R, u_R, p_R) and assuming two simple wave regimes on either side of the piston, we can compute values for $p(x_s^L, t)$ and for $p(x_s^R, t)$ using the method of characteristics [1]. The free piston solution, represented in Figure D.2, can be decomposed into four different regions: the L region corresponding to the constant left state, the L^* region, on the left hand side of the piston, corresponding to the expansion wave, the R^* region, on the right hand side of the piston, corresponding to the compression wave, and the R region which corresponds to the constant right state.

The L region and the L^* regions are separated by the characteristic $\Gamma_L^-(0)$ such that $\frac{\partial x}{\partial t} = -c_L$. Symmetrically, the R region and the R^* regions are separated by the characteristic $\Gamma_R^+(0)$ such that $\frac{\partial x}{\partial t} = c_R$.

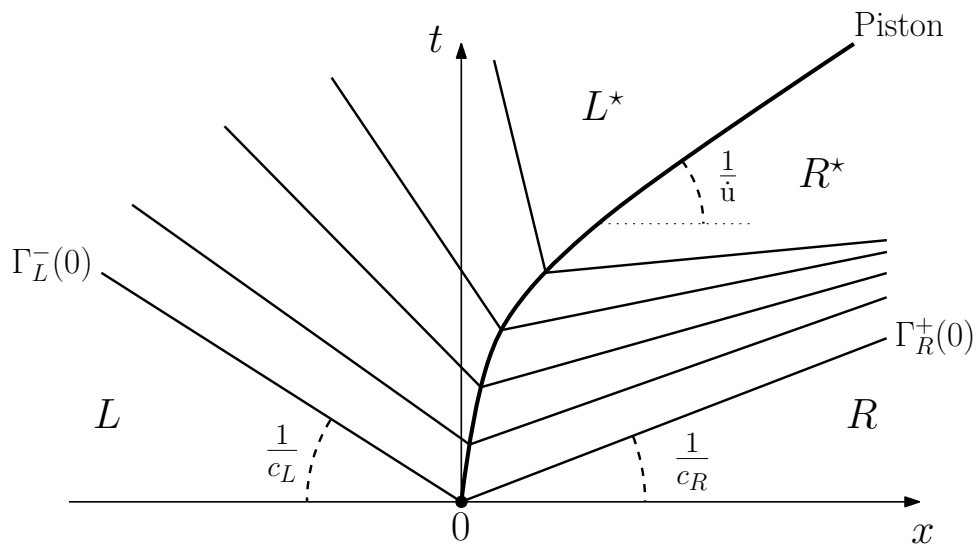


Figure D.2: Wave pattern of the free piston case.

D.2.2 - Computation of the left fluid pressure $p(x_s^L, t)$ exerted on the piston

Starting with the left fluid pressure $p(x_s^L, t)$, we focus on the domain to the left of the piston. This region corresponds to the expansion wave. As for any simple wave regime, we have

$$J^\pm = u \pm \frac{2}{\gamma - 1}c = \text{constant}, \quad (\text{D.5})$$

the constant being identical across the region. c is the sound speed which for a perfect gas is defined as $\sqrt{\frac{\gamma p}{\rho}}$, with γ the specific heat ratio.

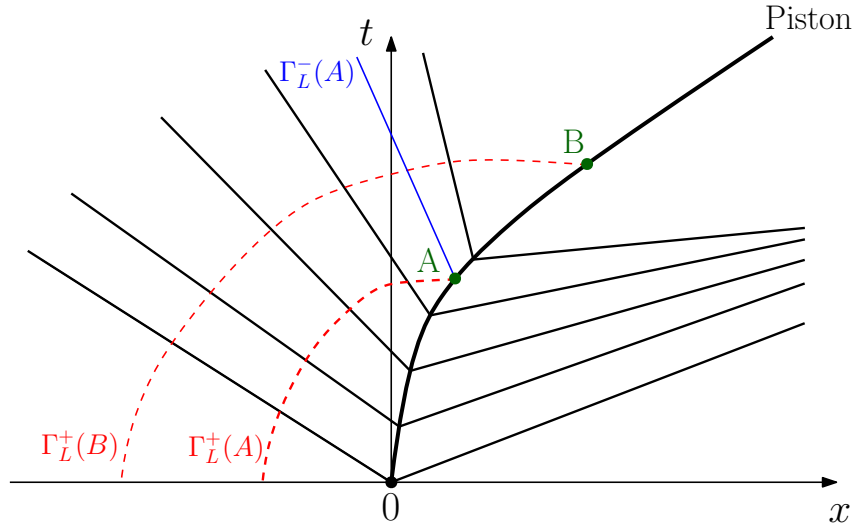


Figure D.3: Characteristics of the left hand side domain of the free piston solution.

As represented in Figure D.3, for the left hand side expansion wave, for any point $A(x_s^L, t)$, J^+ is constant along the characteristic $\Gamma_L^+(A)$, therefore,

$$J_A^+(t) = J_A^+(0) \Leftrightarrow \dot{u}(t) + \frac{2}{\gamma - 1}c_A = \frac{2}{\gamma - 1}c_L. \quad (\text{D.6})$$

Equation D.6, provides the following relation for c_A ,

$$c_A = c_L - \frac{\gamma - 1}{2}\dot{u}(t). \quad (\text{D.7})$$

Using the sound speed definition $c_A = \sqrt{\frac{\gamma P_A}{\rho_A}}$ with the isentropic flow relation $\frac{p_L}{(\rho_L)^\gamma} = \frac{p_A}{(\rho_A)^\gamma}$, we find the following expression for $p_A(t)$ depending on $\dot{u}(t)$ and the left constant state (ρ_L, u_L, p_L) :

$$p_A(t) = p(x_s^L, t) = p_L \left[1 - \frac{\gamma - 1}{2c_L} \dot{u}(t) \right] \quad (\text{D.8})$$

D.2.3 - Computation of the right fluid pressure $p(x_s^R, t)$ exerted on the piston

The equivalent reasoning is performed to find an expression for the right fluid pressure $p(x_s^R, t)$ exerted on the piston.

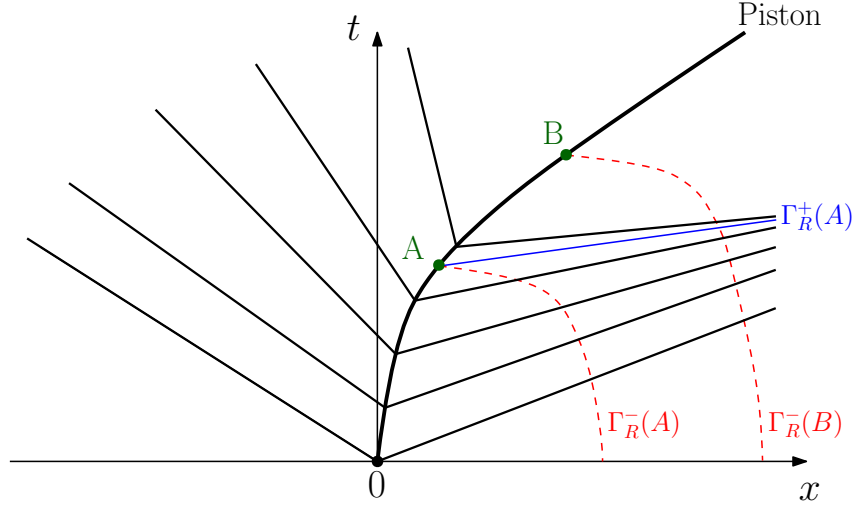


Figure D.4: Characteristics of the right hand side domain of the free piston solution.

As represented in Figure D.4, for the right hand side compression wave, for any point $A(x_s^R, t)$, J^- is constant along the characteristic $\Gamma_R^-(A)$, therefore,

$$J_A^-(t) = J_A^-0 \Leftrightarrow \dot{u}(t) - \frac{2}{\gamma-1}c_A = -\frac{2}{\gamma-1}c_R. \quad (\text{D.9})$$

Equation D.9, provides the following relation for c_A ,

$$c_A = c_R + \frac{\gamma-1}{2}\dot{u}(t). \quad (\text{D.10})$$

Using the sound speed definition $c_A = \sqrt{\frac{\gamma P_A}{\rho_A}}$ with the isentropic relation $\frac{p_R}{(\rho_R)^\gamma} = \frac{p_A}{(\rho_A)^\gamma}$, we find the following expression for $p_A(t)$ depending on $\dot{u}(t)$ and the right constant state (ρ_R, u_R, p_R) :

$$p_A(t) = p(x_s^R, t) = p_R \left[1 + \frac{\gamma-1}{2c_R} \dot{u}(t) \right]. \quad (\text{D.11})$$

Finally, the motion equation of the piston can be written,

$$\ddot{u}(t) = \frac{S}{m_s} \left[p_L \left(1 - \frac{\gamma-1}{2c_L} \dot{u}(t) \right) - p_R \left(1 + \frac{\gamma-1}{2c_R} \dot{u}(t) \right) \right] \quad (\text{D.12})$$

D.2.4 - Time integration of the piston dynamics

Equation D.12, is integrated numerically using a central difference scheme similar to the one presented in section 4.1.4 except that the velocity does not have an implicit correction. Knowing, the piston displacement u^n , velocity \dot{u}^n and acceleration \ddot{u}^n at the discrete time t^n , the quantities u^{n+1} , \dot{u}^{n+1} and \ddot{u}^{n+1} at the discrete time $t^{n+1} = t + \Delta t_n$ are computed using the following scheme:

1. Explicit velocity prediction at half time step:

$$\dot{u}^{n+\frac{1}{2}} = \dot{u}^n + \frac{\Delta t_n}{2} \ddot{u}^n, \quad (\text{D.13})$$

2. Explicit displacement prediction:

$$u^{n+1} = u^n + \Delta t_n \dot{u}^{n+\frac{1}{2}}, \quad (\text{D.14})$$

3. Explicit acceleration update at half time step:

$$\ddot{u}^{n+\frac{1}{2}} = \frac{S}{m_s} \left[p_L \left(1 - \frac{\gamma-1}{2c_L} \dot{u}^{n+\frac{1}{2}} \right) - p_R \left(1 + \frac{\gamma-1}{2c_R} \dot{u}^{n+\frac{1}{2}} \right) \right], \quad (\text{D.15})$$

4. Explicit velocity prediction:

$$\dot{u}^{n+1} = \dot{u}^{n+\frac{1}{2}} + \frac{\Delta t_n}{2} \ddot{u}^{n+\frac{1}{2}}. \quad (\text{D.16})$$

5. Explicit acceleration update:

$$\ddot{u}^{n+1} = \frac{S}{m_s} \left[p_L \left(1 - \frac{\gamma-1}{2c_L} \dot{u}^{n+1} \right) - p_R \left(1 + \frac{\gamma-1}{2c_R} \dot{u}^{n+1} \right) \right], \quad (\text{D.17})$$

Δt_n is chosen depending on the number of solution points that is necessary in order for the analytical solution to be accurate enough (see Equation D.22). Due to the low computational time of such a solution, we have chosen to use a value for $\Delta t_n = 10^{-8}$, lower than the finer grid used for the numerical solutions ($\approx 10^{-3} - 10^{-4}$). This high accuracy of the piston solution is necessary for the computation of the fluid solution. The final dimensionless time of the analytical solution is identical to the numerical test case which is $t_f^* = t_f \dot{u}_\infty / L = 0.106$, where $\dot{u}_\infty \approx 0.277 \text{ m.s}^{-1}$ is the asymptotic speed of the piston in an infinite domain and $t_f = 23 \text{ s}$. The analytical solution of the piston dynamics is represented in Figure D.5 with the piston displacement and velocity profiles.

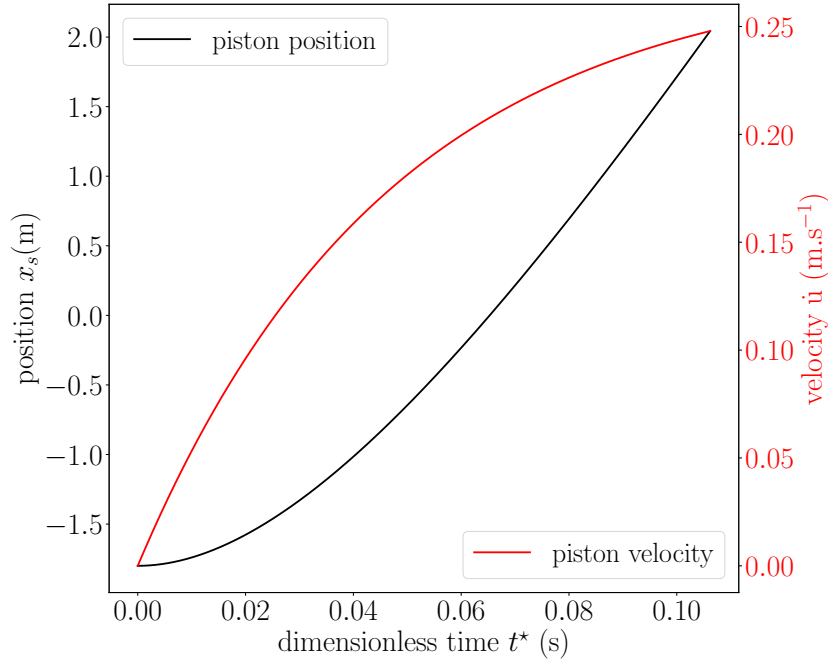


Figure D.5: Piston position x_s and velocity \dot{u} over time.

D.3 - Computation of the fluid solution

Knowing the piston solution at every $t^* \in [0, t_f^*]$, we can compute the fluid solution using the method of characteristics [1].

If $\frac{x}{t} < -c_L$, the fluid state is equal to the constant left state (ρ_L, u_L, p_L) . If $\frac{x}{t} > c_R$, the fluid state is equal to the constant right state (ρ_R, u_R, p_R) . The remaining unknown states correspond to the L^* region on the left hand side of the piston and the R^* region on the right hand side of the piston.

D.3.1 - L^* region

Starting with the L^* region, the fluid solution in the expansion fan region is computed using the method of characteristics [1]. Using Figure D.6, we search the fluid state of a point $B(x, t_f)$ located in the expansion fan. Along the $\Gamma_L^+(B)$ characteristic, J^+ is constant, therefore,

$$J_B^+(t_f) = J_B^+(0) \Leftrightarrow u_B + \frac{2}{\gamma-1}c_B = \frac{2}{\gamma-1}c_L. \quad (\text{D.18})$$

From Equation D.18, the relation between c_B and u_B writes,

$$c_B = c_L - \frac{\gamma-1}{2}u_B. \quad (\text{D.19})$$

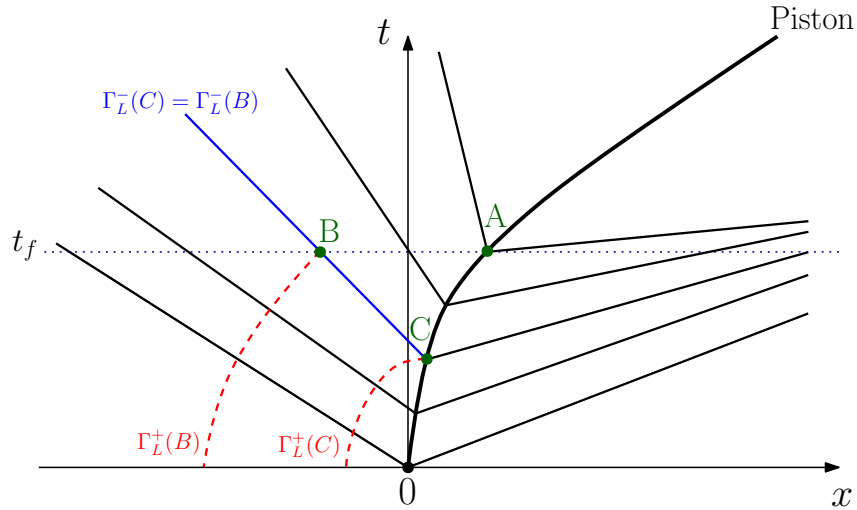


Figure D.6: Description of the characteristics in the expansion fan region.

Along the $\Gamma_L^-(B)$ characteristic,

$$\frac{\partial x}{\partial t} = u_B - c_B = \frac{\gamma+1}{2}u_B - c_L. \quad (\text{D.20})$$

Integrating Equation D.20 along $\Gamma_L^-(B)$ between $B(x, t_f)$ and $C(x_s^L, t_C)$, provides the following expression for u_B ,

$$u_B = \frac{2}{\gamma+1} \left(\frac{x - x_C}{t_f - t_C} + c_L \right). \quad (\text{D.21})$$

The point $C(x_s^L, t_C)$ is searched numerically using the discrete piston solution such that,

$$|(x - x_C) - (\dot{u}(t_C) + c_C)(t - t_C)| \leq \varepsilon, \quad (\text{D.22})$$

with $c_C = c_L - \frac{\gamma-1}{2}\dot{u}(t_C)$ using $J_C^+(t_C) = J_C^+(0)$ and $\varepsilon = 10^{-10}$ is a numerical tolerance to approximate zero which determines the level of accuracy of the analytical solution. The chosen value for ε alters the values of the error computed in the numerical test cases in section 4.3.1 from 10^{-10} which is well below the errors induced by the Chimera method compared to a single grid method ($10^{-5} - 10^{-6}$) and does not change the conclusions that can be drawn from the results. The point $C(x_s^L, t_C)$, corresponds to the piston position and to the time when the $\Gamma_L^-(B)$ characteristic is emitted.

Using Equation D.19,

$$c_B = u_B - \frac{x - x_C}{t_f - t_C}. \quad (\text{D.23})$$

Using the sound speed definition $c_B = \sqrt{\frac{\gamma p_B}{\rho_B}}$ with the isentropic relation $\frac{p_L}{(\rho_L)^\gamma} = \frac{p_B}{(\rho_B)^\gamma}$, we find the following expression for p_B :

$$p_B = p_L \left[\frac{1}{c_L} \left(u_B - \frac{x - x_C}{t_f - t_C} \right) \right]^{\frac{2\gamma}{\gamma-1}}. \quad (\text{D.24})$$

Finally,

$$\rho_B = \rho_L \left[\frac{1}{c_L} \left(u_B - \frac{x - x_C}{t_f - t_C} \right) \right]^{\frac{2}{\gamma-1}}. \quad (\text{D.25})$$

As a result, for a given point $B(x, t_f)$ located in the expansion fan region ($-c_L < \frac{x}{t_f} < \frac{x_s^L(t_f)}{t_f}$), the state (ρ_B, u_B, p_B) is fully defined.

D.3.2 - R^* region

The same reasoning is applied to the R^* region. Using Figure D.7, we search the fluid state of a point $B(x, t_f)$ located in the compression wave region. Along the $\Gamma_L^-(B)$ characteristic, J^- is constant, therefore,

$$J_B^-(t_f) = J_B^-(0) \Leftrightarrow u_B - \frac{2}{\gamma-1}c_B = -\frac{2}{\gamma-1}c_R. \quad (\text{D.26})$$

From Equation D.26, the relation between c_B and u_B writes,

$$c_B = c_R + \frac{\gamma-1}{2}u_B. \quad (\text{D.27})$$

Along the $\Gamma_R^+(B)$ characteristic,

$$\frac{\partial x}{\partial t} = u_B + c_B = \frac{\gamma+1}{2}u_B + c_R. \quad (\text{D.28})$$

Integrating Equation D.28 along $\Gamma_R^+(B)$, between $B(x, t_f)$ and $C(x_s^R, t_C)$, provides the following expression for u_B ,

$$u_B = \frac{2}{\gamma+1} \left(\frac{x - x_C}{t_f - t_C} - c_R \right). \quad (\text{D.29})$$

The point $C(x_s^L, t_C)$ is searched numerically using the discrete piston solution such that,

$$|(x - x_C) - (\dot{u}(t_C) + c_C)(t - t_C)| \leq \varepsilon, \quad (\text{D.30})$$

with $c_C = c_R + \frac{\gamma-1}{2}\dot{u}(t_C)$ using $J_C^-(t_C) = J_C^-(0)$ and $\varepsilon = 10^{-10}$ is the numerical tolerance to approximate zero. The point $C(x_s^L, t_C)$, corresponds to the piston position and to the time when the $\Gamma_R^+(B)$ characteristic is emitted.

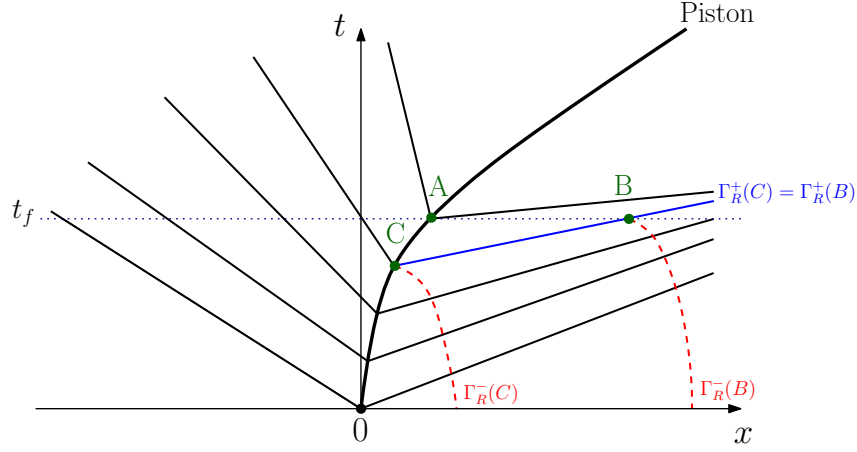


Figure D.7: Description of the characteristics in the compression wave region.

Using Equation D.27,

$$c_B = \frac{x - x_C}{t_f - t_C} - u_B. \quad (\text{D.31})$$

Using the sound speed definition $c_B = \sqrt{\frac{\gamma p_B}{\rho_B}}$ with the isentropic relation $\frac{p_R}{(\rho_R)^\gamma} = \frac{p_B}{(\rho_B)^\gamma}$, we find the following expression for p_B :

$$p_B = p_R \left[\frac{1}{c_R} \left(\frac{x - x_C}{t_f - t_C} - u_B \right) \right]^{\frac{2\gamma}{\gamma-1}}. \quad (\text{D.32})$$

Finally, the density ρ_B is defined as:

$$\rho_B = \rho_R \left[\frac{1}{c_R} \left(\frac{x - x_C}{t_f - t_C} - u_B \right) \right]^{\frac{2}{\gamma-1}}. \quad (\text{D.33})$$

As a result, for a given point $B(x, t_f)$ located in the compression wave region ($\frac{x_s^R(t_f)}{t_f} < \frac{x}{t_f} < c_R$), the state (ρ_B, u_B, p_B) is fully defined. The analytical density ρ , velocity u and pressure p profiles for the fluid are represented in Figure D.8. Those profiles are used in section 4.3.1 for the assessment of the Chimera-MBM in Figure 4.19 and Figure 4.20 for a split grid configuration and in Figure 4.32 for a patched grid configuration.

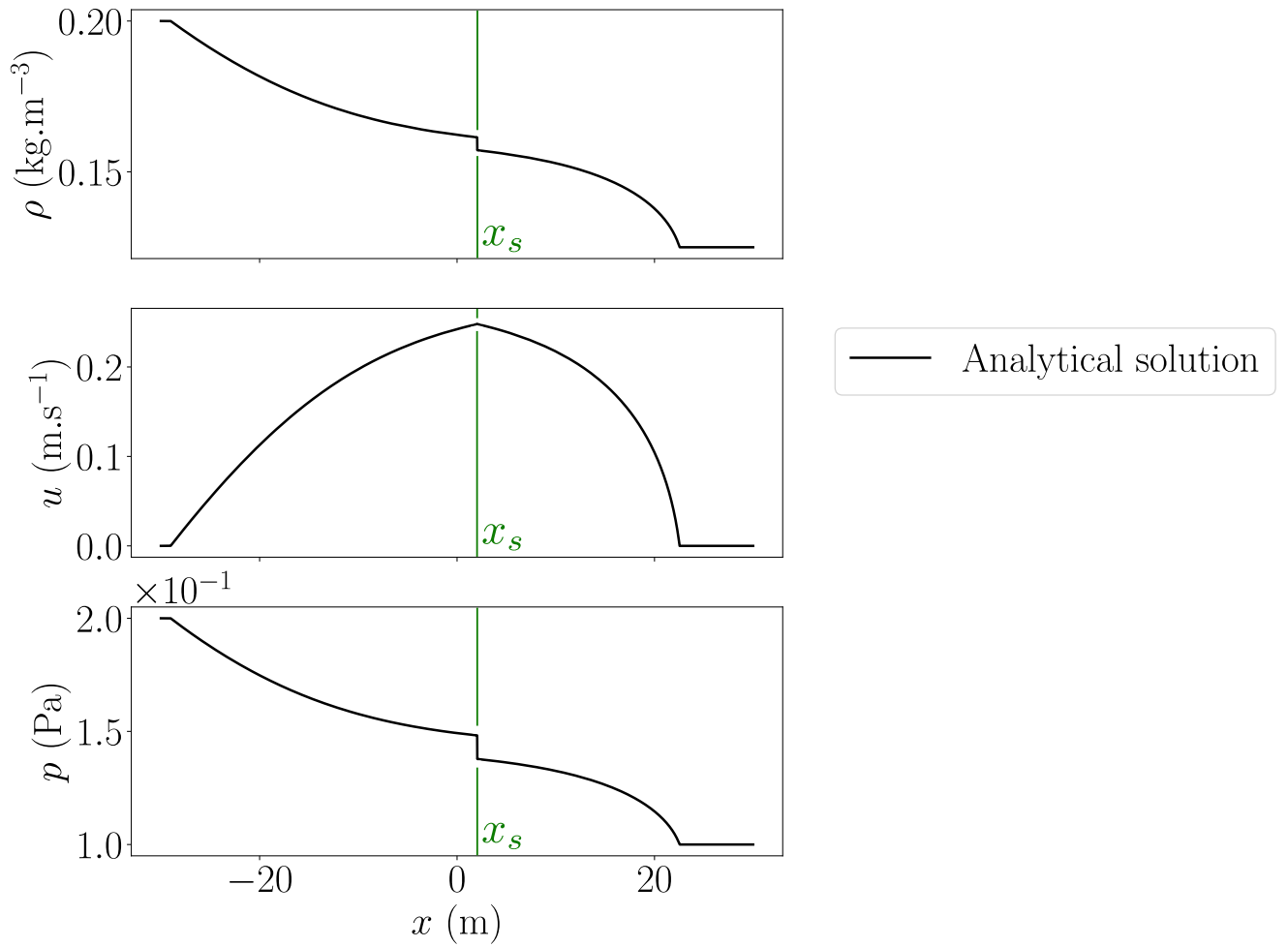


Figure D.8: Free piston density ρ , velocity u and pressure p profiles at $t^* = t_f^*$ of the analytical solution.

Synthèse du manuscrit en français

Introduction et contexte scientifique

L'étude des situations accidentelles impliquant des systèmes à grande échelle sous haute pression dans le cadre de géométries complexes est d'une importance critique pour le dimensionnement et la sécurité des installations dans un environnement industriel. Dans le contexte de l'énergie nucléaire, on retrouve ces conditions extrêmes lorsqu'un réacteur à eau pressurisé (REP) est touché par un Accident de Perte de Réfrigérant Primaire (APRP) ou une explosion H₂ par exemple. Le fonctionnement opérationnel des REP implique des conditions de température et de pression élevées ce qui rend les transitoires accidentels de tels systèmes abruptes avec des conséquences potentiellement sévères.

Ce contexte accidentel brutal implique des écoulements compressibles à haute vitesse se propageant dans les internes du système. Ces écoulements transitoires rapides interagissent alors avec des structures déformables induisant des phénomènes physiques couplés à très petite échelle temporelle. Étant donné les différences d'échelle spatiale et temporelle ainsi que les différences de pressions intervenant dans les transitoires rapides de ces systèmes, des composantes structurelles peuvent subir des déplacements d'amplitude finie.

À cause des risques et de la difficulté à reproduire ces conditions accidentelles avec une échelle géométrique et des conditions initiales représentatives des situations d'intérêt, la simulation numérique se présente comme une alternative permettant de caractériser les réponses de ces systèmes transitoires. La production de résultats numériques précis et fiables dans de telles configurations est une tâche compliquée car le domaine de calcul doit prendre en compte les échelles les plus grandes mais aussi les plus petites. En effet, des détails géométriques de petite échelle peuvent induire des perturbations locales altérant la nature globale de l'écoulement. Cette disparité des échelles est représentée par la Figure 5.9, illustrant le caractère local des perforations des plaques de cloisonnement par rapport à la taille d'une cuve de REP. Généralement négligées dans les modèles à grande échelle de REP, ces perforations impactent pourtant la propagation des ondes dans le cadre de la simulation d'un APRP.

La prise en compte de l'ensemble des échelles au sein d'une même et unique grille implique des procédures de maillage complexes susceptibles de produire un très grand nombre de points et des grilles de qualité moyenne. En plus de la contrainte de maillage induite par la complexité géométrique, une approche monogridde est restrictive lorsque les domaines de fluide et les composantes structurelles sont modélisées à l'aide de maillages topologiquement connectés: la procédure de maillage se complexifie et le déplacement des structures est restreint pour préserver la qualité des cellules fluides connectées.

Pour répondre à ces problématiques, nous proposons d'associer au sein d'une même simulation, des modèles numériques indépendants à la fois en termes de maillage et de géométrie sous la forme d'un ensemble de grilles composites. Chaque modèle peut être adapté à un détail géométrique ou un phénomène physique d'intérêt avec sa propre échelle spatiale et temporelle. Une approche composite permet de découper la géométrie complexe d'un système sous la forme de multiples composantes géométriques plus simples tout en réduisant le coût du modèle en temps de calcul et en utilisation mémoire. Avec une approche composite, les composantes structurelles peuvent subir de grands déplacements sans altérer les grilles du domaine fluide. En parallèle, des grilles de fluide locales peuvent être ajoutées pour prendre en compte des écoulements locaux générés par les déplacements des composantes structurelles.

L'objectif de cette thèse est de développer un outil de modélisation multi-modèle robuste et flexible permettant d'ajouter des détails géométriques dans le cadre d'une simulation à grande échelle. En vue d'une utilisation industrielle, la stratégie numérique que l'on cherche à développer doit être

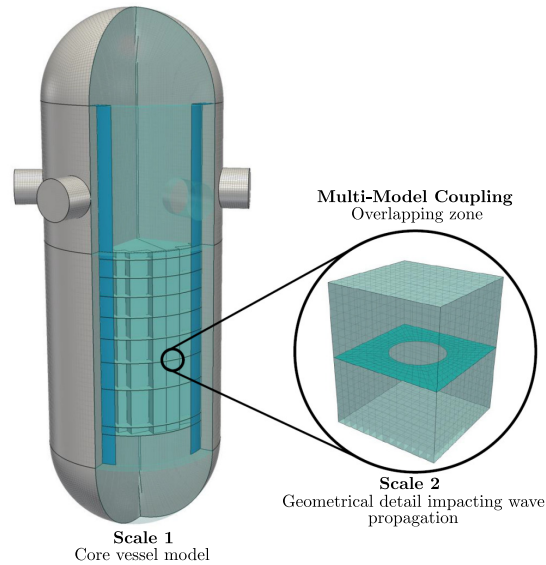


Figure 5.9: Les perforations des plaques de cloisonnement (entourées en noir) et la cuve du réacteur sont maillées indépendamment. La stratégie proposée consiste à superposer des altérations locales (maillage de droite) sur plaques de cloisonnement au sein d'un modèle global à grande échelle représentant la cuve du réacteur (maillage de gauche) dans le but d'améliorer la qualité des résultats numériques sans altérer les grilles du modèle global.

modulaire et compatible avec des ratios de cellules relativement élevés entre les différentes grilles utilisées. Enfin, cet outil doit être compatible avec des écoulements multi-composants en dynamique rapide dans le cadre de la modélisation de phénomènes d'interaction fluide-structure. Dans le cadre du développement de notre approche numérique, nous nous appuyons sur des cas tests simplifiés qui se focalisent sur certains aspects physiques de l'APRP afin de tester rigoureusement la méthode développée. Un exemple est donné par la Figure 5.10 illustrant un cas test simplifié en deux dimensions. Deux cavités sont hermétiquement séparées par une paroi déformable. Une cavité contenant de l'eau sous haute pression (bleu foncé) et une cavité basse pression contenant de la vapeur d'eau (bleu clair). Une perforation locale est ajoutée à la paroi à l'aide d'un patch. Cette perforation induit une fuite de la cavité haute pression dans la cavité basse pression altérant la physique du modèle global.

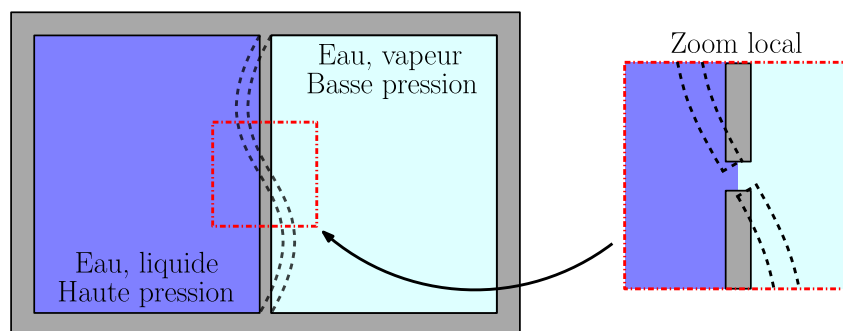


Figure 5.10: Exemple simplifié représentatif des applications visées. Chambres séparées par une paroi hermétique à l'échelle globale. Une chambre contenant de l'eau liquide sous haute pression en bleu foncé et une chambre contenant de la vapeur d'eau sous basse pression en bleu clair. Perforation locale de la paroi ajoutée à l'aide d'un patch induisant une fuite entre les deux chambres à l'échelle locale.

Dans un premier temps, une étude bibliographique a permis de mettre en évidence des méthodes multi-grilles comme l'*Adaptive Mesh Refinement* qui consiste à raffiner localement un modèle global

en subdivisant des cellules existantes du maillage (voir Fig. 5.11). Ce type de méthode altère le modèle global et ne permet pas de superposer des modèles indépendants. Par conséquent, les méthodes AMR ne sont pas retenues dans le cadre de ce travail mais peuvent être envisagée comme un outil complémentaire à l'approche visée.

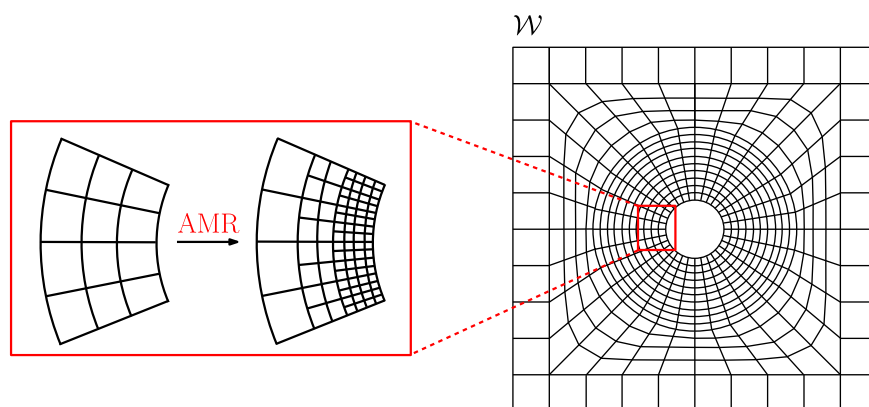


Figure 5.11: Exemple de méthode *Adaptive Mesh Refinement* appliquée à une grille typiquement utilisée pour modéliser un écoulement fluide autour d'un cylindre ou bien une perforation de plaque.

On s'intéresse plutôt aux méthodes de grilles superposées qui utilisent des grilles indépendantes pouvant se chevaucher. De manière générale, ce type de méthode s'appuie sur une grille de fond appelée substrat et une ou plusieurs grilles locales appelées patchs. La méthode Arlequin [37] est une méthode de grilles superposées développée dans un cadre éléments finis qui s'appuie sur la définition d'une zone de couplage et l'utilisation de fonctions de pondération pour superposer plusieurs modèles indépendants (voir Fig. 5.12).

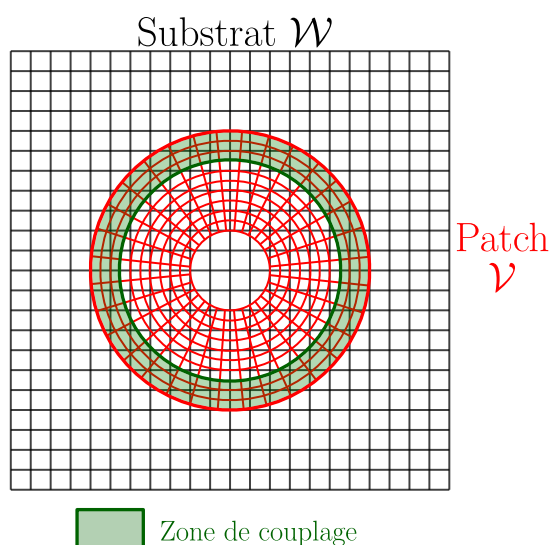


Figure 5.12: Exemple d'utilisation de la Méthode Arlequin avec une grille de fond appelée substrat (en noir) et une grille locale appelée patch (en rouge). La zone de couplage est ici représentée en vert.

Dans le cadre de ce travail de thèse, nous bénéficions des conclusions du travail de Fernier [59] sur l'implémentation et la validation de la méthode Arlequin en éléments finis pour l'étude de systèmes transitoires rapides. En présence d'écoulements compressibles, la méthode Arlequin est susceptible de générer des perturbations impactant la solution globale. De plus, la méthode Arlequin a été conçue à partir d'une approche par éléments finis. La transposition de la méthode à un cadre volumes

finis étant non-triviale, la méthode Arlequin n'est pas retenue comme approche multi-grilles dans ce travail.

La deuxième méthode de grilles superposées considérée est appelée méthode Chimère [166]. Il s'agit d'une méthode de superposition de grilles initialement utilisée pour faciliter le processus de maillage en utilisant un assemblage de grilles superposées pour des calculs en différences finies. La méthode Chimère s'appuie sur la définition d'une zone d'échange entre la frontière extérieure du patch et un contour fermé à l'intérieur du substrat ainsi que l'utilisation d'une "molécule" d'interpolation (voir Fig. 5.13). Cette dernière est constituée de nœuds envoyeurs voisins du nœud receveur. Une interpolation multi-linéaire basée sur les distances entre les nœuds de la molécule d'interpolation est calculée pour chaque nœud receveur. Dans un cadre volumes finis, la molécule d'interpolation s'appuie sur des barycentres de cellules à la place des nœuds du maillage.

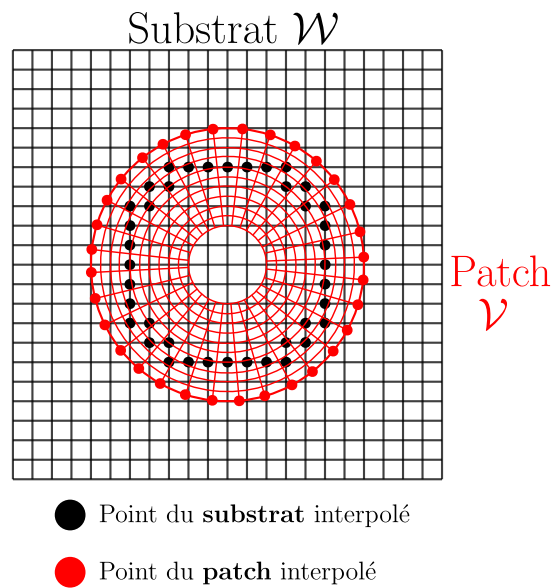


Figure 5.13: Exemple d'utilisation de la Méthode Chimère avec une grille de fond appelée substrat (en noir) et une grille locale appelée patch (en rouge). La zone d'échange est matérialisée par les deux contours fermés définis par les points d'interpolations.

La transposition de la méthode Chimère à un cadre volumes finis a déjà été effectuée dans plusieurs codes industriels comme les codes elsA [64, 136] et TAU [154, 187]. Malgré tout, la méthode Chimère appliquée à des écoulements compressibles en dynamique rapide est un sujet relativement peu traité dans la littérature avec notamment peu de résultats concernant l'étude de l'impact des ratios de cellules entre les différentes grilles. La méthode Chimère est donc retenue comme l'approche multi-grille pour ces travaux. Cependant, un travail d'implémentation et de validation de la méthode Chimère dans le cadre d'écoulements compressibles en dynamique rapide calculés par une approche volumes finis est nécessaire et représente une partie conséquente de cette thèse.

Étant donné que nous souhaitons traiter des problèmes d'interaction fluide-structure (IFS) dans le cadre de la modélisation de systèmes transitoires rapides à grande échelle, la méthode Chimère retenue doit être rendue compatible avec des phénomènes d'interaction fluide-structure impliquant des structures subissant des grands déplacements et des grandes déformations. La modélisation des phénomènes d'interaction fluide-structure s'appuie sur l'établissement d'un couplage entre un domaine fluide et un domaine structure dont les modèles, les maillages, les schémas de discrétisations ainsi que les critères de stabilités peuvent être indépendants.

On distingue deux catégories de méthodes utilisées pour la modélisation de phénomènes d'IFS. D'une part, les méthodes *Arbitrary Lagrangian Eulerian* (ALE) qui s'appuient sur une connexion

topologique entre les maillages fluide et structure. Lorsque la structure se déplace, le maillage fluide se déforme en conséquence. Ce type de méthode n'est donc pas adapté aux problèmes d'interaction fluide-structure impliquant des structures en grands déplacements. D'autre part, les méthodes de frontières immergées qui utilisent des maillages fluide et structure indépendants et utilisent des informations sur la position de la structure par rapport aux cellules du maillage fluide intersectées par cette dernière afin d'appliquer des conditions de couplage entre le fluide et la structure. Ce type de méthode est généralement plus flexible et compatible avec des structures subissant de grands déplacements. Au CEA, nous disposons d'une méthode de frontières immergées en volumes finis appelée *Mediating Body Method* (MBM)[92], testée et validée en interne, qui a donc été retenue pour ce travail. Le couplage de la MBM avec une méthode multi-maillage comme la méthode Chimère n'a pas encore été étudié et fera donc l'objet d'un travail d'implémentation et de validation dans le cadre de cette thèse.

A partir d'une étude bibliographique dont nous avons résumé les principales conclusions, nous pouvons définir les objectifs de cette thèse comme les suivants:

- Nous cherchons à développer une méthode multi-modèle en volumes finis adaptée à la modélisation d'écoulements compressibles en dynamique rapide. Pour des raisons détaillées lors de l'étude bibliographique, cette méthode est basée sur une approche Chimère et doit être:
 - Compatible avec des écoulements multi-constituants.
 - Assez robuste pour supporter des variations de taille de maille raisonnables entre les différentes grilles.
 - Compatible avec des problèmes d'interaction fluide-structure en grands déplacements modélisés à l'aide d'une méthode de frontières immergées telle que la *Mediating Body Method*.

Le développement de cette stratégie numérique s'est déroulé en deux phases distinctes:

1. À partir d'un code de calcul de dynamique rapide interne au CEA compatible éléments finis et volumes finis appelé MANTA, nous avons développé une méthode Chimère en volumes finis. Cette méthode a ensuite été validée sur des cas tests analytiques à une dimension et évaluée par la suite sur des cas tests de référence de la littérature à deux dimensions.
2. La MBM étant déjà disponible et validée au sein du code MANTA. Nous avons développé et implémenté un couplage la méthode Chimère avec la MBM. Ce couplage a été validé sur un cas test analytique à une dimension puis évalué sur un cas représentatif des applications visées en trois dimensions.

Cette synthèse suit la chronologie des travaux de thèse. Dans une première étape, nous résumons le développement d'une méthode de grilles superposées dans un cadre volumes finis basé sur une approche Chimère. Dans une seconde étape, nous présentons le développement d'un couplage de la méthode Chimère en volumes finis avec une méthode d'interaction fluide-structure en frontières immergées appelée MBM.

Le premier chapitre de cette thèse introduit le modèle des équations d'Euler pour des écoulements compressibles non-visqueux utilisé dans ces travaux ainsi que le schéma d'intégration en volumes finis d'ordre deux en temps et en espace de MUSCL-Hancock. Ce modèle fluide est utilisé comme cadre de travail dans l'ensemble des développements détaillés dans le manuscrit.

Développement d'une méthode de grille superposée dans un cadre volumes finis: la méthode Chimère

Dans le deuxième chapitre, une méthode de grilles superposées appelée méthode Chimère a été implémentée dans un cadre volumes finis avec des milieux fluides uniquement. La présentation de la méthode s'appuie sur une grille de fond appelée substrat et sur une grille locale appelée patch. Le nombre de grille se limite à deux pour des raisons de compréhension dans le cadre de la présentation de la méthode mais celle-ci est compatible avec plusieurs grilles de fluide. Cette implémentation s'appuie sur des cellules de maillage du fluide appelées cellules fantômes pour échanger de l'information entre plusieurs grilles.

La première étape de notre implémentation consiste à identifier les cellules fantômes du patch utilisées pour recevoir la solution transférée entre les maillages ainsi que les cellules chargées d'envoyer de l'information. Cette détection utilise la frontière extérieure du patch ainsi que le nombre de rangées de cellules fantômes fixé par l'ordre du schéma numérique choisi pour l'intégration du domaine fluide. Une zone d'échange constituée de cellules fantômes est définie pour chaque maillage recevant de l'information (deux zones d'échanges pour un envoi symétrique du substrat vers le patch et du patch vers le substrat). Pour chaque ensemble de cellules fantômes d'une grille receveuse, un ensemble de cellules envoyeuses est défini comme étant les cellules fluide du maillage envoyeur intersectées par les cellules fantômes du maillage receveur.

Une fois les cellules fantômes et les cellules envoyeuses identifiées pour chaque grille, une reconstruction de la solution est effectuée en utilisant des cellules fluide envoyeuses. Cette implémentation se distingue des différentes versions de la méthode Chimère présentes dans la littérature car elle s'appuie sur des volumes d'intersection entre les cellules envoyeuses et les cellules fantômes et non des distances entre les barycentres des cellules envoyeuses et des cellules fantômes.

La solution fluide transférée est évaluée avec une reconstruction au premier ordre utilisant une moyenne des solutions contenues dans les cellules envoyeuses intersectées par chaque cellule fantôme, pondérée par le volume des intersections (voir Fig. 5.14).

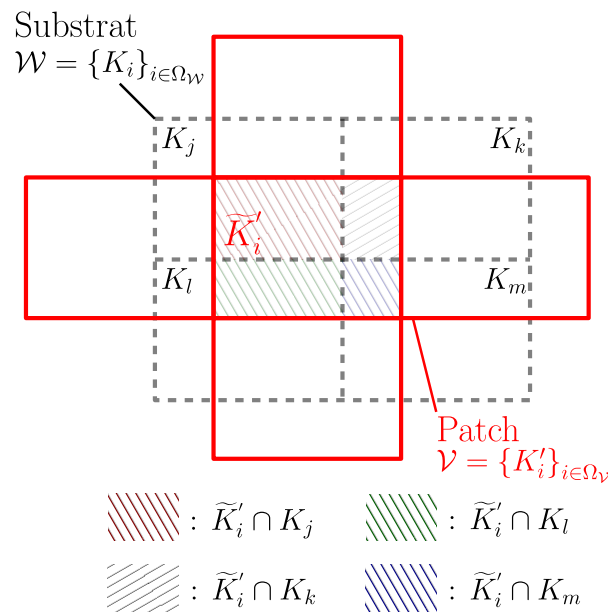


Figure 5.14: Interpolation Chimère de premier ordre basée sur les volumes d'intersection entre chaque cellule fantôme et ses cellules envoyeuses.

Appelée méthode Chimère d'ordre un, cette approche a été améliorée avec un passage au deux-

ième ordre utilisant une reconstruction linéaire de la solution au sein des cellules envoyeuses. Cette approximation linéaire de la solution dans chaque cellule envoyeuse est ensuite évaluée au barycentre des intersections entre les cellules envoyeuses et les cellules fantômes (voir Fig. 5.15). Cette amélioration est appelée méthode Chimère d'ordre deux.

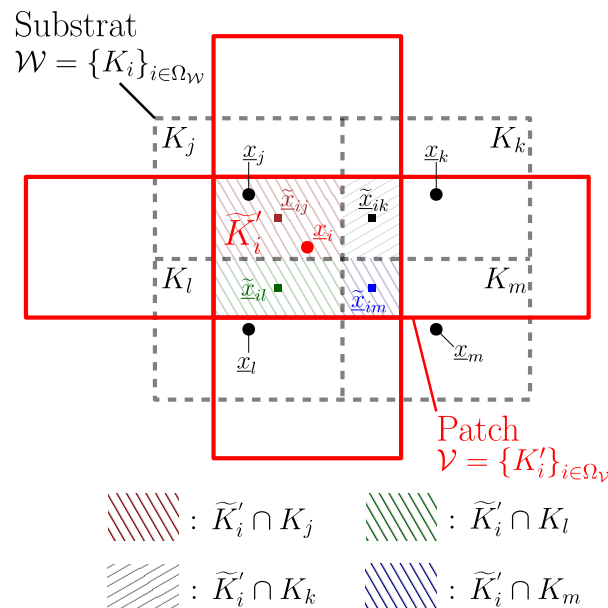


Figure 5.15: Interpolation Chimère de second ordre basée sur une reconstruction linéaire de la solution au sein de chaque cellule envoyeuse. Chaque solution est ensuite évaluée au centre de l'intersection entre la cellule fantôme et la cellule envoyeuse correspondante.

Les deux approches (ordre un et ordre deux) ont été testées sur des cas test analytiques dont l'advection d'une perturbation sinusoïdale, le tube à choc de Sod, une onde de choc stationnaire et enfin l'advection d'un vortex isentropique. Ces différents cas ont démontré la capacité de la méthode Chimère à transférer des structures fluides compressibles simples telles que des ondes de choc ou des ondes de détente sans introduire de perturbations à l'échelle globale.

En présence d'écoulements continus et de tailles de mailles semblables entre les grilles, les deux méthodes Chimère offrent des résultats très proches de configurations monogrilles et ne semblent pas impacter l'ordre de convergence du schéma numérique d'ordre deux. Cependant, la méthode Chimère de second ordre s'est montrée plus proche d'une solution monogrille et moins dépendante de la configuration géométrique des grilles que la méthode de premier ordre en présence de maillages présentant des résolutions très différentes.

De plus, lors du transfert d'une onde de choc d'un maillage grossier vers un maillage plus fin, la méthode Chimère d'ordre deux capture précisément la vitesse de choc de manière équivalente à une méthode monogrille standard, ce qui n'est pas le cas de la méthode Chimère d'ordre un qui surestime la vitesse de choc. Enfin, la traversée d'une zone de raffinement de grille brutale par une onde de choc génère une oscillation locale dans les différentes configurations Chimère traitées mais aussi dans des configurations monogrilles standard. La méthode Chimère d'ordre deux limite l'amplitude de ces oscillations et montre un comportement plus robuste en vue d'une utilisation industrielle.

La méthode Chimère d'ordre un est abandonnée dans la suite des travaux et on s'intéresse, dans le troisième chapitre, au comportement de la méthode Chimère d'ordre deux confrontée à des écoulements plus complexes que les cas tests analytiques traités jusque là. La méthode de Chimère de second ordre a été évaluée sur des cas tests de la littérature en 2D dont l'écoulement supersonique autour d'un cylindre, un cas d'interaction choc-bulle (Hélium et R22) et enfin le cas de la double réflexion de Mach (DMR). Dans chacun de ces cas, la méthode Chimère de second ordre fournit

des résultats comparables à une solution monogrille avec une erreur liée à l'utilisation de la méthode Chimère négligeable pour des ratios de taille de cellule entre les grilles inférieurs à 8. La méthode Chimère de second ordre permet d'augmenter localement la précision de la solution, autour d'un détail géométrique d'intérêt, sans impacter lourdement le temps de calcul comparé à une approche monogrille raffinée. Dans le cas d'écoulements multi-composants, la méthode Chimère d'ordre deux, permet de transférer des interfaces bi-fluides d'une grille fine vers une grille grossière. La méthode Chimère d'ordre deux ne semble pas générer d'altération visible de la solution numérique par rapport à une solution monogrille grossière mais permet de capturer certains détails de l'écoulement uniquement perçus avec une grille fine dans le cadre d'une approche monogrille.

A l'issue des chapitres 2 et 3, nous avons développé une méthode de grilles superposées compatible avec des écoulements transitoires en dynamique rapide calculés par une approche volumes finis. La simulation de transitoires brutaux implique très souvent des interactions entre des écoulements présentant de fortes discontinuités avec des structures déformables. Par conséquent, afin d'ajouter des détails géométriques susceptibles d'impacter le comportement de systèmes transitoires brutaux, la méthode Chimère développée doit être rendue compatible avec des problèmes d'interaction fluide-structure.

Couplage de la méthode Chimère à une méthode de frontières immergées: *The Chimera Mediating Body Method*

Dans le dernier chapitre, la méthode Chimère de second ordre a été couplée à une méthode d'interaction fluide-structure en frontières immergées, appelée *Mediating Body Method* (MBM). La MBM est une méthode de frontières immergées s'appuyant sur la définition d'un *mediating body* composé des cellules de maillage du fluide intersectées par le maillage de la structure (représenté en jaune dans la Figure 5.16). Le maillage fluide est ainsi décomposé en deux ensembles de cellules: les cellules du *mediating body* intersectées par la structures et les cellules de fluide actives qui ne sont pas intersectées par la structure. Particulièrement adaptée aux éléments de coque, la MBM s'appuie sur un calcul des intersections des cellules du *mediating body* avec la structure. L'orientation de la structure au sein de chaque cellule du *mediating body* est utilisée pour calculer les efforts transmis par le fluide à la structure à chaque interface entre les cellules du *mediating body* et les cellules de fluide actives. Inversement, des fonctions de flux prenant en compte le volume de fluide déplacé par la structure sont utilisées aux mêmes interfaces pour calculer les efforts de la structure transmis au fluide.

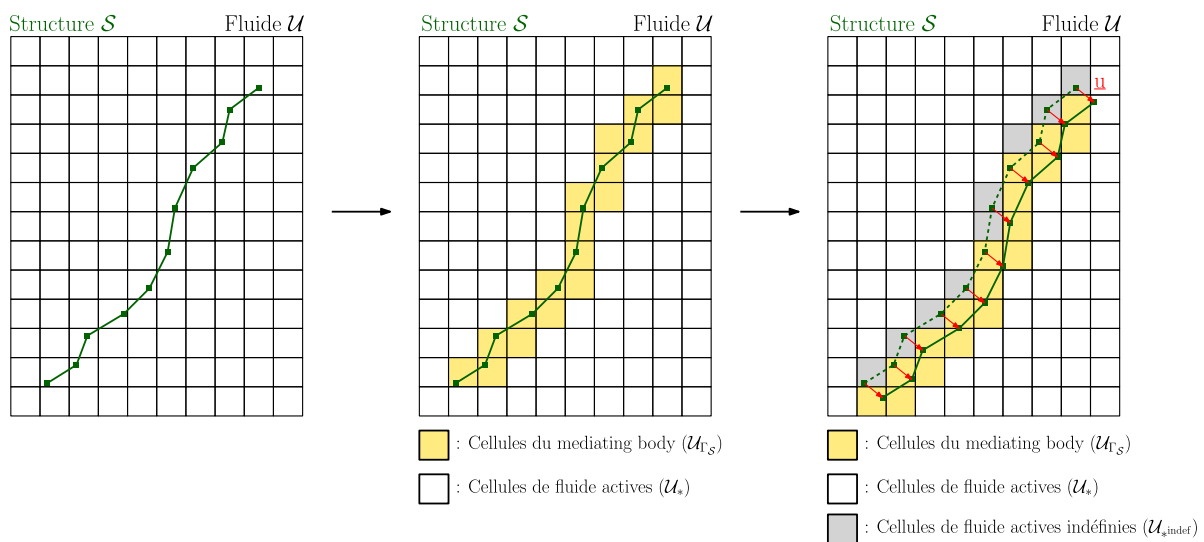


Figure 5.16: Présentation schématique de la *Mediating Body Method*. Le *mediating body* est représenté en jaune. Lorsque la structure subit de grands déplacements, les anciennes cellules du *mediating body* désormais cellules de fluide sont appelées cellules de fluide indéfinies et sont représentées en gris.

Afin de rendre la méthode Chimère compatible avec la MBM, le développement du couplage Chimère-MBM se décompose en trois parties. Dans un premier temps, l'utilisation de plusieurs grilles pour le fluide implique la définition de plusieurs *mediating bodies* comme illustré par la Figure 5.17.

Pour réduire le nombre d'intersections à calculer, les *mediating bodies* sont définis en minimisant les zones de recouvrement. Dans un deuxième temps, une affectation des efforts transmis par le fluide à la structure est effectuée pour éviter que plusieurs grilles de fluide ne transmettent des efforts à la structure dans les zones de recouvrement de grilles de fluide. Dans le cadre de notre travail, l'affectation privilégie les grilles patchées généralement plus fines. Enfin, la MBM comme la méthode Chimère attribue des rôles spécifiques à des cellules du maillage fluide. Dans certaines configurations de grilles, ces rôles entrent en conflit notamment lorsqu'une cellule envoyeuse pour la méthode Chimère est aussi une cellule du *mediating body* pour la MBM. Une extrapolation de la solution fluide de part et d'autre de la structure est alors effectuée pour chaque cellule envoyeuse lorsque la

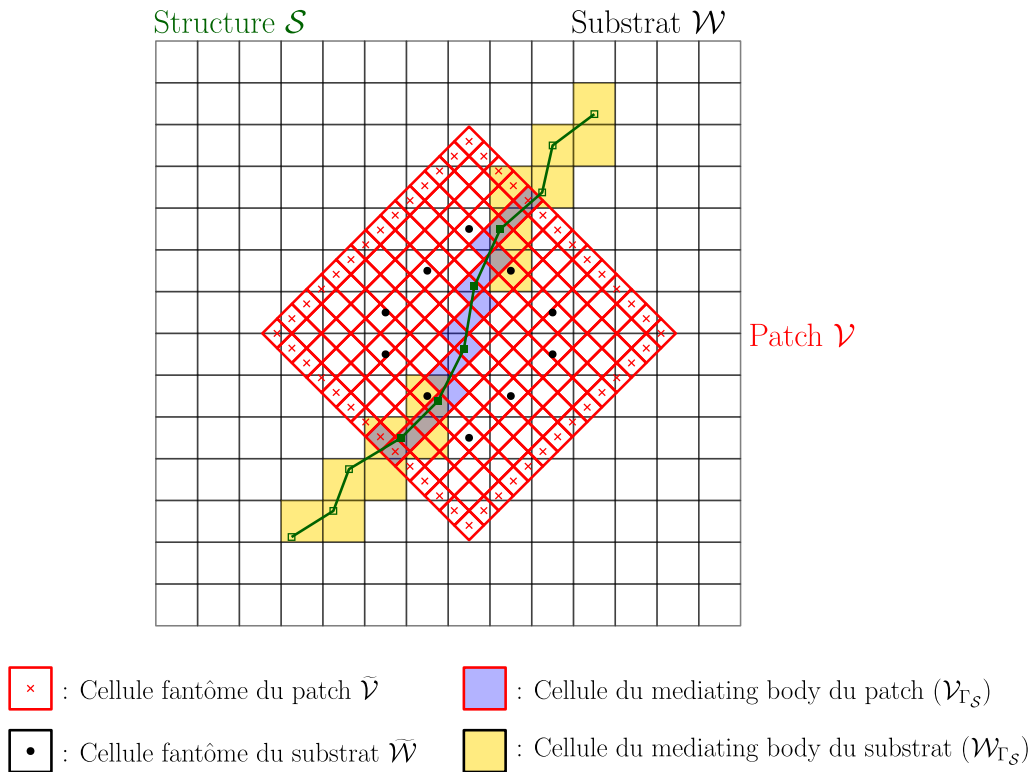


Figure 5.17: Exemple de configuration de grille dans le cadre de la méthode Chimère-MBM. Le *mediating body* du patch est représenté en bleu tandis que le *mediating body* du substrat est représenté en jaune.

structure traverse une zone d'échange Chimère. Cette extrapolation appelée extrapolation +/- permet de reconstruire deux solutions (appelées solution + et solution -) pour chaque cellule envoyeuse aussi cellule du *mediating body* comme illustré par la Figure 5.18. En fonction de la position du centre de l'intersection cellule envoyeuse/cellule fantôme par rapport à la structure, la solution + ou la solution - est utilisée pour l'envoi Chimère.

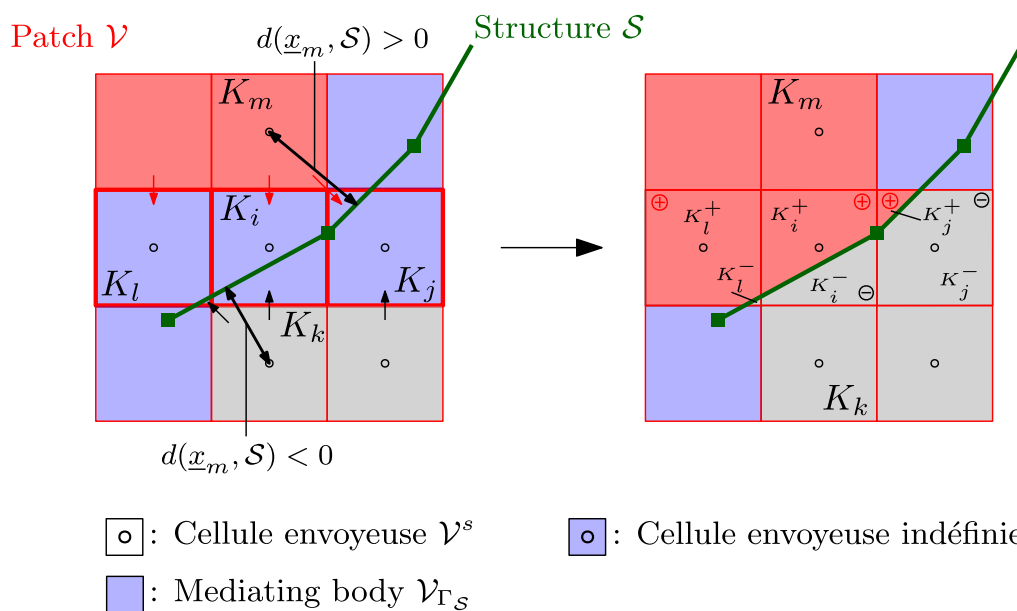


Figure 5.18: Schéma de l'extrapolation +/- exécutée pour une cellule envoyeuse intersectée par la structure. Deux états sont reconstruits pour cette cellule de part et d'autre de la structure.

La méthode Chimère-MBM est évaluée sur un cas test analytique de piston libre séparant deux cavités fluides au repos avec des pressions différentes. L'impact de la méthode Chimère-MBM sur la solution fluide est négligeable pour des ratios de taille de cellule entre grilles inférieurs à 8. Lorsque les ratios de taille de cellule entre les grilles excèdent cette valeur, des perturbations locales issues de l'extrapolation +/- sont générées. Cependant, ces perturbations n'altèrent en aucun cas le profil global de la solution sur ce cas test. Pour terminer, un exemple en trois dimensions, s'appuyant sur une cavité haute pression séparée d'une cavité basse pression par une plaque perforée, est présenté. Ce cas test utilise trois grilles fluides indépendantes et sollicite les méthodes Chimère et Chimère-MBM dans le même calcul, démontrant la flexibilité d'usage des méthodes développées. La configuration Chimère à trois grilles de fluide est comparée à deux approches monogrilles: la première possède une grille grossière de même résolution que le substrat de la configuration Chimère et la seconde possède une grille fine de même résolution que le plus fin des patches de la configuration Chimère. L'utilisation conjointe de la méthode Chimère et de la MBM permet d'obtenir des niveaux de précision des solutions numériques comparables à une approche monogrille fine avec des temps de calculs et des contraintes de maillage réduits. Ce couplage permet notamment de capturer des phénomènes locaux impactant la solution à l'échelle globale sans altérer la grille de fond.

Conclusions et perspectives

Au cours de ces travaux, nous avons développé un outil de modélisation multi-modèle fluide robuste et flexible permettant d'ajouter localement des détails géométriques au sein d'une simulation à grande échelle sans altérer le modèle global. Cet outil est compatible avec des écoulements compressibles multi-constituants en dynamique rapide.

La compatibilité de cet outil a été étendue à des problèmes d'interaction fluide-structure grâce au développement d'un couplage de la méthode multi-modèle avec une méthodes de frontières immergées. Cet outil est une étape importante dans le déblocage de nouvelles capacités de modélisation de phénomènes d'interaction fluide-structure pour des structures complexes à grande échelle. En effet, la méthode Chimère-MBM permet de prendre en compte des détails géométriques ou bien des phénomènes physiques locaux qui impactent la solution numérique à l'échelle globale. Sans cet outil, la capture de détails géométriques ou de phénomènes physiques locaux est coûteuse en temps de maillage et en temps de calcul. Ce couplage apporte une plus-value notable dans le contexte de l'énergie nucléaire, pour des simulations de situations accidentelles à l'échelle du circuit primaire d'un réacteur nucléaire à eau pressurisée.

Malgré tout, cet outil présente certaines limitations comme la génération de perturbations locales en présences de grilles avec des ratios de taille de maille élevés. Dans l'ensemble des cas traités, ces perturbation n'ont pas été impactantes à l'échelle globale mais elles sont à prendre en compte lors du dimensionnement des grilles locales.

Afin de poursuivre ces investigations nous proposons quelques pistes d'approfondissement des travaux menés avec notamment, une poursuite des investigations dans le but de déterminer l'origine des perturbations locales aussi observées en présence d'un raffinement brutal au sein d'une configuration monogridle standard. De la même manière que la méthode Chimère d'ordre un a été améliorée avec une reconstruction linéaire aboutissant à la méthode Chimère d'ordre deux, l'extrapolation +/- peut être améliorée en utilisant une reconstruction linéaire pour extrapoler deux états de part et d'autre de la structure.

L'impact de l'affection des efforts fluides dans le cadre du couplage Chimère-MBM pourrait être examiné en détail et cette dernière pourrait être remplacée par une pondération pour une transition progressive dans la transmission des efforts fluides provenant de plusieurs grilles de fluide.

Dans l'ensemble des cas traités, le pas de temps global est fixé par le plus petit pas de temps des domaines fluides et structure confondus. Le découplage des pas de temps pourrait permettre un gain non-négligeable en temps de calcul.

Pour terminer, le couplage Chimère-MBM pourrait permettre d'ajouter des détails structurels locaux en utilisant des patchs structure locaux associés à des grilles fluides locales. La méthode Chimère développée doit être rendue compatible avec des grilles fluides mobiles ainsi qu'avec une méthode multi-modèle structure telle que la méthode Arlequin.

Bibliography

- [1] M. Abbott. *An Introduction to the Method of Characteristics*. American Elsevier, 1966. URL https://books.google.ch/books?id=H_hQAAAAMAAJ.
- [2] G. Allaire, S. Clerc, and S. Kokh. A five-equation model for the simulation of interfaces between compressible fluids. *Journal of Computational Physics*, 181(2):577–616, 2002. ISSN 00219991. doi: 10.1006/jcph.2002.7143.
- [3] A. Almgren, J. Bell, P. Colella, and T. Marthaler. A cartesian grid projection method for the incompressible euler equations in complex geometries. *SIAM Journal on Scientific Computing*, 18, 10 1996. doi: 10.1137/S1064827594273730.
- [4] A. S. Almgren, J. B. Bell, P. Colella, and L. H. Howell. An adaptive projection method for the incompressible Euler equations. In *AIAA 11th Computational Fluid Dynamics Conference*, pages 530–539, Jan. 1993.
- [5] S. Amarala and J. Wan. Multigrid methods for systems of hyperbolic conservation laws. *SIAM Journal on Multiscale Modeling and Simulation*, 11:586–614, 06 2013. doi: 10.1137/110851316.
- [6] J. D. Anderson. *Hypersonic and high temperature gas dynamics*. American Institute of Aeronautics and Astronautics, Reston, VA, 2000. ISBN 156347459X.
- [7] J. B. Angel, J. W. Banks, and W. D. Henshaw. High-order upwind schemes for the wave equation on overlapping grids: Maxwell’s equations in second-order form. *Journal of Computational Physics*, 352:534–567, 2018. ISSN 10902716. doi: 10.1016/j.jcp.2017.09.037. URL <https://doi.org/10.1016/j.jcp.2017.09.037>.
- [8] T. Aoyama, C. Yang, and S. Saito. Numerical analysis of active flap for noise reduction using moving overlapped grid method. *Journal of the American Helicopter Society*, 52(3):189–200, 2007. ISSN 2161-6027. doi: doi:10.4050/JAHS.52.189.
- [9] E. Atta. Component-adaptive grid interfacing. *19th Aerospace Sciences Meeting*, 1981. doi: 10.2514/6.1981-382. URL <https://arc.aiaa.org/doi/abs/10.2514/6.1981-382>.
- [10] E. H. Atta and J. Vadyak. A grid interfacing zonal algorithm for three-dimensional transonic flows about aircraft configurations. In E. Krause, editor, *Eighth International Conference on Numerical Methods in Fluid Dynamics*, pages 107–114, Berlin, Heidelberg, 1982. Springer Berlin Heidelberg. ISBN 978-3-540-39532-4.
- [11] J. Barth, T. Numerical methods for conservation laws on structured and unstructured meshes. *Technical report, VKI Lecture Series*, 2003.
- [12] E. Basso, A. P. Antunes, and J. L. F. Azevedo. Chimera simulations of supersonic flows over a complex satellite launcher configuration. *Journal of Spacecraft and Rockets*, 40(3):345–355, 2003. doi: 10.2514/2.3969.
- [13] P. Bauman, H. B. Dhia, N. Elkhodja, J. Oden, and S. Prudhomme. On the application of the arlequin method to the coupling of particle and continuum models. *Computational Mechanics*, 42:511–530, 2008.

- [14] A. Beccantini, F. Casadei, and P. Galon. Improvement of the FLSW model for cell-centered finite volumes in EUROPLEXUS. *Technical Note, CEA DEN/DANS/DM2S/STMF/LATF/NT/13-019/A*, 2013.
- [15] M. Ben-artzi and A. Birman. Application of the “generalized riemann problem” method to 1-d compressible flows with material interfaces. *Journal of Computational Physics*, 65(1): 170–178, 1986. ISSN 0021-9991. doi: [https://doi.org/10.1016/0021-9991\(86\)90010-0](https://doi.org/10.1016/0021-9991(86)90010-0). URL <https://www.sciencedirect.com/science/article/pii/0021999186900100>.
- [16] M. Ben-Artzi and J. Falcovitz. A second-order godunov-type scheme for compressible fluid dynamics. *Journal of Computational Physics*, 55(1):1–32, 1984. ISSN 0021-9991. doi: [https://doi.org/10.1016/0021-9991\(84\)90013-5](https://doi.org/10.1016/0021-9991(84)90013-5). URL <https://www.sciencedirect.com/science/article/pii/0021999184900135>.
- [17] J. A. Benek. A grid-embedding technique. *Technical Report*, (DTIC Document), 1986.
- [18] C. Benoit. *Méthode d'adaptation de maillages au moyen d'algorithmes génétiques pour le calcul d'écoulements compressibles*. PhD thesis, 1999. URL <http://www.theses.fr/1999ENAM0009>. Thèse de doctorat dirigée par Lerat, Alain Physique Paris, ENSAM 1999.
- [19] C. Benoit and G. Jeanfavre. Three-dimensional inviscid isolated rotor calculations using chimera and automatic cartesian partitioning methods. *Journal of the American Helicopter Society*, 48(2):128–138, 2003. ISSN 00028711. doi: 10.4050/JAHS.48.128.
- [20] M. Berger and P. Colella. Local adaptive mesh refinement for shock hydrodynamics. *Journal of Computational Physics*, 82(1):64–84, 1989. ISSN 0021-9991. doi: [https://doi.org/10.1016/0021-9991\(89\)90035-1](https://doi.org/10.1016/0021-9991(89)90035-1). URL <https://www.sciencedirect.com/science/article/pii/0021999189900351>.
- [21] M. J. Berger. On conservation at grid interfaces. *SIAM Journal on Numerical Analysis*, 24(5): 967–984, 1987. ISSN 00361429. doi: 10.1137/0724063.
- [22] M. J. Berger and J. Olinger. Adaptive mesh refinement for hyperbolic partial differential equations. *Journal of Computational Physics*, 53(3):484–512, 1984. ISSN 0021-9991. doi: [https://doi.org/10.1016/0021-9991\(84\)90073-1](https://doi.org/10.1016/0021-9991(84)90073-1). URL <https://www.sciencedirect.com/science/article/pii/0021999184900731>.
- [23] T. Berglind. A hybrid structured-unstructured grid method for aerodynamic flow simulations. *AIAA paper*, 95-0051, 1995.
- [24] J. Bonet and R. D. Wood. *Nonlinear Continuum Mechanics for Finite Element Analysis*. Cambridge University Press, 2 edition, 2008. doi: 10.1017/CBO9780511755446.
- [25] P. Brenner. Simulation du mouvement relatif de corps soumis à un écoulement instationnaire par une méthode de chevauchement de maillage. *AGARD*, 1996.
- [26] W. Briggs, V. Henson, and S. McCormick. *A Multigrid Tutorial: Second Edition*. Other Titles in Applied Mathematics. Society for Industrial and Applied Mathematics (SIAM, 3600 Market Street, Floor 6, Philadelphia, PA 19104), 2000. ISBN 9780898719505. URL <https://books.google.de/books?id=ahklDynzz8cC>.

- [27] J. Q. Broughton, F. F. Abraham, N. Bernstein, and E. Kaxiras. Concurrent coupling of length scales: Methodology and application. *Phys. Rev. B*, 60:2391–2403, Jul 1999. doi: 10.1103/PhysRevB.60.2391. URL <https://link.aps.org/doi/10.1103/PhysRevB.60.2391>.
- [28] M. Capuano, C. Bogey, and P. Spelt. Simulations of viscous and compressible gas–gas flows using high-order finite difference schemes. *Journal of Computational Physics*, 361: 56–81, 2018. ISSN 0021-9991. doi: <https://doi.org/10.1016/j.jcp.2018.01.047>. URL <https://www.sciencedirect.com/science/article/pii/S0021999118300573>.
- [29] F. Casadei and N. Leconte. FLSW: A weak, embedded-type fluid-structure interaction model with CCFV in EUROPLEXUS. *Technical Note, PUBSY No. JRC65826*, 2011.
- [30] L. Chamoin, J. T. Oden, and S. Prudhomme. A stochastic coupling method for atomic-to-continuum Monte-Carlo simulations. *Computer Methods in Applied Mechanics and Engineering*, 197(43-44):3530–3546, Aug. 2008. doi: 10.1016/j.cma.2008.04.013. URL <https://hal.archives-ouvertes.fr/hal-01580941>.
- [31] J. Charney, R. Fjortoft, and J. Neumann. Numerical integration of the barotropic vorticity equation. *Tellus*, 2:237–254, 11 1950. doi: 10.3402/tellusa.v2i4.8607.
- [32] G. Chesshire and W. D. Henshaw. Composite overlapping meshes for the solution of partial differential equations. *Journal of Computational Physics*, 90(1):1–64, 1990. ISSN 10902716. doi: 10.1016/0021-9991(90)90196-8.
- [33] P. Colella. A direct eulerian muscl scheme for gas dynamics. *SIAM Journal on Scientific and Statistical Computing*, 6(1):104–117, 1985. doi: 10.1137/0906009. URL <https://doi.org/10.1137/0906009>.
- [34] P. Colella, D. T. Graves, B. J. Keen, and D. Modiano. A cartesian grid embedded boundary method for hyperbolic conservation laws. *Journal of Computational Physics*, 211(1):347–366, 2006. ISSN 0021-9991. doi: <https://doi.org/10.1016/j.jcp.2005.05.026>. URL <https://www.sciencedirect.com/science/article/pii/S0021999105002780>.
- [35] F. Daude, P. Galon, Z. Gao, and E. Blaud. Numerical experiments using a HLLC-type scheme with ALE formulation for compressible two-phase flows five-equation models with phase transition. *Computers and Fluids*, 94:112–138, 2014. ISSN 00457930. doi: 10.1016/j.compfluid.2014.02.008. URL <http://dx.doi.org/10.1016/j.compfluid.2014.02.008>.
- [36] P. De Palma, M. de Tullio, G. Pascazio, and M. Napolitano. An immersed-boundary method for compressible viscous flows. *Computers and Fluids*, 35(7):693–702, 2006. ISSN 0045-7930. doi: <https://doi.org/10.1016/j.compfluid.2006.01.004>. URL <https://www.sciencedirect.com/science/article/pii/S0045793006000065>. Special Issue Dedicated to Professor Stanley G. Rubin on the Occasion of his 65th Birthday.
- [37] H. B. Dhia. Problèmes mécaniques multi-échelles: La méthode Arlequin. *Comptes Rendus de l'Academie de Sciences - Serie IIb: Mecanique, Physique, Chimie, Astronomie*, 326(12): 899–904, 1998. ISSN 12874620. doi: 10.1016/S1251-8069(99)80046-5.
- [38] H. B. Dhia. Numerical modelling of multiscale problems: the arlequin method. *CD ECCM99*, pages 1–1, 1999.

- [39] H. B. Dhia. Further insights by theoretical investigations of the multiscale Arlequin method. *International Journal for Multiscale Computational Engineering*, 6(3):215–232, 2008. ISSN 15431649. doi: 10.1615/IntJMultCompEng.v6.i3.30.
- [40] H. B. Dhia and G. Rateau. Application of the arlequin method to some structures with defects. *Revue Européenne des Éléments Finis*, 11(2-4):291–304, 2002. doi: 10.3166/reef.11.291-304. URL <https://doi.org/10.3166/reef.11.291-304>.
- [41] H. B. Dhia and G. Rateau. The arlequin method as a flexible engineering design tool. *International Journal for Numerical Methods in Engineering*, 62(11):1442–1462, 2005. doi: <https://doi.org/10.1002/nme.1229>. URL <https://onlinelibrary.wiley.com/doi/abs/10.1002/nme.1229>.
- [42] H. B. Dhia and M. Zarroug. Contact in the arlequin framework. In *Contact Mechanics*, pages 403–410, Dordrecht, 2002. Springer Netherlands. ISBN 978-94-017-1154-8.
- [43] C. R. Dohrmann, S. W. Key, and M. W. Heinstein. A method for connecting dissimilar finite element meshes in two dimensions. *International Journal for Numerical Methods in Engineering*, 48(5):655–678, 2000. doi: [https://doi.org/10.1002/\(SICI\)1097-0207\(20000620\)48:5<655::AID-NME893>3.0.CO;2-D](https://doi.org/10.1002/(SICI)1097-0207(20000620)48:5<655::AID-NME893>3.0.CO;2-D).
- [44] J. Donea, A. Huerta, J.-P. Ponthot, and A. Rodriguez-Ferran. *Encyclopedia of Computational Mechanics Vol. 1: Fundamentals., Chapter 14: Arbitrary Lagrangian-Eulerian Methods*. Wiley & Sons, 2004.
- [45] P. T. J. W. Dossa Fernandes, A. Barbarulo, H. B. Dhia, and R. A. Kuche Sanches. A residual-based stabilized finite element formulation for incompressible flow problems in the arlequin framework. *Computer Methods in Applied Mechanics and Engineering*, 370: 113073, 2020. ISSN 0045-7825. doi: <https://doi.org/10.1016/j.cma.2020.113073>. URL <http://www.sciencedirect.com/science/article/pii/S0045782520302577>.
- [46] Z. Dragojlovic, F. Najmabadi, and M. Day. An embedded boundary method for viscous, conducting compressible flow. *Journal of Computational Physics*, 216(1):37–51, 2006. ISSN 0021-9991. doi: <https://doi.org/10.1016/j.jcp.2005.11.025>. URL <https://www.sciencedirect.com/science/article/pii/S0021999105005413>.
- [47] D. Drew and S. Passman. *Theory of Multicomponent Fluids*. Springer, 2014. ISBN 9781468492262. URL https://books.google.fr/books?id=rZb_sgEACAAJ.
- [48] D. Drikakis, J. Majewski, J. Rokicki, and J. Óltak. Investigation of blending-function-based overlapping-grid technique for compressible flows. *Computer Methods in Applied Mechanics and Engineering*, 190(39):5173–5195, 2001. ISSN 00457825. doi: 10.1016/S0045-7825(00)00373-X.
- [49] E. Dvorkin and K.-J. Bathe. A continuum mechanics based four-node shell element for general nonlinear analysis. *Engineering Computations*, 1:77–88, 12 1984. doi: 10.1108/eb023562.
- [50] E. English R., L. Qiu, Y. Yu, and R. Fedkiw. Chimera grids for water simulation. *Proceedings - SCA 2013: 12th ACM SIGGRAPH / Eurographics Symposium on Computer Animation*, pages 85–94, 2013. doi: 10.1145/2485895.2485897.

- [51] E. Fadlun, R. Verzicco, P. Orlandi, and J. Mohd-Yusof. Combined immersed-boundary finite-difference methods for three-dimensional complex flow simulations. *Journal of Computational Physics*, 161(1):35–60, 2000. ISSN 0021-9991. doi: <https://doi.org/10.1006/jcph.2000.6484>. URL <https://www.sciencedirect.com/science/article/pii/S0021999100964842>.
- [52] J. Falcovitz, G. Alfandary, and G. Hanoch. A two-dimensional conservation laws scheme for compressible flows with moving boundaries. *Journal of Computational Physics*, 138(1):83–102, 1997. ISSN 0021-9991. doi: <https://doi.org/10.1006/jcph.1997.5808>. URL <https://www.sciencedirect.com/science/article/pii/S0021999197958083>.
- [53] C. Farhat and V. K. Lakshminarayan. An ALE formulation of embedded boundary methods for tracking boundary layers in turbulent fluid–structure interaction problems. *Journal of Computational Physics*, 263:53–70, apr 2014. ISSN 0021-9991. doi: 10.1016/J.JCP.2014.01.018.
- [54] C. Farhat, A. Rallu, and S. Shankaran. A higher-order generalized ghost fluid method for the poor for the three-dimensional two-phase flow computation of underwater implosions. *Journal of Computational Physics*, 227(16):7674–7700, 2008.
- [55] C. Farhat, K. G. Wang, A. Main, S. Kyriakides, L.-H. Lee, K. Ravi-Chandar, and T. Belytschko. Dynamic implosion of underwater cylindrical shells: Experiments and computations. *International Journal of Solids and Structures*, 50(19):2943–2961, 2013.
- [56] V. Faucher, P. Galon, A. Beccantini, F. Crouzet, F. Debaud, and T. Gautier. Hybrid parallel strategy for the simulation of fast transient accidental situations at reactor scale. *Annals of Nuclear Energy*, 82:188–194, 2015. ISSN 0306-4549. doi: <https://doi.org/10.1016/j.anucene.2014.07.049>. URL <https://www.sciencedirect.com/science/article/pii/S0306454914003806>. Joint International Conference on Supercomputing in Nuclear Applications and Monte Carlo 2013, SNA + MC 2013. Pluri- and Trans-disciplinarity, Towards New Modeling and Numerical Simulation Paradigms.
- [57] R. P. Fedkiw. Coupling an Eulerian fluid calculation to a Lagrangian solid calculation with the ghost fluid method. *Journal of Computational Physics*, 175(1):200–224, 2002.
- [58] R. P. Fedkiw, T. Aslam, B. Merriman, and S. Osher. A non-oscillatory Eulerian approach to interfaces in multimaterial flows (the ghost fluid method). *Journal of computational physics*, 152(2):457–492, 1999.
- [59] A. Fernier. *Multi-model coupling for fluid structure interaction*. Theses, Université Paris-Saclay, Jan. 2019. URL <https://pastel.archives-ouvertes.fr/tel-02086404>.
- [60] A. Fernier, V. Faucher, and O. Jamond. Multi-model Arlequin method for transient structural dynamics with explicit time integration. *International Journal for Numerical Methods in Engineering*, 112(9):1194–1215, 2017. ISSN 10970207. doi: 10.1002/nme.5553.
- [61] A. Fernier, V. Faucher, and O. Jamond. Multi-model arlequin approaches for fast transient, fsi-oriented, fluid dynamics with explicit time integration. *Computers and Fluids*, 199:104428, 2020. ISSN 0045-7930. doi: <https://doi.org/10.1016/j.compfluid.2020.104428>. URL <http://www.sciencedirect.com/science/article/pii/S0045793020300049>.
- [62] F. Feyel. A multilevel finite element method (fe2) to describe the response of highly non-linear structures using generalized continua. *Computer Methods in Applied Mechanics and Engineering*, 192:3233–3244, 2003.

- [63] F. Feyel and J.-L. Chaboche. Fe2 multiscale approach for modelling the elastoviscoplastic behaviour of long fibre sic/ti composite materials. *Computer Methods in Applied Mechanics and Engineering*, 183(3):309–330, 2000. ISSN 0045-7825. doi: [https://doi.org/10.1016/S0045-7825\(99\)00224-8](https://doi.org/10.1016/S0045-7825(99)00224-8). URL <https://www.sciencedirect.com/science/article/pii/S0045782599002248>.
- [64] G. Fillola. *Étude expérimentale et simulations numériques d'écoulements autour des surfaces mobiles de voilure*. PhD thesis, École Nationale Supérieure de l'Aéronautique et de l'Espace (ENSAE), 2006.
- [65] J. Fish and V. Belsky. Multigrid method for periodic heterogeneous media part 1: Convergence studies for one-dimensional case. *Computer Methods in Applied Mechanics and Engineering*, 126(1):1–16, 1995. ISSN 0045-7825. doi: [https://doi.org/10.1016/0045-7825\(95\)00811-E](https://doi.org/10.1016/0045-7825(95)00811-E). URL <https://www.sciencedirect.com/science/article/pii/004578259500811E>.
- [66] J. Fish and V. Belsky. Multi-grid method for periodic heterogeneous media part 2: Multi-scale modeling and quality control in multidimensional case. *Computer Methods in Applied Mechanics and Engineering*, 126(1):17–38, 1995. ISSN 0045-7825. doi: [https://doi.org/10.1016/0045-7825\(95\)00812-F](https://doi.org/10.1016/0045-7825(95)00812-F). URL <https://www.sciencedirect.com/science/article/pii/004578259500812F>.
- [67] P. Gamnitzer and W. A. Wall. An ALE-Chimera method for large deformation fluid structure interaction. *Proceedings of the European Conference on Computational Fluid Dynamics, ECCOMAS CFD, The Netherlands, TU Delft*, (June 2014):1–14, 2006. URL <http://proceedings.fyper.com/eccomascfd2006/documents/550.pdf>.
- [68] A. Ghanem. *Contributions à la modélisation avancée des machines tournantes en dynamique transitoire dans le cadre Arlequin*. PhD thesis, 2013. URL <http://www.theses.fr/2013ISAL0006>. Thèse de doctorat dirigée par Baranger, Thouraya N. Mécanique Lyon, INSA 2013.
- [69] A. Ghanem, M. Torkhani, N. Mahjoubi, T. Baranger, and A. Combescure. Arlequin framework for multi-model, multi-time scale and heterogeneous time integrators for structural transient dynamics. *Computer Methods in Applied Mechanics and Engineering*, 254:292–308, 2013. ISSN 0045-7825. doi: <https://doi.org/10.1016/j.cma.2012.08.019>. URL <https://www.sciencedirect.com/science/article/pii/S004578251200271X>.
- [70] A. Gilmanov and F. Sotiropoulos. A hybrid cartesian/immersed boundary method for simulating flows with 3d, geometrically complex, moving bodies. *Journal of Computational Physics*, 207(2):457–492, 2005. ISSN 0021-9991. doi: <https://doi.org/10.1016/j.jcp.2005.01.020>. URL <https://www.sciencedirect.com/science/article/pii/S0021999105000379>.
- [71] R. Glowinski, T.-W. Pan, and J. Periaux. A fictitious domain method for Dirichlet problem and applications. *Computer Methods in Applied Mechanics and Engineering*, 111(3-4):283–303, 1994.
- [72] R. Glowinski, T.-W. Pan, T. I. Hesla, and D. D. Joseph. A distributed Lagrange multiplier/fictitious domain method for particulate flows. *International Journal of Multiphase Flow*, 25(5):755–794, 1999.

- [73] S. K. Godunov and I. Bohachevsky. Finite difference method for numerical computation of discontinuous solutions of the equations of fluid dynamics. *Matematičeskij sbornik*, 47(89)(3): 271–306, 1959. URL <https://hal.archives-ouvertes.fr/hal-01620642>.
- [74] B. Gustafsson, H.-O. Kreiss, and A. Sundström. Stability theory of difference approximations for mixed initial boundary value problems. ii. *Mathematics of Computation*, 26(119):649–686, 1972. ISSN 00255718, 10886842. URL <http://www.jstor.org/stable/2005093>.
- [75] J.-F. Haas and B. Sturtevant. Interaction of weak shock waves with cylindrical and spherical gas inhomogeneities. *Journal of Fluid Mechanics*, 181:41–76, 1987. doi: 10.1017/S0022112087002003.
- [76] W. Hackbusch. *General Multi-Grid Iteration*. Springer Berlin Heidelberg, Berlin, Heidelberg, 1985. ISBN 978-3-662-02427-0. doi: 10.1007/978-3-662-02427-0_4. URL https://doi.org/10.1007/978-3-662-02427-0_4.
- [77] R. M. Hackett. *Finite Elasticity*, pages 1–3. Springer International Publishing, Cham, 2016. ISBN 978-3-319-23273-7. doi: 10.1007/978-3-319-23273-7_1. URL https://doi.org/10.1007/978-3-319-23273-7_1.
- [78] A. Harten. High resolution schemes for hyperbolic conservation laws. *Journal of Computational Physics*, 49(3):357–393, 1983. ISSN 0021-9991. doi: [https://doi.org/10.1016/0021-9991\(83\)90136-5](https://doi.org/10.1016/0021-9991(83)90136-5). URL <https://www.sciencedirect.com/science/article/pii/S0021999183901365>.
- [79] A. Harten, P. Lax, and B. van Leer. On upstream differencing and godunov-type schemes for hyperbolic conservation laws. *SIAM Rev*, 25:35–61, 01 1983.
- [80] A. Harten, B. Engquist, S. Osher, and S. R. Chakravarthy. Uniformly high order accurate essentially non-oscillatory schemes, iii. *Journal of Computational Physics*, 131(1):3–47, 1997. ISSN 0021-9991. doi: <https://doi.org/10.1006/jcph.1996.5632>. URL <https://www.sciencedirect.com/science/article/pii/S0021999196956326>.
- [81] D. Hartmann, M. Meinke, and W. Schröder. A strictly conservative cartesian cut-cell method for compressible viscous flows on adaptive grids. *Computer Methods in Applied Mechanics and Engineering*, 200(9):1038–1052, 2011. ISSN 0045-7825. doi: <https://doi.org/10.1016/j.cma.2010.05.015>. URL <https://www.sciencedirect.com/science/article/pii/S0045782510001647>.
- [82] W. D. Henshaw. Ogen: An overlapping grid generator for Overture. *LANL unclassified report*, pages 96–3466, 1998.
- [83] W. D. Henshaw and D. W. Schwendeman. An adaptive numerical scheme for high-speed reactive flow on overlapping grids. *Journal of Computational Physics*, 191(2):420–447, 2003. ISSN 00219991. doi: 10.1016/S0021-9991(03)00323-1.
- [84] W. D. Henshaw and D. W. Schwendeman. Moving overlapping grids with adaptive mesh refinement for high-speed reactive and non-reactive flow. *Journal of Computational Physics*, 216(2):744–779, 2006. ISSN 10902716. doi: 10.1016/j.jcp.2006.01.005.
- [85] C. W. Hirt, A. A. Amsden, and J. L. Cook. An arbitrary Lagrangian-Eulerian computing method for all flow speeds. *Journal of Computational Physics*, 14(3):227–253, Mar. 1974. ISSN 0021-9991. doi: 10.1016/0021-9991(74)90051-5.

- [86] G. Houzeaux and R. Codina. A Chimera method based on a Dirichlet/Neumann(Robin) coupling for the Navier-Stokes equations. *Computer Methods in Applied Mechanics and Engineering*, 192(31-32):3343–3377, 2003. ISSN 00457825. doi: 10.1016/S0045-7825(03)00276-7.
- [87] G. Houzeaux, B. Eguzkitza, R. Aubry, H. Owen, and M. Vázquez. A Chimera method for the incompressible Navier-Stokes equations. *International Journal for Numerical Methods in Fluids*, 75(3):155–183, 2014. ISSN 10970363. doi: 10.1002/fld.3886.
- [88] X. Hu, B. Khoo, N. Adams, and F. Huang. A conservative interface method for compressible flows. *Journal of Computational Physics*, 219(2):553–578, 2006. ISSN 0021-9991. doi: <https://doi.org/10.1016/j.jcp.2006.04.001>. URL <https://www.sciencedirect.com/science/article/pii/S0021999106001926>.
- [89] D. Iampietro, F. Daude, and P. Galon. A low-diffusion self-adaptive flux-vector splitting approach for compressible flows. *Computers and Fluids*, 206:104586, 2020. ISSN 00457930. doi: 10.1016/j.compfluid.2020.104586. URL <https://doi.org/10.1016/j.compfluid.2020.104586>.
- [90] A. Jameson. Solution of the euler equations for two dimensional transonic flow by a multigrid method. *Applied Mathematics and Computation*, 13(3):327–355, 1983. ISSN 0096-3003. doi: [https://doi.org/10.1016/0096-3003\(83\)90019-X](https://doi.org/10.1016/0096-3003(83)90019-X). URL <https://www.sciencedirect.com/science/article/pii/009630038390019X>.
- [91] A. Jameson and S. Yoon. Multigrid solution of the euler equations using implicit schemes. *AIAA Journal*, 24(11):1737–1743, 1986. doi: 10.2514/3.9518. URL <https://doi.org/10.2514/3.9518>.
- [92] O. Jamond and A. Beccantini. An embedded boundary method for an inviscid compressible flow coupled to deformable thin structures: The mediating body method. *International Journal for Numerical Methods in Engineering*, 119(5):305–333, 2019. doi: <https://doi.org/10.1002/nme.6051>. URL <https://onlinelibrary.wiley.com/doi/abs/10.1002/nme.6051>.
- [93] O. Jamond and H. B. Dhia. Incompressibility in the multimodel arlequin framework. *International Journal for Numerical Methods in Engineering*, 94(4):374–399, 2013. doi: <https://doi.org/10.1002/nme.4454>. URL <https://onlinelibrary.wiley.com/doi/abs/10.1002/nme.4454>.
- [94] O. Jamond and V. Faucher. Regularized immersed boundary-type formulation for fast transient dynamics with fluid-structure interaction. *Advances in Engineering Software*, 2017. ISSN 0965-9978. doi: 10.1016/j.advengsoft.2017.02.002.
- [95] P. Jenny, S. Lee, and H. Tchelepi. Multi-scale finite-volume method for elliptic problems in subsurface flow simulation. *Journal of Computational Physics*, 187(1):47–67, 2003. ISSN 0021-9991. doi: [https://doi.org/10.1016/S0021-9991\(03\)00075-5](https://doi.org/10.1016/S0021-9991(03)00075-5). URL <https://www.sciencedirect.com/science/article/pii/S0021999103000755>.
- [96] P. Jenny, S. Lee, and H. Tchelepi. Adaptive multiscale finite-volume method for multiphase flow and transport in porous media. *Society for Industrial and Applied Mathematics*, 3:50–64, 09 2004. doi: 10.1137/030600795.
- [97] T. J. Jespersen and D. C. Barth. The design and application of upwind schemes on unstructured meshes. *27th Aerospace Sciences Meeting*, 1989.

- [98] E. Johnsen and T. Colonius. Implementation of weno schemes in compressible multicomponent flow problems. *Journal of Computational Physics*, 219(2):715–732, 2006. ISSN 0021-9991. doi: <https://doi.org/10.1016/j.jcp.2006.04.018>. URL <https://www.sciencedirect.com/science/article/pii/S0021999106002014>.
- [99] M. Joyce. *Nuclear Safety and Regulation*. 2018. ISBN 9780081009628. doi: 10.1016/b978-0-08-100962-8.00014-7.
- [100] K. H. Kao and M. S. Liou. Advance in overset grid schemes: From Chimera to DRAGON grids. *AIAA journal*, 33(10):1809–1815, 1995.
- [101] K. H. Kao, M. S. Liou, and C. Y. Chow. Grid adaptation using chimera composite overlapping meshes. *AIAA journal*, 32(5):942–949, 1994.
- [102] E. Katzer. *Multigrid methods for hyperbolic equations*, pages 253–263. Birkhäuser Basel, Basel, 1991. ISBN 978-3-0348-5712-3. doi: 10.1007/978-3-0348-5712-3_18. URL https://doi.org/10.1007/978-3-0348-5712-3_18.
- [103] R. Künze, I. Lunati, and S. Lee. A multilevel multiscale finite-volume method. *Journal of Computational Physics*, 255:502–520, 12 2013. doi: 10.1016/j.jcp.2013.08.042.
- [104] B. Landmann and M. Montagnac. A highly automated parallel Chimera method for overset grids based on the implicit hoe cutting technique . *International Journal for Numerical Methods in Fluids*, 66:778–804, 2011. ISSN 02712091. doi: 10.1002/flf.
- [105] A. Lani, B. Sjogreen, H. Yee, and W. Henshaw. Variable high-order multiblock overlapping grid methods for mixed steady and unsteady multiscale viscous flows, part ii: Hypersonic nonequilibrium flows. volume 13, 06 2011. doi: 10.2514/6.2011-3140.
- [106] G. Layes, G. Jourdan, and L. Houas. Distortion of a spherical gaseous interface accelerated by a plane shock wave. *Phys. Rev. Lett.*, 91:174502, Oct 2003. doi: 10.1103/PhysRevLett.91.174502. URL <https://link.aps.org/doi/10.1103/PhysRevLett.91.174502>.
- [107] K. R. Lee, J. H. Park, and K. H. Kim. High-order interpolation method for overset grid based on finite volume method. *AIAA Journal*, 49(7):1387–1398, 2011. doi: 10.2514/1.J050620.
- [108] A. Lerat and Z. Wu. Stable conservative multidomain treatments for implicit euler solvers. *Journal of Computational Physics*, 123(1):45–64, 1996. ISSN 0021-9991. doi: <https://doi.org/10.1006/jcph.1996.0004>. URL <https://www.sciencedirect.com/science/article/pii/S0021999196900042>.
- [109] R. LeVeque and Z. Li. The immersed interface method for elliptic equations with discontinuous coefficients and singular sources. *SIAM Journal on Numerical Analysis*, 31(4):1019–1044, Aug. 1994. ISSN 0036-1429. doi: 10.1137/0731054.
- [110] R. J. LeVeque. *Finite volume methods for hyperbolic problems*. Cambridge Texts in Applied Mathematics. Cambridge University Press, 2002. doi: 10.1017/CBO9780511791253.
- [111] R. J. LeVeque and Z. Li. Immersed interface methods for Stokes flow with elastic boundaries or surface tension. *SIAM Journal on Scientific Computing*, 18(3):709–735, 1997.
- [112] Z. Li and M.-C. Lai. The immersed interface method for the Navier–Stokes equations with singular forces. *Journal of Computational Physics*, 171(2):822–842, 2001.

- [113] R. Liska and B. Wendroff. Comparison of several difference schemes for the euler equations in 1d and 2d. In T. Y. Hou and E. Tadmor, editors, *Hyperbolic Problems: Theory, Numerics, Applications*, pages 831–840, Berlin, Heidelberg, 2003. Springer Berlin Heidelberg. ISBN 978-3-642-55711-8.
- [114] X.-D. Liu, S. Osher, and T. Chan. Weighted essentially non-oscillatory schemes. *Journal of Computational Physics*, 115(1):200–212, 1994. ISSN 0021-9991. doi: <https://doi.org/10.1006/jcph.1994.1187>. URL <https://www.sciencedirect.com/science/article/pii/S0021999184711879>.
- [115] R. Löhner, J. R. Cebal, F. E. Camelli, S. Appanaboyina, J. D. Baum, E. L. Mestreau, and O. A. Soto. Adaptive embedded and immersed unstructured grid techniques. *Computer Methods in Applied Mechanics and Engineering*, 197(25):2173–2197, Apr. 2008. ISSN 0045-7825. doi: 10.1016/j.cma.2007.09.010.
- [116] I. Lunati and P. Jenny. Multiscale finite-volume method for compressible multiphase flow in porous media. *Journal of Computational Physics*, 216(2):616–636, 2006. ISSN 0021-9991. doi: <https://doi.org/10.1016/j.jcp.2006.01.001>. URL <https://www.sciencedirect.com/science/article/pii/S0021999106000039>.
- [117] C. Mastin. Implicit finite difference methods on composite grids. *Journal of Computational and Applied Mathematics*, 20:317–323, 1987. ISSN 0377-0427. doi: [https://doi.org/10.1016/0377-0427\(87\)90148-8](https://doi.org/10.1016/0377-0427(87)90148-8). URL <https://www.sciencedirect.com/science/article/pii/0377042787901488>.
- [118] D. Mavriplis. 2003: Revisiting the least-squares procedure for gradient reconstruction on unstructured meshes. *16th AIAA Computational Fluid Dynamics Conference*, 06 2003. doi: 10.2514/6.2003-3986.
- [119] R. L. Meakin. Moving body overset grid methods for complete aircraft tiltrotor simulations. *AIAA paper*, 3350, 1993.
- [120] R. L. Meakin. An efficient means of adaptive refinement within systems of overset grids. *AIAA paper*, 1722, 1995.
- [121] B. E. Merrill and Y. T. Peet. Moving overlapping grid methodology of spectral accuracy for incompressible flow solutions around rigid bodies in motion. *Journal of Computational Physics*, 390:121–151, 2019. ISSN 0021-9991. doi: <https://doi.org/10.1016/j.jcp.2019.01.048>. URL <https://www.sciencedirect.com/science/article/pii/S0021999119301068>.
- [122] J. Mohd-Yusof. For simulations of flow in complex geometries. *Annual Research Briefs*, 317, 1997.
- [123] L. Monasse, V. Daru, C. Mariotti, S. Piperno, and C. Tenaud. A conservative coupling algorithm between a compressible flow and a rigid body using an embedded boundary method. *Journal of Computational Physics*, 231(7):2977–2994, Apr. 2012. ISSN 0021-9991. doi: 10.1016/j.jcp.2012.01.002.
- [124] W. A. Mulder. Multigrid relaxation for the euler equations. *Journal of Computational Physics*, 60(2):235–252, 1985. ISSN 0021-9991. doi: [https://doi.org/10.1016/0021-9991\(85\)90005-1](https://doi.org/10.1016/0021-9991(85)90005-1). URL <https://www.sciencedirect.com/science/article/pii/0021999185900051>.

- [125] W. A. Mulder. A new multigrid approach to convection problems. *Journal of Computational Physics*, 83(2):303–323, 1989. ISSN 0021-9991. doi: [https://doi.org/10.1016/0021-9991\(89\)90121-6](https://doi.org/10.1016/0021-9991(89)90121-6). URL <https://www.sciencedirect.com/science/article/pii/S0021999189901216>.
- [126] R. Muscari, R. Broglia, and A. Di Mascio. An Overlapping Grids Approach For Moving Bodies Problems. All Days, 05 2006. ISOPE-I-06-007.
- [127] S. Müller and Y. Stiriba. A multilevel finite volume method with multiscale-based grid adaptation for steady compressible flows. *Journal of Computational and Applied Mathematics*, 227(2):223–233, 2009. ISSN 0377-0427. doi: <https://doi.org/10.1016/j.cam.2008.03.035>. URL <https://www.sciencedirect.com/science/article/pii/S0377042708001064>. Special Issue on Emergent Applications of Fractals and Wavelets in Biology and Biomedicine.
- [128] R. H. Ni. A multiple grid scheme for solving the Euler equations. In *5th Computational Fluid Dynamics Conference*, pages 257–264, Jan. 1981.
- [129] J. Oden and T. I. Zohdi. Analysis and adaptive modeling of highly heterogeneous elastic structures. *Computer Methods in Applied Mechanics and Engineering*, 148(3):367–391, 1997. ISSN 0045-7825. doi: [https://doi.org/10.1016/S0045-7825\(97\)00032-7](https://doi.org/10.1016/S0045-7825(97)00032-7). URL <https://www.sciencedirect.com/science/article/pii/S0045782597000327>.
- [130] J. T. Oden and K. Vemaganti. Adaptive modeling of composite structures: Modeling error estimation. *Texas Institute for Computational and Applied Mathematics*, 1:1–16, 1999.
- [131] J. T. Oden, K. Vemaganti, and N. Moës. Hierarchical modeling of heterogeneous solids. *Computer Methods in Applied Mechanics and Engineering*, 172(1):3–25, 1999. ISSN 0045-7825. doi: [https://doi.org/10.1016/S0045-7825\(98\)00224-2](https://doi.org/10.1016/S0045-7825(98)00224-2). URL <https://www.sciencedirect.com/science/article/pii/S0045782598002242>.
- [132] J. Park, Y. Cho, S. Kim, and J. Lee. *Effects of leak rate on LOCA probability of pipes in nuclear power plants*. 12 2014. ISBN 9780081002032. doi: 10.1533/9780081002254.203.
- [133] E. Pärt-Enander and B. Sjögreen. Conservative and non-conservative interpolation between overlapping grids for finite volume solutions of hyperbolic problems. *Computers and Fluids*, 23(3):551–574, 1994.
- [134] W. Paul and C. Phillip. The numerical simulation of two-dimensional fluid flow with strong shocks. *Journal of Computational Physics*, 54(1):115–173, 1984. ISSN 0021-9991. doi: [https://doi.org/10.1016/0021-9991\(84\)90142-6](https://doi.org/10.1016/0021-9991(84)90142-6). URL <https://www.sciencedirect.com/science/article/pii/S0021999184901426>.
- [135] R. B. Pember, J. B. Bell, P. Colella, W. Y. Curtchfield, and M. L. Welcome. An adaptive cartesian grid method for unsteady compressible flow in irregular regions. *Journal of Computational Physics*, 120(2):278–304, 1995. ISSN 0021-9991. doi: <https://doi.org/10.1006/jcph.1995.1165>. URL <https://www.sciencedirect.com/science/article/pii/S0021999185711655>.
- [136] S. Péron. *Méthode d'assemblage de maillages recouvrants autour de géométries complexes pour des simulations en aérodynamique compressible*. PhD thesis, Mécanique-Matériaux Paris, ENSAM, 2014.

- [137] S. Péron, C. Benoit, T. Renaud, and i. mary. An immersed boundary method on Cartesian adaptive grids for the simulation of compressible flows around arbitrary geometries. *Engineering with Computers*, 2020. doi: 10.1007/s00366-020-00950-y. URL <https://hal.archives-ouvertes.fr/hal-02502256>.
- [138] C. S. Peskin. Flow patterns around heart valves: A numerical method. *Journal of computational physics*, 10(2):252–271, 1972.
- [139] C. S. Peskin. The immersed boundary method. *Acta numerica*, 11:479–517, 2002.
- [140] A. Posa and R. Broglia. An immersed boundary method coupled with a dynamic overlapping-grids strategy. *Computers and Fluids*, 191:104250, 2019. ISSN 0045-7930. doi: <https://doi.org/10.1016/j.compfluid.2019.104250>. URL <https://www.sciencedirect.com/science/article/pii/S004579301930218X>.
- [141] N. C. Prewitt, D. M. Belk, and W. Shyy. Parallel computing of overset grids for aerodynamic problems with moving objects. *Progress in Aerospace Sciences*, 36(2):117–172, 2000.
- [142] S. Prudhomme, H. B. Dhia, P. Bauman, N. Elkhodja, and J. Oden. Computational analysis of modeling error for the coupling of particle and continuum models by the arlequin method. *Computer Methods in Applied Mechanics and Engineering*, 197(41):3399–3409, 2008. ISSN 0045-7825. doi: <https://doi.org/10.1016/j.cma.2008.03.014>. URL <https://www.sciencedirect.com/science/article/pii/S0045782508001242>. Recent Advances in Computational Study of Nanostructures.
- [143] S. Prudhomme, L. Chamoin, H. B. Dhia, and P. T. Bauman. An adaptive strategy for the control of modeling error in two-dimensional atomic-to-continuum coupling simulations. *Computer Methods in Applied Mechanics and Engineering*, 198(21):1887–1901, 2009. ISSN 0045-7825. doi: <https://doi.org/10.1016/j.cma.2008.12.026>. URL <https://www.sciencedirect.com/science/article/pii/S004578250900005X>. Advances in Simulation-Based Engineering Sciences – Honoring J. Tinsley Oden.
- [144] M. A. Puscas. *Conservative coupling method between an inviscid compressible fluid flow and a three-dimensional deformable structure with possible fragmentation*. Theses, Université Paris-Est, Oct. 2014. URL <https://pastel.archives-ouvertes.fr/tel-01111912>.
- [145] M. A. Puscas and L. Monasse. A three-dimensional conservative coupling method between an inviscid compressible flow and a moving rigid solid. *SIAM Journal on Scientific Computing*, 37: 884–909, 2015. URL <https://hal.archives-ouvertes.fr/hal-00974602>.
- [146] I. Ramière, R. Masson, B. Michel, and S. Bernard. Un schéma de calcul multi-échelles de type Éléments Finis au carré pour la simulation de combustibles nucléaires hétérogènes. In *13e colloque national en calcul des structures*, Giens, Var, France, May 2017. Université Paris-Saclay. URL <https://hal.archives-ouvertes.fr/hal-01922538>.
- [147] L. Ramírez, X. Nogueira, P. Ouro, F. Navarrina, S. Khelladi, and I. Colominas. A higher-order Chimera method for finite volume schemes. *Archives of Computational Methods in Engineering*, 25(3):691–706, 2018. ISSN 18861784. doi: 10.1007/s11831-017-9213-8.
- [148] L. Ramírez, C. Foulquié, X. Nogueira, S. Khelladi, J.-C. Chassaing, and I. Colominas. New high-resolution-preserving sliding mesh techniques for higher-order finite volume schemes. *Computers and Fluids*, 118:114–130, 2015. ISSN 0045-7930. doi: <https://doi.org/10.1016/j>

- compfluid.2015.06.008. URL <https://www.sciencedirect.com/science/article/pii/S0045793015001917>.
- [149] G. Rateau. Méthode arlequin pour les problèmes mécaniques multi-échelles, applications a des problèmes de jonction et de fissuration de structures élancées. 2003.
- [150] T. Renaud, M. Costes, and S. Péron. Computation of goahead configuration with chimera assembly. *Aerospace Science and Technology*, 19(1):50–57, 2012. ISSN 1270-9638. doi: <https://doi.org/10.1016/j.ast.2011.07.001>. URL <https://www.sciencedirect.com/science/article/pii/S127096381100109X>. GOAHEAD.
- [151] D. Rixen, C. Farhat, and M. Géradin. A two-step, two-field hybrid method for the static and dynamic analysis of substructure problems with conforming and non-conforming interfaces. *Computer Methods in Applied Mechanics and Engineering*, 154(3):229 – 264, 1998. ISSN 0045-7825. doi: [https://doi.org/10.1016/S0045-7825\(97\)00128-X](https://doi.org/10.1016/S0045-7825(97)00128-X). URL <http://www.sciencedirect.com/science/article/pii/S004578259700128X>.
- [152] E. Sanchez-Palencia. *Operators in Banach spaces*. Springer Berlin Heidelberg, Berlin, Heidelberg, 1980. ISBN 978-3-540-39317-7. doi: 10.1007/3-540-10000-8_2. URL https://doi.org/10.1007/3-540-10000-8_2.
- [153] D. Sarkar. *General Description of Thermal Power Plants*. 12 2017. ISBN 9780081011126. doi: 10.1016/B978-0-08-101112-6.00001-0.
- [154] D. Schwamborn, T. Gerhold, and R. Heinrich. The DLR TAU-Code: Recent applications in research and industry. 2006.
- [155] P. Schwartz, M. Barad, P. Colella, and T. Ligocki. A cartesian grid embedded boundary method for the heat equation and poisson’s equation in three dimensions. *Journal of Computational Physics*, 211(2):531–550, 2006. ISSN 0021-9991. doi: <https://doi.org/10.1016/j.jcp.2005.06.010>. URL <https://www.sciencedirect.com/science/article/pii/S002199910500286X>.
- [156] P. K. Seshadri and A. De. A novel sharp interface immersed boundary framework for viscous flow simulations at arbitrary mach number involving complex and moving boundaries. *Computers and Fluids*, 206:104579, 2020. ISSN 0045-7930. doi: <https://doi.org/10.1016/j.compfluid.2020.104579>. URL <https://www.sciencedirect.com/science/article/pii/S0045793020301511>.
- [157] S. E. Sherer and J. N. Scott. High-order compact finite-difference methods on general overset grids. *Journal of Computational Physics*, 210(2):459–496, 2005. ISSN 10902716. doi: 10.1016/j.jcp.2005.04.017.
- [158] J. Simo, D. Fox, and M. Rifai. On a stress resultant geometrically exact shell model. part ii: The linear theory; computational aspects. *Computer Methods in Applied Mechanics and Engineering*, 73(1):53–92, 1989. ISSN 0045-7825. doi: [https://doi.org/10.1016/0045-7825\(89\)90098-4](https://doi.org/10.1016/0045-7825(89)90098-4). URL <https://www.sciencedirect.com/science/article/pii/S0045782589900984>.
- [159] J. Sinclair and X. Cui. A theoretical approximation of the shock standoff distance for supersonic flows around a circular cylinder. *Physics of Fluids*, 29(2):26–102, 2017. doi: 10.1063/1.4975983.

- [160] G. A. Sod. A survey of several finite difference methods for systems of nonlinear hyperbolic conservation laws. *Journal of Computational Physics*, 27(1):1–31, 1978. ISSN 0021-9991. doi: [https://doi.org/10.1016/0021-9991\(78\)90023-2](https://doi.org/10.1016/0021-9991(78)90023-2). URL <https://www.sciencedirect.com/science/article/pii/0021999178900232>.
- [161] I. Sokolova, M. G. Bastisya, and H. Hajibeygi. Multiscale finite volume method for finite-volume-based simulation of poroelasticity. *Journal of Computational Physics*, 379:309–324, 2019. ISSN 0021-9991. doi: <https://doi.org/10.1016/j.jcp.2018.11.039>. URL <https://www.sciencedirect.com/science/article/pii/S0021999118307848>.
- [162] D. Solyga and P. Galon. Introduction d'une nouvelle méthode de reconstruction du second ordre en temps et en espace basée sur les variables primitives. *CEA report: Development in the fast transient dynamics code Europlexus.*, (June), 2015. doi: 10.13140/rg.2.1.1471.0888.
- [163] G. Starius. Composite mesh difference methods for elliptic boundary value problems. *Numerische Mathematik*, 28:243–258, 1977.
- [164] G. Starius. On composite mesh difference methods for hyperbolic differential equations. *Numerische Mathematik*, 35:241–255, 1980.
- [165] J. Steger and J. Benek. On the use of composite grid schemes in computational aerodynamics. *Computer Methods in Applied Mechanics and Engineering*, 64:301–320, 1987.
- [166] J. Steger, F. Dougherty, and J. Benek. A Chimera grid scheme. *ASME MiniSymposium on Advances in Grid Generation*, 5:59–69, June 1982.
- [167] J. M. Stone, T. A. Gardiner, P. Teuben, J. F. Hawley, and J. B. Simon. Athena: A new code for astrophysical MHD. *The Astrophysical Journal Supplement Series*, 178(1):137–177, sep 2008. doi: 10.1086/588755. URL <https://doi.org/10.1086/588755>.
- [168] K. Sugaya and T. Imamura. *Unsteady Flow Simulation using the Immersed Boundary Method on the Cartesian Grid with Moving Grid Technique*. doi: 10.2514/6.2021-1549. URL <https://arc.aiaa.org/doi/abs/10.2514/6.2021-1549>.
- [169] P. K. Sweby. High resolution schemes using flux limiters for hyperbolic conservation laws. *SIAM Journal on Numerical Analysis*, 21(5):995–1011, 1984. doi: 10.1137/0721062. URL <https://doi.org/10.1137/0721062>.
- [170] E. F. Toro. *Riemann Solvers and Numerical Methods for Fluid Dynamics*. Springer Berlin Heidelberg, 2009. ISBN 9783540252023. doi: 10.1007/b79761.
- [171] E. F. Toro and J. F. Clarke. A weighted average flux method for hyperbolic conservation laws. *Proceedings of the Royal Society of London. A. Mathematical and Physical Sciences*, 423(1865):401–418, 1989. doi: 10.1098/rspa.1989.0062. URL <https://royalsocietypublishing.org/doi/abs/10.1098/rspa.1989.0062>.
- [172] E. F. Toro, M. Spruce, and W. Speares. Restoration of the contact surface in the hll-riemann solver. *Shock Waves*, 4:25–34, 1994. ISSN 0021-9991. doi: <https://doi.org/10.1007/BF01414629>.
- [173] Y.-H. Tseng and J. H. Ferziger. A ghost-cell immersed boundary method for flow in complex geometry. *Journal of Computational Physics*, 192(2):593–623, 2003. ISSN 0021-9991. doi: <https://doi.org/10.1016/j.jcp.2003.07.024>. URL <https://www.sciencedirect.com/science/article/pii/S0021999103004108>.

- [174] J. Y. Tu and L. Fuchs. Overlapping grids and multigrid methods for three-dimensional unsteady flow calculations in IC engines. *International Journal for Numerical Methods in Fluids*, 15(6): 693–714, 1992. ISSN 10970363. doi: 10.1002/flid.1650150605.
- [175] USNRC. Westinghouse technology systems manual. *USNRC Technical Training Center*, 2012.
- [176] B. Van Leer. Towards the ultimate conservative difference scheme. IV. A new approach to numerical convection. *Journal of Computational Physics*, 23(3):276–299, 1977. ISSN 10902716. doi: 10.1016/0021-9991(77)90095-X.
- [177] B. Van Leer. On the relation between the upwind-differencing schemes of godunov, engquist–osher and roe. *SIAM Journal on Scientific and Statistical Computing*, 5:1–20, 03 1984. doi: 10.1137/0905001.
- [178] H. Versteeg and W. Malalasekera. *An introduction to computational fluid dynamics : the finite volume method*. Pearson Education Ltd., Harlow (GB) New York Boston [etc, second edition edition, 2007. ISBN 978-0-13-127498-3.
- [179] U. S. Vevek, B. Zang, and T. H. New. On alternative setups of the double mach reflection problem. *J. Sci. Comput.*, 78(2):1291–1303, feb 2019. ISSN 0885-7474. doi: 10.1007/s10915-018-0803-x. URL <https://doi.org/10.1007/s10915-018-0803-x>.
- [180] E. A. Volkov. The development of a grid method for the solution of laplace’s equation in finite or infinite regions with piecewise-smooth boundaries. *Mathematical notes of the Academy of Sciences of the USSR*, 2:747–755, 1967.
- [181] E. A. Volkov. The method of composite meshes for finite and infinite regions with piecewise smooth boundary. *Automatic programming, numerical methods and functional analysis*, 96: 117–148, 1968.
- [182] K. Wang, A. Rallu, J.-F. Gerbeau, and C. Farhat. Algorithms for interface treatment and load computation in embedded boundary methods for fluid and fluid–structure interaction problems. *International Journal for Numerical Methods in Fluids*, 67(9):1175–1206, Nov. 2011. ISSN 1097-0363. doi: 10.1002/flid.2556.
- [183] Z. Wang, N. Hariharan, and R. Chen. Recent development on the conservation property of chimera. *International Journal of Computational Fluid Dynamics*, 15:265–278, 11 2001. doi: 10.1080/10618560108970033.
- [184] Z. J. Wang. A fully conservative interface algorithm for overlapped grids. *Journal of Computational Physics*, 122:96–106, 1995.
- [185] Z. J. Wang. A conservative interface algorithm for moving Chimera (overlapped) grids. *International Journal of Computational Fluid Dynamics*, 10(3):255–265, 1998. ISSN 10618562. doi: 10.1080/10618569808961689.
- [186] S. Whitaker. *Single-Phase Flow in Heterogeneous Porous Media*. Springer Netherlands, Dordrecht, 1999. ISBN 978-94-017-3389-2. doi: 10.1007/978-94-017-3389-2_5. URL https://doi.org/10.1007/978-94-017-3389-2_5.
- [187] C. Wolf. *A chimera simulation method and detached eddy simulation for vortex-airfoil interactions*. PhD thesis, Georg-Augus-Universität Göttingen, 2011.

- [188] Z.-N. Wu. Uniqueness of steady-state solutions for difference equations on overlapping grids. *SIAM Journal on Numerical Analysis*, 33(4):1336–1357, 1996. ISSN 00361429. URL <http://www.jstor.org/stable/2158306>.
- [189] Z.-N. Wu. Theoretical aspects of composite grid methods in computational fluid dynamics. In N. Satofuka, editor, *Computational Fluid Dynamics 2000*, pages 749–754, Berlin, Heidelberg, 2001. Springer Berlin Heidelberg. ISBN 978-3-642-56535-9.
- [190] L. Xin and L. Jiequan. A non-oscillatory energy-splitting method for the computation of compressible multi-fluid flows. *Physics of Fluids*, 30(4):040906, 2018. doi: 10.1063/1.5011093. URL <https://doi.org/10.1063/1.5011093>.
- [191] J. Yang, S. Preidikman, and E. Balaras. A strongly coupled, embedded-boundary method for fluid–structure interactions of elastically mounted rigid bodies. *Journal of Fluids and Structures*, 24(2):167–182, 2008.
- [192] H. Yee, N. Sandham, and M. Djomehri. Low-dissipative high-order shock-capturing methods using characteristic-based filters. *Journal of Computational Physics*, 150(1):199–238, 1999. ISSN 0021-9991. doi: <https://doi.org/10.1006/jcph.1998.6177>. URL <https://www.sciencedirect.com/science/article/pii/S0021999198961770>.
- [193] X. Zeng and C. Farhat. A systematic approach for constructing higher-order immersed boundary and ghost fluid methods for fluid–structure interaction problems. *Journal of Computational Physics*, 231(7):2892–2923, apr 2012. ISSN 0021-9991. doi: 10.1016/J.JCP.2011.12.027.
- [194] O. Zienkiewicz, R. Taylor, and D. Fox. Chapter 14 - a nonlinear geometrically exact shell model. In O. Zienkiewicz, R. L. Taylor, and D. Fox, editors, *The finite element method for solid and structural mechanics (Seventh Edition)*, pages 519–588. Butterworth-Heinemann, Oxford, seventh edition edition, 2014. ISBN 978-1-85617-634-7. doi: <https://doi.org/10.1016/B978-1-85617-634-7.00014-4>. URL <https://www.sciencedirect.com/science/article/pii/B9781856176347000144>.

